**The Dissertation Committee for Sungmin Han Certifies that this is the approved version of the following Dissertation**

# Catalytic Activity of 2-D Bimetallic Surfaces and 3-D Metal Organic Frameworks

**Committee:**

Charles Buddie Mullins, Supervisor

Graeme Henkelman

Benjamin K. Keitz

Gyeong S. Hwang

Greg O. Sitz

# Catalytic Activity of 2-D Bimetallic Surfaces and 3-D Metal Organic Frameworks

**by**

**Sungmin Han**

**Dissertation**

Presented to the Faculty of the Graduate School of

The University of Texas at Austin

in Partial Fulfillment

of the Requirements

for the Degree of

**Doctor of Philosophy**

**The University of Texas at Austin**

**May 2020**

# Dedication

To my wife Hee Jeong, my baby Lizzy, and my parents In Taek and Hee Joo.

# Acknowledgements

First of all, I would like to give my sincere thanks to my advisor, Professor C. Buddie Mullins, for all his supports that he has given me over the last five years. Buddie has motivated me to be more progressive and enthusiastic to conduct research and also has been a great role model to me as a senior scientist. With his guidance, now I successfully finish my Ph. D. study, and I am ready to explore the bigger scientific world.

I would also like to acknowledge Prof. Keitz, Prof. Henkelman, Prof. Hwang, and Prof. Sitz for their time and efforts serving on my Ph. D. committee. In particular, I appreciate the insightful comments from Prof. Keitz for the HKUST-1 thin film projects and also the valuable contribution form Prof. Henkelman and Dr. Shin for DFT calculations in the Pd–Au study.

I have been very lucky to have the chance to work with the catalysis subgroup members ("Catalysis boys"), Ryan Ciufo, Michael Floto, Ehren Eichler, and Yongtak Kwon. Additionally, I want to thank Dr. Evans and Dr. Mullen, who taught me how to use UHV systems. Bryan Wygant and Melissa Meyerson were willing to spare their time to help my research, so I also express my appreciation to them. Kenta Kawashima, Yoon Jun Son, and Hohyun Sun have always shared their time for me to chat about various topics, which has been really helpful to refresh myself and get back to research again. Other subgroup members in Mullins group are also all my precious friends. Post-Docs in Mullins group, especially Prof. Duck Hyun Youn and Dr. Jun-Hyuk Kim, were my good mentors, and they gave me priceless advice to go through various personal and scientific problems that I faced. In overall, it has been great time for me to study and hang out together with previous and current Mullins group members.

Additionally, I would like to express my appreciation to Dr. Young Jin Kim and Dr. Kihyun Shin. These two scientists have provided me with valuable advice and coffee whenever I need their help. Mr. Shallaco McDonald ("Shak") is a great engineer and has made various equipment for my research. Without his useful insights in experimental equipment, I could not finish my Ph. D. studies. I really thank his contribution to my research.

Last but not least, I want to give my sincere love and appreciation to my beautiful and wonderful wife, Hee Jeong, and my parents, Hee Joo and In Taek. With their dedication for me, I have been able to conduct my reserach. To my lovely girl Lizzy, I will always stay with you.

# Abstract

## Catalytic Activity of 2-D Bimetallic Surfaces and 3-D Metal Organic Frameworks

Sungmin Han, Ph. D.

The University of Texas at Austin, 2020

Supervisor: Charles Buddie Mullins

The first part of this dissertation involves understanding the fundamentals of 2-D palladium (Pd) - gold (Au) bimetallic surfaces. The special catalytic capabilities of Pd–Au bimetallic surfaces are mainly attributed to ensemble effects related to the compositions of inert Au atoms and active Pd atoms. In particular, we focus on the activation of $O_2$ and various oxidative reactions on the Pd–Au surfaces. Using molecular beam techniques under ultrahigh vacuum (UHV), we prove that $H_2O$ and $O_2$ admolecules form hydrogen bonded clusters, which enhance $O_2$ activation. The direct dissociative adsorption of $O_2$ is also possible on the Pd–Au surfaces. We experimentally estimate the activation barriers for $O_2$ dissociation and the reactivity of oxygen adatoms as a function of the Pd coverage on the Au(111) surface, where a relatively low $O_2$ dissociation barrier (high Pd coverages) corresponds to a higher reaction barrier for oxygen adatoms (due to the higher Pd coverages). Based on these results, we also discover that acetaldehyde molecules can be selectively oxidized to acetic acid on less Pd deposited surfaces, since

the small Pd ensembles on this surface can prevent the decomposition of acetate, which is an intermediate state in the formation of acetic acid.

The second part of this dissertation involves growing and analyzing HKUST-1 metal-organic framework (MOF) thin films. MOFs are a new class of ultra-porous material based on inorganic-organic hybrid structures. We explain a new growth method for HKUST-1 thin films by sequential deposition of Cu and $H_3BTC$ under vacuum. This procedure resulted in first MOF thin film to be controllably grown under vacuum, and the strategy can be applied in various applications. Since this growth method allows delicate quantity control of Cu, we successfully grow 4-6 nm or 8-12 nm Cu nanoparticles (NP) incorporated in HKUST-1 thin films. Applying temperature programmed desorption under vacuum, Cu NP incorporated HKUST-1 thin films show different catalytic activity for the methanol oxidation depending on the Cu NP sizes. The film with smaller Cu NP's has improved selectivity for formaldehyde, and the film with larger Cu NP's generates formaldehyde along with other products, $CO_2$ and $H_2$.

# Table of Contents

# List of Tables

# List of Figures

Figure D.9: XRD patterns of before (black) and after (red) $H_2O$ adsorption & desorption tests on the 5 cycled HKUST-1 thin film .....148

# List of Illustrations

# Chapter 1: Introduction

## 1.1. Surface Science for Heterogeneous Catalysts

Various types of catalysts are used to produce more than 90 % of industrial products.[1,2] In particular, heterogeneous catalysts are the most widely used type of catalysts, which covers approximately 80 % of global catalyst market shares.[1,2] Heterogeneous catalysts are typically solid materials composed of active and support materials, which exist in a different phase compared to the reactants which are presented either via the gas or solution phase. The active materials are generally nobel metal nanoparticles (e.g., Pt, Pd, Ir, Rh), and the support materials are typically porous metal oxides (e.g., $Al_2O_3$, $TiO_2$, $SiO_2$) which provides dispersion sites for the active metal nanoparticles. Catalytic reaction steps on heterogeneous catalysts are simply as follows: (1) Diffusion of reactants from bulk gas or liquid phases to the surface of the catalyst particles (2) Adsorption of reactants on the active sites of the surface of catalyst particles (3) Catalytic conversion of adsorbed reactants and (4) Desorption of products.[1,2] Since heterogeneous catalysis is primarily a surface phenomenon, in order to understand detailed catalytic reaction steps, it is necessary to investigate surface morphology, compositions, and the active metal particle size of heterogeneous catalysts, which affect the adsorption and catalytic conversion of reactant molecules.[1–4] Because of these complexities, fundamental understanding in detailed heterogeneous catalytic reaction mechanisms have been slowly discovered from the late 1950s with the invention of various molecular spectroscopies and material characterization techniques, even though heterogeneous catalysts have been heavily used in the chemical industries since the early 20$^{th}$ century.[5]

Molecular level interactions between heterogeneous catalysts and various gas molecules have been investigated using vacuum surface science techniques. In contrast to catalytic reactions conducted with powder heterogeneous catalysts under high pressure of reactants, ultrahigh-vacuum (UHV) systems combined with model catalytic surfaces allow us to directly observe adsorption, desorption, adsorbate-adsorbate interactions, and catalytic transformations of target molecules.[3,4] With selected facets of metals or controlled metal oxide layers for a certain chemical reaction in the UHV systems, we can determine specific characteristics of the catalysts related to certain product yields. Moreover, the UHV condition itself minimizes the quantity of contaminants that can be also adsorbed on the surface at the time of reaction, which leads to less chances of external molecules influencing the catalytic reaction. Adopting a vacuum surface science approach, Professor Gerhard Ertl successfully identified detailed molecular level reaction mechanisms of the Haber-Bosch process and became a Novel laureate in 2007.[6] I also applied various vacuum surface science techniques in order to investigate the reactivity of oxygen adatoms on a 2-D Pd–Au bimetallic surface and the methanol oxidation reaction on a Cu nanoparticle (NP) incorporated 3-D HKUST-1 metal organic framework (MOF), which will be further discussed in the following sections.

### 1.2. 2-D Pd–Au Bimetallic Surfaces

When two different metals are mixed and form a bimetallic heterogeneous catalyst, it frequently shows improved catalytic performance compared to those of the parent metals, induced from diverse changes in the physical and chemical properties of the metallic components: (i) ensemble effects and (ii) ligand effects.[4,7–9] Ensemble effects originate from local compositions and structures of primary and secondary metallic atoms required to facilitate certain catalytic reactions; ligand effects are derived from

modifications in electronic structures caused by forming metal-metal bonds between two different metal atoms.[4]

Palladium (Pd) and gold (Au) are broadly known to form a bimetallic catalyst, showing promising catalytic properties in the synthesis of $H_2O_2$ directly from $H_2$ and $O_2$,[10–12] the acetoxylation of ethylene to vinyl acetate,[13–15] low temperature CO oxidation,[16–22] and selective alcohol oxidation.[23–27] The catalytic activity of Pd−Au catalysts primarily originates from ensemble effects which are directly related to the local composition of catalytically active Pd and inert Au atoms.[4] In this respect, it is possible to control the activity of the Pd–Au catalyst for specific chemical reactions by changing the composition of Pd and Au atoms on the catalytic surfaces. For instance, alloyed Pd−Au/$SiO_2$ nanoparticles with 4:1 ratio of Pd and Au showed better catalytic activity and stability in CO oxidation compared to other ratios of Pd and Au (16:1 and 8:1) or pure Pd.[22] Moreover, it was observed that Au−Pd/$TiO_2$ catalysts provide a largely improved turnover frequency (～270000/h) for the oxidation of 1-phenylethanol in comparison to hydroxyapatite-supported Pd catalysts (Pd/ HAP, ～12000/h).[24] These catalytic reactions using Pd−Au nanoparticles were conducted under solvent-free conditions, which suggests the use of Pd−Au bimetallic catalysts with an approach for green chemistry.

The Pd–Au model catalyst study under UHV has been adopted to understand the detailed molecular level surface interactions. By investigating ethylene acetoxylation to vinyl acetate on Pd–Au (100) and Pd–Au (111) model catalysts under UHV,[28] it was verified that the dispersion of Pd atoms on the Au surface is a key factor for the reaction between an acid and ethylene fixed on Pd atoms. Moreover, various catalytic reactions involving $H_2$ on the Pd–Au surface have been discovered, such as the generation of $H_2$ by decomposing HCOOH,[29] and the adsorption and activation of $H_2$.[30–32] In particular, $O_2$

molecules shows interesting behavior on the Pd–Au model catalyst, where molecular $O_2$ desorption was observed below 200 K, and recombinative $O_2$ desorption by dissociated O adatoms occurred at 750K on the Au–Pd (100) surface.[18] It was also found that continuous Pd atoms are necessary to dissociate $O_2$ admolecules on the Au–Pd (100) surface.[17] Based on these findings, I have further investigated the activation mechanism of $O_2$ and have conducted the oxidation of acetaldehyde on the Pd–Au(111) surface, showing different catalytic behavior depending on the quantity of deposited Pd atoms.

### 1.3. 3-D HKUST-1 METAL-ORGANIC FRAMEWORK THIN FILMS

Metal-organic frameworks (MOFs) consist of inorganic metal cation building units and organic linkers, which can form long-range ordered highly porous structures.[33] Thin films of MOFs have been widely studied because the chemical and structural characteristics of MOFs can be applied in drug delivery, microporous membranes, and microelectronic devices (e.g., gas sensors,[34–38] low-k dielectrics,[39–41] other electronic & opto-electronic devices[11–13]). For the growth of MOF thin films, the most commonly used method is adapted from bulk MOF powder synthesis methods typically using various solutions of metal cations and organic ligands.[36] These solvent based methods allow control of the crystallinity and thickness of the MOF thin films. Moreover, they can be applied in the direct fabrication of interdigitated electrodes, microbeams, and other various supports as gas sensors.[34,35] In spite of these capabilities, the solvent based methods are not suitable for the majority of microelectronic fabrication processes (e.g., semiconductor microchips) which are typically operated under vacuum. This is primarily because the solvents can contaminate and corrode the fabrication system, and they are also considered to be chemical waste after being used, incurring extra costs for safe disposal.

These limits in the solvent based MOF film growth methods have motivated researchers to develop solvent-free and gas-phase growth of MOF thin films. For example, Stassen et al.[45] developed a gas-phase ZIF-8 thin film growth method by depositing 2-methylimidazole molecules using chemical vapor deposition (CVD) on ZnO layers grown by atomic layer deposition (ALD), a top-down approach. Furthermore, an ALD (or molecular layer deposition, MLD) technique was exclusively used for the sequential deposition of metal cations and organic ligands in a layer-by-layer (LBL) bottom-up growth approach, which was applied to MOF-5[46] and UiO-66[47,48] thin film deposition. For advances in gas-phase MOF deposition methods, I have recently made additional progress regarding bottom-up gas-phase MOF growth strategies adopting physical vapor deposition (PVD) of Cu and CVD of $H_3BTC$ in order to grow a HKUST-1 thin film under vacuum.[49]

The HKUST-1 [$M_3(BTC)_2$] series of MOFs, where M = Cu (II), Zn(II), Mo(II), Cr(II), Ru(II) and BTC = 1,3,5-benzenetricarboxylic acid, have been widely studied because of their environmental friendliness, relatively low cost, high synthesis yields, and coordinately unsaturated open metal sites.[50–53] In particular, the open metal sites in HKUST-1 function as chemically active centers, so the HKUST-1 series have been applied to selective gas adsorption and separation centers,[54–58] Lewis acid catalysis,[59] and proton transfer channels.[60] Additionally, it was reported that the HKUST-1 MOF, once damaged, can be easily reconstructed with a simple treatment using ethanol.[61] These interesting properties of the HKUST-1 series have also led to this structure being widely applied to 2-D thin films deposited on various substrates. Currently there are two types of interfaces mostly used for the growth of 2-D thin film of HKUST-1: Self-assembled monolayer (SAM) interfaces and metal-oxide interfaces. SAMs are a multifunctional organic thin film covalently bound to a metal or metal oxide substrate. They are famous

for their relatively easy preparation and can be patterned using facile micro contact printing.[62,63] Employing SAMs can allow the synthesis of surface bound thin film SURMOFs (SURfaceMOFs) which are large homogeneous atomically flat MOF thin films. Specifically, the -COOH or -OH terminated SAMs are known to promote the growth of highly-oriented HKUST-1 films (the -COOH for the {200} planes and the -OH for the {222} planes).[64,65] As mentioned above, the HKUST-1 MOF thin film can be directly synthesized on bare metal oxide interfaces without SAMs. This method is surface selective and strongly depends on the acid/base properties between the organic linkers and the particular bare oxide surface. In detail, the ligand employed for the HKUST-1 MOF series, $H_3BTC$, is acidic, so it is difficult to grow the HKUST-1 thin film on a $SiO_2$ surface which is also acidic (IEP, Isoelectric point = 2.0 - 2.5), but it can be grown on a bare $Al_2O_3$ surface which is basic (IEP = 9.0).[66] To grow HKUST-1 on a $SiO_2$ surface, it is necessary to modify the $SiO_2$ surface with -COOH or -OH functional groups (e.g., similar to the SAMs on Au substrates).[63] Additionally, copper oxides and copper hydroxides can be precursors for the HKUST-1 thin film growth on various substrates.[67,68] Although SAMs and other oxide interfaces provide growth sites for the deposition of HKUST-1 thin films, they are still solution-based methods basically following the HKUST-1 powder preparation method, which restricts the broader use of HKUST-1. Thus, I have developed a new growth method for HKUST-1 which is fully under vacuum adopting chemical vapor deposition of $H_3BTC$ and physical vapor deposition of Cu. Furthermore, this method allows delicate control of the quantity of Cu in each Cu deposition cycle, so that Cu nanoparticles can be incorporated within the HKUST-1 structure. These Cu nanoparticles have shown interesting catalytic activity under vacuum depending on their sizes. More detailed discussion is contained in the following chapters.

## 1.4. DISSERTATION OVERVIEW

My Ph. D. studies have been composed of two parts: (i) $O_2$ activation and oxidative reactions on 2-D Pd–Au bimetallic surfaces and (ii) full vacuum growth of 3-D HKUST-1 metal-organic framework thin films and its catalytic behavior. Specifically this dissertation consists of seven chapters. Chapter 1 provides general background related to my Ph. D. studies and an overview for this dissertation. Chapters 2 – 4 are about published studies regarding 2-D Pd–Au bimetallic surfaces, and Chapters 5 – 6 regard 3-D HKUST-1 metal-organic framework thin films.

In Chapter 2, we discuss $H_2O$ improved $O_2$ activation on Pd–Au(111) surfaces. Using CO reactive molecular beam scattering (RMBS), we found that the $O_2$ and $H_2O$ coadsorbed Pd–Au surface generates more $CO_2$ molecules because of more activated atomic oxygen species compared to the $O_2$ solely adsorbed surface. This study was published in *Chemical Communications*.[69] As an extension of this study, we continuously worked on investigating the direct dissociation of $O_2$ and the reactivity of atomic oxygen on the Pd–Au surface. With various surface analysis skills, we successfully estimated the dissociation barrier of $O_2$ and the reaction barrier of oxygen adatoms based on the Pd coverages on the Au (111) surface. This research is explained in Chapter 3, which was published in *ACS Catalysis*.[70] On the basis of the results regarding the reactivity of oxygen adatoms on the Pd–Au surface, we conducted acetaldehyde oxidation on Pd–Au surfaces and found that a 2.0 ML Pd deposited Pd–Au surface (composed of 45 % Pd and 55 % Au) can selectively oxidize acetaldehyde to acetic acid near room temperature. On a 3.0 ML Pd deposited surface (composed of 80 % Pd and 20 % Au), acetaldehyde molecules were not selectively oxidized to acetic acid involving the generation of $CO_2$, $CH_4$, and $H_2O$. Adopting DFT calculations, we verified that acetate species (formed by oxygen adatoms and acetaldehyde) can be easily decomposed to $CO_2$ and $CH_4$ on bigger

Pd ensembles. We discuss more details regarding this study in Chapter 4, which was published in *ACS catalysis*.[71]

In Chapter 5 and 6, we demonstrate a new growth method for HKUST-1 thin films under vacuum and their use for methanol oxidation by incorporating catalytically active Cu nanoparticles (NPs) within the HKUST-1 structures. Specifically in Chapter 5, inspired by supramolecular structures of $H_3BTC$, we sequentially deposited $H_3BTC$ from a chemical vapor deposition process and Cu from a physical vapor deposition process for the growth of HKUST-1 thin films. The transition of $Cu^0$ to $Cu^{2+}$ by forming paddle-wheel units of HKUST-1 was facilitated by background gas molecules, $O_2$ and $H_2O$, with no indication of copper oxide formation, as confirmed by XPS and XRD. Additionally, our HKUST-1 thin films were highly oriented, which showed two distinct planes, the (220) and (222) planes, detected by glancing angle XRD and in-plane XRD respectively. The thickness of the HKUST-1 thin films linearly increased with the number of LBL cycles by ~ 20 nm for each LBL cycle as measured by AFM. Finally, we measured the desorption of $H_2O$ from a 100 nm HKUST-1 film and observed the existence of strongly bound $H_2O$ molecules absorbed within the HKUST-1 film, which predominantly desorb at 398 K. This study was published in the *Journal of Material Chemistry A*.[49] Since with our growth method it is easy to control the quantity of Cu in each growth cycle, we incorporated extra Cu atoms in the HKUST-1 thin film structures to see their catalytic activity in Chapter 6. Using tunneling electron microscopy (TEM), we observed 4-6 nm of Cu NPs or 8-12 nm of Cu NPs in/on the HKUST-1 thin films depending on deposited Cu coverages (4 ML or 8 ML Cu) in each growth cycle. Employing UHV temperature programmed desorption methods, the HKUST-1 film with 4-6 nm Cu NPs showed the selective oxidation of methanol to formaldehyde, while the HKUST-1 film with 8-12 nm Cu NPs more strongly oxidized the methanol to generate not only formaldehyde, but also

$CO_2$ caused by the formation of formate species. This study demonstrates the potential to control Cu nanoparticle size during the vacuum deposition of HKUST-1 thin films and how incorporated Cu clusters of different size affect the methanol oxidation catalytic activity under vacuum controlled conditions, which was submitted to *ACS Catalysis*.

In Chapter 7, I summarize my overall Ph. D. studies and suggest future research directions on the basis of my discoveries.

# Chapter 2: $H_2O$-Improved $O_2$ Activation on the Pd–Au Bimetallic Surface

## 2.1. INTRODUCTION

Palladium (Pd) – gold (Au) alloys have demonstrated their ability for various oxidative reactions as classical[23,72–74] and electrochemical[75,76] catalysts in aqueous solutions. To contribute to a more fundamental understanding of the oxidation process, we investigate the enhanced reactivity of $O_2$ from co-adsorbed $H_2O$ on Pd–Au (111) model catalysts (Pd: 2.5 ML) under ultrahigh vacuum (UHV) conditions. Model catalyst studies of Pd–Au bimetallic surfaces under UHV have allowed enhanced understanding of the detailed molecular level interactions on this catalytic surface, including studies of various physical properties,[77–79] the adsorption and activation of $H_2$,[30–32] the generation of vinyl acetate from $C_2H_4$ and $CH_3COOH$ and the production of $H_2$ by decomposition of HCOOH.[28,29] The interaction of $O_2$ and the Pd–Au surface has also been investigated in previous model catalyst studies,[6] which verified that continuous Pd sites are necessary to dissociate $O_2$ admolecules on the Pd–Au surface. In a previous study of $O_2$ on the Pd–Au (111) surface,[80] we have shown that the desorption energy of $O_2$ depends on the size of the Pd ensembles, and CO oxidation can be initiated at ~180 K, much lower than the threshold temperature for CO oxidation on the pure Pd surface (~ 400 K).[81,82]

The experiments reported in this chapter were performed in a UHV chamber with a base pressure of ~ $1.0 \times 10^{-10}$ Torr employing temperature programmed desorption (TPD) methods as well as molecular beam techniques.

---

*Han, S.; Evans, E. J.; Mullen, G. M.; Mullins, C.B. $H_2O$-Improved $O_2$ Activation on the Pd–Au Bimetallic Surface. *Chem. Commun.*, **2017**, 53, 3990-3993.
S. Han, E. J. Evans, and G. M. Mullen and C. B. Mullins conceived and designed experiments, analyzed and discussed results, and commented on the manuscript. S. Han performed experiments, analyzed data and wrote the paper.

## 2. 2. EXPERIMENTAL METHODS

The experiments were performed in a UHV chamber which has been described previously,[83] however brief details regarding the apparatus and experiments are described below. The Au (111) single crystal sample (12 mm in diameter × 2 mm thickness) is held in the UHV chamber by a Mo wire that can resistively heat the sample and also provide thermal contact with a liquid nitrogen bath. For the preparation of the Pd–Au bimetallic model surface, we believe the growth of Pd overlayers on Au (111) is governed by a layer-by-layer mechanism, in which the Pd atoms can diffuse in to the bulk of the Au (111) sample upon heating to form a Pd–Au alloy at the surface.[78] The Pd–Au surface for this chapter was made by depositing 2.5 ML of Pd atoms from a homemade thermal evaporator onto the Au (111) surface at 77 K, and then the surface was annealed at 500 K for 10 min. All the gas molecules were delivered to the sample surface via a collimated molecular beam, enabling accurate control of the number of target molecules impinging on our model catalyst. We also utilized a Fourier transform infrared (FTIR) spectrometer with a mercury-cadmium-telluride (MCT) detector cooled by liquid nitrogen for reflection-adsorption infrared spectroscopy (RAIRS).

## 2.3. RESULTS AND DISCUSSION

### 2.3.1. Temperature Programmed Desorption (TPD) of $O_2$ and $H_2O$ from the Pd–Au(111) Surface

Initially, we conducted TPD experiments to understand $O_2$ desorption behaviour from the Pd–Au (111) surface. In these tests, we directed $O_2$ molecules to the surface at 77 K *via* a molecular beam and then heated the sample to 500 K at 1 K/s for the TPD measurement. As indicated in Figure 2.1a, 1 ML of adsorbed $O_2$ on the Pd–Au surface shows a broad desorption spectrum compared to TPD tests for $O_2$ on Pd (111), where

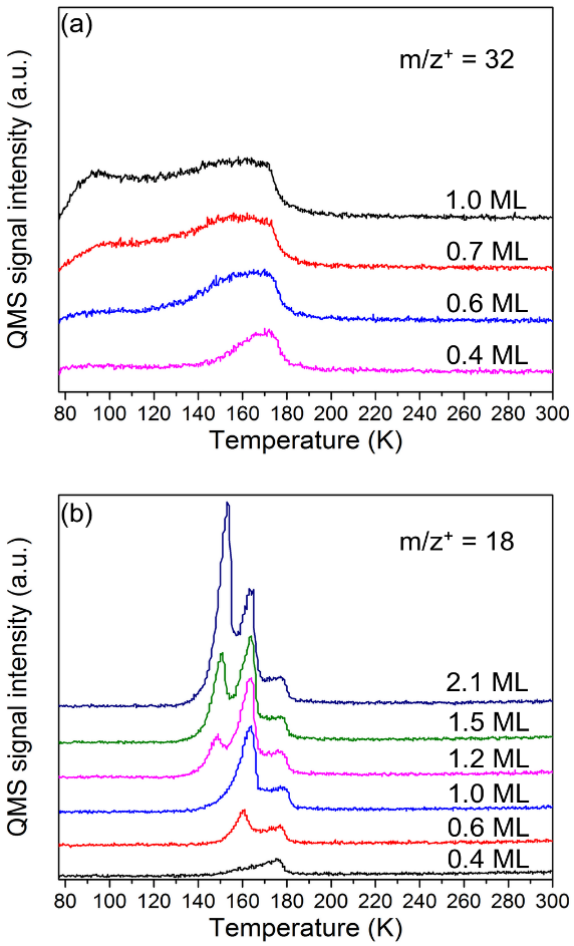


Figure 2.1. TPD of various coverages of (a) $O_2$ and (b) $H_2O$ on the Pd–Au (111) surface. Each sample was dosed at 77 K and then heated to 500 K with 1 K/s of heating rate. Above 200 K, there were no extra peaks observed for any of the cases.

sharp molecular $O_2$ desorption peaks can be observed at the following temperatures (~ 130 K, ~ 160 K, ~ 210 K) with $O_2$ dissociation occurring between 180 K – 200 K.[84–86] There are no desorption features above 200 K for our Pd–Au surfaces indicating that $O_2$ molecules are more weakly bound on the Pd–Au surface compared to the pure Pd surface. Furthermore, the broad $O_2$ desorption feature is likely caused by the heterogeneity of the annealed Pd–Au surface since the $O_2$ desorption energies are mainly dependent on the sizes of the Pd ensembles as explained by Yu et al.[80] Specifically, for

lower $O_2$ coverages such as 0.4 ML, most of the $O_2$ molecules desorb in a relatively high temperature range (150 K – 180 K) compared to the broader TPD spectrum observed with 1.0 ML of $O_2$. We believe this is because at low coverages the $O_2$ molecules are mainly adsorbed on the relatively larger Pd ensembles, where they can more strongly interact with Pd atoms. However, when more $O_2$ molecules are adsorbed (0.6 ML to 0.7 ML), the additional $O_2$ molecules adsorb on relatively smaller Pd ensembles, so the onset for $O_2$ desorption continuously moves to lower temperatures, and finally for 1.0 ML of $O_2$, the overall $O_2$ desorption occurs from 80 K to 200 K, with most of the desorption complete by 180 K.

The TPD experiments for adsorbed $H_2O$ on the Pd–Au surface show similar desorption behaviour compared to previous TPD measurements for $H_2O$ on Pt group metals.[87–90] It has been observed that $H_2O$ molecules on the Pd surface form hydrogen-bonded (H-bonded) clusters, which consist of the strongly bound $H_2O$ desorbing at 180 K and weakly bound $H_2O$ desorbing at 165 K.[88–92] Consistent with this desorption behaviour, and as indicated in Figure 2.1b, $H_2O$ molecules on our Pd–Au surface strongly interact with the Pd ensembles, and this water desorbs with a peak at 177 K. With increasing amounts of $H_2O$ another peak appears at 160 K, which is made up of more weakly bound $H_2O$ molecules on the Pd ensembles. An additional peak is also observed at 148 K after the peak at 160 K is saturated. Based on previous studies, the peak at 148 K corresponds to the desorption temperature of $H_2O$ molecules from a clean gold surface[93] or multilayers of $H_2O$ molecules[87,94]. Thus, in this chapter, we define 1.0 ML of $H_2O$ on the Pd–Au surface to be when the 160 K peak is just saturated, which implies that all the $H_2O$ molecules are associated with the Pd ensembles as with a 1.0 ML coverage of $O_2$ molecules on the Pd–Au surface. Additionally, to further characterize adsorbed $H_2O$ on our Pd–Au surface, we conducted reflection-adsorption infrared spectroscopy

(RAIRS) measurements, which shows two different –OH vibrational ranges for 1 ML of $H_2O$ in Figure A.1b consistent with TPD results. (see the Appendix A for more details.)

### 2.3.2. Co-adsorbed $H_2O$ and $O_2$ Desorption from the Pd–Au(111) surface

After separately measuring the desorption of $O_2$ and $H_2O$ molecules from the Pd–Au bimetallic surface, we investigated the effects of co-adsorbed $H_2O$ and $O_2$ on the Pd–Au surface. In these experiments, we first adsorbed 1.0 ML of $O_2$ on the Pd–Au surface,

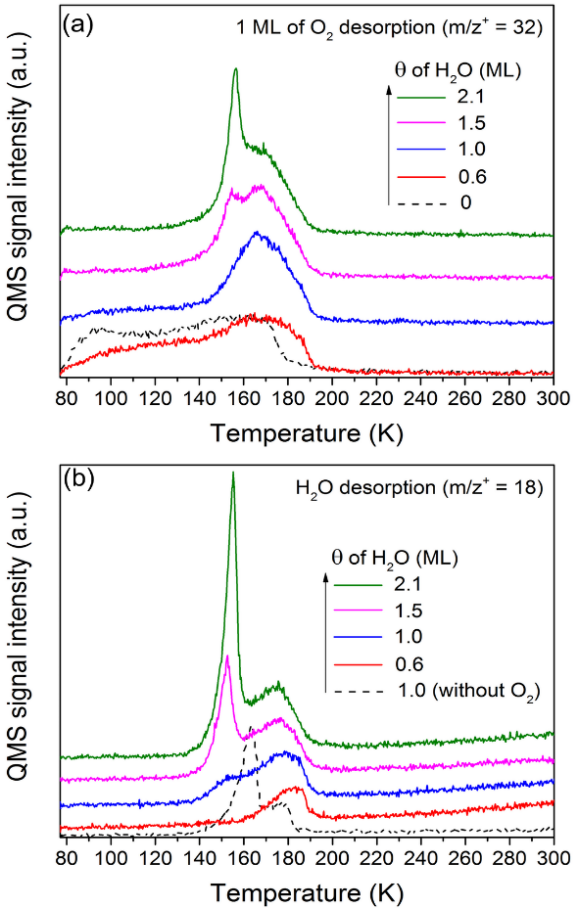


Figure 2.2. TPD of $O_2$ and $H_2O$ from Pd–Au (111) surface. All the samples were initially dosed with 1.0 ML $O_2$ at 77 K, and then 0.6, 1.0, 1.5, and 2.1 ML of $H_2O$ were impinged also at 77 K. (a) shows 1.0 ML of $O_2$ desorption in each $H_2O$ coverage, and (b) indicates various coverages of $H_2O$ desorption when 1.0 ML of $O_2$ is pre-adsorbed.

and then co-adsorbed various coverages of $H_2O$ molecules. Additionally, during $H_2O$ exposure, negligible $O_2$ desorption/displacement is observed (Figure A.5). However, as shown in Figure 2.2, $H_2O$ molecules dramatically change the $O_2$ desorption behaviour compared to the clean surface. Upon increasing the coverage of $H_2O$, $O_2$ molecules are more strongly adsorbed on the Pd–Au surface, showing a concerted desorption between 150 K and 190 K. Specifically, as shown in Figure 2.2a, when 0.6 ML of $H_2O$ is co-adsorbed, a higher proportion of $O_2$ molecules remain on the surface until near 190 K compared to the case in which no water is co-adsorbed. The co-adsorbed 0.6 ML of $H_2O$ molecules (Figure 2.2b) also leave the surface within a relatively higher temperature range (160 K – 190 K) showing just one peak at 180 K (compare to 1.0 ML of $H_2O$ alone on the Pd–Au surface). When the $H_2O$ coverage is increased to 1.0 ML, most of the $O_2$ molecules desorb from the Pd–Au surface between 150 K and 190 K with a peak at 165 K, while the $H_2O$ molecules have two different desorption peaks, at 152 K and 180 K. Thus, we can expect that the $H_2O$ molecules are bound differently depending upon the degree of molecular interactions with $O_2$. This supposition is supported by results from RAIRS as shown in Figure A.1c, where it shows two -OH vibrational regions for the 1 ML of $H_2O$ / 1ML of $O_2$ case, which are different than the 1 ML of $H_2O$ solely-adsorbed case. Moreover, the desorption of $O_2$ and $H_2O$ does not measurably affect the Pd ensembles as confirmed via CO-RAIRS (shown in Figure A.6). When $O_2$ adsorbed on the Pd–Au surface is exposed to more than 1.0 ML of $H_2O$, the $H_2O$ desorption peak at 152 K is shifted a little bit to 155 K but higher and sharper as shown in Figure 2.2b, and the $O_2$ starts to show a new desorption peak at 156 K as indicated in Figure 2.2a. It seems that the new peak for $O_2$ is caused by the strong interactions with the additional $H_2O$ molecules, which causes more $O_2$ desorption below 165 K compared to the 1.0 ML $H_2O$ case. Thus, we can speculate that the weakly bound $O_2$ molecules on the relatively small

Pd ensembles are more likely to interact with surrounding $H_2O$ molecules instead of Pd atoms if they are exposed to a relatively large amount of $H_2O$ (> 1.0 ML).

These strong interactions between the co-adsorbed $O_2$ and $H_2O$ shown in Figure 2.2 suggest that the $H_2O$ molecules are not just physically adsorbed. When the $H_2O$ coverage is higher than 1.0 ML, the adsorbed $O_2$ and $H_2O$ molecules desorb over similar temperature ranges (150 K – 190 K), and even 0.6 ML of $H_2O$ apparently affects the desorption behaviour of $O_2$. Since the amount of $H_2O$ used in these experiments is quite small we do not expect to form a crystalized porous film which could yield "molecular volcano-like" effects (which used ~ 30 ML of $H_2O$)[95,96]. The conditions used here are closer to those used in previous research for hydrogen and water interactions on transition metal surfaces.[97,98] As shown in Figure A.3, we also find that the small amount of $O_2$ admolecules exposed after pre-adsorbing 1 ML of $H_2O$ on the Pd–Au surface can change the desorption behaviour of $H_2O$ compared to when it is solely adsorbed. To understand the nature of these $O_2$ – $H_2O$ interactions, we conducted TPD experiments using $H_2{}^{18}O$ with $^{16}O_2$ co-adsorbed on the Pd–Au model surface to explore the generation of $^{16}O^{18}O$ ($m/z^+ = 34$), which could indicate the formation of hydroxyl (–OH) groups on the surface.[93] However, in testing with 1.0 ML of $H_2{}^{18}O$ / 1.0 ML of $O_2$, we observe only a very small amount of $^{16}O^{18}O$ generation (Figure A.4a), so we conclude that co-adsorbed $O_2$ and $H_2O$ on the Pd–Au surface are more likely to form a strong H-bonded complex rather than adsorbed hydroxyls (–OH). (More details are in Appendix A.)

To understand the interactions between Pd–$O_2$ and $H_2O$ more quantitatively, using Figure 2.2, we estimated the relative amount of desorbing $O_2$ molecules in the range from 77 K – 145 K to reflect the weakly bound $O_2$, and the quantity from 165 K – 200 K to account for the strongly bound $O_2$, and compared each of them to the corresponding total amount of $O_2$ desorption from 77 K to 200 K. As summarized in

Table A.1, the percentages of $O_2$ molecules that desorb below 145 K continuously decreases with increasing coverage of $H_2O$, from 58.4 % for 1.0 ML $O_2$ without any water adsorbed on the surface to 19.6 % for the case 2.1 ML $H_2O$ / 1.0 ML $O_2$. The ratio of $O_2$ molecules desorbing above 165 K also continuously increases from 17.8 % on the 1.0 ML $O_2$ surface without co-adsorbed water to 42.9 % on the 1.0 ML $H_2O$ / 1.0 ML $O_2$ surface, but it decreases slightly when the $H_2O$ coverages are 1.5 ML (~ 40 %) and 2.1 ML (~ 37 %). This is related to the second $O_2$ desorption peak at 156 K formed by the extra $H_2O$ molecules, which means the extra water molecules not only affect the weakly bound $O_2$, but also influence some of the strongly bound $O_2$ molecules that desorb above 165 K. Moreover, if we assign the total amount of molecular $O_2$ desorption below 200 K from 1.0 ML of $O_2$ adsorbed on the surface to be 100 %, the relative amount of $O_2$ desorption below 200 K continuously decreases with growing $H_2O$ coverages until 1.0 ML (81.5 %) and then slightly increases when the Pd–Au surface is covered with 1.5 (81.7%) and 2.1 ML (84.8 %) of $H_2O$, which is the same trend for relative amounts of $O_2$ molecules desorbing above 165 K. Thus, we can expect that the more $O_2$ desorption that occurs in the higher temperature range, the more activated oxygen species remain on the Pd–Au surface above 200 K, which can enhance the oxidative reactivity of the Pd–Au surface. We will verify this supposition by measuring the amount of generated $CO_2$ *via* CO-reactive molecular beam scattering (CO-RMBS) in the latter part of this paper because we are unable to detect recombinative $O_2$ desorption during TPD tests, which has been observed at 750 K on a Au–Pd (100) surface.[18] Since Pd atoms significantly diffuse into the Au (111) sample when annealed higher than 500 K,[80] we avoid heating above this temperature.

### 2.3.3. Oxidative Reactivity of the Pd–Au surface by $H_2O$ and $O_2$

Now we discuss the measurements of the oxidative reactivity of the Pd–Au surface after treatment with $H_2O$ and $O_2$ co-adsorption *via* CO-RMBS, which is a titration technique that can probe surface oxygen at lower temperatures.[17,18] To do this, we prepared samples similar to those used in acquiring the data displayed in Figure 2.2. After that, samples were heated to 250 K and then a molecular beam of CO was directed onto

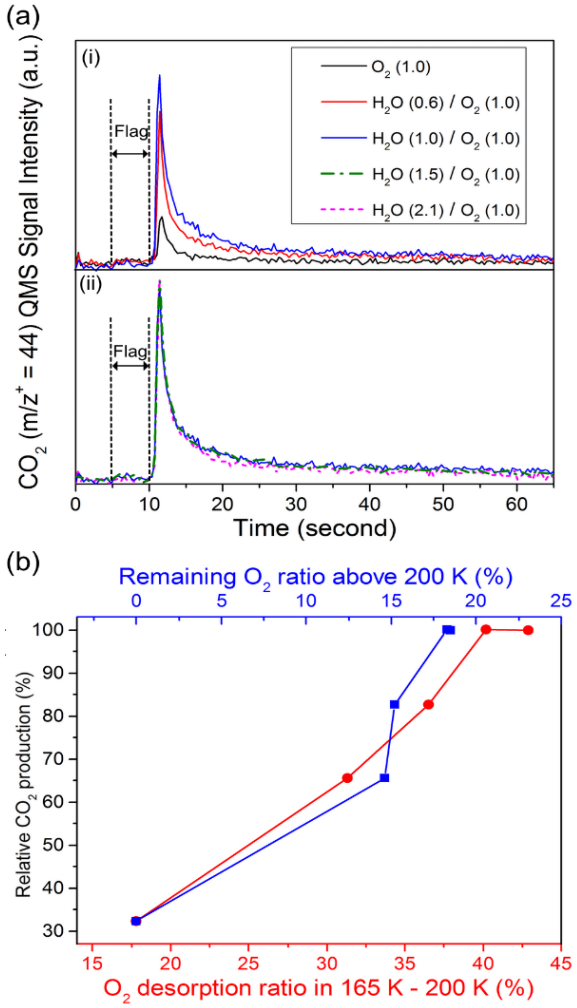


Figure 2.3. (a) The generation of $CO_2$ detected from QMS during CO-RMBS measurements at 250 K ((i) for $H_2O$ coverages less than 1.0 ML and (ii) for more than 1.0 ML of $H_2O$) and (b) the plots for the $O_2$ desorption ratio in 165 K – 200 K (%, bottom x axis) and the remaining $O_2$ ratio above 200 K (%, top x axis) vs the relative $CO_2$ production (%).

an inert flag placed in front of the Pd–Au sample (blocking the beam) for 5 s (from 5 – 10 s in Figure 2.3), which gives a baseline signal with minimal surface chemical reactions, and then the beam was directed onto the $O_2$ and $H_2O$ treated Pd–Au surface (a temperature of 250 K showed the highest activity for $CO_2$ generation in a previous study[80]). As shown in Figure 2.3 and Table A.1, the measured quantity of $CO_2$ has a clear relation with the amount of $O_2$ desorbing above 165 K, which indicates that for the cases in which $H_2O$ was co-adsorbed with $O_2$ there are apparent enhancements in the $CO_2$ generation, and hence the creation of active oxygen species (likely oxygen adatoms), compared to the case of $O_2$ solely adsorbed on the Pd–Au surface. To be specific, in Figure 2.3a–(i), the 1.0 ML $H_2O$ / 1.0 ML $O_2$ co-adsorbed sample shows the highest yield of $CO_2$, but the quantity of generated $CO_2$ molecules continuously decreases with decreasing coverages of adsorbed $H_2O$ (with 1.0 ML of $O_2$). If we assign the total amount of $CO_2$ evolved from the 1.0 ML of $H_2O$ / 1.0 ML of $O_2$ co-adsorbed surface as 100%, the 0.6 ML of $H_2O$ / 1.0 ML of $O_2$ co-adsorbed surface gives 65.5 % and the 1.0 ML of $O_2$ solely adsorbed sample accounts for 32.2 %. In Figure 2.3a–(ii), the 1.5 ML of $H_2O$ case has no clear differences compared to the 1.0 ML $H_2O$ case, but the 2.1 ML $H_2O$ case shows slightly lower $CO_2$ generation (~ 83 % compared to the 1.0 ML $H_2O$ case – note that the generated $CO_2$ is lower from ~16 s onward compared to the 1.0 ML and 1.5 ML $H_2O$ adsorbed cases). As mentioned earlier, the quantity of generated $CO_2$ is strongly related to the amount of $O_2$ remaining on the surface after 165 K and the generated active oxygen species. Specifically, as described in Figure 2.3b, the quantity of $O_2$ remaining above 165 K shows a linear relationship with the relative amounts of $CO_2$ generated in CO-RMBS until the percentage of $O_2$ reaches around 40%, and then the production of $CO_2$ levels out. The ratios (%) of remaining $O_2$ above 200 K, which can be estimated from the relative $O_2$ desorption coverages (77 K – 200 K) in Table A.1 (i.e., taking 100

(%) minus each of the relative total $O_2$ desorption coverages (%)), also form a proportional relationship with the $CO_2$ generation. From this analysis, we believe that the interactions between $O_2$ and $H_2O$ on the Pd–Au surface cause more $O_2$ molecules to remain at higher temperatures (i.e., above 165K) inducing $O_2$ admolecules to become more activated, so they have a higher probability to be converted into reactive oxygen species. Furthermore, the presence of Au on the surface enables CO oxidation to proceed at 250 K, which is a much lower temperature than for CO oxidation on the pure Pd surface (~ 400 K)[81,82]. We also conducted CO-RMBS experiments using $H_2{}^{18}O$ to test for the generation of $C^{16}O^{18}O$ ($m/z^+ = 46$). This is another way to check for the formation of hydroxyls (-$^{18}$OH) formed by the interactions between $O_2$ and $H_2{}^{18}O$.[93] As indicated in Figure A.4b, the intensity for $C^{16}O^{18}O$ ($m/z^+ = 46$) is much lower than the $C^{16}O_2$ ($m/z^+ = 44$) signal, so we speculate once again that co-adsorbed $H_2O$ and $O_2$ molecules on our model Pd–Au surface are mainly forming a H-bonded complex, and only a small fraction of them exist as hydroxyls.

### 2.4. CONCLUSION

In summary, we have observed enhanced reactivity of $O_2$ molecules on the Pd–Au surface (Pd: 2.5 ML) when co-adsorbed with $H_2O$ molecules. The strong interactions between $O_2$ and $H_2O$ allow more $O_2$ molecules to become activated oxygen species on the surface above 200 K, which results in more $CO_2$ generation at 250 K from impingement of a CO molecular beam. Therefore, $H_2O$ apparently improves the activity of $O_2$ on the Pd–Au surface, and it can be used in various oxidative reactions on Pd–Au bimetallic catalysts which may require additional activated oxygen.

# Chapter 3: Surface Alloy Composition Controlled $O_2$ Activation on Pd−Au Bimetallic Model Catalysts

## 3.1. INTRODUCTION

Adding a second metal to a host metal can create favorable catalytic properties (e.g., selectivity, activity, and stability) in forming a bimetallic catalyst.[7–9,99] The combination of palladium (Pd) and gold (Au) is widely known as a bimetallic catalyst and it has shown promising catalytic properties in the synthesis of vinyl acetate[13–15] and hydrogen peroxide[10–12]. The catalytic activity of Pd–Au catalysts primarily originates from ensemble effects which are directly related to the local composition of catalytically active Pd and inert Au atoms.[4] The relative compositions of Pd and Au can be controlled in various chemical ways,[100,101] and, as mentioned above, Pd–Au catalysts have shown enhanced reactivity and selectivity in several oxidative reactions including the oxidation of alcohols,[23–27] CO, [16–22] and aromatic C-H bonds[102]. Specifically, when the Pd and Au ratio is 4:1, alloyed Pd–Au/$SiO_2$ nanoparticles not only have better catalytic activity than other ratios of Pd and Au (16:1 and 8:1) or pure Pd, but also become more stable than the pure Au catalysts for long term usage.[22] Furthermore, Au–Pd/$TiO_2$ catalysts can provide a largely improved turnover frequency (~270,000/hour) for the oxidation of 1-phenyl ethanol compared to hydroxyapatite-supported Pd catalysts (Pd/HAP, ~ 12,000/hour),[24] and they are also highly active for the selective oxidation of toluene to benzyl

benzonate.[102] All these catalytic reactions based on Pd–Au nanoparticles were conducted under mild solvent free conditions, which supports the use of Pd–Au

*Han, S.; Mullins, C.B. Surface Alloy Composition Controlled $O_2$ Activation on Pd−Au Bimetallic Model Catalysts, **2018**, 8, 3641-3649.
S. Han and C. B. Mullins conceived and designed experiments, analyzed and discussed results, and commented on the manuscript. S. Han performed experiments, analyzed data and wrote the paper.

bimetallic catalysts as an approach for green chemistry. The goal in this chapter is to uncover additional fundamental insights into the interactions and activation of molecular oxygen with Pd–Au surfaces of various compositions. It is our hope the experimental results and analysis reported here will assist in the rational design of improved Pd–Au bimetallic catalysts.

Striving for a better understanding of chemical reactions on these catalysts, Pd–Au bimetallic model surfaces have been widely studied under ultrahigh vacuum (UHV) conditions.[4] It has been shown that the Pd–Au interface is a critical portion of the surface regarding promising catalytic reactions such as $H_2$ production from formic acid[29] and the generation of vinyl acetate from ethylene and acetic acid, where the distance between the mono-dispersed Pd atoms is especially important.[28] Moreover, Pd monomers on the Au(111) surface are known to be able to dissociatively adsorb hydrogen molecules.[32] Dissociated hydrogen atoms at the Pd–Au interface recombinatively desorb at temperatures lying between 150 K and 300 K, which are higher than those for $H_2$ desorption from the pure Au(111) (~ 110 K)[103] surface and lower than on pure Pd surfaces (~ 350 K)[104,105]. When the Pd coverage on the Au(111) surface is large enough to form Pd(111)-like islands, $H_2$ desorbs with features appearing at temperatures above 300 K, similar to $H_2$ desorption from a pure Pd surface.[30] In particular, dissociated H atoms were observed on the top-layer of the surface,[32] and they are not likely to diffuse into the sublayers below the Pd–Au surface to form a palladium hydride when the surface is held at 77 K during $H_2$ exposure.[30] Since the spillover of H from Pd to Au, which is necessary for H diffusion between Pd ensembles across Au atoms, is known to be unfavorable,[106,107] $H_2$ molecules provide information regarding the Pd ensembles from which they desorb. Thus, the different $H_2$ desorption behavior regarding various Pd

coverages have been used for the characterization of the surface composition: namely, Pd–Au interface sites and Pd(111)-like island sites.[29,30,108]

Pd–Au surfaces can also activate the dissociation of $O_2$ molecules between 180 K – 200 K: indeed, during temperature programmed desorption broad desorption features appear until ~200 K without evidence of the "sharp desorption peaks" observed from pure Pd surfaces.[69,80] It has been shown that neighboring adsorbed Pd atoms are necessary to initiate $O_2$ dissociation, in contrast to $H_2$ activation.[17,80] Furthermore, $H_2O$ molecules can form hydrogen bonded clusters with adsorbed $O_2$ molecules on Pd–Au surfaces, which can enhance $O_2$ activation.[69] This activated oxygen on the Pd-Au surface is very reactive compared to that on pure Pd surfaces (since it can oxidize CO molecules below 200 K[80] however, oxygen adatoms on pure Pd surfaces will not react with CO to generate $CO_2$ until about 400 K[81,82]). The enhanced reactivity on the Pd-Au bimetallic surface is likely related to the existence of Pd–Au interface sites, in which the alloyed Au can weaken the oxygen–Pd interactions.

The activated $O_2$ is involved in catalytic reactions on the Pd–Au surfaces as a Brønsted base in the synthesis of vinyl acateate ($CH_3COOH + C_2H_5 + ½O_2 \rightarrow CH_3COOCHCH_2 + H_2O$) and as an oxidant in the oxidation of CO ($CO + ½O_2 \rightarrow CO_2$). Although there have been several studies regarding the properties of atomic oxygen on pure Pd surfaces created by adsorbing $O_2$ at 300 K (to eliminate molecularly adsorbed oxygen),[89,94,109,110] the direct observation and analysis of active oxygen species (likely oxygen adatoms) on Pd–Au surfaces have not yet been carefully studied. Thus, we adopt an approach developed for the successful investigation of pure Pd surfaces[89,94,109,110] for the study reported here with Pd–Au bimetallic surfaces. We have found that the dissociative adsorption of $O_2$ is measureable on the Pd–Au surface at temperatures above 300K, and these formed oxygen adatoms are sufficiently reactive for oxidizing CO at 140

K. By controlling the amount of Pd on the Au(111) surface, we can also estimate the relationship between the Pd coverage and the activation barriers for $O_2$ dissociation and CO oxidation. These results elucidate the roles of Pd and Au on the Pd–Au bimetallic surfaces, in which the Pd(111)-like island sites are responsible for the dissociative adsorption of $O_2$, and the dissociated oxygen adatoms at the Pd–Au interface sites are likely the relevant species in subsequent oxidative reaction chemistry.

### 3.2. EXPERIMENTAL METHODS

All of the experiments in this chapter were performed in a UHV molecular beam system which has been described in detail previously.[83] Briefly, the UHV chamber (base pressure of ~ 1.0 x $10^{-10}$ Torr) is equipped with two separate molecular beams, a quadrupole mass spectrometer (Extrel C-50), an Auger electron spectrometer (Physical Electronics 10-500), and a Fourier transform infrared spectrometer (Bruker Tensor 27) with a mercury-cadmium-telluride (MCT) detector. A disk-shaped Au(111) single crystal sample (12 mm in diameter × 2 mm thickness) is held by a Mo wire fitted in a groove cut on the edge of the Au(111) sample in the UHV chamber. This wire is both used to resistively heat the sample and provide thermal contact with a liquid nitrogen bath. The temperature of the sample was measured by a K-type (Alumel-Chromel) thermocouple which lies in a small hole on the top edge of the disk type sample. The Au(111) surface was regularly cleaned by Ar sputtering, and then annealed to 800 K.

We prepared the Pd–Au bimetallic model surface based on a layer-by-layer growth mechanism of Pd overlayers on the Au(111) surface, in which the Pd atoms can diffuse into the bulk of the Au (111) sample upon heating to form a Pd–Au alloy at the surface.[78] The deposition rate of Pd in this chapter was calibrated by a quartz crystal microbalance (QCM) controller (Maxtek Inc.) with an assumption of the thickness of 1

monolayer (ML) of Pd as 0.274 nm. Based on the QCM calibrations, various amounts of Pd (1.0, 1.5, 2.0, 2.5, 3.0, 4.0, and 6.0 ML) were deposited on the Au(111) surface at 77 K, and then annealed to 500 K for 10 min as with previous studies from our laboratory.[29,30,69,80] Moreover, in this chapter, we exposed our Pd–Au surfaces to $O_2$ molecules at various temperatures (200 K – 475 K) for measuring the dissociative adsorption of oxygen. Exposure to oxygen at elevated temperatures can increase the size of Pd ensembles based on the stronger affinity of O towards Pd than Au, which induces the Pd atoms to remain in the top layer instead of interdiffusing into the sublayers of Au(111).[111] We exposed each prepared surface to $O_2$ molecules at 475 K *via* the molecular beam to treat the surface with $O_2$ after the annealing of the Pd–Au sample to 500 K. We believe that this provides us with a surface which is consistent over the entire temperature range that we employed for studying adsorption (77 – 475 K).

All of the tested gas molecules were delivered to the sample surfaces *via* a collimated molecular beam, which allows for the accurate control of the exposure of target molecules impinging on the model catalyst. We conducted $H_2$-TPD to identify the surface compositions of the Pd–Au surfaces after initially saturating the surface with $H_2$ at 77 K *via* a $H_2$ molecular beam, a method which has been used in previous studies.[29] As with the $H_2$-TPD, the $O_2$-TPD spectra were also measured on the samples saturated with $O_2$ at 77 K, which was heated to 500 K at 1 K/s. The King and Wells technique[112] was adopted to investigate the overall $O_2$ adsorption behavior. Specifically, the $O_2$ molecules were first impinged on a stainless steel inert flag in the chamber which blocks the beam from the sample and the partial pressure in the chamber is monitored by the QMS to provide a measure of the intensity of the beam. Subsequently, the $O_2$ beam was directed on the Pd–Au sample surfaces (i.e., the inert flag was moved from blocking impingement on the sample) while monitoring the QMS signal for $O_2$ ($m/z^+ = 32$); here the decreased

signal intensity indicates the fraction of impinging $O_2$ molecules that adsorb on the surface. To simplify determination of the initial adsorption probability we employed a modified King and Wells technique[113] in which the $O_2$ beam exposure time is controlled to both the flag (for 1.5 seconds) and the sample (for 1.5 seconds – as shown in Figure B.1). The signal-time area under each of the gas pulses as measured by the QMS are then used to determine the initial adsorption probability: in particular the area under the gas pulse from the sample is divided by the area from the gas pulse impinging on the inert flag and this quantity is subtracted from one to obtain the initial adsorption probability. Carbon monoxide reactive molecular beam scattering (RMBS) was used as a measure of the reactivity of the surface oxygen adatoms on the various Pd covered surfaces.[17–19,69,77,80] In particular, $O_2$ molecules from an oxygen molecular beam were directed onto the sample surfaces at 300 K to cover the surface with oxygen adatoms prior to exposing the surface to carbon monoxide molecules via a CO molecular beam. For observing the reactivity of the oxygen adatoms, the oxygen adatom pre-covered surfaces were first heated to specific temperatures (100 K – 400 K), where 400 K is a temperature at which atomic oxygen on the pure Pd surface can oxidize CO,[81,82] and then CO molecules were directed at the surface and the generation of $CO_2$ ($m/z^+ = 44$) was measured.

## 3.3. Results and Discussion

### 3.3.1. $H_2$ and $O_2$ Desorption from the Various Pd–Au Surfaces

To quantify the surface composition dependence on Pd exposure, we conducted $H_2$-TPD tests on the various Pd–Au surfaces that we synthesized. During the TPD tests, we avoid heating the samples above 500 K because Pd atoms significantly diffuse into the Au(111) bulk at this and higher temperatures.[80] $H_2$-TPD spectra on Pd–Au surfaces show two features based on the relative surface compositions which correspond to (i) Pd–

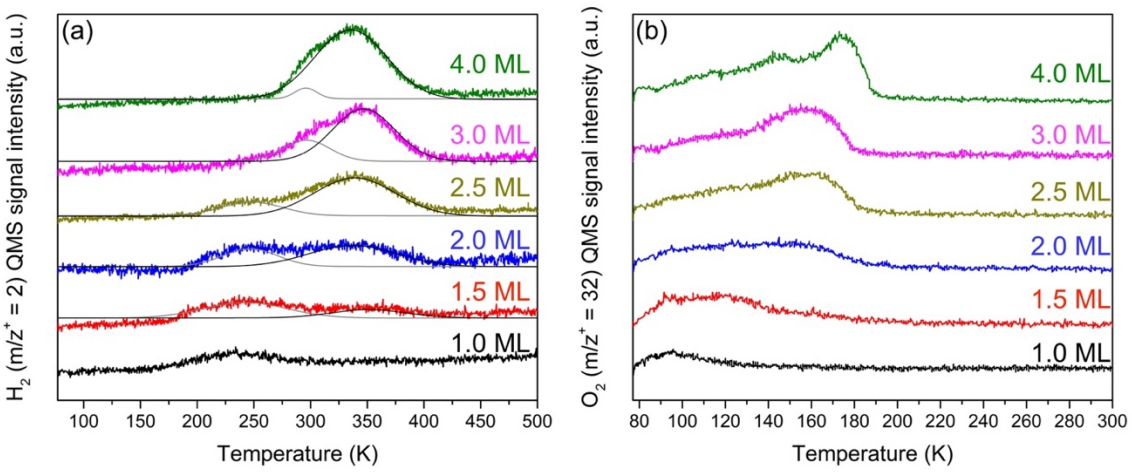


Figure 3.1. TPD of $H_2$ (a) and molecularly adsorbed $O_2$ (b) from Pd–Au surfaces with various coverages of Pd (1.0 – 4.0 ML). All the gas molecules were impinged *via* the molecular beam at 77 K until the samples were saturated. After that, the saturated samples were heated to 500 K by 1 K/s for the TPD measurement.

Au interface sites (or discontinuous and small Pd ensembles, 150 K – 300 K) and (ii) Pd(111)-like island sites (or big enough Pd ensembles to have pure Pd like properties, 300 K – 400 K).[29,30] We investigated the surface composition of our Pd–Au surfaces employing $H_2$-TPD and performing peak deconvolution of the spectra. Since we exposed these surfaces to $O_2$ (via molecular beam) at 475 K after annealing the Pd-as deposited samples at 500 K for 10 minutes, which is known to make the Pd ensembles larger,[111] the samples studied here tend to have relatively stronger Pd(111)-like character compared to our previous study.[29] As shown in Figure 3.1a, there is no indication of palladium hydride formation in any of our $H_2$-TPD spectra, which would show a clear $H_2$ desorption feature at ~140 K, as we previously observed.[30] The desorption of $H_2$ from a 1 ML Pd deposited Au(111) surface is completed below 300 K, which means the surface is mainly composed of Pd–Au interface sites.[29,30] With a 1.5 ML Pd on Au (111) surface we begin to observe desorption features for $H_2$ above 300 K. This result indicates that at this

Pd coverage there are continuous Pd ensembles which show Pd(111)-like behavior. At a coverage of 2.0 ML of Pd, the intensity of the desorption peak representing the Pd(111)-like sites becomes slightly larger than the intensity of that representing the Pd–Au interfaces (gray lines). After this point, the deconvoluted peaks for the Pd–Au interface sites are continuously lower and shifted to higher temperatures upon increasing Pd coverages, but the $H_2$ desorption features for the Pd(111)-like islands grow larger and clearly show a peak at ~ 330 K, similar to that observed on pure Pd surfaces[104,105]. Interestingly, at a Pd coverage of 4.0 ML, we observe that the surface is largely covered with continuous Pd atoms but also includes some small number of discontinuous Pd–Au interface sites because the overall $H_2$ desorption spectrum is composed of a large peak at ~ 340 K and a smaller peak at ~ 290 K. Similar to our previous study,[29] we also observed an apparent Pd–Au interface caused $H_2$ desorption peak even at a coverage of 4 ML of Pd without the $O_2$ treatment at 475 K (Figure B.2), but as we mentioned above, the $O_2$ treatment made the Pd(111)-like character stronger as suggested by Yu et al.[111] Since our samples have been annealed after the Pd deposition, their initial Pd coverages cannot be directly interpreted as the quantity of Pd on top of the Au(111) surface. Therefore, we conducted $H_2$-TPD for a 6.0 ML Pd deposited surface to estimate the relative number of Pd atoms as a function of the initial Pd coverage. As shown in Figure B.3, the 6.0 ML Pd deposited surface does not show any hydrogen desorption peaks below 300 K, and it also does not show peaks for Au in the Auger spectra, which confirms the top layer of this surface is fully covered with Pd atoms even after the annealing process. By integrating the $H_2$-TPD spectra, we calculated the relative number of Pd atoms on each surface compared to the 6.0 ML Pd deposited surface. As indicated in Table 1, the relative number of Pd atoms is 1.0, 0.89, 0.8, 0.64, 0.48, 0.34, and 0.15 corresponding to 6.0, 4.0, 3.0, 2.5, 2.0, 1.5, and 1.0 ML Pd deposited surfaces, respectively. Additionally,

| Initial Pd coverages (ML) | Relative Pd atoms[a] | Fraction of Pd–Au interfaces[b] | Fraction of Pd(111) like islands[b] |
|---|---|---|---|
| 1 | 0.15 | 1 | - |
| 1.5 | 0.34 | 0.68 | 0.32 |
| 2 | 0.48 | 0.34 | 0.66 |
| 2.5 | 0.64 | 0.21 | 0.79 |
| 3 | 0.8 | 0.22 | 0.78 |
| 4 | 0.89 | 0.04 | 0.96 |
| 6 | 1.0 | - | 1.0 |

Table 3.1. Relative amount of surface Pd atoms, Fraction of Pd–Au interfaces, and Fraction of Pd(111) like islands depending on Initial Pd coverages. [a]Relative to the annealed 6 ML of Pd–Au(111) surface. [b]Estimated from the $H_2$-TPD spectra in Figure 3.1a.

we estimated the ratios between the deconvoluted regions in Figure 3.1a, which is also listed on Table 3.1. This analysis once again confirms that with increasing the initial Pd coverages, the relative amount of Pd–Au interface sites steadily decreases, and the relative amount of Pd (111)-like island sites continuously increases.

The $O_2$ desorption spectra in Figure 3.1b also shows different desorption behavior based on the Pd coverages on the Au (111) surface. Most of the $O_2$ molecules on a 1.0 ML Pd deposited Au(111) surface desorb below 150 K, but beginning with a coverage of 1.5 ML of Pd, the $O_2$ desorption spectra continues to broaden to ~200 K. Although the tested Pd–Au surfaces show broad desorption spectra instead of the strong desorption peaks observed on pure Pd surfaces,[84,85,94] the higher the coverage of Pd on the Au(111) surface, the more $O_2$ desorption occurs above 150 K and continues over 180 K at which $O_2$ dissociation has been observed on continuous domains of Pd atoms during molecular $O_2$ desorption.[17,80] Thus, it seems that the Pd(111)-like islands, which exist for a coverage of 1.5 ML of Pd (and higher), is a key for strong adsorption and dissociation of $O_2$ on Pd–

Au surfaces, so we carefully examined the dissociative adsorption of $O_2$ at surface temperatures of 300 K and higher.[89,94,109,110]

### 3.3.2. King and Wells Measurements of $O_2$ on the Various Pd–Au Surfaces.

As shown in Figure 3.2a, we conducted King and Wells measurements on variously prepared Pd–Au surfaces to observe the general $O_2$ adsorption trends at 77 K and 300 K. In these measurements, the $O_2$ molecular beam was first directed on the inert flag for 5 seconds to determine the relative intensity and then on the Pd–Au surface (again, the decreased signal intensity is proportional to the fraction of $O_2$ molecules that adsorb on the surface). At 77 K, more $O_2$ molecules are absorbed with increasing Pd coverages. Interestingly, the dissociative adsorption of $O_2$ at 300 K is just observable with a 1.5 ML Pd deposited surface, which has some Pd (111)-like islands. However, the

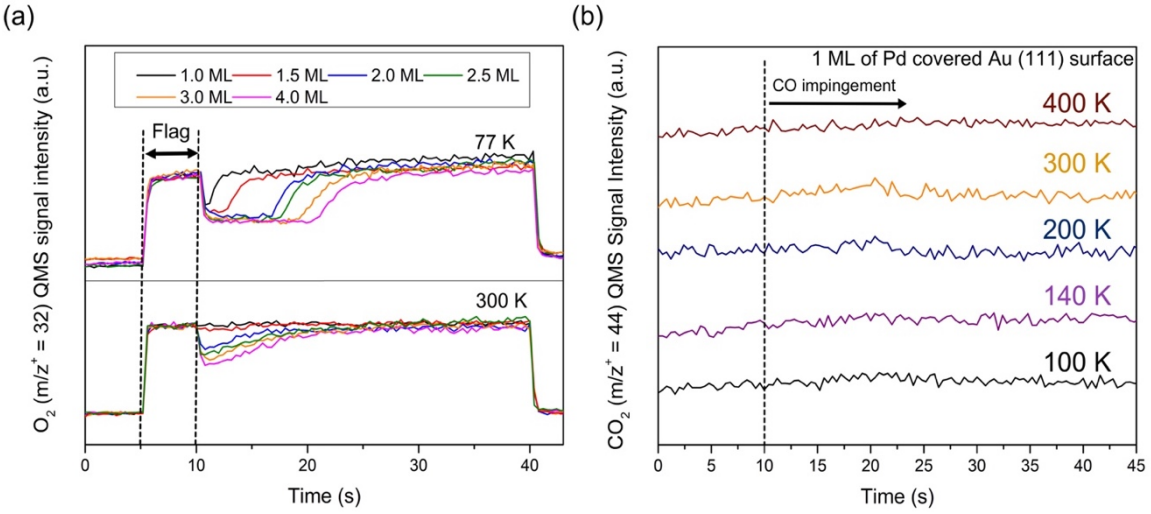


Figure 3.2. (a) King and Wells measurements of $O_2$ on the Pd–Au surfaces at 77 K (top) and 300 K (bottom). The $O_2$ molecular beam impinges on the inert flag for 5 seconds and is then directed on 1.0, 1.5, 2.0, 2.5, 3.0, and 4.0 ML of Pd deposited Pd–Au surfaces at t=10 seconds. (b) CO-RMBS on 1 ML of Pd deposited Au (111) surface. The surface was first exposed to the $O_2$ molecular beam at 300 K, and then exposed to the CO molecular beam (from 10 seconds forward) at 100 K, 140 K, 200 K, 300 K, and 400 K which indicates no production of $CO_2$ suggesting no adsorbed oxygen adatoms.

1.0 ML Pd deposited surface case, which is composed of predominantly Pd–Au interface sites, does not show measureable (*via* King and Wells) dissociative adsorption of $O_2$ at 300 K despite the fact that it can molecularly adsorb $O_2$ at 77 K. To verify the presence/absence of oxygen adatoms on the 1ML Pd deposited surface, we conducted CO-RMBS at various temperatures (100 K – 400 K) after exposing the sample to $O_2$ at 300 K, which titrates the oxygen adatoms *via* generation of $CO_2$.[17–19,69,80] This method was adopted to avoid heating the surfaces above 500 K, so we are not able to observe the recombinative desorption of $O_2$ during TPD tests, which has been observed at ~ 750 K on a Au–Pd(111) surface.[18] Furthermore, for our experimental conditions, CO molecules do not make observable changes to the surface composition. (More details are in Figure B.8). As indicated in Figure 3.2b, there is no $CO_2$ generation observed for any of the tested temperatures on the 1ML Pd deposited surface. This result once again confirms that Pd(111)-like islands are necessary for dissociative adsorption of $O_2$ on the Pd–Au surface. In the following section, we will also analyze the results of CO-RMBS measurements on 1.5 – 4.0 ML Pd deposited surfaces to verify the presence of surface oxygen atoms and their reactivity.

### 3.3.3. CO Oxidation on the Various Pd–Au Surfaces at 140 K, 200 K, and 400 K

As seen in Figure 3.3a, all of the tested Pd–Au surfaces clearly show $CO_2$ generation at the lower temperature of 140 K, a temperature at which CO molecules do not accumulate on the Au sites.[93,114] Although we are also able to observe $CO_2$ generation at a temperature as low as 100 K (as shown in Figure B.4), the $CO_2$ signals are weak and uncertain especially for the 3.0 ML and 4.0 ML Pd deposited surfaces, compared to their $CO_2$ generation at 140 K. Moreover, the amount of $CO_2$ generated at 140 K (Figure 3.3a) and 200 K (Figure 3.3b) is not proportional to the Pd deposition, which, as

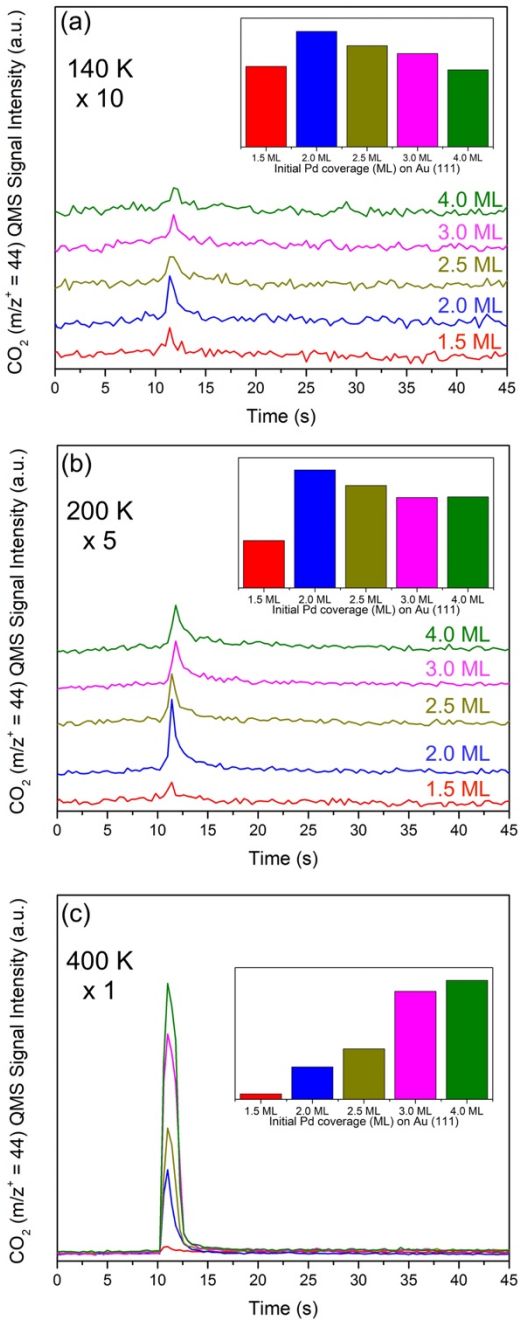


Figure 3.3. The $CO_2$ generation measured from the QMS at (a) 140 K, (b) 200 K, and (c) 400 K during CO-RMBS. The CO molecular beam was exposed to the samples starting from 10 seconds. The y-scale for (a) and (b) are magnified by x 10 and x 5 compared to (c). Insets in each figure indicate the relative amount of generated $CO_2$ by integrating the QMS signals.

mentioned earlier, is related to the amount of dissociatively adsorbed $O_2$ at 300 K. In

particular, as shown in the inset on each figure, we also investigated the relative amount of reactive oxygen adatoms on each surface at those tested temperatures by integrating the generated $CO_2$ signal following impingement by the CO beam. When we compare the amount of $CO_2$ produced by these reactive oxygen adatoms, the 2.0 ML Pd deposited surface shows the highest $CO_2$ generation at 140 K and 200 K, and the 2.5 ML case is also higher than the 3.0 ML and 4.0 ML cases. It seems that the Pd–Au interfaces, or small sizes of the Pd ensembles, affect the low temperature reactivity, which can have Au like reactivity. We have reported earlier in this paper that the Pd–Au interface character is stronger on the 2.0 ML and 2.5 ML Pd deposited surfaces as shown in Figure 3.1a. (It is hard to directly compare the quantity of $CO_2$ generated from the 1.5 ML Pd deposited surface to others since it only shows a tiny amount of $O_2$ dissociation at 300 K as shown in Figure 3.2. However, it has the lowest general activation barrier for CO oxidation compared to others, which will be provided in the next section.) With increasing surface temperatures, the quantity of generated $CO_2$ molecules is a strong function of the quantity of adsorbed oxygen adatoms, which is directly related to the Pd coverage, because the oxygen adatoms on relatively larger Pd ensembles, which have more Pd like properties, are able to oxidize CO molecules at high temperatures. Specifically in Figure 3.3c, the 4.0 ML Pd deposited surface, which is largely covered with the Pd(111)-like islands, shows the highest quantity of $CO_2$ generation at 400 K, and it continuously diminishes with decreasing Pd coverages. As we just mentioned, this is primarily because the 4.0 ML case has many Pd(111)-like islands, so it can hold the largest amount of oxygen adatoms among the tested samples, which are reactive at relatively high temperatures as with pure Pd surfaces. Moreover, the amount of generated $CO_2$ in all tested samples continuously grows with increasing temperatures, as shown in Figure B.5 for the 2.0 ML case. It is also because the oxygen atoms on the bigger Pd ensembles or Pd(111)-like

islands, which exist for the 1.5 ML Pd deposited surface and higher coverages, need more thermal energy to be reactive. Thus, the higher temperatures lead to more oxygen adatoms being reactive on the Pd–Au surfaces.

### 3.3.4. $O_2$ Dissociation Barriers Depending on Pd Coverages

To relate the $O_2$ dissociation behavior to the reactivity of the resulting oxygen adatoms (which depends on Pd coverage), we estimated the dissociation energy barriers for $O_2$ and compared these values to the reaction energy barriers for CO oxidation, which indirectly indicates the reactivity of the adsorbed atomic oxygen. To determine an activation barrier to dissociation, we adopted a simple model used to describe molecular chemisorption-mediated oxygen dissociation, which has been used previously for $O_2$ dissociation on transition metals such as Pd,[85,115,116] Pt,[117–121] Ir,[122] and Ru.[123] It is based on a two potential energy well model for $O_2$, one for the molecularly chemisorbed $O_2$ and

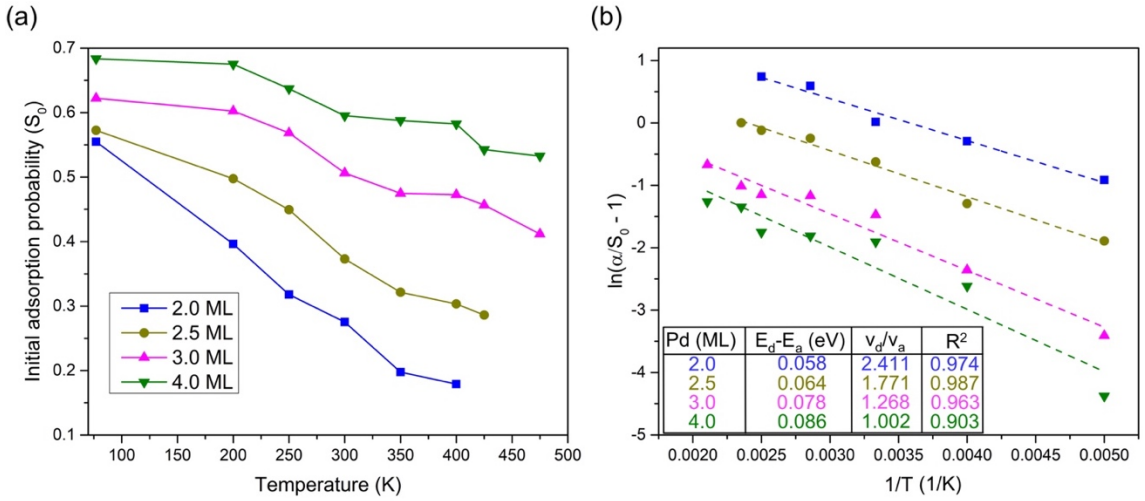


Figure 3.4. (a) Initial adsorption probability ($S_0$) of $O_2$ on 2.0, 2.5, 3.0, and 4.0 ML of Pd deposited Pd–Au (111) surfaces at different temperatures. We assumed $\alpha$ as a $S_0$ value measured at 77 K and drew (b) Arrhenius plots of ln ($\alpha/S_0$-1) vs 1/T based on the $S_0$ values measured in (a). The table in (b) shows $E_d$-$E_a$ derived from the slopes, $\nu_d/\nu_a$ estimated from the y intercepts, and $R^2$ values resulting from linear fittings.

the other for the dissociated (atomic) oxygen (ignoring a well for physical adsorption). To provide data for the analysis, we obtained values for the experimental initial dissociative adsorption probability for $O_2$ ($S_0$) as a function of surface temperature. $S_0$ values are generally higher with higher Pd deposited surfaces, which means that $O_2$ dissociation more readily occurs on the more highly Pd covered surfaces, and steadily decreases when the samples were held at higher temperatures as indicated in Figure 3.4a. Without explicitly considering the kinetic effects of physically adsorbed molecules, $S_0$ in the limit of zero coverage is modeled as written below:

$$S_0 = \frac{\alpha k_a}{k_a + k_d},$$

where α indicates the probability of molecular chemisorption, and $k_a$ and $k_d$ are the rate constants for the dissociation and desorption of chemisorbed molecular species, respectively. Assuming that $k_a$ and $k_d$ can be accurately described by the Arrhenius equation, $S_0$ can be rewritten in the following form:

$$\ln\left(\frac{\alpha}{S_0} - 1\right) = \ln\left(\nu_d/\nu_a\right) - \frac{(E_d - E_a)}{k_B T_s},$$

where $k_B$ is Boltzmann's constant, $T_s$ represents the sample temperature, $E_d$ and $E_a$

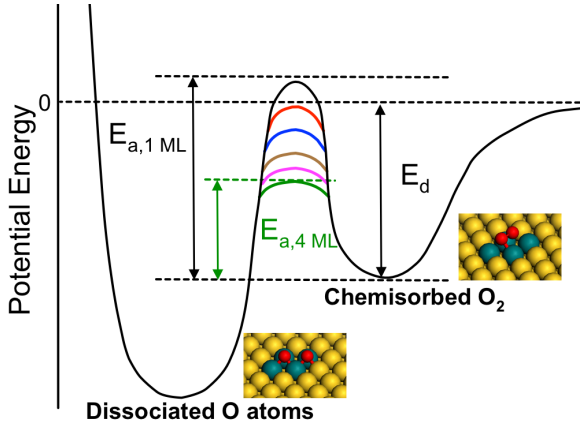


Illustration 3.1. One dimensional potential energy surface schematic for oxygen adsorption on 1 ML (black), 1.5 ML (red), 2.0 ML(blue), 2.5 ML (dark yellow), 3.0 ML (pink), and 4 ML (green) of Pd deposited Pd–Au (111) bimetallic surface.

indicate activation energies for desorption and dissociation, and $v_d/v_a$ is the ratio of pre-exponential factors.[115–120,124,125] Arrhenius plots of ln ($\alpha/S_0$-1) vs 1/T for 2 ML, 2.5 ML, 3.0 ML, and 4 ML Pd deposited surfaces are shown in Figure 3.4b assuming $\alpha$ as the adsorption probability at 77 K, which allows us to calculate the value of $E_d - E_a$ from the slope. By comparing the 4 ML Pd deposited surface with the 2 ML Pd deposited surface, we notice that the 4 ML case shows a higher $E_d - E_a$ value (0.086 eV, 8.3 kJ/mol) and lower $v_d/v_a$ ratio (1.002) than the corresponding values for the 2 ML case, 0.058 eV, 5.6 kJ/mol for $E_d - E_a$ and 2.411 for $v_d/v_a$. Since the positive $E_d - E_a$ value indicates that $E_a$ is lower than $E_d$, $O_2$ dissociation on the 4ML Pd deposited surface is more likely to occur (since the $E_d - E_a$ value is larger) than for the 2 ML case. Furthermore, the larger $v_d/v_a$ ratio for the 2ML case can be entropically interpreted as the transition state for the dissociation of $O_2$ is more constrained on the 2ML case than on the 4 ML case and/or the available phase space for desorption is relatively larger for the 2 ML case. The 2.5 ML and 3 ML Pd deposited surfaces also follow these trends, where their $E_d - E_a$ values (2.5 ML: 0.064 eV and 3 ML: 0.078 eV) and $v_d/v_a$ ratios (2.5 ML: 1.779 and 3.0 ML: 1.268) fit between the corresponding values from the 2 ML and 4 ML cases. The schematic one dimensional potential energy surface is described in Illustration 5.1 based on the estimated $E_d - E_a$ values. Since the 1 ML Pd deposited surface does not show measureable $O_2$ dissociation (confirmed from no measureable $CO_2$ generation during the CO-RMBS measurements), its $E_d - E_a$ could be negative, suggesting that $E_a$ is higher than the vacuum level energy (= 0). The 1.5 ML Pd deposited surface does show $CO_2$ generation by CO-RMBS measurements, but it is still difficult to directly observe the dissociative adsorption of $O_2$ via King and Wells measurements; thus, we believe that the $E_d - E_a$ value for the 1.5 ML case is close to zero but is probably a positive value. From 2.0 ML to 4.0 ML, the $E_d - E_a$ values continuously increase, surmised as lowering $E_a$

values with increasing Pd coverages. Therefore, these results support the notion that $O_2$ dissociation is more favorable on the more Pd covered surfaces as one might expect intuitively.

### 3.3.5. Reactivity of Oxygen Adatoms Depending on Pd Coverages

We estimate the $E_a$ values as a function of Pd deposition by calculating $E_d$ values based on a Redhead analysis.[126] The desorption energy of molecularly adsorbed $O_2$ ($E_d$) at low coverages (20 ~ 30 % for each of the saturated coverages) turns out to be ~ 41 kJ/mol on all tested Pd–Au surfaces (a desorption peak near 170 K is observed as shown in Figure B.6). By combining these data, we determined the activation barrier for the dissociation of $O_2$ ($E_a$) for the various Pd–Au surfaces, and these values are plotted in Figure 3.5 (red line). The overall trend for $O_2$ dissociation on Pd–Au surfaces shows it to be more likely to occur on the more highly Pd covered surfaces. Thus, the 4 ML Pd deposited case shows a value of ~ 0.34 eV (~ 33 kJ/mol) for $E_a$, which is close to a previously measured value, 0.32 eV, for a pure Pd (111)[115] surface. We have also

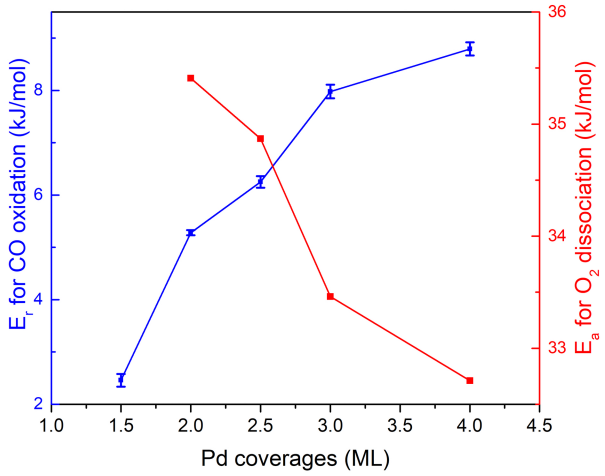


Figure 3.5. The estimated activation barriers for CO oxidation (blue) and $O_2$ dissociation (red) on the various amount of Pd deposited Pd–Au (111) surfaces.

estimated the general tendency for the reactivity of oxygen adatoms on each of the Pd deposited surfaces. For this analysis, we derive the Arrhenius plots regarding the overall generation of $CO_2$ at different temperatures (Figure B.7) to estimate a general activation barrier for CO oxidation ($E_r$) by CO and oxygen adatoms on each of the oxygen pre-covered Pd–Au surfaces. Thus, $E_r$ does not involve the energetics of $O_2$ activation, which is known as a main rate limiting factor for CO oxidation on Au and Pd based catalysts.[127–129] As we mentioned early, the surface temperatures affect the quantity of "reactive" oxygen adatoms on each sample, which means that the higher the temperatures applied to a sample, the more oxygen adatoms on the relatively larger Pd ensembles can be involved in the reaction with CO. Nevertheless, we also have seen that the surface compositions still determine the total amount of oxygen adatoms on each Pd–Au surface and strongly influence their reactivity, particularly at relatively low temperatures. Thus, from this analysis, we want to understand the general reactivity of oxygen adatoms as a function of Pd coverage. Specifically to do this, we integrated the area of the generated $CO_2$ signal after the initial CO molecular beam impingement for all the tested temperatures; 140 K, 200 K, 300 K, and 400 K (and for the different Pd-covered surfaces). We then plotted the $CO_2$ production (P) as ln P vs 1/T to create an Arrhenius plot of the CO oxidation rate on each of the Pd covered surfaces and from this plot a general activation energy for reaction could be determined (Figure B.7). In contrast to the $O_2$ dissociation barriers, the general activation barrier for CO oxidation (blue line in Figure 3.5), which is directly related to the reactivity of the surface oxygen atoms, increases with the more heavily Pd covered surfaces. These trends once again confirm the roles of Pd and Au on the Pd–Au surfaces: the Pd (111)-like islands most easily dissociatively adsorb $O_2$ on their surfaces, and the dissociated oxygen atoms react

at the Pd–Au interfaces with CO where the existence of Au makes the surface oxygen highly reactive compared to that of a pure Pd surface.

### 3.4. CONCLUSION

In summary, we have studied the dissociative adsorption of $O_2$ and the reactivity of oxygen adatoms on various Pd–Au bimetallic surfaces. We first analyzed the surface compositions of various Pd covered Au (111) surfaces employing $H_2$ temperature programmed desorption, and found that more Pd(111)-like islands are on the Pd–Au surfaces with higher Pd coverages. It has been found that the existence of the Pd(111)-like islands is directly related to the dissociative adsorption of $O_2$ at 300 K, and the amount of dissociatively adsorbed $O_2$ is also proportional to the quantity of Pd(111)-like islands. CO-RMBS (Reactive Molecular Beam Scattering) was used to titrate the surface oxygen atoms and determine their reactivity by observing the rate of generation of $CO_2$ at various temperatures. $CO_2$ generation began to be clearly observed at 140 K, and we found that the rate of $CO_2$ generation at low temperatures (below 200 K) is strongly related to the quantity of Pd–Au interface sites. Moreover, at relatively high temperatures (~ 400 K), the amount of generated $CO_2$ depended on the quantity of Pd(111)-like islands since this temperature is in the range in which oxygen atoms on pure Pd surfaces can react with CO to produce carbon dioxide. We also estimated the activation barriers for $O_2$ dissociation and CO oxidation as a function of Pd coverage. From this analysis, it was verified that when the Pd coverage is increased on the Au (111) surface, the $O_2$ dissociation energy barrier is lower, but the CO oxidation reaction barrier is relatively higher. Therefore, we confirmed that the enhanced reactivity of the oxygen atoms is based on Pd–Au interfaces, and the amount of dissociatively adsorbed $O_2$ correlates with the coverage of Pd(111)-like islands.

# Chapter 4: Selective Oxidation of Acetaldehyde to Acetic acid on Pd–Au Bimetallic Model Catalysts

## 4.1. INTRODUCTION

Acetic acid ($CH_3COOH$, AcOH) is familiar as a food preservative, such as vinegar, and is produced by alcohol fermentation. AcOH is also a major reactant for synthesizing commercial chemicals such as vinyl acetate, acetic anhydride, and various esters (e.g., ethyl acetate, n-butyl and isobutyl acetate).[130–132] Because of its wide use the global demand for AcOH grew from 5.4 million tons in 1997 to 13 million tons in 2015, and it is expected to reach 18 million tons in 2020.[130,131]

One of the conventional routes for manufacturing AcOH is the oxidation of acetaldehyde ($CH_3CHO$, AcAl) at 150 °C and 55 atm with manganese (II) or cobalt (II) acetate catalysts.[130–132] This process produces some side products, such as ethyl acetate, formic acid, and formaldehyde, although the overall yield of this process can reach 95%. After the first adaptation of the methanol carbonylation process in 1960 by BASF, most industrial synthesis of AcOH has followed the Monsanto and Cativa processes, which are the more advanced methanol carbonylation schemes.[130–132] In these operations, Rh and Ir based organometallic catalysts are used in the temperature and pressure ranges of 150 - 200 °C and 30 - 50 atm, and the selectivity towards AcOH is ~99%.[130,131] Since all the methanol carbonylation processes are solution based, distillation and separation steps are necessary for purifying the AcOH from the reaction mixture.[133]

Here we report a new vapor-phase heterogeneous catalytic process for the

*Han, S.; Shin, K.; Henkelman, G.; Mullins, C.B. Selective Oxidation of Acetaldehyde to Acetic Acid on Pd–Au Bimetallic Model Catalysts, *ACS Catalysis*, **2019**, 9, 4360-4368.
S. Han and C. B. Mullins conceived and designed experiments, analyzed and discussed results, and commented on the manuscript. K. Shin and G. Henkelman conducted DFT calculations. S. Han performed experiments, analyzed data and wrote the paper.

selective oxidation of AcAl to AcOH near room temperature over Pd–Au bimetallic model catalysts which would require fewer separation steps.

Pd–Au nanoparticles have shown impressive catalytic activities in the synthesis of vinyl acetate,[13,14] $H_2O_2$,[10–12] the oxidation of alcohols[23,24,27] and CO,[16,21,22] which are mainly due to the so-called ensemble effect, determined by the local compositions of Pd and Au atoms. For a better understanding of these catalytic reactions based on surface composition, the detailed molecular level chemistry has been also investigated by adopting Pd–Au model catalytic surfaces under ultrahigh vacuum (UHV). Specifically, it has been found that the distance between Pd monomers on Au surfaces is a key for the promotional effect in vinyl acetate synthesis,[28] and that the Pd–Au interfaces are the reactive areas for the selective production of $H_2$ from the decomposition of formic acid (HCOOH).[29] The behavior of simple molecules (e.g., $O_2$,[70,80] $H_2$,[30,32,134] CO,[17,18,82] $H_2O$,[69] and $CH_3CH_2OH$[108]) on Pd–Au surfaces has also been widely studied. In particular, the $H_2$ desorption behavior can be used to analyze the surface composition of Pd and Au. The recombinative desorption of $H_2$ occurs between 150 K - 300 K for Pd–Au interface sites (or discontinuous and small Pd ensembles),[29,30,70,108] which is higher than the desorption temperatures of $H_2$ on the pure Au(111) surface (< 150 K)[103] and lower than on pure Pd surfaces (> 300 K)[104,105]. When the Pd coverage on the Au(111) surface becomes large enough to form Pd(111)-like islands (or sufficiently large Pd ensembles to have pure Pd-like character), there is another $H_2$ desorption feature above 300 K, which corresponds to the desorption of $H_2$ from pure Pd surfaces.[29,30,70,108] Moreover, we have experimentally verified that Pd(111)-like island sites (large enough Pd ensembles to have Pd(111)-like character) are necessary for the dissociative adsorption of $O_2$.[70] Furthermore, the reactivity of the dissociated oxygen adatoms depends on the concentration of Pd–Au interface sites.[70]

Motivated by these results, we now focus on the oxidation of AcAl to AcOH on Pd–Au(111) model catalysts. Previously, it has been found that oxygen adatoms placed on Au(111) [via ozone] can oxidize acetaldehyde to acetic acid from ~ 460 K.[135] Although AcOH is also produced from the oxidation of AcAl on pure Pd surfaces above 400 K,[136] it is accompanied by the generation of other oxidized products (e.g. CO, $CO_2$, and $H_2O$), thereby decreasing the selectivity towards AcOH. This is primarily because the acetate species ($CH_3COO$*) on pure Pd surfaces, formed by oxygen adatoms (O*) and acetyl ($CH_3CO$*, deprotonated acetaldehyde) can be decarboxylated, which is initiated by the dissociation of β-C-H bonds in the acetate species.[136–138] However, we have found that the decarboxylation of acetate can be prevented by controlling the surface composition of Pd and Au, and it leads to the selective oxidation of AcAl to AcOH near room temperature. We have investigated the detailed chemistry using quadrupole mass spectroscopy and FT-IR spectroscopy as well as density functional theory (DFT) calculations.

## 4.2. Experimental & Computational Methods

### 4.2.1. Ultrahigh Vacuum (UHV) Experiments

All experiments in the present chapter were conducted in a UHV molecular beam surface scattering system with a base pressure of 1.0 x $10^{-10}$ Torr, which has been carefully described in a previous paper.[83] In brief, the apparatus can generate two separate molecular beams, and is equipped with an Auger electron spectrometer (Physical Electronics 10-500), a quadrupole mass spectrometer (Extrel C-50), and a Fourier transform infrared spectrometer (Bruker Tensor 27) with a mercury−cadmium−telluride (MCT) detector. A disk shaped Au(111) single crystal sample (12 mm in diameter x 2 mm thickness) is held by a Mo wire fitted in a groove cut on the edge of the Au(111)

sample in the UHV chamber. This Au(111) sample was periodically cleaned by Ar sputtering and then annealed to 800 K. The Mo wire is used to resistively heat the sample and also to cool the sample to 77 K by providing thermal contact with a liquid nitrogen bath. The sample temperature was measured by a K-type thermocouple placed in a small hole in the edge of the sample.

The Pd–Au model surface was prepared based on a layer by layer growth mechanism, in which the Pd atoms can diffuse into the bulk of the Au(111) sample by heating to form a Pd–Au alloy on the top surface.[78] The Pd deposition was calibrated by a quartz crystal microbalance (QCM) and controller (Maxtek Inc.) with the assumption of a thickness of 1 monolayer (ML) for Pd as 2.74 Å. In this chapter, two different Pd coverages (2.0 ML and 3.0 ML) were deposited on the Au(111) surface at 77 K and then annealed to 500 K for 10 minutes as with our previous studies to form a Pd–Au alloy at the surface.[29,69,70,80] Each of the annealed Pd–Au surfaces was also exposed to $O_2$ molecules at 475 K *via* the molecular beam to treat the surfaces with $O_2$ for consistency with our previous $O_2$ activation and reactivity study.[70]

All gas molecules were delivered *via* a molecular beam, which allows for the accurate control of the amount of adsorbed target molecules on the surface. Temperature-programmed desorption (TPD) was adopted in this chapter to analyze the surface composition of Pd–Au surfaces using $H_2$ and to investigate the oxidation chemistry of acetaldehyde. For the $H_2$-TPD, we initially saturated the Pd–Au surfaces with $H_2$ *via* a $H_2$ molecular beam at 77 K and then heated to 500 K at 1 K/s while observing the $m/z^+ = 2$ signal with the QMS. To test the oxidation of AcAl, each Pd–Au surface was first exposed to a $O_2$ molecular beam at 300 K until it was saturated with oxygen adatoms, and then the surface was cooled to 77 K. AcAl molecules were then impinged on the O-precovered Pd–Au surfaces at 77 K *via* an AcAl molecular beam, followed by heating of

the sample to 500 K at 1 K/s while detecting various masses using the QMS. Heating the surfaces to 500 K did not affect to their Au and Pd compositions, which has been verified in our previous studies.[69,70,80] After finishing the TPD of AcAl, we titrated remaining CO or other carbon species on the surface by imping $O_2$ via the molecular beam at 475 K (as we did during the sample preparation step) in order to conduct other experiments. We also used reflection adsorption infrared spectroscopy (RAIRS) to characterize the remaining molecular species on the Pd–Au surfaces during the desorption and oxidation of the AcAl. All the IR spectra were averaged from 512 scans with a resolution of 4 $cm^{-1}$.

### 4.2.2. Density Functional Theory (DFT) Calculations

We performed spin-polarized DFT calculations with the Vienna ab initio simulation package.[139] The projector augmented wave framework was employed to treat interactions between the core and valence electrons.[140] Electronic exchange and correlation were described with the Revised-Perdew-Burke-Ernzerhof (RPBE) functional.[141] The cutoff energy of the plane wave basis was set to 400 eV and the Brillouin zone was sampled at 2 x 2 x 1 with the Monkhorst-Pack scheme[142]. The convergence criteria for the electronic structure and geometry were set to $10^{-5}$ eV and 0.01 eV·$Å^{-1}$, respectively.

The Au slabs used in this chapter supported different size Pd ensembles in the surface layer. These slabs were constructed with a 5 x 5 supercell containing 4 atomic layers with the bottom 2 layers fixed in their bulk positions. Different numbers of Pd atoms (2, 3, 4, 7, and 25 atoms) of the ensemble were considered to study the effect of the Pd ensemble on adsorption of each intermediate during the AcAl oxidation reaction. These structures are shown in Figure C.8 Each slab is separated by a 10 Å vacuum gap in the z-direction to avoid self-interaction.

## 4.3. Results and Discussion

### 4.3.1. Pd–Au Composition Analysis Using $H_2$-TPD

Since our samples have been annealed at 500 K after the initial deposition of Pd onto Au(111) at 77 K, which causes Pd atoms to diffuse into the Au lattice, the temperature programmed desorption (TPD) of $H_2$ was conducted on both 2.0 and 3.0 ML Pd deposited surfaces to quantify the fraction of Pd atoms remaining on the surface after annealing, identified as 0.45 Pd / 0.55 Au and 0.8 Pd / 0.2 Au respectively. As previously verified,[30,32] $H_2$ molecules can be dissociatively adsorbed on the Pd–Au surface. Hydrogen adatoms located at Pd–Au interfaces (or discontinuous and small Pd ensembles) recombinatively desorb between 150 K and 300 K, which is higher than the desorption temperature of $H_2$ from the pure Au(111) surface (100 K – 150 K)[103] and lower than pure Pd surfaces (> 300 K)[104,105]. When the Pd coverage is increased to have Pd(111)-like islands (or continuous and sufficiently large Pd ensembles to have pure Pd-

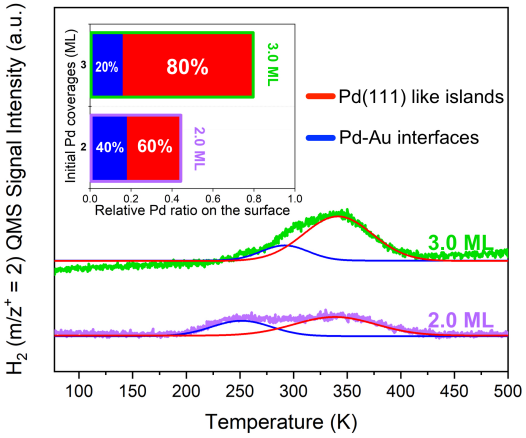


Figure 4.1. Temperature-programmed desorption (TPD) of $H_2$ on Pd–Au surfaces. $H_2$ molecules were impinged at 77 K via a molecular beam on a 2.0 ML Pd initially deposited surface (purple) and 3.0 ML Pd initially deposited surface (green) until the samples were saturated. The saturated samples were heated to 500 K by 1 K/s. Each spectrum is deconvoluted to indicate Pd–Au interface sites (blue) and Pd(111)-like island sites (red). The inset quantifies the relative coverages of the Pd–Au interface sites. and the Pd(111)-like island sites on the 2.0 ML and 3.0 ML Pd deposited surfaces.

like character), the recombinative desorption of $H_2$ can also occur above 300 K, similar to pure Pd surfaces.[29,30,70,108] As shown in Figure 4.1, we performed a peak deconvolution of the $H_2$-TPD spectra for which the blue trace represents $H_2$ desorbing from the Pd–Au interface sites and the red trace indicates $H_2$ desorption from the Pd(111)-like islands. Based upon the deconvoluted peak areas, the 2.0 ML Pd deposited surface is composed of 40 % Pd–Au interface sites and 60% Pd(111)-like islands. On the 3.0 ML Pd deposited surface, the $H_2$ TPD peak due to the Pd–Au interface sites decreases in magnitude and is shifted to higher temperatures (compared to the 2.0 ML case) showing 20 % Pd–Au interface sites and 80 % Pd(111)-like island sites. The relative fraction of surface Pd atoms is estimated to be 0.45 for the 2.0 ML case and 0.8 for the 3.0 ML case, determined by comparing each of their $H_2$-TPD spectra to the spectrum for a 6.0 ML Pd deposited surface (Figure C.1) which is fully covered with Pd atoms on its top layer (even after annealing). All these analyses confirm that the 3.0 ML Pd deposited surface has a stronger Pd-like character than the 2.0 ML case; later we will describe how the surface composition affects the interaction between acetaldehyde ($CH_3CHO$, AcAl) molecules and oxygen adatoms.

### 4.3.2. AcAl Desorption from the O-free and O-precovered 2.0 ML Pd Initially Deposited Au(111) Surfaces.

For a better understanding of AcAl surface chemistry, we conducted TPD tests of various coverages of AcAl on the O-free and atomic O-precovered Pd–Au surfaces (Pd: 2.0 ML), where we found that the AcAl molecules are more stabilized on the O-precovered Pd–Au surface and selectively oxidized to acetic acid. In these TPD measurements, we deposited various quantities of AcAl molecules on the Pd–Au surface at 77 K via a molecular beam and then heated the surface to 500 K (at or below which the

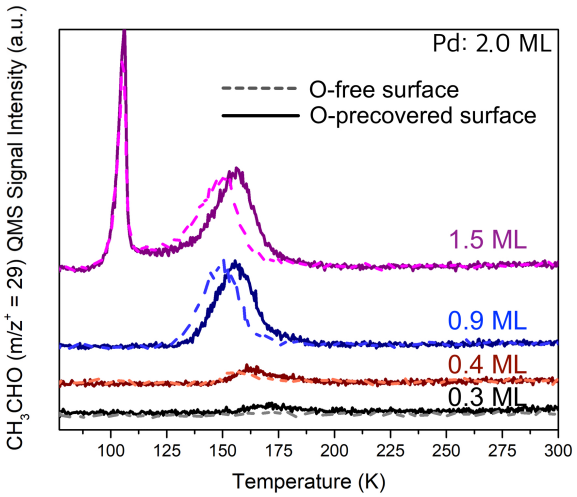


Figure 4.2. TPD of AcAl on the 2.0 ML Pd deposited surface. Different coverages of the AcAl were impinged via a molecular beam at 77 K, and then they were heated to 500 K by 1 K/s. No desorption features were observed above 200 K. The solid lines indicate AcAl desorption from the oxygen-precovered Pd–Au surface, and the dashed lines describe the AcAl desorption from the oxygen-free Pd–Au surface.

surface composition is stable). As shown in Figure 4.2, molecular AcAl desorption ($m/z^+$ =29) begins at slightly higher temperatures on the O-precovered Pd–Au surface (solid lines) compared with the oxygen-free Pd–Au surface (dashed lines), and no desorption features are observed above 200 K for either surface. Specifically, the oxygen-free surface does not show a molecular desorption feature for 0.3 ML AcAl, but it is observed on the O-precovered surface at ~ 175 K. This is an indication that all the AcAl molecules dissociate on the oxygen-free Pd-Au surface (the products of dissociation are displayed in Figure C.2) but total dissociation is prevented on the O-precovered surface – a point that will be discussed more fully in the following section. When the AcAl coverage is at 0.4 ML, the oxygen-free surface also starts to show molecular desorption of AcAl with a small peak at 155 K; nevertheless, it does not continue above 175 K. At a coverage of 0.9 ML, the AcAl desorption from the oxygen-free surface begins at 125 K and ends at 175 K with a peak at 150 K, which is a slightly lower temperature than for that on the pure Pd

surface (~160 K).[143] The intensity of the AcAl desorption peak at 150 K is a maximum at a coverage of 0.9 ML AcAl. This can be verified via comparison with the 1.5 ML AcAl adsorbed surface (as shown in Figure C.3) which fully covers the surface (i.e., 1 ML) with AcAl and also shows some multilayer desorption of AcAl at 110 K. The desorption spectrum of 0.9 ML AcAl on the O-precovered surface is from 130 K to 200 K forming a peak at 160 K, where the overall desorption spectrum is shifted to a slightly higher temperature range compared with the oxygen-free surface. This suggests that the interactions between the AcAl molecules and the surface oxygen adatoms stabilize the AcAl molecules on the Pd –Au surface (which has also been observed on the pure Pd surface[136]). 1.5 ML of AcAl on the O-precovered surface also shows a multilayer desorption peak at 110 K, as with the O-free surface.

On the basis of the results above, we conducted a detailed product analysis during the TPD of AcAl on both oxygen-covered and oxygen-free Au–Pd (2.0 ML Pd) surfaces. In brief, we have discovered that the AcAl molecules are decomposed on the O-free surface, but they are selectively oxidized to AcOH near room temperature on the O-precovered surface. From previous studies on pure Pd, it has been found that residual AcAl molecules remaining after molecular AcAl desorption are fully decomposed to generate $H_2$ (~300 K), $CH_4$ ( ~ 290 K), and CO (~ 475 K).[143,144] AcAl decomposition also mainly occurs on the oxygen-free Pd–Au surface (Pd: 2.0 ML). In the TPD spectra for 0.9 ML AcAl on the oxygen-free Pd–Au surface (Figure 4.3a), $H_2$ desorption takes place from 175 K to 400 K, immediately following the desorption of the molecularly adsorbed monolayer of AcAl. The initiation of $H_2$ desorption from the oxygen-free Au–Pd (2.0 ML) surface is lower than that from pure Pd surfaces, since the Pd–Au interfaces are the sites for the $H_2$ desorption from 150 K to 300 K, and the Pd(111)-like islands evolve $H_2$ desorption from 300 K to 400 K, as with pure Pd surfaces. The desorption of $CH_4$ is

observed from 250 K to 375 K, which is evidence of C-C bond dissociation, and this temperature range corresponds to $CH_4$ desorption subsequent to AcAl decomposition on pure Pd surfaces.[143,144] After $CH_4$ desorption begins, the intensity of desorbing $H_2$ molecules decreases. This observation indicates that the $CH_3^*$ fragments from AcAl recombine with H adatoms and leave the surface as $CH_4$ ($CH_3$*+ H*), which diminishes the $H_2$ desorption intensity during $CH_4$ generation. The remaining C-O fragments on the surface desorb from the surface as CO molecules above 400 K.

On the O-precovered 2.0 ML Pd deposited surface (Figure 4.3b), the AcAl chemistry is different from that of the oxygen-free Pd–Au surface and, as mentioned earlier, a large increase in the selectivity to production of acetic acid is observed. According to a previous study regarding the O-precovered Pd (pure) surface, oxygen

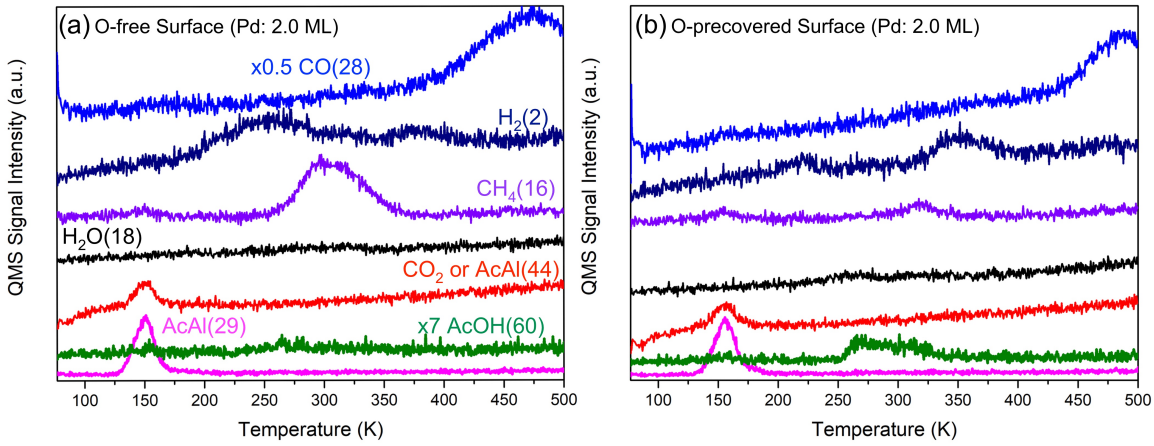


Figure 4.3. Detailed product analysis during the desorption of 0.9 ML AcAl adsorbed on (a) the O-free Pd–Au surface (Pd: 2.0 ML) and (b) the O-precovered Pd–Au surface (Pd: 2.0 ML). The 0.9 ML AcAl was impinged on the samples at 77 K via the molecular beam, and then the AcAl covered surfaces were heated to 500 K by 1 K/s with observing CO ($m/z^+ = 28$, blue), $H_2$ ($m/z^+ = 2$, dark blue), $CH_4$ ($m/z^+ = 16$, mauve), $CO_2$ or AcAl ($m/z^+ = 44$, red), AcOH ($m/z^+ = 60$, green), and AcAl ($m/z^+ = 29$, magenta). To include all those spectra in the same scale, the intensity of $m/z^+ = 60$ is increased by a factor of 7, and the intensity of $m/z^+ = 28$ is decreased by half.

adatoms fully oxidize the AcAl molecules to form $H_2O$ (~300 K and ~ 400 K), $CO_2$ and AcOH (~ 400 K), and CO from 450 K.[136] However, we have recently discovered that oxygen adatoms on the Pd–Au surfaces have higher reactivity at relatively low temperatures (especially below 200 K) compared to pure Pd surfaces.[70] Thus, the AcAl molecules can be more selectively oxidized to the acetate and desorb from the surface as AcOH before the decarboxylation of the acetate on the surface occurs. As shown in Figure 4.3b, when 0.9 ML of AcAl is adsorbed on the O-precovered surface (which is prepared by exposing the Pd–Au surface to $O_2$ at 300 K[70]) the amount of $H_2$ and $CH_4$ generated from the dissociation of AcAl largely decreases during the production of AcOH from 250 K to 340 K. Specifically, the $H_2$ desorption peak is no longer broad and continuous as on the oxygen-free Pd–Au surface; instead there are two desorption features, one before the generation of AcOH, from 200 K to 250 K, and the other after most of the AcOH generation is complete, from 325 K to 400 K. These results indicate that H atoms are still deprotonated from adsorbed AcAl molecules and are closely related to the formation of AcOH because $H_2$ desorption terminates during AcOH generation. The desorption intensity of $CH_4$ (300 K - 325 K) is less than for the oxygen-free Pd–Au case, and the CO generation starts from 450 K, which is higher than for the oxygen-free case (from 400 K) and indicates a lower amount of CO on the oxygen-precovered surface.[145,146] Thus, the O adatoms on the Pd–Au surface both prevent the AcAl molecules from being dissociated and contribute to the formation of AcOH. Since we do not observe the production of $CO_2$ and $H_2O$, which is key evidence for the full oxidation of AcAl, it is likely that most of the oxygen adatoms are used to generate AcOH. The AcOH production and desorption temperature is the same as the desorption temperature of AcOH molecularly adsorbed on this Pd–Au surface suggesting a desorption-limited process. The production of AcOH via the oxidation of 0.9 ML of AcAl is estimated to be

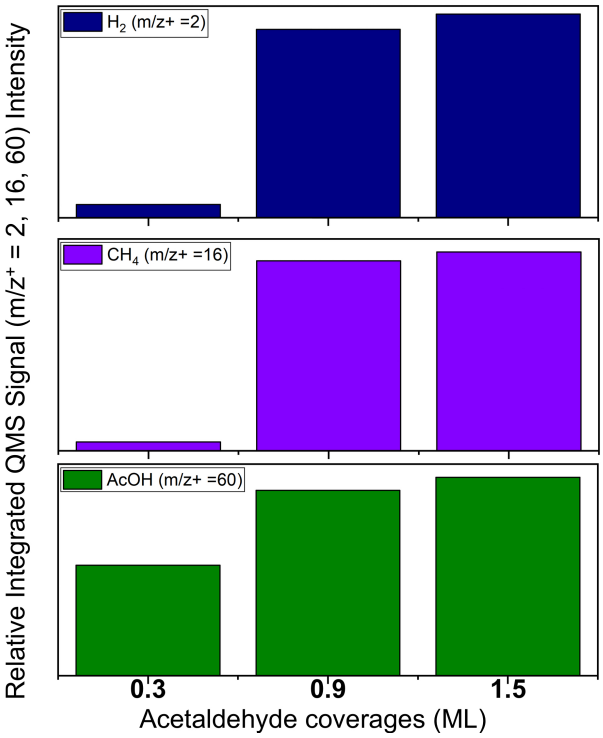


Figure 4.4. Relative integrated QMS signal intensities of $H_2$ ($m/z^+ = 2$), $CH_4$ ($m/z^+ = 16$), and AcOH ($m/z^+ = 60$) generated during the TPD of 0.3 ML, 0.9 ML, and 1.5 ML AcAl on the O-precovered Pd–Au (Pd: 2.0 ML) surface.

~ 0.3 ML AcOH based on the experiment illustrated in Figure C.4 which involves an exposure of 0.3 ML AcOH and its molecular desorption from the surface between 240 K to 340 K which gives the same integrated area. Therefore, the AcAl can be selectively oxidized to AcOH on the 2.0 ML Pd deposited surface without generating other oxidized products during the AcOH production, such as $CO_2$ and $H_2O$, which have been observed on the pure Pd(111) surface.[136]

For a detailed understanding of the dependence of the production of AcOH on the AcAl coverage, we also analyzed the relative amount of generated $H_2$ (from C-H bond dissociation) $CH_4$ (from C-C bond dissociation) and AcOH as shown in Figure 4.4. (The TPD spectra for 0.3 ML and 1.5 ML AcAl are shown in Figure C.5.) Since the surface is fully saturated with AcAl on a 1.5 ML AcAl covered surface, it shows about

5%, 7.5 %, and 6.5 % more production of $CH_4$, $H_2$, and AcOH respectively, compared to a 0.9 ML AcAl covered surface, which indicates that 0.9 ML of AcAl molecules react with most of the precovered oxygen adatoms to make AcOH on the 2.0 ML Pd deposited Au (111) surface. The 0.3 ML AcAl covered surface still shows ~ 55 % of the AcOH production in comparison to the 1.5 ML AcAl case, but the generation of $CH_4$ and $H_2$ molecules can be no greater than 5%, as the features at the temperatures over which these molecules desorb have a low signal-to-noise ratio. These results mean that $H_2$ and $CH_4$ generation from the 0.9 ML or 1.5 ML AcAl cases are primarily a result of the over-abundance of AcAl molecules which do not interact with the surface oxygen atoms. This again confirms that the oxygen adatoms are the principal contributor to oxidation of AcAl to AcOH and that selectivity toward AcOH can be enhanced when the appropriate coverage of AcAl is provided to the O-precovered Pd–Au surface.

### 4.3.3. Reflective-Absorption Infrared Spectroscopy (RAIRS) on the AcAl Adsorbed Pd–Au Surfaces

After observing the selective oxidation of AcAl to AcOH on the oxygen precovered surface from the TPD measurements, we performed reflective-absorption infrared spectroscopy (RAIRS) measurements to confirm the formation of acetate via the interaction of oxygen adatoms and adsorbed acetaldehyde molecules, which is additional evidence for the production of AcOH, as previously determined. [136,137,147–149] As shown in Figure 4.5, we focus on the range from 1300 $cm^{-1}$ to 2000 $cm^{-1}$, in which the carbonyl groups of the adsorbed species can be identified, since we want to compare the $\nu$(CO) stretch from the adsorbed acetaldehyde to the $\nu$(CO) stretch from acetate formation. At 160 K, AcAl molecules on the oxygen-free Pd–Au surface (Pd: 2.0 ML) in Figure 4.5a have two different adsorbed configurations: $\eta^2$(C,O)-acetaldehyde as identified by $\nu$(CO)

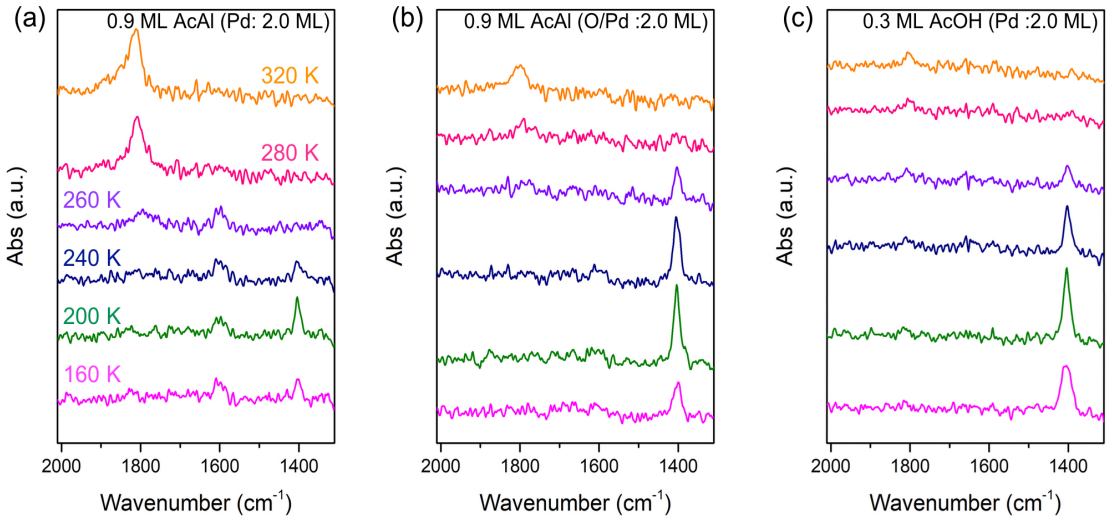


Figure 4.5. Reflective-absorption infrared spectroscopy (RAIRS) spectra of (a) 0.9 ML AcAl on the oxygen-free Pd–Au surface (Pd: 2.0 ML), (b) 0.9 ML of AcAl on the oxygen-precovered Pd–Au surface (Pd: 2.0 ML), and (c) 0.3 ML AcOH on the oxygen-free Pd–Au surface (Pd: 2.0 ML). All gas molecules were directed on the samples at 77 K via the molecular beam, and then the samples were heated and held at 160 K, 200 K, 240 K, 260 K, 280 K, and 320 K for the IR spectroscopy. The y-axis of all of IR spectra under the same scale.

at ~1400 $cm^{-1}$ and $\eta^1$(C)-acetyl as identified by $\nu$(CO) at ~1600 $cm^{-1}$ (via the deprotonation of AcAl); these assignments correspond to previous observations on pure Pd surfaces.[143,150] After the desorption of most of the AcAl molecules (at 200 K), the intensity of the $\eta^2$-acetaldehyde peak increases because some of the weakly bound or $\eta^1$-coordinated AcAl molecules are converted to the $\eta^2$(C,O) configuration while heating the surface, but this $\eta^2$-acetaldehyde peak begins to decrease above 240 K. (These changes in the $\eta^2$(C,O)-acetaldehyde peak are consistent with a previous study on the pure Pd(111) surface.[150]) When the temperature reaches 260 K, the $\eta^2$-acetaldehyde peak finally disappears; however, the $\eta^1$-acetyl peak still exists on the surface, and becomes slightly larger and broader than when it was annealed to 200 K. A small and broad peak at ~1805 $cm^{-1}$ begins to be observed from 260 K, and this peak is likely from carbonyl species *via*

the decomposition of the AcAl molecules on Pd ensembles. This feature continuously grows larger and sharper at higher temperatures with a peak at ~ 1815 $cm^{-1}$, corresponding to CO *via* the decomposition of the AcAl as previously detected on pure Pd surfaces.[143,150] This transition indicates C-C bond dissociation, in which the $\eta^1$-acetyl peak also fades out during this process. All of these results are not only similar to the previous observations regarding the decomposition of AcAl on pure Pd surfaces,[143,150] but also agree with our observations from TPD measurements.

For the case of the O-precovered surface (Pd coverage is still 2.0 ML), the IR spectrum of 0.9 ML AcAl in Figure 4.5b generally shows different vibrational behavior compared to the oxygen-free surface. At 160 K, Figure 4.5b shows a more intense peak at ~ 1400 $cm^{-1}$ compared with the peak at the same wavenumber in Figure 4.5a (the AcAl on the oxygen-free surface) via the formation of $\eta^2$-acetaldehyde. Although we can also see a very weak signal from $\eta^1$-acetyl at ~1600 $cm^{-1}$ in Figure 4.5b from 160 K to 260 K, it is not as indicative as in Figure 4.5a and it is also hard to distinguish the peak from the background noise. Based on these differences in molecular behavior, we can expect the peak at ~1400 $cm^{-1}$ in Figure 4.5b to be due to $\eta^2$(O,O)-acetate since AcOH generation was detected on this surface. This assignment is also supported by the detection of a $\nu$(CO) peak near 1400 $cm^{-1}$ by $\eta^2$-acetate as reported in previous studies regarding acetaldehyde oxidation on Pd(111)[136] and AcOH adsorption and desorption from Pd(111),[137,147] Au–Pd(100)[148] and Au–Pd(111)[149] surfaces. This peak is highest at 200 K, and starts to diminish at 240 K, which is near the temperature at which the initial production of AcOH is observed. At 280 K, a weak peak at ~1800 $cm^{-1}$ is observed, and it grows slightly larger at 320 K, but is still much less intense than for the oxygen-free surface case. This peak can be attributed to decomposed CO species such as on the oxygen-free surface, but these temperatures are still in the range of AcOH production, so

the peak at 1800 $cm^{-1}$ could also possibly be formed by physisorbed AcOH monomer based on previous observations, which has $\nu$(CO) positioned at ~ 1799 $cm^{-1}$.[149] To compare these results with the AcOH adsorbed on the oxygen-free Pd–Au surface, we measured the IR spectrum of 0.3 ML AcOH adsorbed at 77 K on the oxygen-free Pd–Au (Pd: 2.0 ML) surface. Figure 4.5c shows similar IR spectra to the case of AcAl co-adsorbed on the O-precovered surface for all tested temperatures. Specifically, at 160 K, there is one strong peak near 1400 $cm^{-1}$, which is the $\nu$(CO) feature for $\eta^2$-acetate formed by the deprotonation of AcOH.[137,147–149] With increasing temperatures, the $\eta^2$-acetate peak becomes larger at 200 K, but starts to decrease from 240 K onwards. At 280 K the $\eta^2$-acetate peak disappears but there is a weak peak at ~ 1800 $cm^{-1}$, which grows slightly larger at 320 K. These measured vibrational features for a 0.3 ML coverage of AcOH on the oxygen-free surface are analogous to that obtained with 0.9 ML AcAl on the O-precovered surface. This confirms the formation of acetate via the interaction between AcAl and oxygen adatoms. Furthermore, the acetate species formed on this surface can desorb primarily as AcOH instead of undergoing decarboxylation and forming other products as observed on the O-free 2.0 ML Pd deposited surface in Figure 4.3a.

### 4.3.4. AcAl Oxidation on the 3.0 ML Pd Initially Deposited Au(111) Surface

As shown in Figure 4.6, when the initial Pd coverage is increased to 3.0 ML, the AcAl molecules can be fully oxidized to $CO_2$ and $H_2O$ at ~ 375 K while also generating $H_2$, $CH_4$, AcOH and CO, similar to results from pure Pd surfaces. With an increased Pd coverage, there are more Pd-(111) like islands, as verified from the $H_2$ TPD in Figure 4.1, leading to a stronger Pd character for the surface. On the oxygen-free 3.0 ML Pd deposited surface, thus, there is less molecular desorption of AcAl, which is 60 % as compared to the 2.0 ML Pd deposited surface, so the production of $CH_4$, $H_2$, and CO

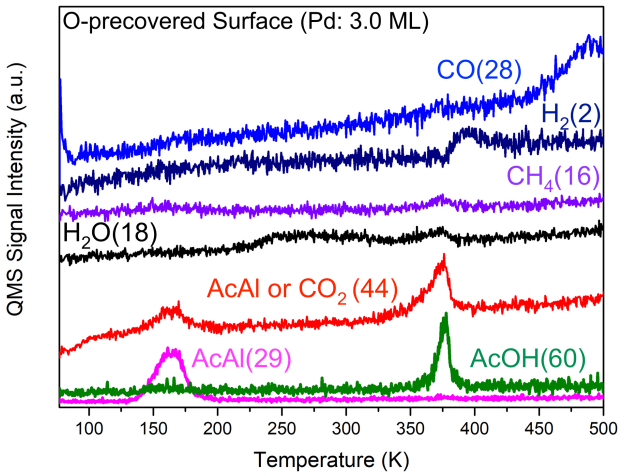


Figure 4.6. TPD of 0.9 ML AcAl adsorbed on the O-precovered Pd–Au surface (Pd: 3.0 ML). The 0.9 ML AcAl was directed on the surface at 77 K via the molecular beam and then heated to 500 K by 1 K/s with observing CO (m/z+ = 28, blue), H2 (m/z+ = 2, dark blue), CH4 (m/z+ = 16, purple), CO2 or AcAl (m/z+ = 44, red), AcOH (m/z+ = 60, green), and AcAl (m/z+ = 29, magenta). To include all those spectra in the same scale, the intensity of m/z+ = 60 is increased by a factor of 7, and the intensity of m/z+ = 28 is decreased by half.

from decomposing AcAl is increased, as shown in Figure C.6. These results indicate stronger interactions between the surface and adsorbed AcAl molecules as with pure Pd surfaces.[143] Moreover, more oxygen adatoms can be adsorbed onto the 3.0 ML Pd deposited surface because of the higher Pd coverage, which is about 2.6 times more than the 2.0 ML case, observed via the titration of O adatoms using CO at 400 K in our previous study.[70] However, we have also found that the stronger Pd character in the 3.0 ML case causes the oxygen adatoms to be more strongly bound on the surface and become less reactive at relatively low temperatures compared to the 2.0 ML case.[70] Thus, the 0.9 ML AcAl molecules on the O-precovered surface (Pd: 3.0 ML) in Figure 4.6 have stronger interactions with the surface itself and also react with oxygen adatoms at higher temperatures in comparison with the 2.0 ML Pd case discussed previously. Specifically, the production of AcOH is observed above 350 K and forms a peak at 375 K, which

accompanies the generation of $CO_2$, $H_2O$, and $CH_4$. $H_2$ also evolves from this surface starting at 375 K, which is quite different from the 2.0 ML case (as shown in Figure 4.3b) since it only generates AcOH without other oxidized species (e.g., $H_2O$ and $CO_2$). While the $m/z^+ = 44$ signal can be due to either AcAl or $CO_2$, we notice that its lower temperature peak is coupled with a $m/z^+ = 29$ signal, and its higher temperature peak does not have a corresponding $m/z^+ = 29$ signal, indicating that the lower temperature $m/z^+ = 44$ peak is caused by AcAl desorption, and the higher temperature peak is generated via $CO_2$ production. The oxidized species, AcOH, $H_2O$, and $CO_2$, are evidence of the decarboxylation of acetate on the surface, which is known to be initiated by dissociating C-H bonds of the acetate species on the surface. This chemistry has also been observed in previous studies regarding the oxidation of AcAl on Pd(111)[136] and the desorption of AcOH on Pd(100)[138] and Pd(111)[147]. Note that in Figure 4.6 there are two desorption features for $H_2O$, one of which is from 225 K to 330 K while the other is from 330 K to 380 K. The lower temperature feature is mainly due to extra oxygen adatoms which scavenge the deprotonated hydrogen atoms on the surface instead of interacting with adsorbed AcAl molecules.[136] The higher temperature water desorption feature is generated during the decarboxylation of the acetate which also generates $CO_2$ and AcOH. The lower $H_2O$ desorption feature indicates that the H atoms are still deprotonated from the AcAl molecules by forming the acetate species as with the 2.0 ML case, but there is no desorption feature for the AcOH because the formed acetate species on this surface do not recombine with the H adatoms. The less reactive acetate species seem to be decarboxylated from 350 K onwards leading to the production of AcOH, $H_2O$, $CO_2$, $CH_4$, and $H_2$. Although there are some differences in the intensity of the desorbing molecules, the lower (0.3 ML) and higher (1.5 ML) AcAl coverages also show the production of AcOH, $H_2O$, and $CO_2$ simultaneously as shown in Figure C.7, which means the

decarboxylation occurs on this surface independent of the coverage of AcAl. Once again, these observations are similar to previous studies conducted on pure Pd surfaces.[136] Thus, the increased Pd coverage (and hence size of the Pd ensembles) allows the AcAl molecules to be more easily dissociated and less selectively oxidized to AcOH while also generating $CO_2$ and $H_2O$, which does not occur on the 2.0 ML case. These results can be understood via DFT calculations of AcAl oxidation at the Pd ensembles on the Au surface.

### 4.3.5. DFT Calculations for the AcAl Oxidation Mechanisms on the Pd–Au Surfaces

With our DFT calculations, we aimed to determine the general size effect of Pd ensembles on the adsorption and reaction of AcAl molecules employing a range from 2 Pd atoms to 25 Pd atoms (which covers the whole Au slab as one ML). We subdivide the catalytic oxidation of AcAl into its component steps to understand the chemistry on the Pd–Au surface, where various intermediates are adopted from the experimental TPD analysis to get the most feasible reaction pathways. As shown in Figure 4.7, the first step involves introducing atomic oxygen onto the surface. The oxygen adatom does not spill over to pure Au sites and is more stable on larger Pd ensembles, as also shown in previous studies.[70] When an AcAl molecule is subsequently adsorbed on the surface in the second step, there are two possible reaction pathways with adsorbed atomic oxygen. In the energetically favorable pathway, a hydrogen atom deprotonates from the AcAl and then the deprotonated AcAl molecule reacts with an oxygen adatom to form a surface bound acetate ($CH_3COO$*), where the deprotonated H atoms do not spill over to pure Au sites but stay on the Pd(111)-like islands as experimentally verified from the $H_2$ desorption temperatures in Figure 4.1 and Figure 4.3. A less favorable pathway has the oxygen adatom scavenging the deprotonated hydrogen from AcAl, which leads to the

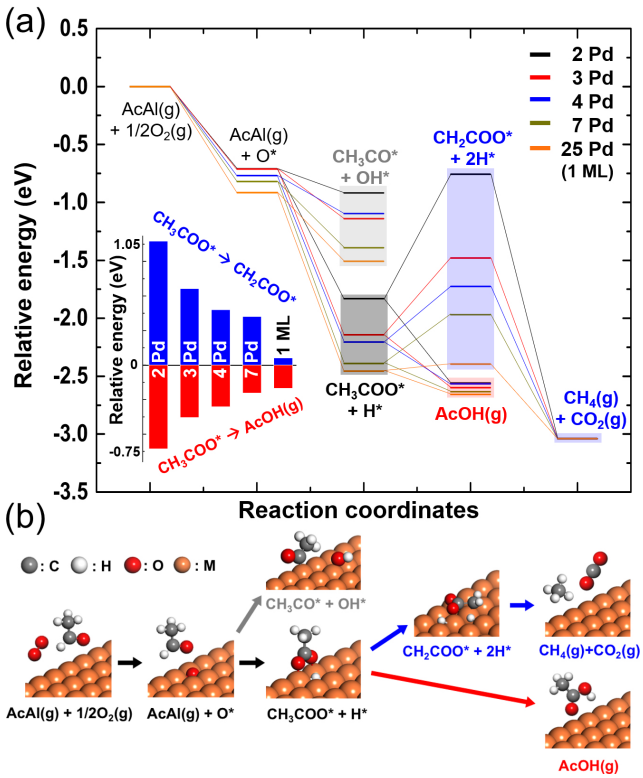


Figure 4.7. (a) Energy diagram for the catalytic oxidation of AcAl to AcOH or $CH_4$+$CO_2$ as a function of Pd ensemble size: 2Pd, 3Pd, 4Pd, 7Pd, and 25Pd (1 ML). (b) The reaction pathways that we consider for AcAl oxidation.

formation of a hydroxyl (OH*) and an acetyl ($CH_3CO$*) on the surface. Acetate formation is about 1 eV favorable as compared to acetyl and hydroxyl formation on all surfaces tested, and the acetate species are more stable on higher Pd coverages as shown in Figure 4.7a. Specifically, the acetate formation is more energetically favorable on the atop sites of the interior of Pd atoms than on the Pd–Au interfaces or on the pure Au sites as shown in Figure C.9. We have also found (in Figure 4.5) that the vibrational frequency of the $\eta^2$(O,O)-acetate (~ 1400cm$^{-1}$) on the 2.0 ML Pd deposited surface is close to previously studied values on pure Pd surfaces.[136,148] Moreover, the acetate with a deprotonated hydrogen formed on the 2 or 3Pd atoms is less stable than on the 7Pd atoms as indicated in Figure 4.7a (-1.83 eV on 2Pd and -2.14 eV on 3Pd, and -2.37 eV on

7Pd) because the acetate and deprotonated hydrogen cannot simultaneously occupy the most stable adsorption sites (e.g., the interior of Pd atoms) on the relatively smaller Pd ensembles. In the third step, the acetate species on each surface has two possible reaction paths: initiation of decarboxylation (blue path); and the formation of AcOH (red path). As shown in Figure 4.7b (blue arrows) decarboxylation is initiated by dissociation of the β-C-H acetate bond, as has been observed in previous studies.[136–138,147] This process is not energetically favorable; the acetate molecule requires additional energy to surmount this step. The energy difference between the acetate and the initial decarboxylation step ($CH_2COO$*+2H*), as indicated by the blue bar graph in the inset of Figure 4.7a, is highly dependent on Pd ensemble size, where 2 Pd atoms (black) show a 1.08 eV energy difference, and 25 Pd atoms (1 ML Pd, orange) shows only 0.06 eV. Although AcOH formation (red path in Figure 4.7a and 4.7b) is an energetically favorable path for all Pd coverages, its relative stability compared to acetate continuously decreases, as indicated by the red bar graph in the inset of Figure 4.7a. Thus, the energy differences between acetate and the initial decarboxylation step are reduced with Pd coverage and become very small at 1 ML, indicating that it is feasible for the acetate species to overcome the initial decarboxylation step and become fully decarboxylated as $CH_4$ and $CO_2$ on highly Pd-covered surfaces. This analysis implies that higher Pd coverages lead to a lower selectivity towards AcOH in the oxidation of AcAl. These calculations support the experimental observations described above, in which AcOH production is less selective on surfaces with more Pd (3.0 ML), and more selective on surfaces with less Pd (2.0 ML).

Based on these experimental and computational results we can say that the selectivity towards AcOH formation is highly dependent on the Pd ensemble size. As described in Figure 4.7b (blue arrows), acetate is tilted on the surface to initiate

decarboxylation by dissociating the β-C-H bond. If the Pd ensembles are small enough, the tilted acetate species will spill over to the Pd–Au interface or pure Au sites, which are less reactive compared to the Pd(111)-like islands. Thus, the acetate species on the smaller Pd ensembles are unlikely to undergo decarboxylation, and instead desorb as AcOH below the initiation temperature for decarboxylation.

## 4.4. CONCLUSION

We have investigated the selective oxidation of acetaldehyde (AcAl) to acetic acid (AcOH) on Pd–Au(111) heterogeneous model catalysts. For testing AcAl oxidation, we used two different Pd coverages on the Au(111) surface: 2.0 ML and 3.0 ML (0.45 and 0.8 relative amount of Pd atoms on the top surface respectively after annealing to 500 K). On the 2.0 ML Pd deposited surface, the selective production of AcOH from 250 K to 340 K was observed during temperature programmed desorption measurements without generating $CO_2$ and $H_2O$. We also detected the formation of acetate species on this surface from 160 K to 260 K using RAIRS, which is a representative adsorbed configuration of the AcOH molecule on metal surfaces. We also confirmed that the molecular vibrations caused by co-adsorbed oxygen adatoms and AcAl molecules are quite similar to the molecular vibrations of AcOH molecules placed on this surface. However, on a 3.0 ML Pd deposited surface, AcAl molecules were less selectively oxidized to AcOH at higher temperatures (~ 375 K) and $CO_2$, $H_2O$, $CH_4$, and $H_2$ were also generated. This is clear evidence for the decarboxylation of the acetate, chemistry which has also been observed on pure Pd surfaces.[136–138,147] DFT calculations show that the relative energy between the acetate state and the initial decarboxylation step is systematically reduced with increasing Pd ensemble size, which leads to facile decarboxylation at higher Pd coverages. This chapter shows that it is possible to

selectively oxidize acetaldehyde to acetic acid near room temperature by controlling the Pd ensemble sizes on a model palladium gold alloy surface.

# Chapter 5: Solvent-free Vacuum Growth of Oriented HKUST-1 Thin Films

## 5.1. INTRODUCTION

Metal-organic frameworks (MOFs) are a new class of microporous materials, which consist of metal containing inorganic nodes and organic linkers.[151,152] Because of their ultrahigh porosity and tunability, they have been widely applied in gas storage,[153–159] $CO_2$ capture,[160–164] hydrocarbon separation,[165–171] catalysis,[172–174] and as microporous magnets[37,175–178]. In addition to these applications, the growth of MOF thin films has received significant attention because it could facilitate the direct fabrication of MOFs into microelectronic devices, such as gas sensors,[38,179,180] electronic & opto-electronic devices,[42–44] and also drug delivery[181,182]. MOF thin films can be also applied to microporous membranes for gas separations.[183–185] The majority of MOF thin film deposition methods that have been developed thus far have been adapted from powder-type MOF preparation methods using various solvents. In particular it has been reported that solvent based MOF thin film growth methods can be widely applied in the field of gas sensors by directly fabricating the MOF on the surface of electrodes and other supports.[34–37,186,187] However the solvent based MOF growth methods have limits regarding direct applications in the semiconductor micro-chip fabrication process which is typically conducted under vacuum.

Primarily because the aqueous solvents can contaminate the vacuum chambers

---

*Han, S.; Ciufo, R. A.; Meyerson, M. L.; Keitz, B. K.; Mullins, C.B. Solvent-free Vacuum Growth of Oriented HKUST-1 Thin Films. *J. Mater. Chem. A,* **2019***,* 7, 19396-19406.

S. Han, R. A. Ciufo, M. L. Meyerson, B. K. Keitz, and C. B. Mullins conceived and designed experiments, analyzed and discussed results, and commented on the manuscript. S. Han performed experiments, analyzed data and wrote the paper.

and also corrode the fabrication system. Furthermore, the used solvents become environmentally harmful chemical wastes, involving additional costs for their safe disposal.

To overcome these disadvantages, vapor-based methods for growing MOF films are required. Stassen *et al*. has recently reported a solid-vapor based ZIF-8 thin film growth method using chemical vapor deposition (CVD) of 2-methylimidazole (HmIm).[188,189] In this study, the ZnO layers grown by an atomic layer deposition (ALD) technique were exposed to HmIm vapor for the transformation of ZnO to ZIF-8 on the basis of a neutralization reaction (ZnO + HmIm ➔ ZIF-8 + $H_2O$). They showed that patterned ZIF-8 films could be prepared employing patterned ZnO layers. An analogous ZIF-8 growth method was used to grow gas separation membranes by converting ZnO layers to ZIF-8 on permeable $Al_2O_3$ substrates.[185] Because these techniques for ZIF-8 film growth involve the conversion of ZnO precursor layers to the ZIF-8 structure, which is a top-down approach, they are susceptible to self-inhibition when thick ZnO layers are used. Specifically, in both studies,[185,188] the authors found that the continuous diffusion of HmIm to the bottom ZIF-8 - ZnO interface is slower and limited by initially converted ZIF-8 layers, which are on the top of the ZnO layers. These studies highlight the need for improved methods to control MOF thin film synthesis.

HKUST-1, $[Cu_3(BTC)_2]$ (BTC: Benzene-1,3,5,-tricarboxylic acid), is one of several commercialized MOFs and is widely studied because of its coordinately unsaturated open metal sites.[52,53] The open metal sites in HKUST-1 function as chemically active centers, and thus, HKUST-1 has shown various interesting applications such as selective gas adsorption and separation,[54–58] Lewis acid catalysis,[59] and proton transfer channels.[60] Thin films of HKUST-1 have also been widely investigated primarily regarding highly-oriented growth using self-assembled organic monolayers (SAMs).[64,65]

The SAMs are famous for their relatively easy preparation and can be patterned using facile micro contact printing. Thus, employing the SAMs can allow the synthesis of surface bound thin film SURMOFs (SURfaceMOFs) which are homogeneous and atomically flat. Specifically, the -COOH or -OH or -$CH_3$ terminated SAMs, which are the main functional groups in the organic linker for HKUST-1 ($H_3BTC$), can promote the successful growth of 2D thin film HKUST-1 via immersing SAM coated films in the metal ion (e.g., $Cu^{2+}$ or $Zn^{2+}$) and the ligand (BTC) containing solutions sequentially.[64,65] This SAM based method leads to the growth of highly-oriented HKUST-1 films (the -COOH for the {200} planes and the -OH for the {222} planes). HKUST-1 MOF thin films can also be directly grown on basic metal oxide interfaces (e.g., $Al_2O_3$) without SAMs,[66] and the overall growth can be controlled using UV irradiation.[190] Similar to the case of ZnO, copper oxides and copper hydroxides can be precursors for HKUST-1 thin film growth on various substrates.[66–68] Although SAMs and other oxide interfaces provide growth sites for the deposition of HKUST-1 thin films, they are still solution-based methods basically following the HKUST-1 powder preparation method.

As a new approach, we report the physical vapor deposition (PVD) of $Cu^0$ and

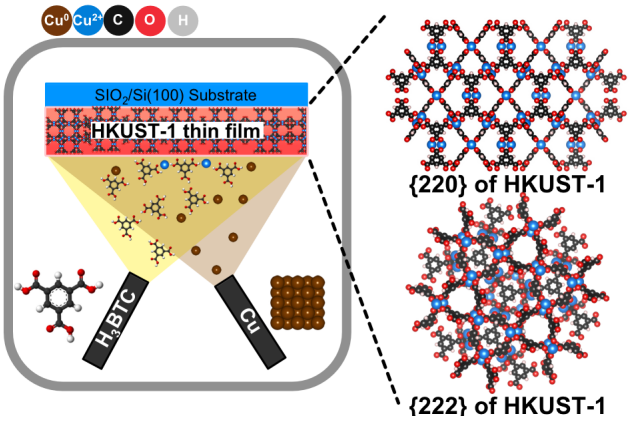


Illustration 5.1. Schematic description of HKUST-1 thin film growth in the high vacuum chamber

the chemical vapor deposition (CVD) of $H_3BTC$ on a $SiO_2$/Si(100) substrate for the solvent-free growth of HKUST-1 thin films (~20-200 nm in thickness) in a high vacuum chamber (base pressure 2.0 x $10^{-8}$ Torr), which is also expected to be applicable in the microelectronic fabrication process. (See Illustration 5.1). Similar to the suggested growth concept in this chapter, the combined method of PVD of metal atoms and CVD of organic ligands has been applied to forming "so-called" 2D-metal organic networks on various metal surfaces previously (typically one layer in thickness).[191–193] Improving this 2D based method, the layer-by-layer (LBL) growth concept was adopted in this chapter as a way of achieving bottom-up thin film growth. Our successfully grown HKUST-1 thin films have polycrystalline features, but they are preferentially grown and show the (220) and (222) planes as their primary planes measured from glancing angle XRD and in-plane XRD respectively. We have further analyzed our HKUST-1 thin films using XPS and AFM and also successfully measured the adsorption and desorption of $H_2O$ on our HKUST-1 thin films under high vacuum. Overall, we suggest a new growth method of highly oriented HKUST-1 thin films by controlling the depositions of $H_3BTC$ and Cu under high vacuum.

## 5.2. EXPERIMENTAL METHODS

HKUST-1 thin films were grown in a high vacuum system with a base pressure of ~2.0 x $10^{-8}$ Torr. Our high vacuum system consists of two different parts. One part is a sample growth chamber equipped with an e-beam evaporator for the PVD of Cu and a thermal evaporator for the CVD of $H_3BTC$. The other part is a sample loading and thermal analysis chamber equipped with a quadrupole mass spectrometer (QMS). We used a $SiO_2$/Si(100) wafer from MTI as a substrate for the growth of HKUST-1 thin films, where 300 nm $SiO_2$ layers were grown on a Si(100) substrate. A piece of the

$SiO_2$/Si(100) wafer, which has the dimensions 0.9 cm x 0.9 cm x 0.5mm, was loaded on to a sample holder composed of a tantalum plate located in the sample loading chamber. The sample holder is mounted to two tantalum wires which can resistively heat the loaded sample and also provide a thermal contact between the sample and a liquid nitrogen bath for cooling. The sample temperature was measured by a K-type thermocouple spot-welded to the top edge of the tantalum plate.

As mentioned earlier, we used an e-beam evaporator for the PVD of Cu. The electrons from a tungsten filament were directed (via biasing) to metallic Cu pellets filled in a molybdenum (Mo) crucible. The Cu deposition rate was held at 0.05 Å/s, as calibrated by a quartz crystal microbalance (QCM) and its controller (Inficon SQM-160) assuming the thickness of 1 ML (monolayer) Cu to be 2.56 Å. To perform the CVD of $H_3BTC$, 95% $H_3BTC$ powders (from Sigma Aldrich) were placed in a $Al_2O_3$ crucible and resistively heated while also monitoring its temperature by a K-type thermocouple. The $H_3BTC$ temperature was fixed at 473 K (200 °C) during the deposition process. Using manual shutters in front of both the Cu and $H_3BTC$ evaporators, it was possible to control the deposition time of each evaporator. Before the beginning of the HKUST-1 thin film growth, the sample growth chamber was back-filled with $H_2O$ ($2.5 \times 10^{-5}$ Torr) and $O_2$ ($2.5 \times 10^{-5}$ Torr), which increased the chamber pressure to $5.0 \times 10^{-5}$ Torr. 4 ML Cu were initially deposited on the $SiO_2$/Si(100) wafer sample, and then $H_3BTC$ and Cu were exposed sequentially. The sample was held at 323 K during the deposition of Cu and $H_3BTC$, followed by annealing at 343 K for 15 minutes after completion of the deposition process while maintaining the back-filled $H_2O$ and $O_2$ in the chamber at $5.0 \times 10^{-5}$ Torr. Successfully grown HKUST-1 thin film samples were further characterized by ex-situ analysis using X-ray diffraction (XRD), X-ray photoelectron spectroscopy (XPS), and atomic force microscopy (AFM). To minimize complications due to the $SiO_2$/Si(100)

substrate during XRD analysis, we adopted two different XRD techniques with Cu $K_\alpha$ radiation in the Rigaku Ultima IV; glancing-angle XRD (GAXRD) and in-plane XRD (IPXRD), which allow us to observe the crystallinity of the HKUST-1 thin films. The GAXRD was conducted with a scan rate of 0.5°/min in 0.02° steps, and the IPXRD was operated with a scan rate of 0.1°/min in 0.02° steps. Surface chemical states and bonds were identified by a Kratos Axis Ultra XPS system using a monochromatic Al-$K_\alpha$ X-ray source (1486.6 eV), and the spectra were calibrated by the C1s peak at 284.6 eV as a standard. Casa XPS analysis software was used to conduct peak deconvolution of measured XPS spectra adopting a Shirley background and line shapes with a combination of the Gaussian and Lorentzian functions, which keeps the full-width at half maximum (FWHM) of deconvoluted peaks in all XPS spectra lower than 2.5 eV. The thickness and roughness of the HKUST-1 thin films were characterized by a non-contact atomic force microscope (XE-100). We also measured $H_2O$ adsorption and desorption capability of the HKUST-1 thin films employing temperature programmed desorption (TPD). To conduct the TPD experiments, we first activated the HKUST-1 thin film sample by heating it from 298 K to 398 K at a temperature ramp rate of 0.5 K/s and then holding it at 398 K for 20 minutes, at which time there was no longer any further $H_2O$ desorption as detected by the QMS. The activated HKUST-1 thin film was then cooled to 120 K and exposed to back-filled $H_2O$ molecules at 2.0 x $10^{-6}$ Torr for 30 minutes. After that, the $H_2O$ exposed HKUST-1 thin film was heated from 120 K to 398 K at a rate of 0.5 K/s and held at 398 K for 20 minutes to complete the $H_2O$ desorption. During this process, a $m/z^+$=18 signal was recorded by the QMS (Extorr xt100m). We did not increase the HKUST-1 sample temperature above 398 K in order to prevent the decomposition of the deposited HKUST-1 structures.

## 5.3. RESULTS AND DISCUSSION

As shown in Illustration 5.1, the CVD of $H_3BTC$ and the PVD of Cu are performed to grow the HKUST-1 thin film on a $SiO_2$/Si(100) substrate under vacuum. Oxidized Cu precursor layers (e.g., $Cu_xO_y$, $Cu(OH)_2$)[66–68] were not required to grow the HKUST-1 film. Adopting a bottom-up growth concept, $H_3BTC$ and Cu were directly exposed to the substrate sequentially establishing a layer-by-layer (LBL) growth protocol. At the beginning of the growth, 4 ML of Cu (~ 1 nm thick) was deposited directly on the $SiO_2$//Si(100) substrate. This initial Cu layer was mainly used as a substrate upon which $H_3BTC$ molecules in the first deposition cycle can be organized. It is known that $H_3BTC$ molecules can form porous supramolecular structures not only by themselves but also on various surfaces, such as Cu, Ag, Au and graphite.[194–202] We were inspired by these studies to use the supramolecular structures of $H_3BTC$ as templates to grow the HKUST-1 thin films.

### 5.3.1. Optimization of the Quantity of Cu in Each Growth Cycle

We found the optimized growth conditions to consist of an exposure time of $H_3BTC$ of 3 minutes in each cycle while holding the evaporation temperature of $H_3BTC$ at 473 K (200 °C). The vacuum chamber was back-filled with $H_2O$ and $O_2$ to a total pressure of 5.0 x $10^{-5}$ Torr. During the growth, the sample was held at 323 K, which was followed by annealing at 343 K for 15 minutes all with 5.0 X $10^{-5}$ Torr of $H_2O$ and $O_2$. As shown in Figure 5.1, we optimized the amount of Cu in each cycle using a 5 LBL cycled HKUST-1 thin film as a representative case by measuring the oxidation state of Cu via XPS, which is a widely used analysis method for confirming the $Cu^{2+}$ state in HKUST-1.[42,203–210] Specifically, a 1 ML Cu deposition in each cycle for the 5 cycled film shows the highest ratio of $Cu^{2+}$ to $Cu^{1+}$(or $Cu^0$), 92 % and 8 % respectively by integrating

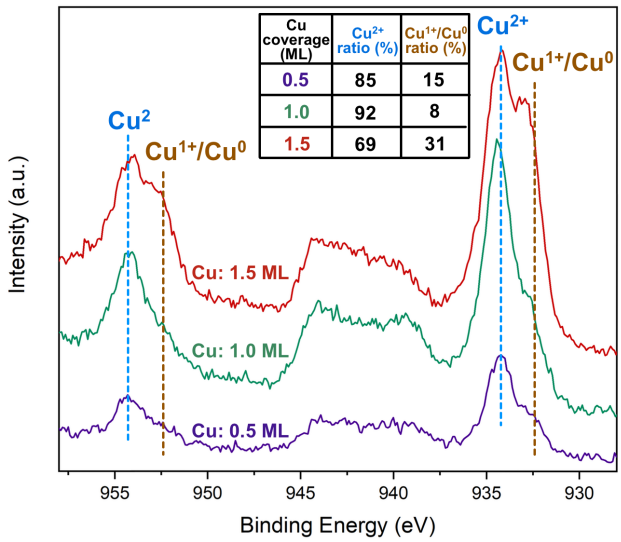


Figure 5.1. XPS analysis for the Cu2p region of 5 LBL cycles of HKUST-1 thin films. To optimize the amount of Cu in each layer, the 5 cycled HKUST-1 thin films were grown by using 0.5 ML Cu (purple), 1.0 ML Cu (green), and 1.5 ML Cu (red) in each LBL cycle. We highlighted the main peak for Cu2+ (~ 934 eV) and its sub peak with light-blue and the Cu1+/Cu0 peak (~ 932 eV) and its sub peak with brown.

the deconvoluted peak area of $Cu^{2+}$ (~ 934 eV, light-blue line) and $Cu^{1+}/Cu^{0}$ (~ 932 eV, brown line), which also has clear satellite peaks by $Cu^{2+}$ from 936 eV – 946 eV. This $Cu^{2+}$ to $Cu^{1+}/Cu^{0}$ ratio is similar to previously reported values from the HKUST-1 powders and thin films.[209,210] When we decreased the amount of Cu to 0.5 ML, the $Cu^{2+}$ peak intensity is about a half of the 1.0 ML case, which indicates that 0.5 ML Cu does not fully saturate the $H_3BTC$ layers. However, a deposition of 1.5 ML Cu in each cycle causes over-saturation of the $H_3BTC$ layers, as it shows a higher intensity of the $Cu^{1+}/Cu^{0}$ ratio with almost the same intensity of $Cu^{2+}$ compared to the 1.0 ML Cu case. This result indicates that the extra Cu atoms are partially oxidized or remain unreacted. Based on these results, we fixed the deposition amount of Cu in each cycle at 1 ML. There was no indication of copper oxide formation in any of the tests since their O1s XPS spectra do

not show any components in the range of 530.5 eV - 529.5 eV as shown in Figure D.1, which is a typical range for the O1s feature from $Cu_2O$ and CuO.[204,211,212]

### 5.3.2. Characteristics of the $H_3BTC$ and HKUST-1 Thin Films

As mentioned above, Cu and $H_3BTC$ deposited samples were annealed at 343 K for 15 mins to complete the HKUST-1 film growth. After finishing growth, we measured the crystallinity of our samples using glancing-angle XRD (GAXRD). GAXRD is a widely adopted asymmetric out-of-plane XRD technique, which can analyze variously oriented planes in thin films with less interruption from their supporting substrates and the techniques have also been adopted for HKUST-1 thin film analysis previously.[42,43,213–215] Our HKUST-1 thin films displayed peaks at ~ 9.2° and ~ 18.5° in the GAXRD (gray line in Figure 5.2a), which corresponds to the (220) and (440) planes of HKUST-1 respectively. (We will further discuss its crystallinity in the following section.) The unannealed 5 cycles of $H_3BTC$ (blue line in Figure 5.2a, five consecutive rounds of $H_3BTC$ deposition on the substrate for 3 mins each, 15 mins in total), which is directly grown on the initial Cu layer without including Cu deposition between each $H_3BTC$ deposition, shows very similar XRD patterns compared to the HKUST-1 thin films even though there are still some differences between these two XRD patterns above 25° in 2θ as shown in Figure D.2. The unannealed 5 cycled $H_3BTC$ fully covers the top surface of the substrate, which shows a different color compared to a blank $SiO_2$/Si(100) substrate. (Figure D.3) Moreover we did not detect Cu features in the Cu2p region in its XPS spectrum in Figure D.2b, which would appear if the $H_3BTC$ molecules did not fully cover the 4 ML Cu deposited $SiO_2$/Si(100) substrate. This means there are multilayers of $H_3BTC$ forming 3D structures by themselves. From the XRD results, we propose that the deposited $H_3BTC$ molecules are long-range ordered on the initial Cu layer (~ 1 nm of

thickness) on the $SiO_2$/Si(100) substrate to form the supramolecular structures based on hydrogen bonds (H-bonds) which leads to the HKUST-1 like structures. Similar to this

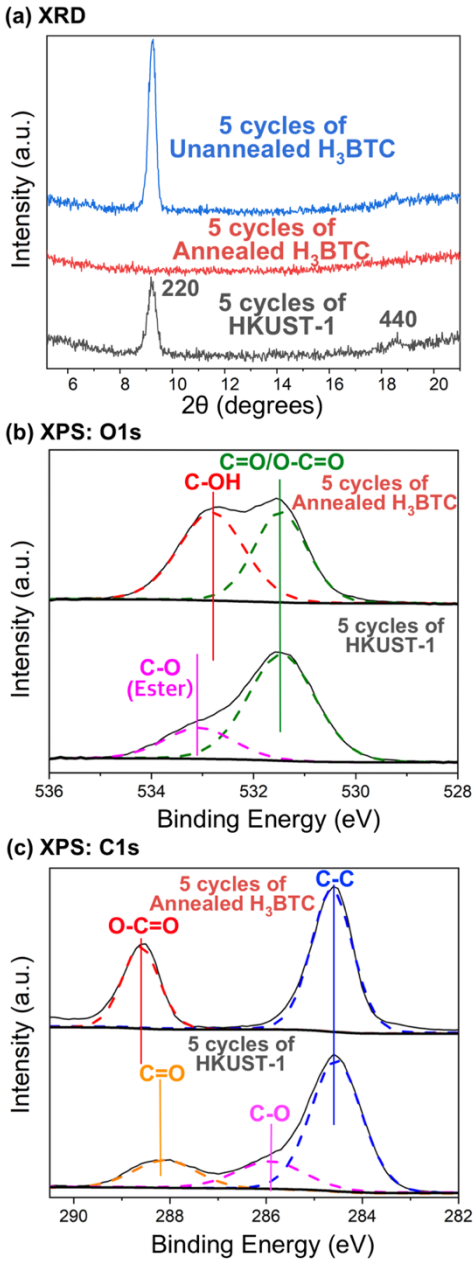


Figure 5.2. (a) XRD patterns for the 5 cycles of unannealed $H_3BTC$ (blue, 5 times of $H_3BTC$ deposition for 3 minutes in each), the 5 cycles of HKUST-1 films (gray), and the 5 cycles of annealed $H_3BTC$ at 343 K for 15 mins (red). (b) and (c) show the XPS spectra of O1s and C1s regions respectively for the 5 cycles of annealed $H_3BTC$ and the 5 cycles of HKUST-1 film.

chapter, it has been found that the Cu layer on the Au(111) surface provides binding and regular organization sites for $H_3BTC$ molecules without changing the oxidation state of the Cu atoms.[216]

Since the $H_3BTC$ molecules are connected to each other only by H-bonds, they lose their crystallinity after annealing at 343 K for 15 mins (red line in Figure 5.2a), likely being converted into randomly ordered H-bonded clusters. Even though the 5 cycles of $H_3BTC$ were annealed at 343 K, it is not a high enough temperature to cause the desorption of multilayers of $H_3BTC$, which needs to be heated to ~ 573 K as previously found.[217] There is also no color change between the unannealed and annealed films as shown in Figure D.3, and it was possible to detect the $H_3BTC$ molecules on the annealed surface by O1s and C1s XPS measurements (which will be discussed in the following section). The lack of crystallinity in the annealed 5 cycled $H_3BTC$ sample (see Figure 5.2a) supports the notion that Cu atoms in the initial 4 ML Cu layer do not broadly diffuse into the $H_3BTC$ layers to form a HKUST-1 structure and also there is no trace of Cu in the Cu2p region in XPS as described in Figure D.2b. This lack of crystallinity is very interesting since an HKUST-1 structure can be annealed to 343 K and retain its crystallinity after annealing.

As we mentioned above, the XRD patterns of the 5 cycled HKUST-1 are similar to the unannealed 5 cycled $H_3BTC$. Both cases have a main peak at ~ 9.2° of 2θ. The full-width half maximum (FWHM) of this peak in the unannealed 5 cycled $H_3BTC$ is ~ 0.3°, which is slightly smaller than the FWHM of the same peak in the 5 cycled HKUST-1 (~ 0.37°) indicating the decrease of average grain sizes. Relatedly, deposited Cu atoms in each cycle react with $H_3BTC$ molecules, which shrinks the structure by forming coordinate bonds between Cu and $H_3BTC$, which leads to the FWHM of the HKUST-1 film at ~ 9.2° being increased. We can also see that the unannealed 5 cycled $H_3BTC$ have

a stronger peak at ~ 9.2° than the corresponding peak on the HKUST-1 film, but its peak at 18.5° is weaker than the one on the HKUST-1 film related to the (440) plane of HKUST-1. These results indicate that the crystal structures of the HKUST-1 thin film are originating from the 3D supramolecular structures of $H_3BTC$, but there are still some structural changes caused by the 1.0 ML Cu deposition after each $H_3BTC$ deposition. Furthermore, it has been found that $H_3BTC$ molecules can be densely packed and regularly organized on Cu surfaces by forming chain structures composed of up-right oriented $H_3BTC$ molecules anchored on Cu atoms, and then extra $H_3BTC$ molecules form 3D structures based on hydrogen bonds (H-bonds) with each other.[217,218]

We also compared differences in O1s and C1s XPS spectra of the annealed 5 cycles of $H_3BTC$ (the same growth conditions as the HKUST-1 thin film except with no Cu deposition between $H_3BTC$ cycles) and the 5 cycled HKUST-1 thin film in order to prove that the deposited Cu atoms interact with the $H_3BTC$ structure. The O1s spectrum of the annealed 5 cycles of $H_3BTC$ shows two peaks having similar intensities at 531.5 eV for C=O/O-C=O bonds by carboxyl groups and its split peak at 532.8 eV for C-OH bonds,[207,219–221] which is similar to previously observed H-bonded $H_3BTC$ molecules on a Ag coated Au(111) surface and a Cu(100) surface.[200,217] However, the 5 cycled HKUST-1 films has a peak at 533.1 eV for C-O bonds (ester type oxygen) and the other peak is at 531.5 eV for C=O/O-C=O bonds (carboxylate type oxygen).[207,219–221] Consistent with previous HKUST-1 studies,[208,219,220] the C-O bond peak shows lower intensity than the C=O/O-C=O bond peak. This ester type C-O bond can be formed when the $H_3BTC$ is deprotonated and forms coordinate bonds with $Cu^{2+}$, Cu-O-C. These results also confirm that $H_3BTC$ molecules in the annealed 5 cycled $H_3BTC$ are not fully deprotonated to make new covalent bonded clusters by forming ester type C-O bonds with each other, but they still exist as H-bonded clusters. The C1s XPS spectra of $H_3BTC$ and HKUST-1 also

shows clear differences depending on their chemical status (see Figure 5.2c). The annealed 5 cycles of $H_3BTC$ mainly shows C-C sp2 bonds at 284.6 eV[203,219,222,223] and also has a peak for O-C=O(~ 288.7 eV) bonds from the carboxyl group of $H_3BTC$[219,222,224,225]. When we compare these results to the 5 cycled HKUST-1 thin film, the HKUST-1 sample has a peak at 284.6 eV for C-C bonds and shows the formation of C-O bonds at ~ 285.9 eV by the ester type bond formation with $Cu^{2+}$ ions (Cu-O-C) as previously observed,[219,222,223] which also has been detected in the O1s spectrum. Furthermore, there is a peak at 288.3 eV indicating C=O bonds,[219,222,225] which is 0.4 eV lower than the peak of carboxyl groups (O-C=O) observed in the annealed $H_3BTC$ sample, so it also supports the deprotonation of $H_3BTC$ to form the Cu-O-C bond in HKUST-1.

### 5.3.3. Effects of $H_2O$ and $O_2$ During the HKUST-1 Thin Film Growth

As we explained above, we directly deposited $Cu^0$ atoms on the $H_3BTC$ covered surface instead of using other Cu based solid precursors, such as CuO and $Cu(OH)_2$, which have been used in previous studies.[66–68] However, we adopted $O_2$ as a background gas expecting it to work as the ionization agent of Cu and the deprotonation agent of $H_3BTC$. Furthermore, it has been found that water vapor enhances the solid state conversion of ZnO to ZIF-8.[188] To investigate the synergistic effect of the background gases, $H_2O$ and $O_2$, we grew HKUST-1 films under two different pure $O_2$ back-filled conditions ($2.5 \times 10^{-5}$ Torr and $5.0 \times 10^{-5}$ Torr) and compared them to the sample grown under a $H_2O$ and $O_2$ mixed condition (total pressure: $5.0 \times 10^{-5}$ Torr, $H_2O$ ($2.5 \times 10^{-5}$ Torr) + $O_2$ ($2.5 \times 10^{-5}$ Torr)). Since the formation of copper oxide has not been found in XPS in any of our tests (see Figure D.1 and D.4), we assumed that the oxidation of $Cu^0$ to $Cu^{2+}$ is caused by the formation of the paddle-wheel units of HKUST-1, which consist of

$BTC^{3-}$ (deprotonated $H_3BTC$) and $Cu^{2+}$. As shown in Figure 5.3, it is possible to detect $Cu^{2+}$ in XPS even by back-filling the chamber with the pure $O_2$. However, there are differences in the ratio of $Cu^{2+}$ to $Cu^{1+}$(or $Cu^0$) depending on the applied pressure of $O_2$. When the $O_2$ pressure is increased from 2.5 x $10^{-5}$ to 5.0 x $10^{-5}$, there is more $Cu^{2+}$ formation, which means the $O_2$ molecules are involved in the oxidation of the Cu atoms. There is still no indication of any Cu oxides based on the O1s XPS in each case (Figure D.4), so the $O_2$ molecules mainly work to ionize Cu and deprotonate $H_3BTC$. The $H_2O$ and $O_2$ mixed case showed the highest ratio of $Cu^{2+}$ compared to others. This phenomenon can be caused by the solvation effect of water, for which it has been thermodynamically proven that the coordinated $H_2O$ molecules stabilize the paddle-wheel units of the HKUST-1.[51,226,227] In particular, it is also known that the deprotonation of ligands is essential in the growth of various MOFs,[228] so we suspect that

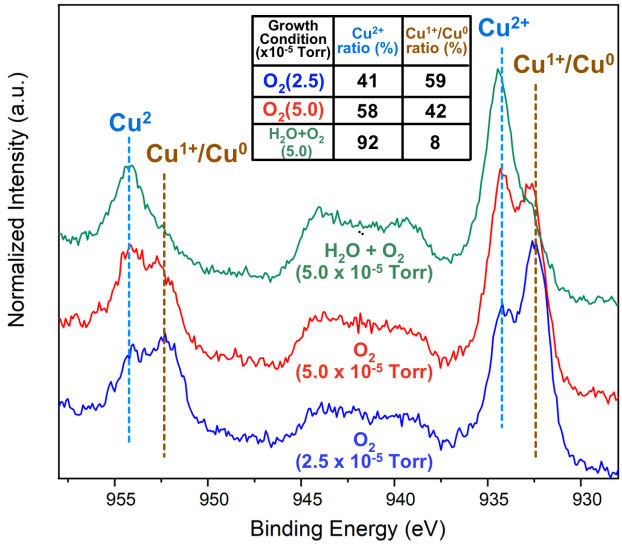


Figure 5.3. XPS analysis for the Cu2p region of 5 LBL cycles (1 ML Cu deposited in each cycle) of HKUST-1 thin films grown with $H_2O$ + $O_2$ background gases at total pressure of 5.0 x $10^{-5}$ Torr (2.5 x $10^{-5}$ Torr in each), pure $O_2$ at 5.0 x $10^{-5}$ Torr, and pure $O_2$ at 2.5 x $10^{-5}$ Torr. We highlighted the main peak for $Cu^{2+}$ (~ 934 eV) and its satellite peak (~ 954 eV) with light-blue and the main $Cu^{1+}/Cu^0$ peak (~ 932 eV) and its satellite peak (~ 952 eV) with brown.

the background $H_2O$ molecules facilitate the deprotonation of $H_3BTC$, which allows more facile oxidation of $Cu^0$ to $Cu^{2+}$.

### 5.3.4. Crystallinity, Roughness, and Thickness of the Vacuum-Deposited HKUST-1 Thin Films

We also grew 2, 5, and 10 cycled samples to check their crystallinity by adopting two different XRD techniques, the glancing-angle XRD (GAXRD) and the in-plane XRD (IPXRD) as shown in Figure 5.4a and 5.4b respectively. These samples are uniformly coated on the substrates and highly reflective, like a mirror, which show different color depending on the number of growth cycles as indicated in Figure D.5. In overall XRD measurements, the (220) plane at 9.2° in 2θ shows the strongest intensity in the GAXRD (Figure 5.4a), and the (222) plane at 10.8° in 2θ is a dominant plane in the IPXRD (Figure 5.4b), which means our HKUST-1 thin films are highly oriented.[42,43,52,229] However, additional peaks for HKUST-1 above 20° appear as indicated in Figure D.6, which are due to the polycrystalline properties of our HKUST-1 thin films. The XRD peaks in both measurements are slightly shifted towards lower angles compared with HKUST-1 simulated peaks[52] It has been found that the top surface compositions of the substrate directly affect the thin film structures grown on it.[230] Thus, we suspect that the XRD peak shifts could be related to the alignment of $H_3BTC$ molecules on the Cu covered $SiO_2$/Si(100) substrate since we have already found that the HKUST-1 structure is derived from the deposited $H_3BTC$ layers as shown in Figure 5.2. Moreover, there would be some accumulated strains within the $H_3BTC$-Cu-$SiO_2$/Si(100) structures, which possibly affects the HKUST-1 thin film structures.[230–232] Specifically in the GAXRD measurements, the peak intensity for the (220) plane at 9.2° continuously gets bigger with increasing number of LBL cycles, but the FWHM of this peak stays almost the same, ~

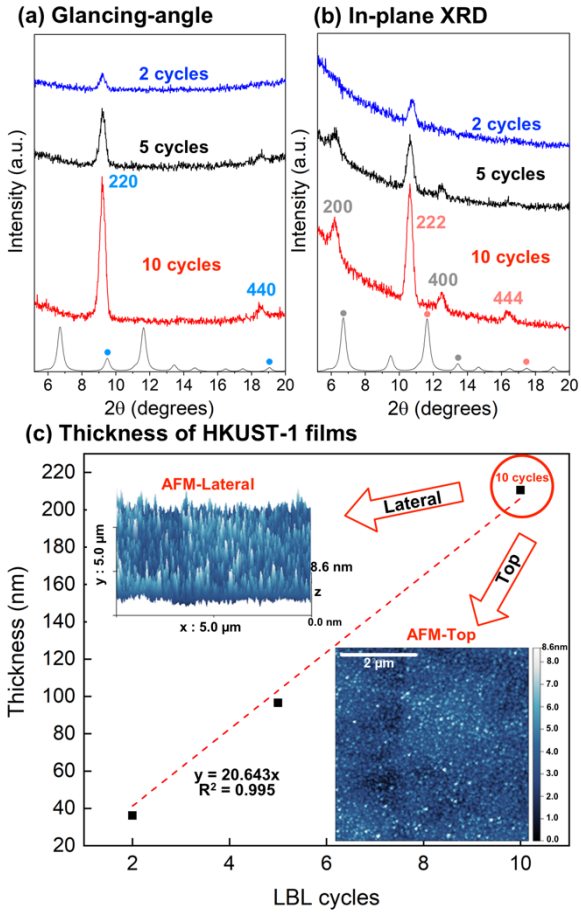


Figure 5.4. (a) the glancing-angle and (b) the in-plane XRD measurements for 2, 5, 10 LBL cycles of HKUST-1 thin films with simulated HKUST-1 XRD patterns (black lines at the bottom of each figure). (c) shows the thickness of these HKUST-1 thin films measured by AFM. Top and lateral views of the 10 cycled HKUST-1 film are also included as insets.

0.37°, in all tested HKUST-1 films. The (440) plane is also observed at ~ 18.5°, which is a sub-plane of (220). However, our samples do not show other main planes for HKUST-1, such as peaks at ~ 6.5° for the (220) plane and ~ 11.5° for the (222) plane. For the IPXRD, the peak for the (220) plane located between 9° and 10° is not observed, but all the samples have a peak at 10.8°, which is close to the (222) plane of HKUST-1. As with the (220) peak in the GAXRD, the thicker the sample is, the more intense the peak for the (222) plane, with a similar FWHM value (~ 0.36°). From the 5 cycled samples,

XRD peaks for the (200) and (400) planes are also observed at ~6.5° and ~ 13° respectively, and they also get larger on the 10 cycled sample. Although the (222) plane is detected as a main plane in the IPXRD measurement, which shows our HKUST-1 thin films are highly oriented, the observation of the (200) plane on thicker films indicates a polycrystalline character for our samples. The two dominant planes in our measurements, (220) and (222), have also been observed in a previous study in which octahedral shaped HKUST-1 particles grown along the <100> direction are well organized on a gold substrate.[229]

After analyzing the structural properties of our HKUST-1 thin films, we investigated their thickness and surface characteristics using atomic force microscopy (AFM). As shown in Figure 5.4c, the thickness of our 2, 5, and 10 cycled HKUST-1 thin films are analyzed. (more detailed results are in Figure D.7) To conduct these measurements, we masked some portions of the substrates and then grew the HKUST-1 films. With more LBL cycles, the thickness of our samples linearly increases, as expected, with a $R^2$ value of 0.99. Specifically, the 2, 5, and 10 cycled samples have average thicknesses of 37.5, 97, and 210 nm respectively, where each LBL cycle deposits a ~ 20 nm-thick HKUST-1 film. The root mean square (RMS) roughness also increases depending on the number of LBL cycles as with other MOF thin film growth studies,[233] but our samples are quite flat since even the 200 nm thick sample (10 cycles) has ~ 1 nm for the RMS roughness. This can be observed from the top view and lateral view of the 10 cycled HKUST-1 film in the inset to Figure 5.4c. The top view shows its continuous and homogeneous top surface. In the lateral view, it is interesting to see that the densely packed nano rods on the surface are regularly organized in an up-right orientation. These AFM observations are further evidence for the highly-oriented structure of our HKUST-1 thin films.

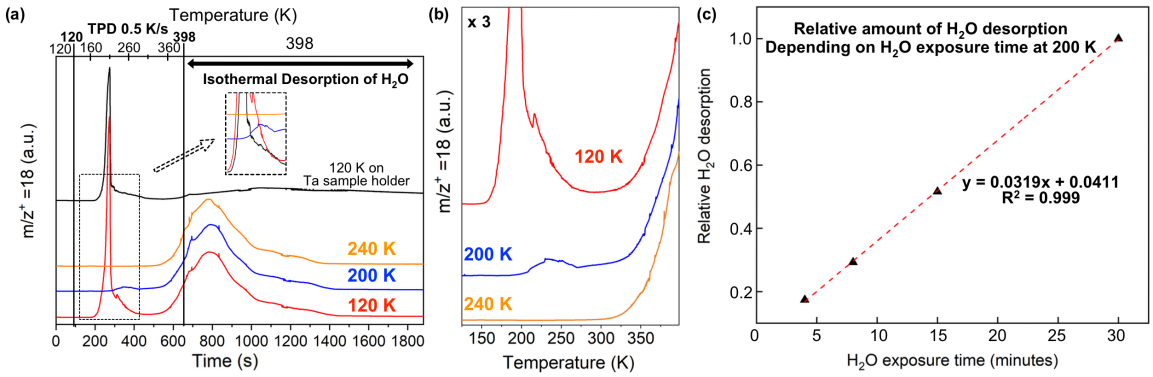


Figure 5.5. (a) The desorption spectra of $H_2O$ molecules exposed to the 5 cycled HKUST-1 thin film at 120 K (red), 200 K (blue), and 240 K (orange) for 30 mins at 2 x $10^{-6}$ Torr $H_2O$ for each. As a reference, we also added the desorption spectrum of $H_2O$ exposed to the sample holder (made of tantalum) at 120 K for 30 mins at 2 x $10^{-6}$ Torr $H_2O$ (black). After the $H_2O$ adsorption at different temperatures, the samples were held at 120 K for 2 mins and then heated to 398 K at 0.5 K/s to conduct temperature programmed desorption (TPD). The inset describes a 5 times magnified temperature range of 130 K to 300 K. When the samples reached at 398 K, they were kept at 398 K for 20 mins for the isothermal $H_2O$ desorption. (b) Zoomed out $H_2O$ desorption spectra. (c) Relative amount of $H_2O$ desorption by different $H_2O$ exposure times at 200 K. (30, 15, 8, and 4 mins)

### 5.3.5. $H_2O$ Desorption from the 5 Cycled HKUST-1 Thin Film

It is known that the HKUST-1 is an exceptional $H_2O$ sensor, which tends to be adsorbed at the 9 Å main cages of HKUST-1.[180,234–236] Although the adsorption energy of $H_2O$ is known to be 48 - 55 kJ/mol,[237–240] previous $H_2O$ isotherm measurements have shown hysteresis during the $H_2O$ desorption process,[241,242] which indicates some water molecules are strongly chemisorbed in the HKUST-1 structure. These strongly chemisorbed $H_2O$ molecules can be removed by an activation process, which typically involves holding the HKUST-1 structure at ~ 120 °C under vacuum.[190,239,242] Furthermore it has been found that the weight of HKUST-1 powders rapidly decreases from the evaporation of strongly bound $H_2O$ and other solvent molecules when the temperature increases from 25 °C to 150 °C in previous TGA analysis.[206,243] In this chapter, we also

tested the adsorption and desorption of $H_2O$ in order to measure the porosity and gas uptake properties of our HKUST-1 thin films. To conduct this experiment, the activated 5 cycled HKUST-1 thin film was exposed to back-filled $H_2O$ molecules ($2.0 \times 10^{-6}$ Torr). This is a constant pressure $H_2O$ adsorption experiment at a significantly lower pressure compared to previous isotherm tests using HKUST-1 powders in which the vapor pressures of $H_2O$ were varied up to its saturated vapor pressure (~23 Torr) at room temperature.[237–242] We first tested the adsorption of $H_2O$ while the sample was held at 120 K for 30 mins. Shown in Figure 5.5a are the results of temperature programmed desorption (TPD) measurements. Our measurement protocol is similar to that used extensively in surface science experiments performed under ultrahigh vacuum conditions. Here we measured the desorption of $H_2O$ by heating the sample from 120 K to 398 K at a rate of 0.5 K/s to 398 K and then holding the sample at 398 K for 20 mins to complete the desorption of water [again, we did not heat the sample above 398 K to prevent decomposition of the HKUST-1 film]. It is the same heating process used for the activation of our HKUST-1 thin films in this chapter. The $H_2O$ desorption shown in Figure 5.5a and Figure 5.5b first displays a desorption peak at 190 K, which starts from 150 K. This peak is due to the multilayers of $H_2O$ on the HKUST-1 surface and is characterized by the $H_2O$ signal intensity increasing sharply from ~ 150 K and then rapidly dropping right after 190 K. This desorption behavior is similar to the zeroth order desorption by multilayers of $H_2O$ molecules on metal and metal oxide surfaces as previously studied.[96,244] Although the $H_2O$ molecules continuously desorb until 270 K, the desorption behavior is slightly changed after finishing the multilayer $H_2O$ desorption at 190 K, which could involve another desorption feature. Moreover, the sample holder itself, which is made of tantalum (Ta), shows multilayer $H_2O$ desorption at ~ 190 K (black line in Figure 5.5a), but its intensity quickly drops above 190 K, and also has a

lower intensity compared to the 5 cycled HKUST-1, which is indicated in the inset of Figure 5.5a and Figure D.8. Thus, we also tested the adsorption of $H_2O$ at 200 K with the same $H_2O$ pressure and exposure time as with the 120 K experiments to avoid the formation of $H_2O$ multilayers. Water adsorption at 200 K will not create a multilayer so no desorption feature for multilayer water is expected.

During the desorption test of $H_2O$ adsorbed on the 5 cycled HKUST-1 film at 200 K, there is a new broad desorption peak at ~ 240 K. Its desorption range (200 K to 270 K) corresponds to the temperature range in which the desorption behavior of $H_2O$ adsorbed at 120 K was changed. The $H_2O$ molecules desorbing in this temperature range could be molecularly adsorbed $H_2O$ molecules near the MOF-vacuum interface.[245] If we assume that these $H_2O$ molecules desorb from the near surface, a Redhead analysis can be adopted to estimate the desorption energy of the $H_2O$,[126] and this analysis yields a value of ~ 60 kJ/mol. This value is close to previously measured $H_2O$ adsorption energies for HKUST-1 (48 - 55 kJ/mol).[237–240] As shown in Figure D.8, chemisorbed $H_2O$ molecules on our Ta sample holder desorb from 215 K to 290 K when the Ta sample holder is solely exposed to $H_2O$ at 200 K. Although this temperature range is a little bit higher than the low temperature $H_2O$ desorption feature observed in the HKUST-1 sample, it could contribute to the $H_2O$ desorption from the 5 cycled HKUST-1 film. However, we have already observed in the $H_2O$ adsorption tests at 120 K that the 5 cycled HKUST-1 film shows more $H_2O$ desorption above 190 K compared to the Ta sample holder. Furthermore, the top surface of the sample holder was covered by a HKUST-1 thin film sample during the $H_2O$ adsorption and desorption tests of the HKUST-1 thin film. Thus the $H_2O$ generation during the TPD of the HKUST-1 thin film can be mainly attributed to the HKUST-1 structures. When adsorption of $H_2O$ is

conducted at 240 K, the relatively small desorption feature between 200 and 270 K disappears as indicated in Figure 5.5 (blue traces).

In all the $H_2O$ desorption tests, with $H_2O$ molecules adsorbed at 120 K, 200 K, and 240 K, the remaining strongly chemisorbed $H_2O$ molecules begin to desorb from ~ 320 K and continue the desorption through 398 K. In particular, most of the $H_2O$ desorption occurs while the sample is held at 398 K, which is further evidence for the gas capture capability of our HKUST-1 thin films, since the Ta sample holder itself does not show any $H_2O$ desorption features above 190 K. This $H_2O$ desorption temperature range is similar to the previous TGA analysis of HKUST-1,[206,243] which shows a rapid weight loss from 25 °C (298 K) to 150 °C (423 K) by water and other solvents. The number of adsorbed $H_2O$ molecules is also controllable based on the $H_2O$ exposure time as shown in Figure 5.5c for an adsorption temperature of 200 K. Here we arbitrarily define the relative quantity of desorbing $H_2O$ molecules for the 30 minute $H_2O$ exposure case as 1.0. With decreasing $H_2O$ exposure time from 30 mins to 4 mins, the quantity of desorbing $H_2O$ molecules linearly decreases, with a $R^2$ value of 0.99. After these $H_2O$ adsorption and desorption tests, GAXRD of the HKUST-1 film showed the same XRD diffraction patterns as the fresh sample (shown in Figure D.9). These results indicate that our HKUST-1 thin films grown under vacuum also have the capability to repeatably capture gas molecules in their pores similar to HKUST-1 powder samples. Our results demonstrate that TPD is an effective experimental method for analyzing the desorption behavior of strongly adsorbed gas molecules on MOFs under vacuum at various temperatures, some of which may be difficult to be detected in conventional isotherm experiments.

## 5.4. CONCLUSION

We developed a new solvent-free HKUST-1 thin film growth method employed under vacuum by adopting a LBL deposition strategy involving the sequential physical vapor deposition of Cu followed by chemical vapor deposition of $H_3BTC$. After back-filling $O_2$ and $H_2O$ gases up to 5.0 x $10^{-5}$ Torr, we initially deposited 4 ML of Cu (~ 1 nm) on a $SiO_2$/Si(100) substrate and then exposed $H_3BTC$ and Cu in turn using layer-by-layer (LBL) growth. The $H_3BTC$ source evaporator was held at 200 °C during the growth, and we fixed the amount of evaporation time of $H_3BTC$ in each cycle at 3 mins. Based on this fixed amount of $H_3BTC$, we optimized the amount of Cu in each cycle by growing 5 cycled samples and measuring XPS to verify the oxidation state of Cu. As determined by XPS, 1 ML Cu deposition after each $H_3BTC$ deposition cycle showed the best $Cu^{2+}$ to $Cu^{1+}$/$Cu^0$ ratio compared to other tested amounts of Cu (0.5 ML and 1.5 ML) in our experimental setup, and there was no trace of copper oxide formation. We also found that the unannealed 5 cycles of $H_3BTC$ formed supramolecular structures which exhibited similar XRD patterns to the 5 cycles of the HKUST-1 film. However, after annealing the 5 cycled $H_3BTC$ at 343 K for 15 mins, which is the same annealing process to finalize the growth of our HKUST-1 films, they no longer showed crystallinity and became randomly ordered. This suggests that the HKUST-1 thin film structures are derived from the 3D supramolecular structures of $H_3BTC$ molecules, and deposited Cu atoms work as joints for the $H_3BTC$ ligand to keep their HKUST-1 like structure. For investigating the effect of background gases of $O_2$ and $H_2O$ during HKUST-1 growth, we grew several 5 cycled HKUST-1 films with different background gas conditions and discovered that $H_2O$ molecules clearly enhance the conversion of $Cu^0$ to $Cu^{2+}$ in the HKUST-1 film deposition. In the analysis of the crystallinity of the HKUST-1 thin films, the (220) and (222) planes were determined to be dominant planes in the GAXRD and

IPXRD measurements respectively, which shows that our HKUST-1 thin films are highly oriented. Furthermore, the thickness of HKUST-1 thin films increased linearly depending on the number of LBL cycles, ~ 20 nm for each LBL cycle as verified by AFM. We also conducted $H_2O$ adsorption and desorption tests on a 5 cycled HKUST-1 film, which has a thickness of ~ 100 nm. The $H_2O$ adsorption was conducted at 120 K, 200 K, and 240 K by back-filling the vacuum chamber with 2.0 x $10^{-6}$ Torr of $H_2O$ for 30 mins. The $H_2O$ desorption measured by QMS showed that most of the $H_2O$ desorption occurred when the sample was isothermally heated at 398 K (125 °C). These results correspond to previous TGA measurements on HKUST-1 and indicate that these constant pressure $H_2O$ adsorption and desorption tests under vacuum are able to detect strongly bound $H_2O$ molecules in HKUST-1. Therefore, this chapter suggests that HKUST-1 thin films can be grown under vacuum without the use of any solvents, where its thickness is also controllable within ~ 20 nm scale. We expect this vacuum based MOF growth can be applied in various fields such as semiconductors, sensors and membranes.

# Chapter 6: Methanol Oxidation Catalyzed by Copper Nanoclusters Incorporated in Vacuum-Deposited HKUST-1 Thin Films

## 6.1. INTRODUCTION

As a relatively new class of porous materials, metal organic frameworks (MOFs) have been widely studied because of their potential with regard to sensors, microelectronics, and gas capture & separation.[36,37,163,171,190,246,247] MOFs are composed of inorganic metal cation units and organic ligands, which provide diverse structural configurations.[33] Thus, they can have uniform long-range ordered pores and structures with relatively larger surface areas compared to conventional micro and mesoporous materials, such as zeolites and silica.[173,248]

Inspired by the structural tunability and high surface area of MOFs, many researchers have investigated methods to use MOFs as catalysts, especially for heterogeneous catalysis.[173,174,248] Although some MOFs can be directly applied as Lewis acid catalysts based on their coordinately unsaturated open metal sites,[174,249] more interesting catalytic properties can be realized through the inclusion of secondary metal nanoparticles (MNPs) in/on the pores of mechanically and thermally stable MOFs (e.g., ZIF-8,[250–255] MOF-5,[256–259] NU-1000,[172,260–263] UiO-66[264–272] etc.). The pores of MOFs can provide good dispersion sites for MNPs, which prevents the MNPs from aggregating.[251,265–267,269,273,274] Specifically, various MNPs, such as Au, Pd, Ag/Pd, Ni/Pt, and Ir, have been incorporated into ZIF-8 and showed impressive catalytic activities.[250–

---

*Han, S.; Ciufo, R. A.; Wygant B. R.; Keitz, B. K.; Mullins, C.B. Methanol Oxidation Catalyzed by Copper Nanoclusters Incorporated in Vacuum-Deposited HKUST-1 Thin Films, *ACS Catalysis,* **2020***,* Accepted.
S. Han, R. A. Ciufo, B. R. Wygant, B. K. Keitz, and C. B. Mullins conceived and designed experiments, analyzed and discussed results, and commented on the manuscript. S. Han performed experiments, analyzed data and wrote the paper.

[255] Moreover, it was found that Cu NPs in MOF-5 can generate methanol from synthesis gas mixtures ($CO/CO_2/H_2$), and it shows better catalytic activity when Cu atoms are loaded on ZnO nanoparticles imbedded in MOF-5.[256,257] NU-1000 has been used as a stable support for single atom catalysts by introducing secondary metal atoms into its stable Zr(IV)-oxo couples based structures.[172,260] Secondary Cu(II)-oxo clusters can also be placed in the NU-1000 MOF to work as catalytically active centers for oxidizing methane to methanol.[261]

Additionally, UiO-66 has stable Zr(IV)-oxo building units, and has been used as a substrate for single metal atoms, MNPs, and metal oxide clusters for catalysis.[264–272] In particular, Cu[268] and Pd[269] NPs incorporated into UiO-66 performed better for methanol production from $CO_2$ & $H_2$ mixtures and $H_2$ generation from ammonia borane respectively, when those particles are fully surrounded by the UiO-66 structures instead of simply resting on the surface of the UiO-66 MOF. This interesting phenomenon is related to the concentration of MNP-MOF interfaces, at which the catalytic activity can be improved.[268,269]

Most of the previous studies regarding MOF-heterogenous catalysts have been powder-based high pressure experiments. This study of methanol oxidation by Cu NP incorporated HKUST-1 thin films is the first surface science study of a MNP incorporated MOF thin film under vacuum. The Cu paddle-wheel unit is a basic component of HKUST-1, which is composed of two $Cu^{2+}$ cations coordinated with four deprotonated $H_3BTC$ (benzene-1,3,5-tricarboxylic acid) molecules in a square planar shape as highlighted with blue planes in Figure 6.1. The continuously connected Cu paddle-wheel units link one pore to other neighboring pores of HKUST-1, which has two different sizes of pores with diameters of ~ 9 Å and ~ 5 Å as indicated in Figure 6.1b with red and blue colored arrows respectively. HKUST-1 is also well-known as a

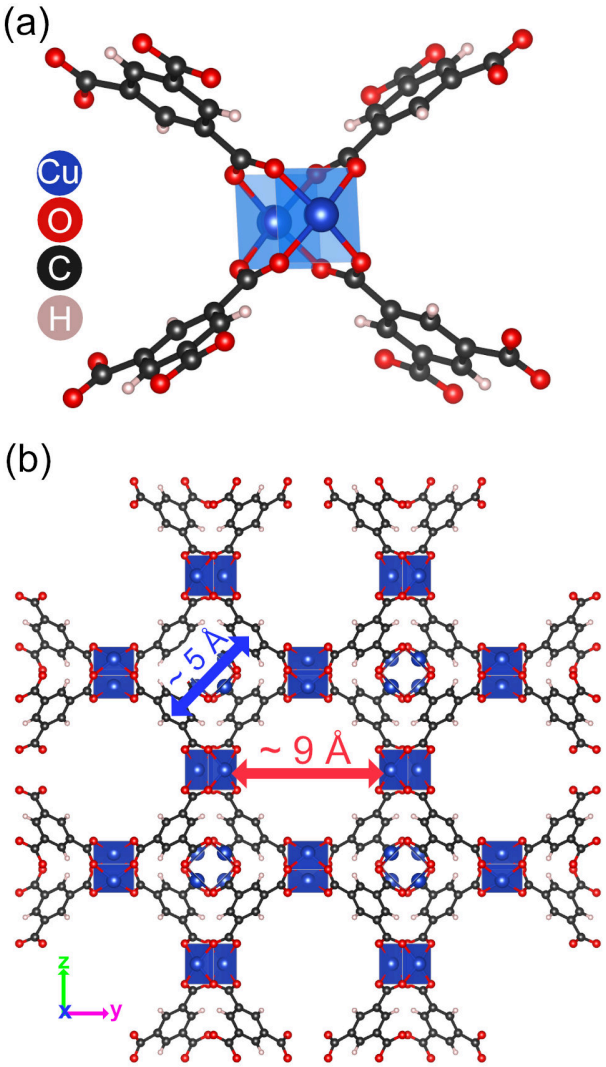


Figure 6.1. (a) The Cu paddle-wheel unit composed of $Cu^{2+}$ cations and deprotonated $H_3BTC$ ligands. The square planar type coordination is also highlighted. (b) The periodic structure of HKUST-1 composed of the Cu paddle-wheel units which have two different cage sizes, with the larger (red) one having a ~ 9 Å diameter and the smaller one (blue) with a ~ 5 Å diameter.

potential gas storage material because of the Cu open metal sites on its paddle-wheel units.[234,241,275,276] Recently, we successfully developed a new growth protocol for HKUST-1 thin films under vacuum without the use of solvents.[49] We found that highly oriented HKUST-1 films can be grown by directly depositing $Cu^0$ (physical vapor

deposition, PVD) and $H_3BTC$ (chemical vapor deposition, CVD) on a $SiO_2$/Si(100) substrate sequentially based on a layer-by-layer (LBL) growth concept. Different from other solvent-free and CVD adapted growth methods, our HKUST-1 thin film growth procedure is a bottom-up approach, which does not use any precursor layers (e.g., ZnO for the growth of the ZIF-8 thin film[45,185]). Thus, it is possible to control the deposited amount of Cu and $H_3BTC$ in each growth cycle. Using this method here, we report on our investigations of methanol oxidation catalyzed by various sizes of Cu NP's incorporated within vacuum deposited HKUST-1 thin films.

Previously, there have been several studies regarding the oxidation of methanol (MeOH) catalyzed by a Cu(110) surface.[277–285] It was discovered that adsorbed oxygen atoms enhance the adsorption of MeOH and its deprotonation to form methoxy ($CH_3O$*) above 170 K while also generating $H_2O$.[279–281,284] The accumulation of $H_2O$ on the Cu surface during the methoxy formation can be prevented by increasing the MeOH exposure temperature higher than 240 K based on previous studies, in which $H_2O$ generation was not observed during MeOH oxidation.[279,280,285] The methoxy species on the Cu surface are known to be stable up to 300 K.[279–281,284] The decomposition of methoxy species on the Cu(110) surface was detected above 300 K, generating formaldehyde ($H_2CO$) and $H_2$ ($CH_3O^* \rightarrow H_2CO(g) + H^*$) accompanied by the recombinative desorption of MeOH as well.[279,282,283,285] Some formaldehyde molecules were found to be oxidized to formate (HCOO*) followed by decomposition to $CO_2$(g) and $H_2$(g) above 400 K.[279,281] It was also determined that too high a coverage of oxygen adatoms on the Cu(110) surface decreased the surface reactivity, which leads to less uptake of methanol, generating less oxidized species, e.g., $H_2CO$ and $CO_2$.[277,279,285] Furthermore, Cu NPs on a $TiO_2$ (110) were not aggregated even after annealing at 800 K under vacuum.[286] In this current chapter, we investigate methanol oxidation employing a

HKUST-1 thin film with incorporated Cu NPs. By controlling the amount of Cu in each growth cycle, we were able to grow 4-6 nm Cu NPs as well as 8-12 nm Cu NPs that are incorporated within HKUST-1 thin films. Depending on the Cu NP sizes, they show different MeOH oxidation behavior under vacuum. Henceforth in this paper we discuss the use of HKUST-1 as a support for MNPs to conduct catalytic reactions and analyze the detailed chemistry related to the MeOH oxidation reaction via various sizes of Cu NPs incorporated within the HKUST-1 thin film.

## 6.2. EXPERIMENTAL SECTION

### 6.2.1. Growth of Cu NP Incorporated HKUST-1 Thin Films

In order to grow HKUST-1 films with Cu NP's incorporated within the film, we used a layer-by-layer (LBL) growth concept in our high vacuum chamber (base pressure: $2.0 \times 10^{-8}$ Torr) and deposited more copper than that required to simply grow the stoichiometric HKUST-1 thin film. Our high vacuum system is composed of two parts: one for the sample growth and the other for the thermal catalytic behavior analysis. The part of the chamber used for sample growth is equipped with an e-beam evaporator for physical vapor deposition (PVD) of Cu and a thermal evaporator for chemical vapor deposition (CVD) of $H_3BTC$ (benzene-1,3,5,-tricarboxylic acid). Small $SiO_2$/Si(100) wafers (~10 mm X 10 mm X 0.5 mm - from MTI) were used as the growth substrate for various HKUST-1 thin films by placing it on to a sample holder made of a tantalum (Ta) plate. The sample holder is mounted on two Ta wires which resistively heat the sample and also work as a thermal contact between the sample and a liquid nitrogen cooling bath. The sample temperature was detected by a K-type thermocouple spot-welded on to the Ta sample holder.

For the HKUST-1 film growth, we followed our previously developed growth method.[49] In brief, the sample growth chamber was back-filled with 5.0 x $10^{-5}$ Torr of $H_2O$ and $O_2$, and $H_3BTC$ and Cu were sequentially deposited on the substrate. Based on the LBL growth concept, we define one growth cycle in this chapter as a $H_3BTC$ deposition by CVD followed by a subsequent Cu deposition by PVD. For the CVD of $H_3BTC$, $H_3BTC$ powders (95%, Sigma Aldrich) were placed in a $Al_2O_3$ crucible and heated to 473 K (200 °C) during the $H_3BTC$ deposition cycle. We used an e-beam evaporator for the PVD of Cu, which used a tungsten filament to supply electrons which were accelerated by a voltage bias to a molybdenum crucible holding metallic Cu pellets. The amount of deposited Cu was monitored by a quartz crystal microbalance (QCM) and its controller (Inficon SQM-160) assuming the thickness of 1 monolayer (ML) of Cu to be 2.56 Å. The sample was held at 323 K (50 °C) during $H_3BTC$ and Cu deposition cycles, and then it was annealed at 343 K (70 °C) for 15 minutes with an ambient of 5.0 x $10^{-5}$ Torr of $O_2$ and $H_2O$ each. The $SiO_2$/Si(100) substrate was placed about ~ 10 cm away from the $H_3BTC$ and Cu evaporators. We found in our previous study that 3 minutes of deposition of $H_3BTC$ with the crucible held at 473 K during evaporation followed by 1 ML of Cu deposition creates what we are reporting as 1 growth cycle and is the optimized growth condition in our experimental setup for HKUST-1 thin film deposition (without incorporated Cu nanoparticles). Following this procedure yields $Cu^{2+}$ as its main oxidation state.[49] In this chapter, we deposited more Cu atoms than the optimized amount (1 ML Cu) in each growth cycle in order to incorporate Cu NPs in/on the HKUST-1 structure. In particular, we grew two different extra Cu deposited 5 cycle HKUST-1 films: a 4 ML Cu-HKUST-1 film (i.e., 3 additional ML's of Cu beyond the "optimized amount" of Cu required to grow the HKUST-1 thin films without Cu nanoparticles) and 8 ML Cu-HKUST-1 (i.e., 7 additional ML's of Cu beyond the

optimized amount), and compared their catalytic activities for the methanol oxidation reaction.

### 6.2.2. Characterization

To characterize the physical and chemical properties of the extra Cu deposited HKUST-1 thin films, we employed X-ray diffraction (XRD), X-ray photoelectron spectroscopy (XPS), atomic force microscopy (AFM), and transmission electron microscopy (TEM) techniques. XRD measurements were conducted by using a Rigaku Ultima IV with Cu $K_\alpha$ radiation; glancing-angle XRD (GAXRD), which is asymmetric out-of-plane XRD,[214] and in-plane (IPXRD) techniques were used to minimize the complications due to the $SiO_2$/Si(100) substrate and maximize signals from the grown HKUST-1 thin film. These two XRD techniques have been used previously for analyzing the crystallinity of MOF thin films.[42,43,287,288] The GAXRD was operated with a scan rate of 0.5° $min^{-1}$ in 0.02° steps, and the IPXRD was conducted with a scan rate of 0.1° $min^{-1}$ in 0.02° steps. The chemical states of samples were measured by a Kratos Axis Ultra XPS system with a monochromatic Al-$K_\alpha$ X-ray source (1486.6 eV). All measured XPS spectra were calibrated by the C1s peak at 284.6 eV as a standard, and we used the Casa XPS analysis software package to conduct peak deconvolution of the measured XPS spectra adopting a Shirley background and fitting line shapes with a combination of Gaussian and Lorentzian functions, which makes the full-width at half maximum (FWHM) of deconvoluted peaks lower than 2.5 eV. The thickness and roughness of the HKUST-1 thin films were detected by a non-contact atomic force microscopy (Park systems NX10), and the measured images were analyzed by Gwyddion software[289]. A JEOL 2010f-TEM operating at 200 keV was used to image Cu NPs that have incorporated in/on the HKUST-1 films.

### 6.2.3. Temperature-Programmed Desorption (TPD) Tests

We employed temperature programmed desorption (TPD) to probe MeOH oxidation on the 4 ML Cu and 8 ML Cu deposited HKUST-1 films in the high vacuum chamber. Initially, both samples were activated by holding them at 398 K (125 °C) for 15 minutes as we have done in our previous study.[49] Each activated sample was exposed to 1.0 x $10^{-6}$ Torr of $O_2$ at 300 K for 3 minutes to make sure that the sample was saturated with oxygen adatoms. After that, it was cooled to 250 K and was also exposed to 5.0 x $10^{-7}$ Torr of MeOH for 20 minutes. After finishing the exposure to MeOH, it was heated from 250 K to 398 K at a rate of 0.5 K/s and held at 398 K for 15 minutes while monitoring various masses using a quadrupole mass spectrometer (QMS, Extorr xt100m). We avoided heating the HKUST-1 thin films above 398 K in order to prevent the decomposition of the deposited HKUST-1 structures.[49]

## 6.3. RESULTS AND DISCUSSION

### 6.3.1. Crystallinity of the Extra Cu Deposited HKUST-1 Thin Films

In this chapter, we tested three different 5 cycled HKUST-1 films by depositing 1 ML Cu (optimized amount of Cu for a simple HKUST-1 thin film without Cu NPs), 4 ML (~ 1 nm thick) Cu, and 8 ML (~ 2 nm thick) Cu in the Cu deposition cycle of each sample. Specifically, following the HKUST-1 vacuum growth protocol developed in our previous study,[49] the vacuum chamber was back-filled with $H_2O$ and $O_2$ to a total pressure of 5.0 x $10^{-5}$ Torr, and then $H_3BTC$ molecules were sequentially deposited by CVD and Cu atoms by PVD on the 4 ML Cu (~ 1 nm thick) initially covered $SiO_2$/Si(111) substrate. (1 growth cycle = 3 minutes of $H_3BTC$ deposition + Cu deposition) After $H_3BTC$ and Cu deposition cycles, the samples were annealed at 343 K for 15 minutes while still in an ambient of 5.0 x $10^{-5}$ of $H_2O$ and $O_2$ (each) to finish the

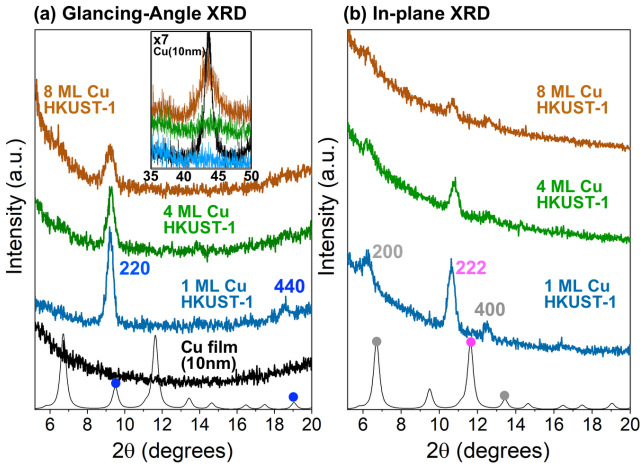


Figure 6.2. (a) The glancing angle and (b) the in-plane XRD measurements for three different 5 cycled HKUST-1 thin films. 1 ML Cu (optimized amount for HKUST-1), 4 ML Cu, and 8 ML Cu were deposited in their growth cycles respectively. The XRD pattern from a pure Cu thin film (10 nm thick) is also added, and the simulated XRD pattern of HKUST-1 is at the bottom of each figure as a black solid line.

overall growth. We discovered that the sequential depositions of $H_3BTC$ for 3 minutes and 1 ML Cu form the optimized HKUST-1 structures, where most of the Cu atoms are in a $Cu^{2+}$ state.[49] By depositing more Cu atoms than the optimal amount to form the HKUST-1 structure, we investigated whether excess Cu atoms could serve as catalytic reaction centers.

As shown in Figure 6.2a, we measured the crystallinity of the HKUST-1 thin film samples using glancing angle XRD (GAXRD) to maximize signals from the coated films, which is a broadly adopted asymmetric out-of-plane XRD technique and is also used for analyzing MOF thin films. [42,43,213–215,287,288] Although the optimized HKUST-1 film (1 ML Cu in each growth cycle) is poly-crystalline, it is highly oriented, showing a main peak at 9.2° in 2θ for the (220) plane of HKUST-1 as detected by GAXRD.[49] In-plane XRD (IPXRD) was also conducted, with results shown in Figure 6.2b. The (222) plane is measured as a main plane for the optimized HKUST-1 film in the IPXRD while also

showing a weak peak for the (200) plane. As with our previous study,[49] these peaks in both XRD measurements are slightly shifted to lower angles compared to simulated XRD patterns for HKUST-1. These shifts are likely caused by some accumulated strain within the $H_3BTC$-Cu-$SiO_2$/Si(100) structures and could have also originated from the 3D supramolecular structure of $H_3BTC$, which forms the template for HKUST-1 thin films and also affects the crystallinity of HKUST-1 thin films in our growth method as previously discovered.[49]

Employing the growth method described here, it was possible to control the amount of Cu during the deposition to accommodate extra Cu within the HKUST-1 structure. As indicated with green and brown lines in Figure 6.2a and 6.2b, we successfully grew extra Cu deposited HKUST-1 thin films, where 4 ML Cu and 8 ML Cu were deposited in each sample. By depositing more Cu than its optimized amount, the HKUST-1 related peaks of both samples in XRD get less intense and more broad as indicated by larger FWHM values for the (220) plane peak (0.36° for 1 ML Cu HKUST-1, 0.55° for 4 ML Cu HKUST-1, and 0.65° for 8 ML Cu HKUST-1). However, a peak for metallic Cu at ~ 43.5° for 2θ continuously increases with additional Cu deposition in each growth cycle as shown in the inset of Figure 6.2a, in which the trace for the 1 ML Cu-HKUST-1 is flat. Similar trends in XRD have also been observed in previous studies, where the primary peaks related to the main MOFs decrease or are broadened, but the metal peaks continuously grow with an increasing quantity of MNPs.[250,251,266,267,269,273,274,290] In these studies, the incorporated MNPs are larger than the pores of their corresponding MOF structures, so they are surrounded by the MOF structures instead of fitting into the pores. From our XRD results, we also believe that the extra Cu deposited samples may have Cu NPs that are larger than the pore size of HKUST-1, which leads to less intense HKUST-1 related XRD peaks and broader FWHM

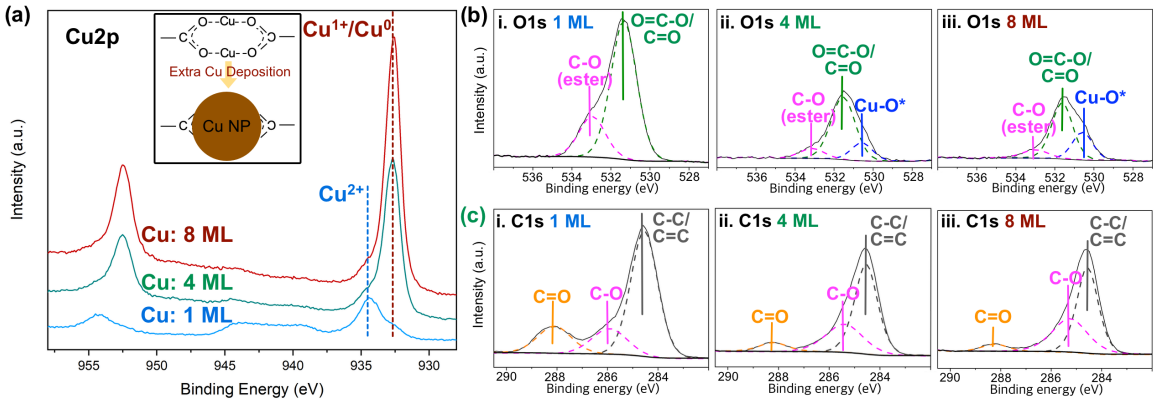


Figure 6.3. The XPS spectra of the (a) Cu2p, (b) O1s, and (c) C1s regions of 1 ML Cu (blue), 4 ML Cu (green), and 8 ML Cu (brown) deposited 5 cycled HKUST-1 thin films. The inset in (a) schematically describes a 2-D Cu paddle-wheel unit and a nucleated Cu NP mainly covered by oxygen atoms after the extra Cu deposition.

values, likely caused by more discontinuous HKUST-1 grains which are induced by the Cu NPs. (This will be confirmed and more discussed in following sections.) In these two extra Cu deposited samples, there is also no indication of new peaks for copper oxides ($Cu_2O$ or CuO) compared to the optimized HKUST-1 sample (1 ML Cu), which are expected to be located in the range of 30° - 40° for 2θ based on previous studies.[291,292] (See Figure E.1) These XRD results confirm that our HKUST-1 growth method allows us to incorporate extra metallic Cu in/on the HKUST-1 structure. Moreover the HKUST-1 thin films show slightly different colors depending on the amount of deposited Cu as shown in Figure E.2.

### 6.3.2. Chemical Effects of Extra Cu Atoms on the HKUST-1 Structures

For a better understanding of the chemical state and bonds of the extra Cu deposited HKUST-1 films, we conducted XPS analysis. In Figure 6.3a, the Cu 2p region was initially analyzed to prove the existence of extra Cu atoms in the HKUST-1 structure. The optimized HKUST-1 sample grown with 1 ML Cu in each cycle is

composed of 92 % $Cu^{2+}$ and 8 % $Cu^{1+}/Cu^{0}$, which corresponds to previous XPS results of HKUST-1 powders.[63,210] On extra Cu deposited samples, their overall Cu2p intensities are largely increased, especially for the $Cu^{1+}/Cu^{0}$ region (~ 932 eV). However, the $Cu^{2+}$ peak areas are decreased to 80 % and 58 % in the 4 ML Cu and the 8 ML Cu-HKUST-1 thin films respectively compared to the 1 ML Cu-HKUST-1 film, which might be caused by the extra Cu atoms covering $Cu^{2+}$ cations in the paddle-wheel units. From the metallic Cu peak in the XRD measurements shown in Figure 6.2, without any evidence of copper oxide, we believe that the increase of the $Cu^{1+}/Cu^{0}$ peak from the extra Cu deposited samples is mainly caused by the accumulation of metallic Cu atoms.

More interesting features were observed in the O1s (Figure 6.3b) and C1s (Figure 6.3c) regions. In general, the O1s and C1s spectra from the optimized HKUST-1 is similar to previous spectra from powder-type HKUST-1.[63,207,208,293] Increasing the amount of Cu in each growth cycle, the overall intensity of the O1s region is largely decreased, while the C1s intensity is slightly diminished. As schematically described in the inset of Figure 6.3a, we suspect that the extra Cu atoms are mainly nucleated and grown near oxygen atoms of deprotonated BTC ligands which form paddle-wheel structures with $Cu^{2+}$ cations. Specifically, on the 4 ML Cu deposited HKUST-1, the C=O/O=C-O peak (carboxylate oxygen, 531.5 eV) and the C-O peak (ester type oxygen, 533.1 eV) are significantly lower than the optimized HKUST-1 film (1 ML Cu).[207,208,219–221,293] We also observed features from oxygen adatoms (O*) directly bonded on Cu atoms (Cu-O*) at ~ 530.5 eV.[294] The 8 ML Cu deposited HKUST-1 exhibits slightly lower intensities for the C=O/O=C-O & C-O peaks compared to the 4 ML Cu-HKUST-1, but shows about a 1.5 times larger intensity for the Cu-O* peak than the 4 ML Cu-HKUST-1. By doing so, the relative area ratios of the C=O/O=C-O and C-O bonds in the 8 ML Cu-HKUST-1 decrease (78.7 % and 8.5 % respectively in the 4 ML Cu-HKUST-1→ 64

% and 7.4 % in the 8 ML Cu-HKUST-1) because of the increased oxygen adatom signal from 12.8 % (the 4 ML Cu case) to 28.5 % (the 8 ML Cu case). As we mentioned earlier, the Cu-O* peak in both cases is primarily caused by surface oxygen adatoms on extra metallic Cu clusters instead of forming bulk $Cu_xO_y$ since we have not observed any peaks for copper oxides in XRD, but the metallic Cu peak has been clearly detected from increasing amounts of Cu. The surface oxygen atoms are possibly formed during the growth cycles and the annealing process, in which the sample is exposed to 5.0 x $10^{-5}$ Torr of $O_2$ and $H_2O$ at 323 K and 343 K respectively, which is known to be suitable conditions for the dissociative adsorption of $O_2$ on Cu surfaces under vacuum.[277,279,285] These temperatures are also higher than the temperature (~ 290 K) at which hydroxyl groups on Cu surfaces disappear because of the disproportionation reaction (2 OH* → $H_2O$ + O*) leaving O adatoms on the surface. Thus, the Cu-O* is caused by the O adatoms on Cu.[295,296] Additionally, this condition is not possible to cause a Cu to $Cu_xO_y$ transition since it has been shown that Cu surfaces need to be annealed above 473 K after saturating them with O* adatoms or exposing them to $O_2$ above 473 K in order to form $Cu_xO_y$ layers.[297–299] We also did not observe any traces of $Cu_xO_y$ in TEM images, which will be discussed in more detail later.

Even though the overall C1s intensities of the 4 ML and 8 ML cases in Figure 6.3c do not decrease like the O1s spectra, we still find clear chemical changes in the HKUST-1 structure caused by the extra Cu atoms. In particular, by increasing the amount of Cu, the C=O bond peak at 288.3 eV[219,222,223] has decreased (19 %, 1 ML Cu → 8.8 %, 4 ML Cu → 7.7 % 8 ML Cu in the relative area ratio), but the peak for C-O bonds at 285.9 eV[219,222,223] becomes larger and shifted to a slightly lower B.E., ~ 285.4 eV (16 %, 1 ML Cu → 18.4 %, 4 ML Cu → 28.8 %, 8 ML Cu in the relative area ratio), which is still in the range for C-O bonds.[224,300] These results in the O1s and C1s regions indicate

that the extra Cu atoms are mainly nucleated and grown near the square planar coordinated Cu-O atoms of the paddle-wheel units, and they strongly interact with the O atoms. We can also understand this phenomenon based on the geometry of the paddle-wheel units, at which the square plane formed by Cu and O is perpendicular to benzene rings of the deprotonated $H_3BTC$ ligands as shown in Figure 6.1a. Thus, the Cu NPs grown on the Cu-O square plane will have less contact with C atoms than O atoms of the deprotonated $H_3BTC$ ligands. For building HKUST-1 structures, Cu atoms should interact with O atoms of deprotonated $H_3BTC$ ligands to form Cu-O bonds, so the O atoms can provide nucleation sites for Cu NPs. By doing so, the O atoms in BTC ligands less strongly interact with C atoms consisting of the carboxylate/ester groups verified from the weakened C=O bond peak, but the peaks related to C-O bonds get intensified by the interaction between the O atoms in BTC and the extra Cu atoms. In particular, the paddle-wheel units are surrounding the pores of HKUST-1 by connecting one pore to other neighboring pores, so the initially nucleated Cu atoms can be continuously grown and aggregated across pores and neighboring paddle-wheel units to form various sizes of Cu NPs, which will be confirmed in the following section.

### 6.3.3. Cu NP Sizes and Surface Roughness on the Cu NP Incorporated HKUST-1 Thin Films

On the basis of the XPS results above, the extra Cu atoms were predicted to form discontinuous clusters. To confirm this, we conducted TEM measurements with 4 ML and 8 ML Cu deposited HKUST-1 thin films (2 growth cycles for these samples to make them thin enough (~ 40 nm) for TEM). As described in Figure 6.4a for the 4ML Cu-HKUST-1 and 3b for the 8 ML Cu-HKUST-1, Cu nanoparticles are clearly observable in these two samples. Fast Fourier transform (FFT) patterns of lattice fringes in each film

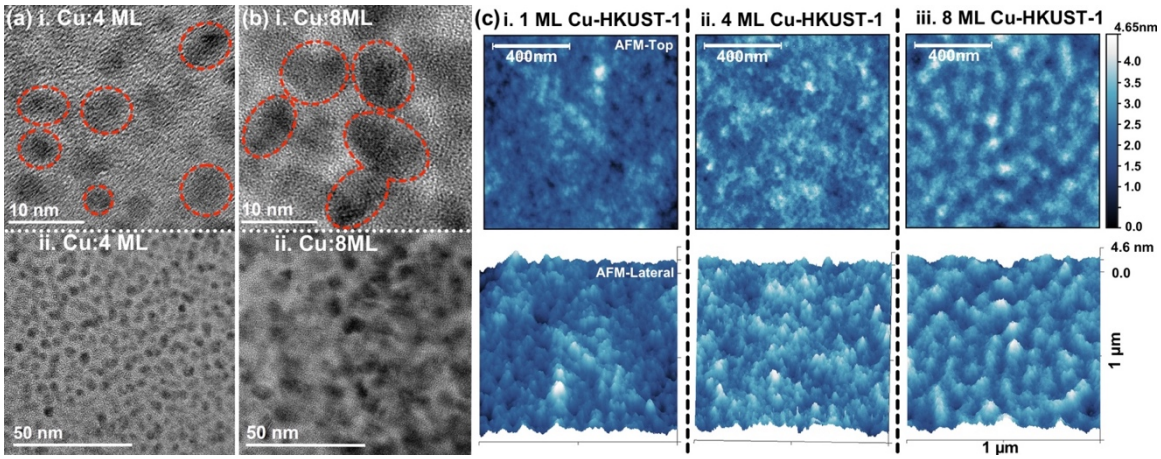


Figure 6.4. The TEM images of 2 cycles of (a) 4 ML Cu-HKUST-1 and (b) 8 ML Cu-HKUST-1 thin films. In Figure 4a and 4b, i and ii describe more (i) and less (ii) magnified TEM images. Some Cu NPs in each magnified TEM image are highlighted with red circles for clarification. (c) shows the top and lateral AFM images of 5 cycles of (i) 1 ML Cu-HKUST-1, (ii) 4 ML Cu HKUST-1, and (iii) 8 ML Cu HKUST-1 films.

shown in Figure E.3 verify that they are Cu NPs without $Cu_xO_y$ formation. The 4 ML Cu-HKUST-1 film shows homogeneously dispersed 4-6 nm Cu nanoparticles. The 8 ML Cu-HKUST-1 film has larger Cu nanoparticles, 8-12 nm, and some of them have aggregated to form continuous clusters of Cu. The observed Cu NPs in both samples are bigger than the pore size of HKUST-1, so they are surrounded by the HKUST-1 structures instead of fitting into pores, where similar phenomena have also been observed in previous MNP incorporated MOFs.[250,251,266,267,269,273,274,290] We also used AFM to compare general surface morphology for 1 ML, 4 ML, and 8 ML Cu deposited 5 cycled HKUST-1 films. The top surface morphology is shown in Figure 6.4c, and we observe that the extra Cu deposition lifts the overall top surface height of the samples. Thus, the 4 ML and 8 ML Cu deposited cases have more heightened features compared to the 1 ML Cu-HKUST-1, which are likely caused by the Cu nanoclusters. Moreover the 8 ML Cu-HKUST-1 has broader and larger features in comparison to the 4 ML Cu-HKUST-1, which correlates

with the TEM images. The 1 ML and 4 ML Cu-HKUST-1 films show similar root mean square (RMS) roughness, ~ 500 pm, but the 8 ML Cu-HKUST-1 is slightly rougher, with an ~ 530 pm RMS roughness. The overall thickness of the 1 ML Cu-HKUST-1 film is measured as 104.1 nm, which is consistent with our previous measurement,[49] and the 4 ML and 8 ML Cu HKUST-1 films are slightly thicker, 107.8 nm and 111.1 nm respectively. More details regarding the film thicknesses are available in Figure E.4.

### 6.3.4. Methanol Oxidation on the Cu NP Incorporated HKUST-1 Thin Films

After characterizing the structural and chemical properties of the extra Cu deposited HKUST-1 films, we conducted methanol oxidation experiments in the vacuum chamber to measure the catalytic activity of MOF incorporated Cu nanoparticles. In previous studies on a 0.25 ML oxygen-precovered Cu(110) surface, methoxy ($CH_3O$*) species were formed by the deprotonation of MeOH molecules, based on their interactions with O* adatoms, in which the O* adatoms scavenged H atoms from the adsorbed MeOH molecules.[279–281,284] The methoxy species can be deprotonated to formaldehyde (> 300 K),[279,282,283,285] and some were further oxidized to $CO_2$ by the decomposition of formate (HCOO*) species (~ 400 K).[279,281] The generation of $H_2O$ was also observed during these reactions above 170 K.[279–281,284] However the accumulation of $H_2O$ on the Cu(110) surface caused by MeOH oxidation could be prevented by exposing the surface to MeOH above 240 K.[278–280,285] This was because most of the generated $H_2O$ molecules during the reaction between MeOH and O* are known to desorb at temperatures below 240 K.[278–280,285]. Following these previous studies, we first exposed the 4 ML and 8 ML Cu-HKUST-1 thin films (5 cycles) to 1.0 x $10^{-6}$ Torr of $O_2$ for 3 minutes at a substrate temperature of 300 K in order to insure saturation with O*, although they had previously been exposed to 5.0 x $10^{-5}$ Torr of $O_2$ and $H_2O$ at 343 K for

15 minutes during their growth. If this amount of $O_2$ is exposed to pure single-crystalline macroscopic Cu surfaces, the Cu surfaces could be deactivated as observed in

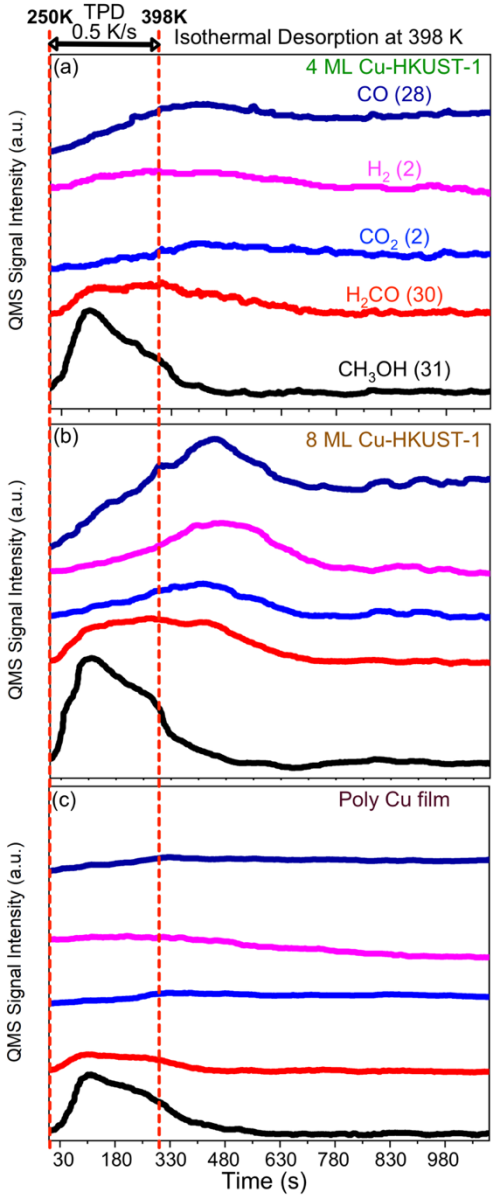


Figure 6.5. The desorption spectra of $CH_3OH$ (black), $H_2CO$ (red), $CO_2$ ( blue), $H_2$ (magenta), CO (dark blue) from (a) 4 ML Cu-HKUST-1, (b) 8 ML Cu-HKUST-1 films (5 growth cycles in each), and (c) 10 nm thick polycrystalline Cu film. They were treated with 1.0 x $10^{-6}$ Torr of $O_2$ at 300 K for 3 minutes and then were exposed to 5.0 x $10^{-7}$ Torr of methanol at 250 K for 20 minutes. The samples were heated from 250 K to 398 K at a rate of 0.5 K/s, and they were isothermally held at 398 K for 15 minutes.

previous studies.[277,279,285] However, our Cu NP incorporated HKUST-1 films clearly show catalytic activity, as is discussed below.

Following the $O_2$ exposure, the 4 ML and 8 ML Cu deposited 5 cycled HKUST-1 films were exposed to 5 x $10^{-7}$ Torr of MeOH for 20 minutes at 250 K in order to avoid the interruption of background molecules, especially $H_2O$, as with the previous studies mentioned above.[278–280,285] It was also found that MeOH molecules are dissociatively adsorbed on Cu surfaces as methoxy species at 250 K,[278–280,285] so we also believe that the methoxy is the main species adsorbed on Cu NPs on our Cu-HKUST-1 thin films. There is also the molecular adsorption of MeOH on the HKUST-1 structure since it can also uptake MeOH under this condition as shown in Figure E.5. Using a temperature-programmed desorption (TPD) method, we observed the desorption of various molecules from these samples by heating them from 250 K to 398 K at a rate of 0.5 K/s and holding them at 398 K isothermally for 15 min. We belive that our MeOH exposure condition causes MeOH molecules to be mainly adsorbed near the top surface of each sample since the exposure pressure is much lower than the saturated vapor pressure of MeOH (~ 97 Torr at room temperature) as used previously in conducting BET measurements to saturate powder-type HKUST-1 samples.[276] Moreover when we compared the amount of desorbing MeOH molecules adsorbed on the 4 ML Cu-HKUST-1 film at 120 K and 250 K in Figure E.6, the total amount of MeOH desorption above 250 K from the 250 K adsorbed case is less than 1% of the MeOH desorption above 250 K from the 120 K adsorbed case.

The 8ML Cu-HKUST-1 film in Figure 6.5b shows more desorption of MeOH and other products (CO, $H_2CO$, $CO_2$, and $H_2$) compared with the 4 ML Cu-HKUST-1 film shown in Figure 6.5a. We speculate that the Cu NPs on each sample, which have been measured by TEM and XPS as discussed previously, can improve the adsorption of

MeOH and also oxidize the adsorbed MeOH molecules. This conclusion is supported by the fact that the 1 ML Cu-HKUST-1 film (see Figure E.5), generates the least amount of MeOH desorption (compared to the 4 ML Cu case it is about 33 % less). Additionally the 1 ML Cu-HKUST-1 film (with no Cu MNPs) shows almost flat mass spectra signals for CO, $H_2$, and $CO_2$, which indicates there is no catalytic reaction. One of the ionized MeOH fragments also has a $m/z^+$= 30 fragment signal as with $H_2CO$ molecules;[301] the $m/z^+$= 30 signal from the 1 ML Cu-HKUST-1 film is primarily from the fragmented MeOH signal, since it follows the exact same trend as the MeOH signal ($m/z^+$= 31). However, the $m/z^+$=30 signal from the 4 ML and 8 ML Cu-HKUST-1 samples shows a distinct desorption behavior. Moreover, as mentioned above, more oxidized products of MeOH are observed on the higher Cu deposited samples while also involving increased MeOH desorption.

Specifically, MeOH desorption occurs with heating the sample from 250 K for both the 4 ML and 8 ML Cu- HKUST-1 films, and desorption continues until 398 K. Previous studies have shown that formaldehyde ($H_2CO$) and $H_2$ generation through methoxy decomposition are observed in the range of 250 K - 398 K along with the recombinative desorption of MeOH.[279–285] Although the fragmented MeOH signal can affect the $m/z^+$= 30 signal, the $H_2CO$ ($m/z^+$= 30) signal increases rapidly until 300 K and then slowly rises up to 398 K in both samples. While each sample is held at 398 K, the 8 ML Cu-HKUST-1 film shows a relatively steady generation of $H_2CO$ for ~ 3 minutes, but the $H_2CO$ from the 4 ML Cu-HKUST-1 film continuously decreases. Furthermore the $H_2$ and $CO_2$ signals in the 8 ML Cu-HKUST-1 film increase slowly during the sample heating from 250 K to 398 K and show their maximum intensities when the sample is held at 398 K. The $H_2$ generation can be caused by two different reaction pathways; one is the decomposition of methoxy ($CH_3O^* \rightarrow H_2CO(g) + H^*$), which also generates

formaldehyde (280 K – 400 K), and the other is formate decomposition (HCOO* → $CO_2$(g) + H*).[279–285] The formate species are formed by extra O* and $H_2CO$ remaining on the surface ($H_2CO$* + O* → HCOO* + H*), which can be decomposed to $CO_2$ and $H_2$ on the Cu(110) surface.[279,281] Via formate decomposition, $H_2$ was observed to desorb from the surface from 350 K to 440 K, and the $CO_2$ generation was detected from 390 K to 480 K on Cu surfaces previously.[279,281] Therefore, the MeOH oxidation on Cu surfaces is a reaction-limited process, which is also applicable in our Cu NP incorporated HKUST-1 thin films. The 4 ML Cu-HKUST-1 film produces significantly less $CO_2$ and $H_2$, which can be related to less uptake of MeOH at 250 K and also its catalytic superiority based on the smaller Cu NPs compared to the 8 ML Cu-HKUST-1 film, which will be further investigated in the following section. In previous studies, CO generation was observed from the decomposition of methanol.[302–309] We also observe CO generation, however, there is less production of CO with the 4 ML Cu-HKUST-1 film than with the 8 ML Cu-HKUST-1 film. As shown in Figure E.7, both samples show the same XRD peaks regarding HKUST-1 structures before and after the methanol oxidation experiment, which proves the HKUST-1 structures are durable under this experimental condition.

Interestingly, a polycrystalline Cu film (10 nm thick) which was grown and treated with the same amount of $O_2$ as the HKUST-1 films loses its reactivity, so there is less uptake of MeOH and less generation of oxidized products of MeOH as shown in in Figure 6.5c (even compared to the 4 ML Cu-HKUST-1 film). Similar phenomenon was observed on the Cu (110) surface with a large amount of $O_2$ exposure, during which populated O adatoms prevented the adsorption and activation of MeOH.[277,279,285] Even though the extra Cu deposited HKUST-1 films are also exposed to a large amount of $O_2$, which causes the polycrystalline Cu surface to be deactivated, Cu NPs incorporated on HKUST-1 are not deactivated and show their catalytic activity by oxidizing MeOH. We

suspect the Cu NP – HKUST-1 interface could be the site at which the MeOH molecules become stabilized and react with O* adatoms on Cu NPs. This MNP–MOF interface is also suggested as the main reaction site in the $CO_2$ hydration to MeOH on Cu NP incorporated UiO-66[268] and in the dehydration of ammonia borane on Pd NP incorporated UiO-66[269]. Therefore, these results indicate that our Cu NP incorporated HKUST-1 films have higher reactivity for oxidizing MeOH compared with a polycrystalline Cu film. Moreover, the 8 ML Cu-HKUST-1 film, which has less Cu NP – HKUST-1 interfaces, shows similar catalytic behavior compared to the 0.25 ML O*-precovered Cu(110) surface, but the 4 ML Cu-HKUST-1 film, which has more Cu NP – HKUST-1 interfaces, seems to more selectively oxidize MeOH to formaldehyde.

To estimate the relative selectivity towards $H_2CO$ between the extra Cu deposited HKUST-1 films, we compared the relative production of target molecules ($H_2CO$, $CO_2$, and $H_2$, directly generated by the MeOH oxidation) between the 4 ML and 8 ML Cu-HKUST-1 films derived from the TPD results in Figure 6.6. As explained above, each

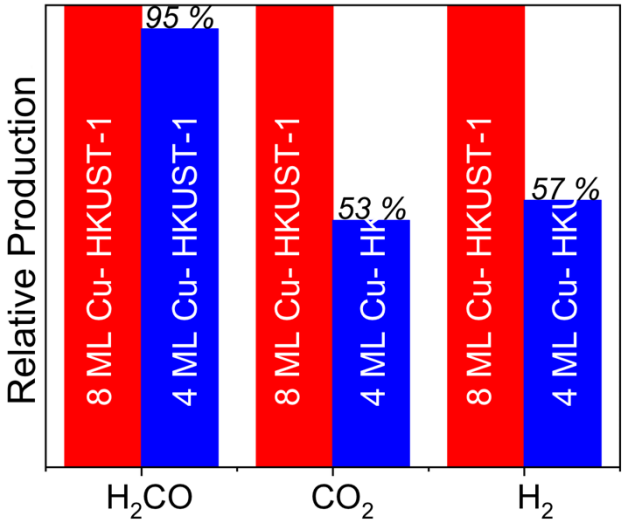


Figure 6.6. The relative production of $H_2CO$, $CO_2$, and $H_2$ from 5 cycled 4 ML Cu-HKUST-1 (blue) and 5 cycled 8 ML Cu-HKUST-1 (red) thin films normalized by the amount of methanol desorption from each sample. These results were calculated based on the TPD data.

sample adsorbs a different amount of MeOH depending on the amount of Cu, which can be indirectly estimated from the MeOH desorption. Thus, it is incorrect to directly compare the absolute amount of each product between the samples for evaluating the relative $H_2CO$ selectivity, since the amount of adsorbed MeOH affects the amount of generated target molecules. In order to reflect this factor in our analysis, we normalized the amount of desorbing target molecules by the amount of the corresponding MeOH desorption. For the case of $H_2CO$ in this analysis there is an additional complicating matter that arises due to the fact that gas-phase methanol can decompose via electron bombardment in the quadrupole mass spectrometer into a mass 30 fragment which overlaps with the $H_2CO$ $m/z^+= 30$ signal. Thus, to evaluate the true amount of formaldehyde production from each sample we must subtract the mass 30 signal caused by the ionization fragment of MeOH. To do this, we determined the ratio between $m/z^+= 31$ and $m/z^+= 30$ signals that are generated from only MeOH and then used this parameter as a multiplier of the methanol signal for Cu nanoparticle containing samples for subtraction from the $m/z^+= 30$ signal created by both the MeOH ionization fragment and formaldehyde. The results of all of this analysis are shown in the bar graphs in Figure 6.6 which display the relative production of $H_2CO$, $H_2$, and $CO_2$ from the 8 ML Cu-HKUST-1 compared to the 4 ML Cu-HKUST-1, and show that there is 95 % of the production for $H_2CO$ for the 4 ML Cu-HKUST-1 sample with less relative production of $CO_2$ and $H_2$, 53 % and 57 %, respectively. These results clearly verify a better $H_2CO$ selectivity for the 4 ML Cu-HKUST-1 film than for the 8 ML-Cu-HKUST-1 film. In particular, the $CO_2$ production is directly related to the formate (HCOO*) formation on each sample, so we suspect that there are less formate species on the 4 ML Cu-HKUST-1 film. Moreover, we believe that this could be affected by the quantity of O* adatoms on each sample, where the 8 ML Cu-HKUST-1 has 1.5 times more O* adatoms than the 4

ML Cu-HKUST-1 as measured in Figure 6.3 by XPS. This is primarily because the extra O* adatoms are known to oxidize formaldehyde, which is already oxidized from MeOH, in order to form formate on the Cu(110) surface.[279,281] Thus, these analyses confirm that the 4 ML Cu-HKUST-1 thin film, which has well dispersed 4-6nm Cu nanoparticles, can more selectively oxidize MeOH to formaldehyde compared to the 8 ML Cu-HKUST-1 thin film. Furthermore, it has been proven that HKUST-1 can be a good scaffold for incorporating Cu nanoparticles which have catalytic activity.

## 6.4. CONCLUSION

This is the first study to grow MNP incorporated MOF thin films under vacuum and investigate their catalytic activity by surface science methods. We successfully grew two different extra Cu deposited HKUST-1 thin films in a high vacuum system and measured their catalytic activity for MeOH oxidation. As described in Illustration 6.1, we grew 4 ML and 8 ML Cu in Cu deposition cycles of each sample to incorporate Cu NPs in/on the HKUST-1 structure. This quantity of Cu is more than the optimized amount needed (1 ML Cu) for one growth cycle of a simple HKUST-1 thin film without Cu NPs.

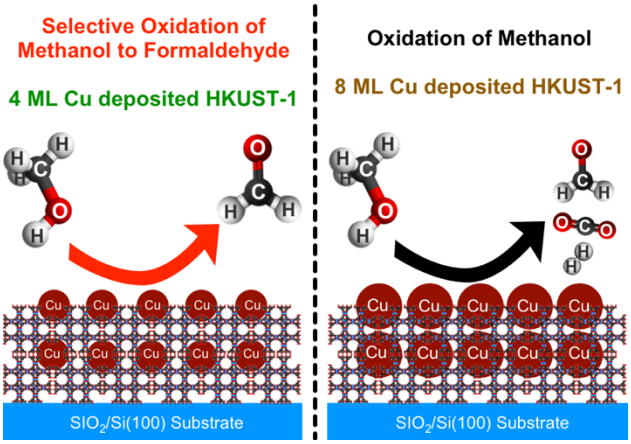


Illustration 6.1. Schematic descriptions of main products from the methanol oxidation on both 4 ML Cu and 8 ML Cu deposited HKUST-1 thin films.

Various sizes of Cu NPs were incorporated in/on the HKUST-1 structure: the Cu NPs were in the range of 4-6 nm for the 4 ML Cu-HKUST-1 and 8-12 nm for the 8 ML Cu-HKUST-1 films, as determined by TEM measurements. In particular, the XPS measurements showed a large intensity decrease in the O1s spectra for these two films compared to the optimized HKUST-1 film. This could be related to the notion that extra Cu atoms are mainly interacting with O atoms in $BTC^{3-}$ ligands. In the MeOH oxidation experiments, the optimized HKUST-1 film (without Cu NPs) did not show any catalytic behavior, but the extra Cu deposited HKUST-1 films showed different catalytic behavior depending on the size of the Cu particles. The 4 ML Cu-HKUST-1 film (5 growth cycles) more selectively oxidized MeOH to formaldehyde than the 8 ML Cu-HKUST-1 film (5 growth cycles) which less selectively oxidized the MeOH to generate not only formaldehyde, but also $CO_2$, caused by the generation of formate species. We believe that this is mainly because more O* adatoms are introduced on the 8 ML Cu-HKUST-1 film, as measured by XPS, so the additional O* adatoms oxidize formaldehyde to $CO_2$, as was also observed on a Cu (110) surface.[279–285] Moreover, when we conducted MeOH oxidation reactions on a Cu polycrystalline film, which was also treated with the same amount of $O_2$ as the other samples, its catalytic activity was much lower than the 4 ML and 8 ML Cu-HKUST-1 films, since this surface was deactivated due to being fully surface saturated with O* adatoms, as previously investigated.[277,279,285] Therefore, we believe that the Cu NP – HKUST-1 interface sites can facilitate MeOH molecule stabilization for continuous oxidative reactions. In this chapter, we have shown that the HKUST-1 MOF can be a scaffold for incorporating Cu NPs without their aggregation in order to conduct catalytic reactions.

# Chapter 7: Conclusions

## 7.1. Overview of Completed Studies

In this dissertation, we conducted three projects using 2-D Pd–Au(111) bimetallic surfaces and two projects growing 3-D HKUST-1 metal-organic framework thin films under vacuum. From Chapter 2 to Chapter 4, we investigated the enhanced $O_2$ activation and a new catalytic reaction mechanism for selective oxidation of acetaldehyde to acetic acid on Pd–Au(111) surfaces. Specifically in Chapter 2, we found improved activation of adsorbed $O_2$ by co-adsorbed $H_2O$ on the Pd–Au(111) surface. When co-adsorbed with $H_2O$, $O_2$ admolecules on the Pd–Au surface were more strongly bound via their interactions with $H_2O$. This interaction leaded to large enhancements in the dissociation of $O_2$ as determined via the generation of $CO_2$ upon exposure to CO. With advancing the study in Chapter 2, we probed the influence of the atomic makeup of the surface of Pd−Au catalysts regarding control of the catalytic activity toward $O_2$ dissociation and the reactivity of the resulting oxygen adatoms in Chapter 3. From various investigations, we found that, upon increasing Pd coverage, the dissociation barrier for $O_2$ steadily decreases and, further, the reaction barrier for CO oxidation continuously increases. Finally, oxygen molecularly adsorbed on the Pd−Au bimetallic surface and was a precursor to dissociative $O_2$ chemisorption, just as with pure Pd surfaces, and additionally, the enhanced reactivity of adsorbed atomic oxygen originated at the interfaces between Pd and Au domains. In Chapter 4, we reported a catalytic reaction pathway for the gas-phase selective oxidation of acetaldehyde to acetic acid on the Pd–Au surfaces. On an oxygen precovered Pd−Au surface (composed of 45 % of Pd and 55 % of Au), acetaldehyde was selectively oxidized to acetic acid from 250 to 340 K. With higher Pd coverages (80 % Pd and 20 % Au), the acetaldehyde was less selectively oxidized to acetic acid, and near

375 K, $CO_2$ , $H_2O$, $CH_4$ , and $H_2$ are evolved, evidence for the decarboxylation of acetate. In our density functional theory calculations, we confirmed that the relative energy difference between the acetate state and the decarboxylated state decreases as Pd ensemble size increases.

In Chapter 5 and 6, we introduced the newly developed HKUST-1 thin film growth method under vacuum and the use of HKUST-1 thin films as catalytic supports with incorporating Cu NPs. Adopting a layer-by-layer (LBL) growth concept, we sequentially deposited $H_3BTC$ by CVD and Cu by PVD. With this methodology, we grew HKUST-1 thin films by sequentially depositing one monolayer (ML) of Cu after each $H_3BTC$ deposition cycle. The successfully grown HKUST-1 thin film had highly oriented crystallinity showing the (220) and (222) planes as its main plane depending on XRD operating methods, glancing angle XRD and in-plane XRD respectively. More details regarding the HKUST-1 thin film growth under vacuum are explained in Chapter 5. Advancing this study, we incorporated Cu NPs in/on the HKUST-1 thin film to observe the catalytic activity for methanol oxidation using UHV temperature programmed desorption methods in Chapter 6. The Cu-HKUST-1 film with 4-6 nm Cu NPs selectively oxidized methanol molecules to formaldehyde. However the Cu-HKUST-1 film with 8-12 nm Cu NPs generated not only formaldehyde, but also $CO_2$ and $H_2$ from methanol, caused by the decomposition of formate species. These papers are the first to report the growth and use of HKUST-1 thin films under vacuum. Our growth technique can be further applied to growing other MOFs, especially for $H_2BDC$ (benzene-1,4-dicarboxylic acid) containing MOFs. Several $H_2BDC$ MOFs (e.g. MOF-5 and UiO-66) are widely known for their thermal and chemical stability. By growing various MNP incorporated $H_2BDC$ based MOFs under vacuum, we can investigate

various molecular level catalytic reactions. I will discuss this topic in more detail in the following section.

### 7.2. Ongoing and Future Works

The schematic diagram directly below pictorially describes the essential features of the technical aspects of the proposed project. Briefly, we propose to study the use of a supporting substrate with adsorbed $H_2BDC$ molecules which will self-organize into a surface aligned lattice template for the growth of several different terephthalic acid-based MOF ultrathin films. Growth of the ultrathin MOF film will proceed from the surface aligned template without solvents (in vacuum) through a layer-by-layer growth method in which alternating layers of the $H_2BDC$ ligand and metal atoms are evaporatively deposited to achieve the desired film thickness. We will also incorporate metal

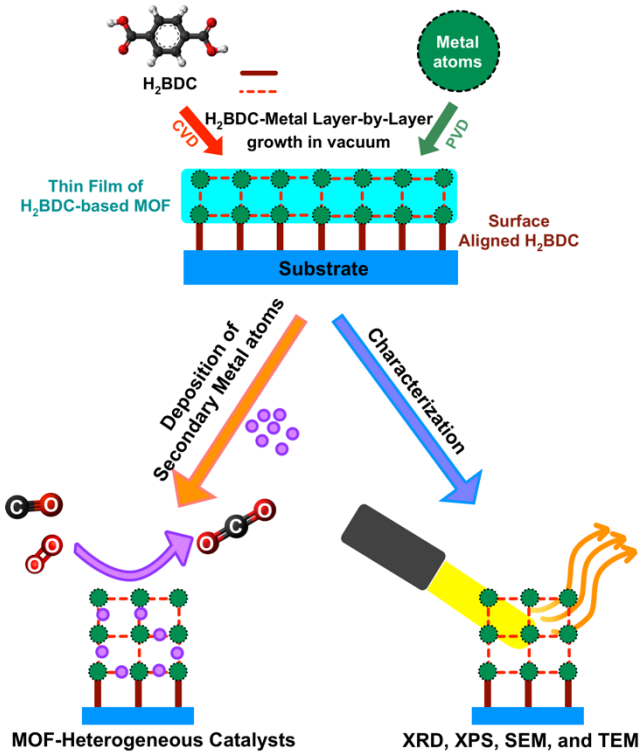


Illustration 7.1. Schematic of Technical Portion of the Proposed Study

nanoparticles (MNPs) both in and on MOF structures. Such MNP incorporated MOF thin films will allow us to investigate molecular level catalytic reactions under vacuum and also apply them to catalytic membranes for gas separation and conversion at relatively high pressures. The deposited films will be characterized *ex situ* employing x-ray diffraction, atomic force microscopy, scanning and transmission electron microscopy, and x-ray photoelectron spectroscopy. We will also use ultrahigh vacuum (UHV) surface science tools for study of these films and their chemistry. The primary UHV surface science techniques to be employed include (i) molecular beam scattering methods for high precision measurements of adsorption of relevant molecules by the MOF structure, and (ii) temperature programmed desorption mass spectrometry which will provide information regarding catalytic reactions by various reactants on and within the MOF.

Specifically, we will begin our catalytic investigations by studying the oxidation of methanol along with two oxidizing agents, molecular oxygen and water, and then extend it to other complex alcohol molecules. Selective oxidation of methanol to formaldehyde is industrially important since formaldehyde is a precursor for other syntheses, e.g. urea-formaldehyde, melamine resin, and 1,4-butanediol. Moreover, formic acid, which can be another possible product from methanol oxidation, is widely used as a preservative and an antibacterial agent in livestock feed and is also employed as a hydrogen storage molecule for fuel cells. Thus, discovering new catalytic mechanisms for methanol oxidation using MOFs can contribute to industrial progress. Employing a quartz crystal microbalance in our vacuum chamber, control over the quantity of deposited metal atoms can be achieved and we can measure their oxidation states via XPS to check whether they remain as metal atoms or convert to metal cations via their interactions with the $H_2BDC$ ligands. Previously, when Cu atoms were loaded into the ZnO nanoparticle imbedded MOF-5 which formed a (Cu/ZnO)@MOF-5 composite, the methanol yield

generated from the synthesis gas mixture was about 60% of that typically produced via the industrial Fischer-Tropsch process, even at a relatively low Cu loading (~ 1.4 wt%) and with a small Cu specific surface area < 1 $m^2g^{-1}$.[256] Moreover, Cu NPs incorporated in UiO-66 showed different activity in the synthesis of methanol from $CO_2$ and $H_2$ depending on the quantity of MOF-Cu NP interface sites.[267] This study verified that additional MOF-MNP interface sites turn out to improve catalytic activity.[267] Inspired from this study we plan to control the size of MNP's, as we have done for the Cu NP incorporated HKUST-1,[49] which will directly affect the concentration of MOF – MNP interface sites, and investigate the difference in catalytic mechanisms. In particular, we will investigate the methanol oxidation/decomposition mechanisms in Cu NP incorporated MOF-5 and UiO-66. In previous studies on a Cu (110) surface under vacuum, methanol molecules were oxidized to $CO_2$ accompanied with generation of $H_2$ and $H_2CO$. However, as demonstrated in our prior experiments using Cu NP incorporated HKUST-1 thin films, methanol can be selectively oxidized to $H_2CO$ depending on the Cu NP sizes. Although we found meaningful results from methanol oxidation experiments using our Cu-HKUST-1 thin films, the HKUST-1 MOF is not thermally stable above ~ 420 K, which does not allow us to conduct catalytic activity tests at higher temperatures. Thus we seek to develop Cu incorporated MOF-5 and UiO-66, which are stable up to ~770 K, and verify more detailed oxidation/decomposition mechanisms for methanol oxidation by conducting experiments at high temperatures while also comparing them to the results from our HKUST-1 studies.

# Appendix A: Supporting Information for $H_2O$-Improved $O_2$ activation on the Pd–Au bimetallic surface

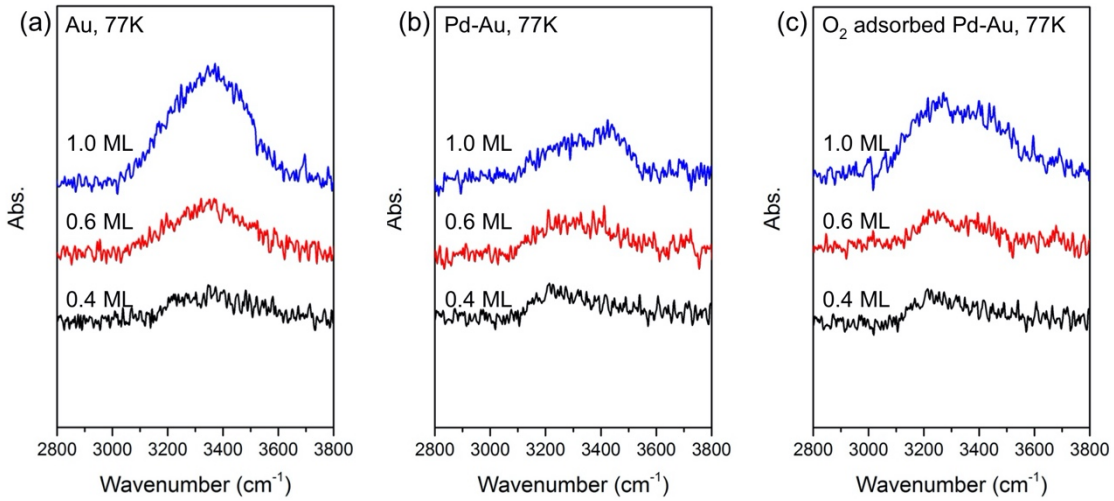


Figure A.1. RAIRS spectra measured in the region of O–H bond frequencies for 0.4 ML, 0.6 ML, and 1.0 ML of $H_2O$ impinged on (a) Au (111) (b) Pd–Au (111), and (c) 1.0 ML of $O_2$ adsorbed Pd-Au (111) surface. All those spectra were measured at 77 K, and the $H_2O$ coverages were controlled based on the results from the $H_2O$ desorption on Pd–Au surface (Figure 1b).

### A.1. RAIRS SPECTRA OF $H_2O$ ON VARIOUS PD–AU SURFACE

As indicated in Figure A.1b, when the Pd–Au surface is covered with 0.4 ML of $H_2O$, RAIRS shows a peak near 3200 $cm^{-1}$, but the overall spectrum becomes broader with 0.6 ML of $H_2O$, and then 1.0 ML of $H_2O$ makes two different regions, 3100 $cm^{-1}$ – 3360 $cm^{-1}$ and 3360 $cm^{-1}$ – 3540 $cm^{-1}$, corresponding to weaker O–H bonds induced by stronger Pd–$H_2O$ interactions (177 K peak on TPD in Figure 1b) and stronger O–H bonds with weaker Pd–$H_2O$ interactions (160 K peak on TPD in Figure 2.1b). As a reference, we also measured RAIRS for $H_2O$ on Au (111) where the $H_2O$ molecules are not so strongly interacting with the surface, and here there is just a broad spectrum for the different coverages as shown in Figure A.1a. The intensity of each spectrum increases

with $H_2O$ coverage since more $H_2O$ molecules make more H-bonds among them. This interpretation is also supported by the TPD results shown in Figure A.2, which shows a peak temperature for each $H_2O$ coverage on Au (111) that is shifted a little bit from near 140 K to 146 K as coverage increases.

Increasing the amount of $H_2O$ coverage on the 1ML of $O_2$ adsorbed Pd–Au surface, it also shows two different regions for O–H bond frequencies. Different from the $H_2O$ solely adsorbed cases, however, the intensity for the lower frequency region in the 1.0 ML of $H_2O$ / 1ML of $O_2$ adsorbed Pd–Au surface, 3100 $cm^{-1}$ – 3250 $cm^{-1}$ for the relatively weaker O–H bonds (180 K peak on TPD in Figure 2.2b), is higher than the higher frequency region, 3250 $cm^{-1}$ – 3500 $cm^{-1}$ for the relatively stronger O–H bonds (152 K peak on TPD in Figure 2.2b), depending on the degree of interactions with the adsorbed $O_2$ on the Pd–Au surface.

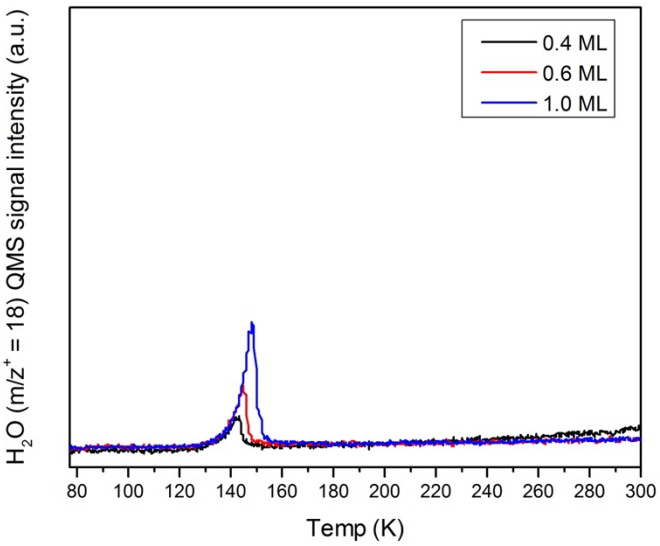


Figure A.2. TPD results for $H_2O$ ($m/z^+ = 18$) from 0. 4 ML, 0.6 ML, 1.00 ML of $H_2O$ adsorbed Au (111).

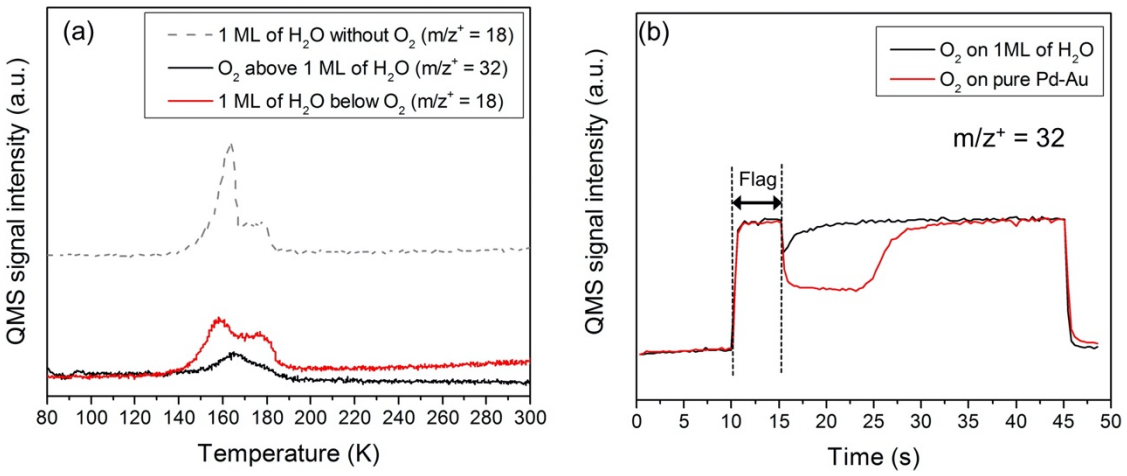


Figure A.3. (a) TPD spectra of 1 ML of $H_2O$ without $O_2$ (gray dotted line) and small amount of $O_2$ (black solid line) adsorbed above 1 ML of $H_2O$ (red solid line) on the Pd–Au surface and (b) King and Wells measurements of $O_2$ directly adsorbed on the Pd–Au surface (red solid line) and 1 ML of $H_2O$ pre-adsorbed Pd–Au surface (black solid line).

### A.2. $O_2$ ADSORPTION ON 1 ML OF $H_2O$ COVERED PD–AU SURFACE.

As described in Figure A.3a and A.3b, relatively small amount of $O_2$ molecules are adsorbed on 1 ML of $H_2O$ pre-adsorbed Pd–Au surface compared to the pure Pd–Au surface. However, even this small amount of $O_2$ admolecules clearly affects the desorption of the pre-adsorbed $H_2O$ molecules, where they simultaneously desorb in the range of 140 K – 190 K.

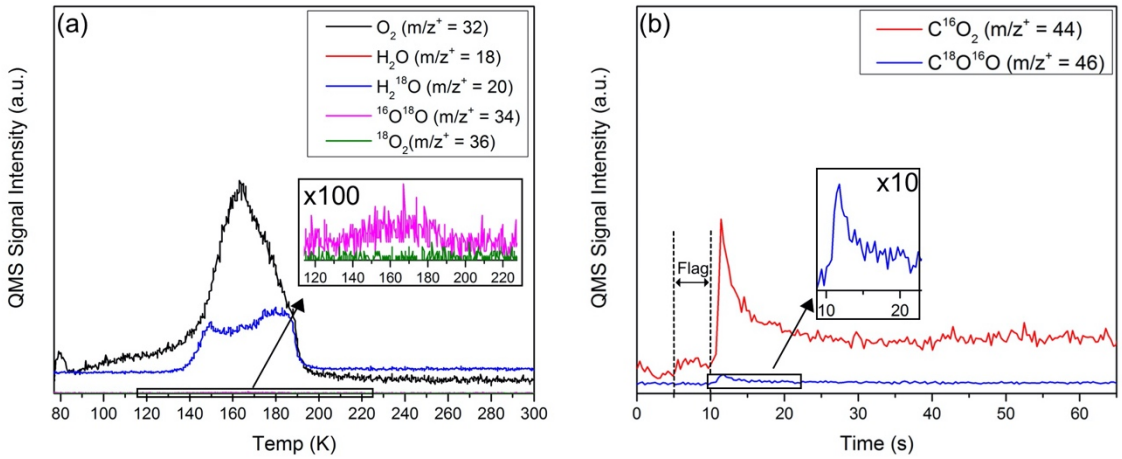


Figure A.4. (a) TPD and (b) CO-RMBS results from 1.0 ML $H_2{}^{18}O$ and 1.0 ML $O_2$ adsorbed Pd–Au surface. The inset in (a) shows a very low desorption of $^{16}O^{18}O$, and the inset in (b) also describes a very low generation of $C^{18}O^{16}O$.

### A.3. ISOTOPICALLY LABELED $H_2{}^{18}O$ USED TPD AND CO-RMBS

In our TPD experiments for $H_2O$ and $O_2$ co-adsorbed on the Pd–Au surface, as shown in Figure 2.2, we do not observe another $H_2O$ desorption peak around 240 K which would be related to the associative desorption of hydroxyl (–OH) groups on the surface, and which has been reported in previous Pd model catalyst studies.[89,90] For the Pd–Au bimetallic surface case, thus, it is expected that $O_2$ and $H_2O$ molecules tend to form H-bonded complexes instead of making hydroxyls (–OH) by dissociating O=O and H–OH bonds. To confirm this, we also conducted TPD experiments using $H_2{}^{18}O$ with $^{16}O_2$ co-adsorbed on the Pd–Au model surface to measure the generation of $^{16}O^{18}O$ (m/z$^+$ = 34). Based on our previous study regarding co-adsorbed $H_2{}^{18}O$ with atomic O on an Au

(111) surface,[93] formation of adsorbed hydroxyls (–OH), should generate $^{16}O^{18}O$ ($m/z^+$ = 34) during TPD via the associative desorption of $O_2$ from the coupling of the isotopically labeled hydroxyls ($–^{16}OH + –^{18}OH$). However, in testing with 1.0 ML of $H_2{}^{18}O$ and 1.0 ML of $O_2$ co-adsorbed on the model Pd–Au surface, we do not observe the generation of $^{16}O^{18}O$ (see Figure A.3a in which the signal for $m/z^+$ = 34 is very small compared to the $^{16}O_2$ ($m/z^+$ = 32) signal). Therefore, we conclude that co-adsorbed $O_2$ and $H_2O$ on the Pd–Au surface are more likely to form a strong H-bonded complex rather than adsorbed hydroxyls (–OH).

Additionally, we also conducted CO-RMBS experiments on a 1.0 ML of $H_2{}^{18}O$ + 1.0 ML of $O_2$ co-adsorbed surface to test for the generation of $C^{16}O^{18}O$ ($m/z^+$ = 46). This is another way to check for the formation of hydroxyls from the interactions of adsorbed $H_2O$ and $O_2$ on the Pd–Au surface.[114] In Figure A.3b, the intensity for $C^{16}O^{18}O$ ($m/z^+$ = 46) is much lower than for the standard $CO_2$ ($m/z^+$ = 44) signal, and the m/z+ = 46 signal only becomes visible by magnifying the scale by a factor of 10. This very small signal is possibly caused by a tiny amount of $-^{18}OH$ on the surface. Therefore, from these results, it is expected once again that co-adsorbed $H_2O$ and $O_2$ molecules on our model Pd–Au surface are mainly forming a H-bonded complex, and only a small fraction of them exist as hydroxyls.

## A.4. OTHER SUPPOR

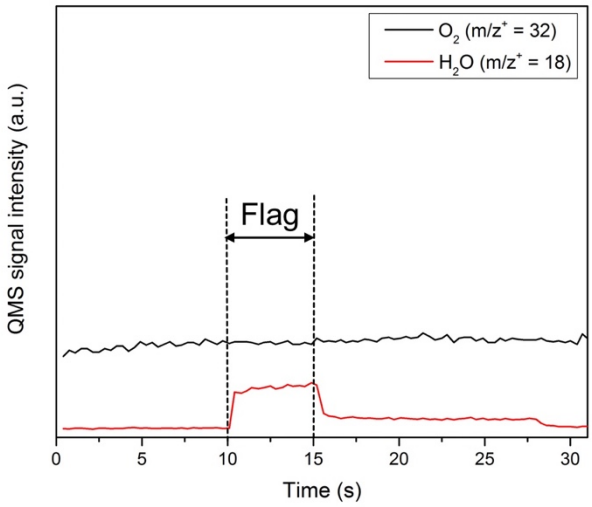


Figure A.5. King-Wells measurement of a $H_2O$ beam impinging on 1 ML of $O_2$ covered Pd–Au surface. From 10 s to 15 s, the $H_2O$ beam was directed to the inert flag and then hit the sample from 15 s to 28 s for impinging 1 ML of $H_2O$.

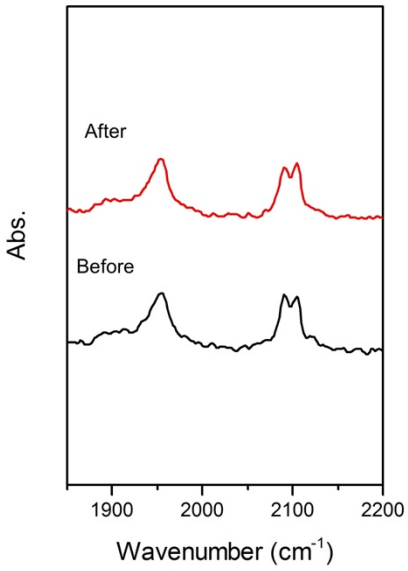


Figure A.6. RAIRS spectra of saturated CO on Pd–Au (111) surface before (bare surface, black) and after (red) the adsorption and desorption of 1.0 ML of $O_2$ and 1.0 ML of $H_2O$.

As shown in Figure A.6, our Pd – Au (111) surface has Pd ensembles, which can be verified from the existence of vibrational frequencies for CO molecules on the continuous Pd sites ($\nu$CO: 1900 – 2000 $cm^{-1}$). Furthermore, the desorption of 1.0 ML $H_2O$/ 1.0 ML $O_2$ negligibly affect the compositions of Pd ensembles because the IR spectra of before and after the desorption of $O_2$ / $H_2O$ are almost identical to each other.

| $H_2O$ coverages (ML) | $O_2$ desorption ratio in 77 K – 145 K (%) | $O_2$ desorption ratio in 145K – 165 K (%) | $O_2$ desorption ratio in 165 K – 200 K (%) | Total amount of $O_2$ desorption ratio in 77 K – 200 K (%) | Total amount of $CO_2$ generation ratio (%) |
|---|---|---|---|---|---|
| 0 | 58.4 | 23.8 | 17.8 | 100 | 32.2 |
| 0.6 | 44.5 | 24.2 | 31.3 | 85.4 | 65.5 |
| 1 | 28.2 | 28.9 | 42.9 | 81.5 | 100 |
| 1.5 | 24.2 | 35.6 | 40.2 | 81.7 | 100.2 |
| 2.1 | 19.6 | 43.9 | 36.5 | 84.8 | 82.7 |

Table A.1. Estimated percentages for $O_2$ desorption and $CO_2$ generation on the basis of $H_2O$ coverages.

## Appendix B: Supporting Information for Surface Alloy Composition Controlled $O_2$ Activation on Pd–Au Bimetallic Model Catalysts

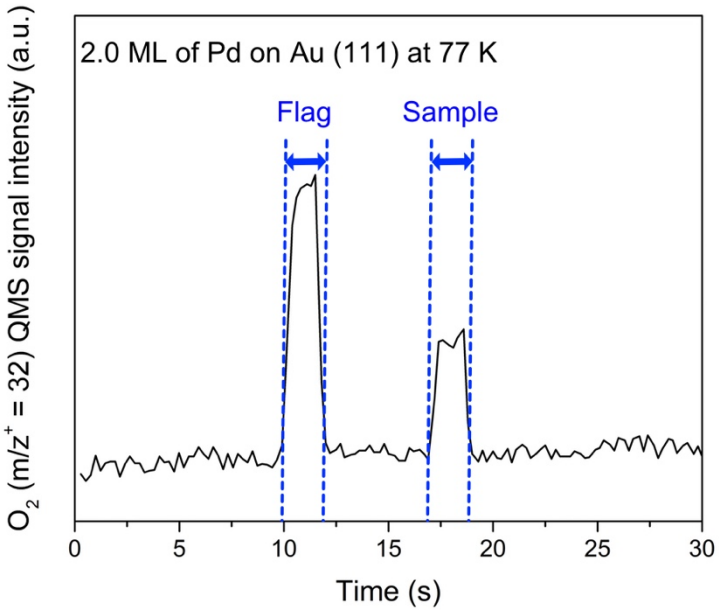


Figure B.1. A sample of King and Wells measurement of $O_2$ on the Pd-Au surfaces for estimating an initial adsorption probability. The $O_2$ molecular beam was first impinged on the inert flag for 1.5 seconds to generate a saturated signal, and then directed on the sample for 1.5 seconds. The ratio of the decreased area from the sample to the saturated area from the flag indicates the initial adsorption probability.

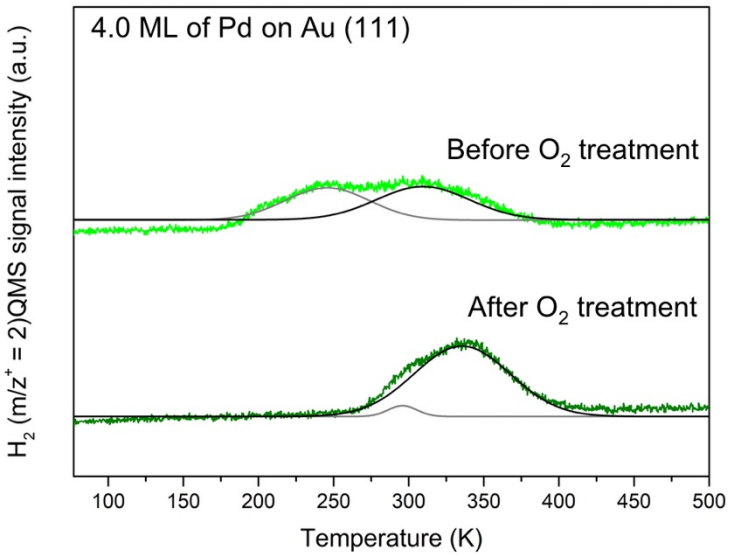


Figure B.2. $H_2$-TPD to show the effect of $O_2$ treatment at 475 K on the anned 4.0 ML of Pd covered Pd–Au (111) surface. The gray line is for the Pd–Au interfaces, and the black line indicates the amount of the Pd (111) like islands.

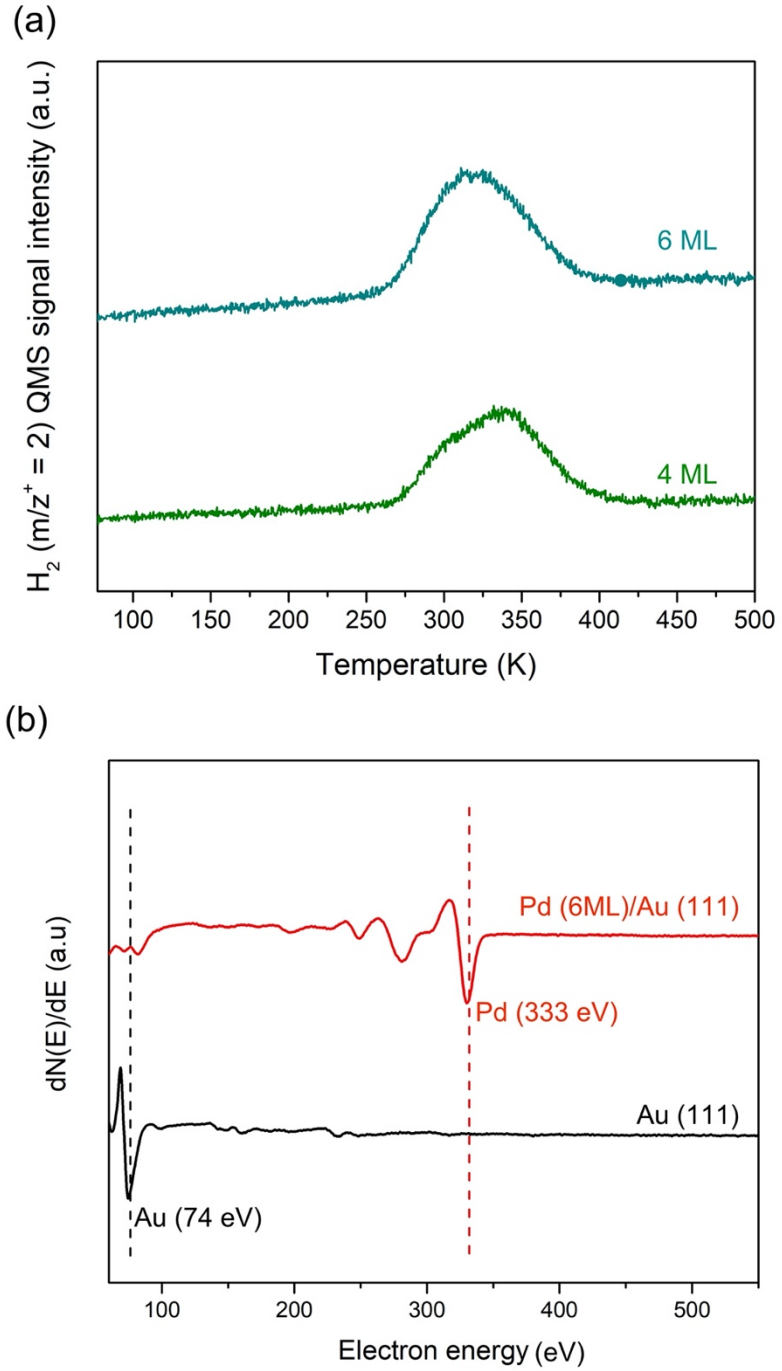


Figure B.3. (a) $H_2$-TPD spectra for the annealed 4 ML and 6ML of Pd covered surfaces. (b) Auger spectra for Au (111) and the annealed 6 ML of Pd covered Pd–Au (111) surface.

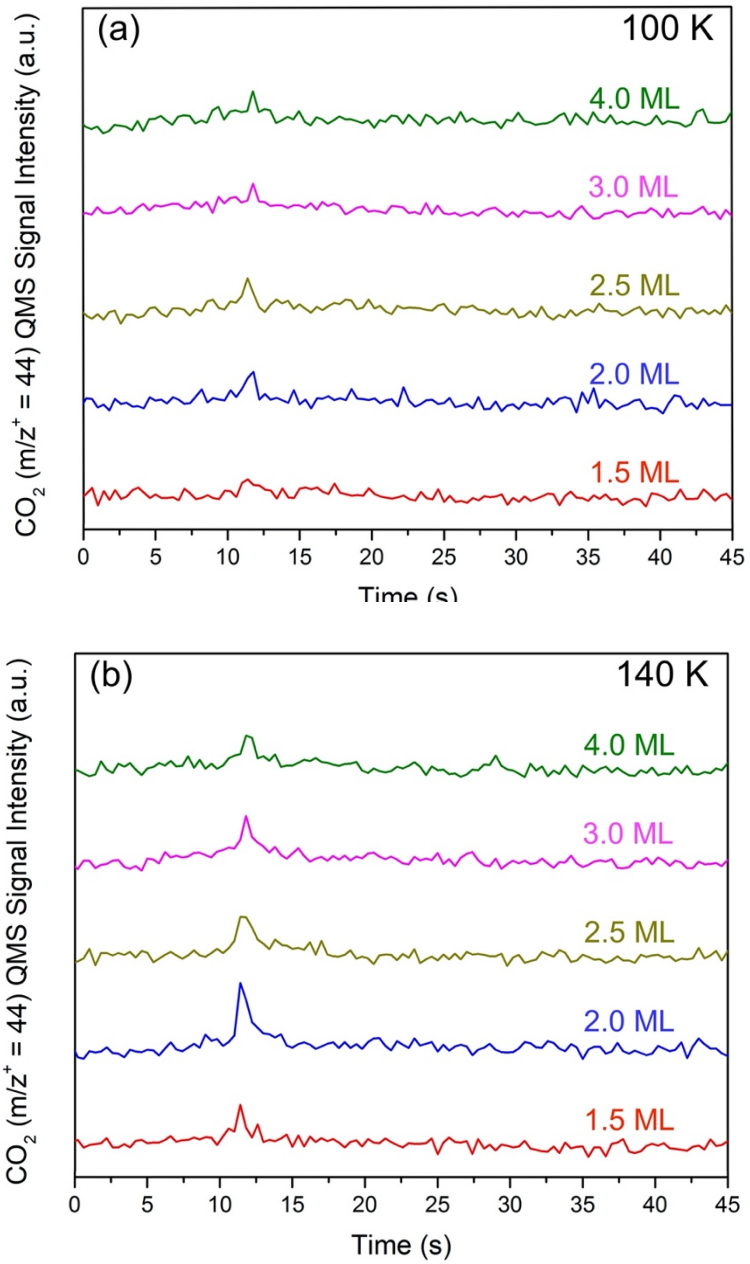


Figure B.4. CO-RMBS at (a) 100 K and (b) 140 K. Overall peaks are weak at 100 K compared to 140 K. The CO molecular beam was impinged on the samples from 10 seconds forward.

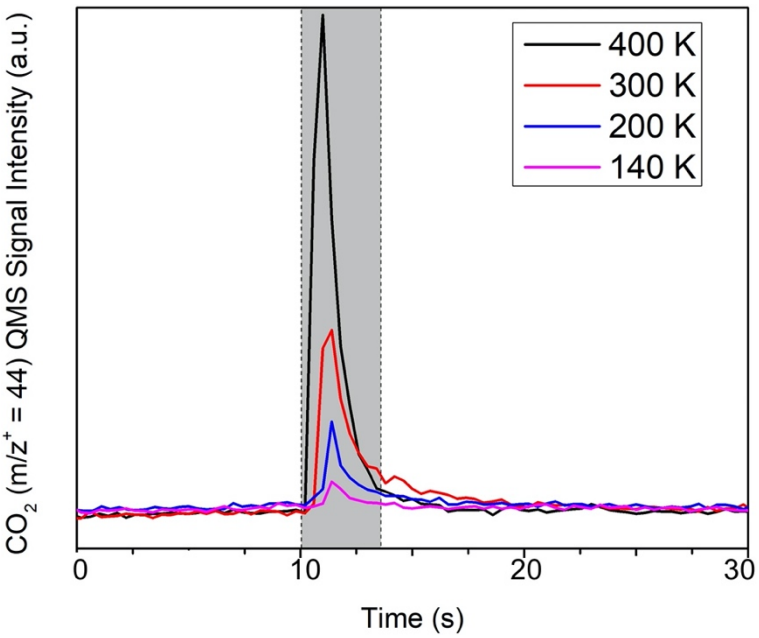


Figure B.5. CO-RMBS at 140 K, 200 K, 300 K, and 400 K on the 2.0 ML of Pd deposited Pd–Au surface.

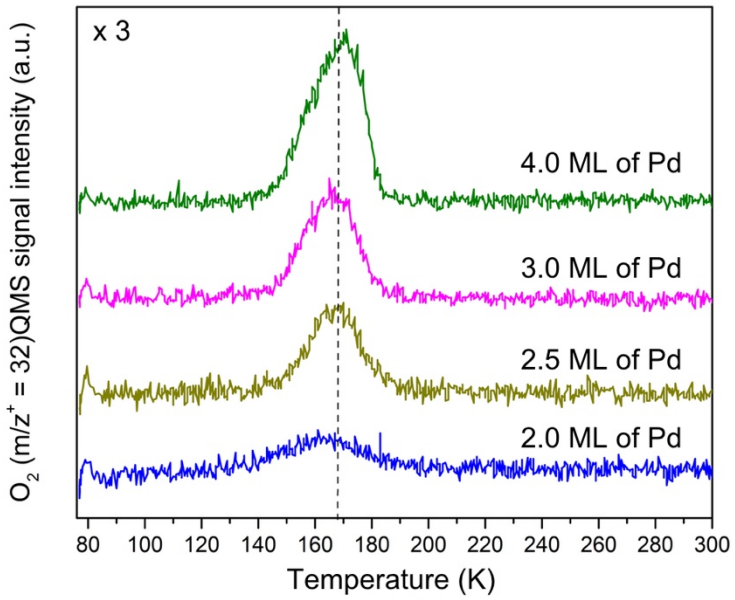


Figure B.6. $O_2$-TPD spectra for 20 – 30 % of $O_2$ saturated surfaces compared to the fully saturated surfaces in Figure 1b. The scale is 3 times enlarged over that of Figure 1b in the text of the paper.

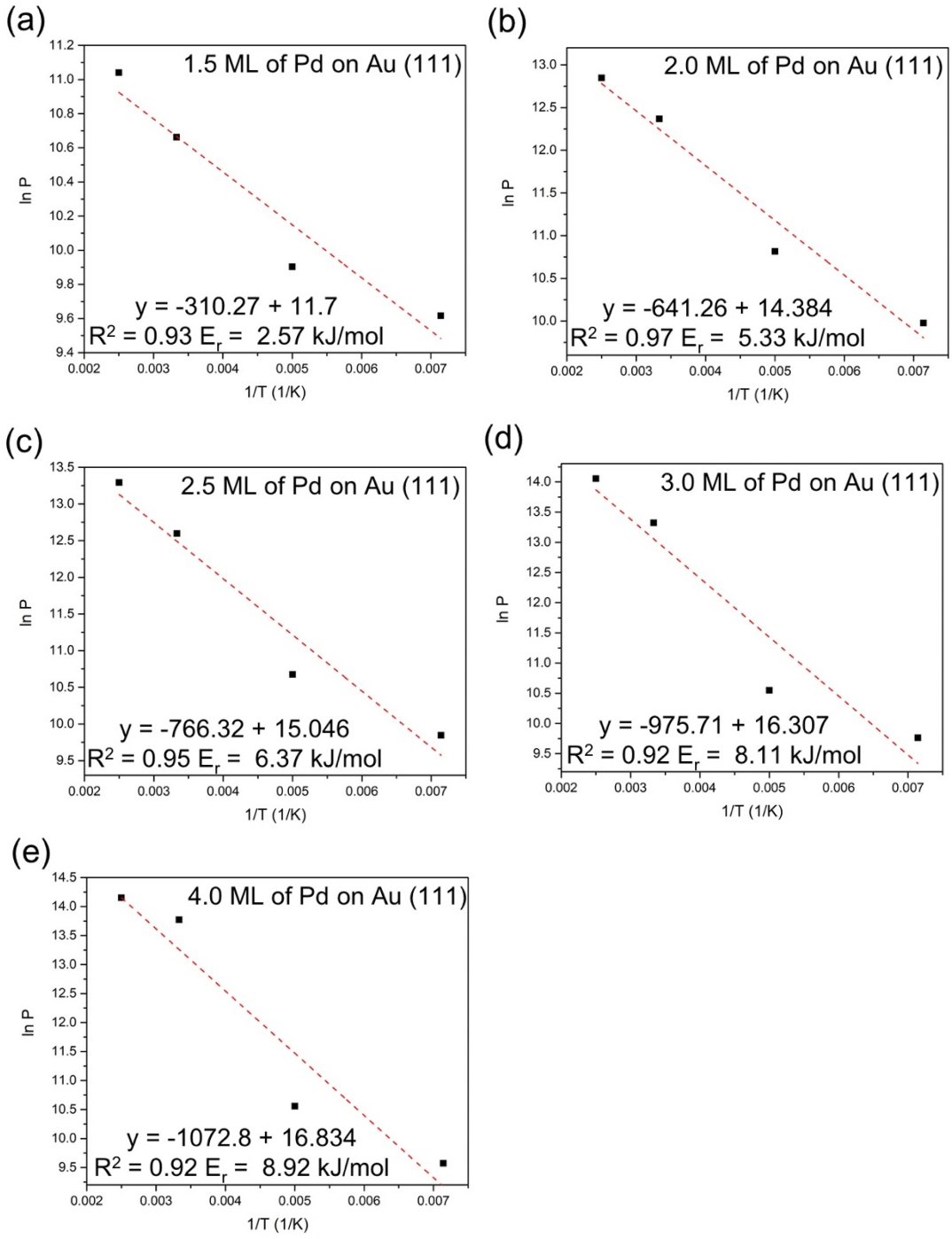


Figure B.7. Arrhenius plots for log of total productions of $CO_2$ (P) vs 1/T on various Pd–Au surfaces. The slope in each plot indicates the reaction barrier ($E_r$) for CO oxidation on each particular Pd covered surface.

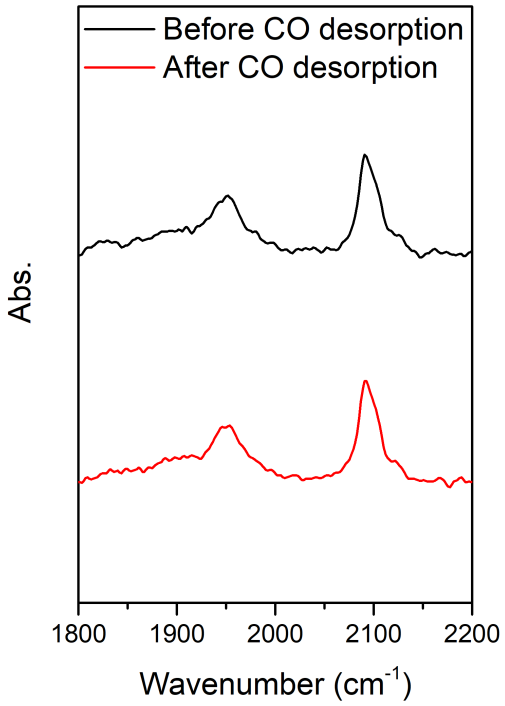


Figure B.8. RAIRS spectra of saturated CO on 2.5 ML of Pd deposited Pd–Au (111) surface before (black) and after (red) the adsorption and desorption of CO. *v*CO at 1800 – 2000 $cm^{-1}$ corresponds to CO on continuous Pd sites, and *v*CO at 2050 - 2100 $cm^{-1}$ is for atop CO on isolated Pd atoms, and *v*CO > 2100 $cm^{-1}$ is for atop CO on Au sites.

We analyzed the surface composition of 2.5 ML of Pd desposited Pd – Au (111) surface using CO molecules, which widely used for the analysis of surface compositions of Pd – Au surfaces. As shown in Figure B.8, the CO desorption negligibly affects the surface composition in our experimental conditions since there is no apparent difference between the RAIRS spectra.

# Appendix C: Selective Oxidation of Acetaldehyde to Acetic acid on Pd–Au Bimetallic Model Catalysts

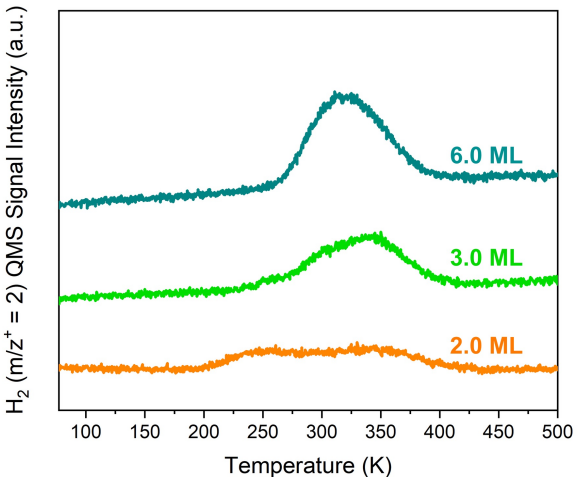


Figure C.1. Temperature-programmed desorption (TPD) of $H_2$ on 2.0 ML, 3.0 ML, and 6.0 ML of Pd deposited surfaces.

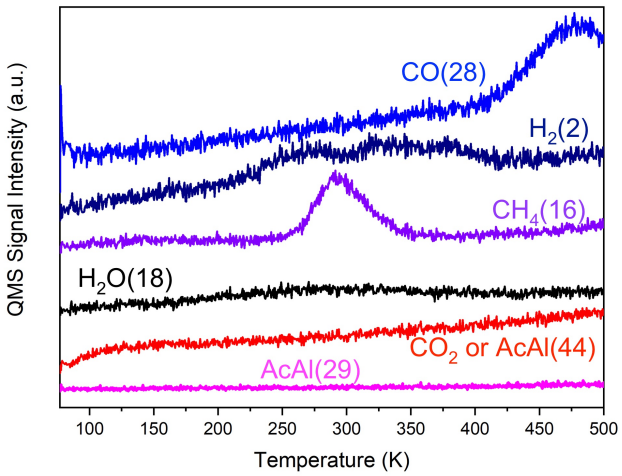


Figure C.2. Detailed TPD of 0.3 ML AcAl adsorbed on the oxygen-free Pd–Au (Pd: 2.0 ML) surface. There is no molecular desorption feature for the AcAl ($m/z^{+}$=29), but it still shows desorption features for $CH_4$ and $H_2$, which are strong evidences for the decomposition of the AcAl.

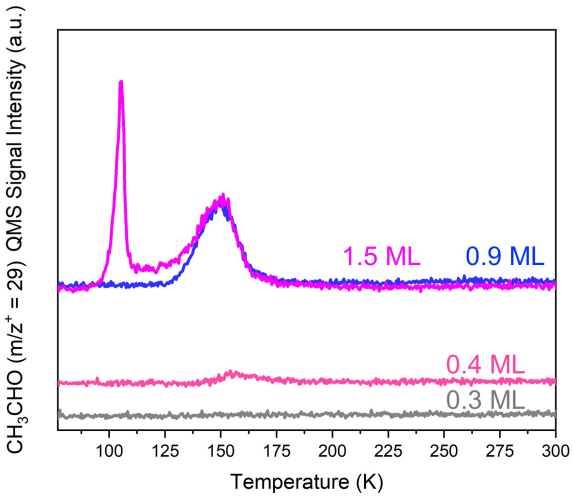


Figure C.3. TPD of AcAl on the oxygen-free Pd–Au surface (Pd: 2.0 ML). Different coverages of the AcAl were impinged via a molecular beam at 77 K, and then they were heated to 500 K by 1 K/s. No desorption features were observed above 200 K. The desorption peak intensity at 150 K is saturated with 0.9 ML AcAl.

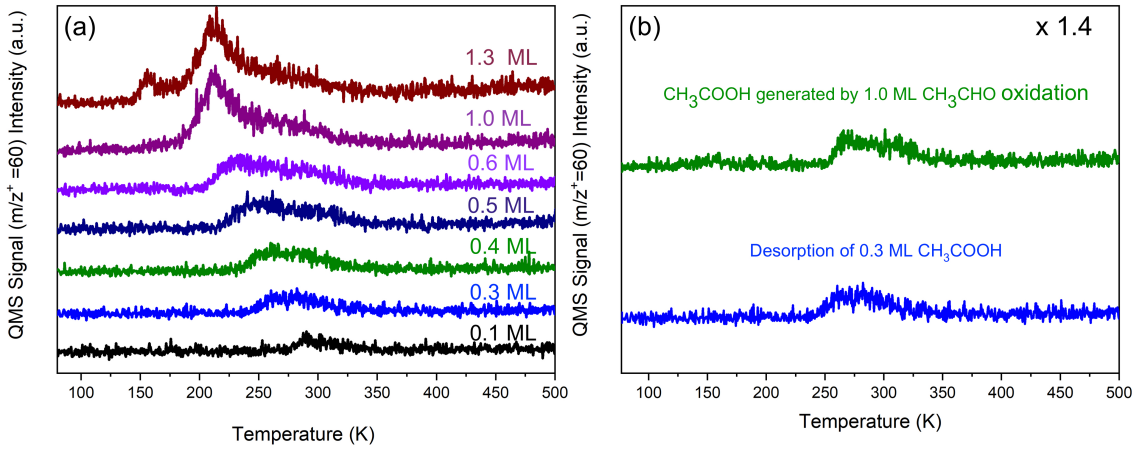


Figure C.4. TPD of (a) various coverages of acetic acid ($m/z^+=60$) on 2.0 ML Pd deposited surface. The comparison between the acetic acid generated by the 1 ML acetaldehyde ($CH_3CHO$, AcAl) oxidation (green) and the desorption of 0.3 ML acetic acid ($CH_3COOH$ (blue)) is described in (b), which is 1.4 times magnified in Y-axis compared to (a).

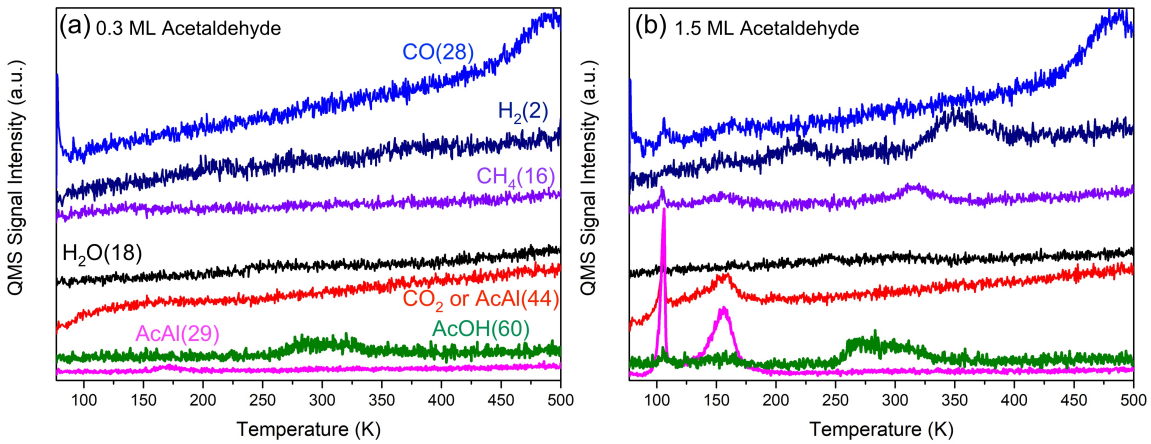


Figure C.5. Detailed TPD of (a) 0.3 ML acetaldehyde (AcAl) and (b) 1.5 ML AcAl on the oxygen-precovered Pd–Au (Pd: 2.0 ML) surface. The AcAl molecules were impinged *via* the molecular beam at 77 K. The AcAl covered surfaces were heated to 500 K by 1 K/s with observing CO ($m/z^+ = 28$, blue), $H_2$ ($m/z^+ = 2$, dark blue), $CH_4$ ($m/z^+ = 16$, mauve), $CO_2$ or AcAl ($m/z^+ = 44$, red), AcOH ($m/z^+ = 60$, green), and AcAl ($m/z^+ = 29$, magenta)

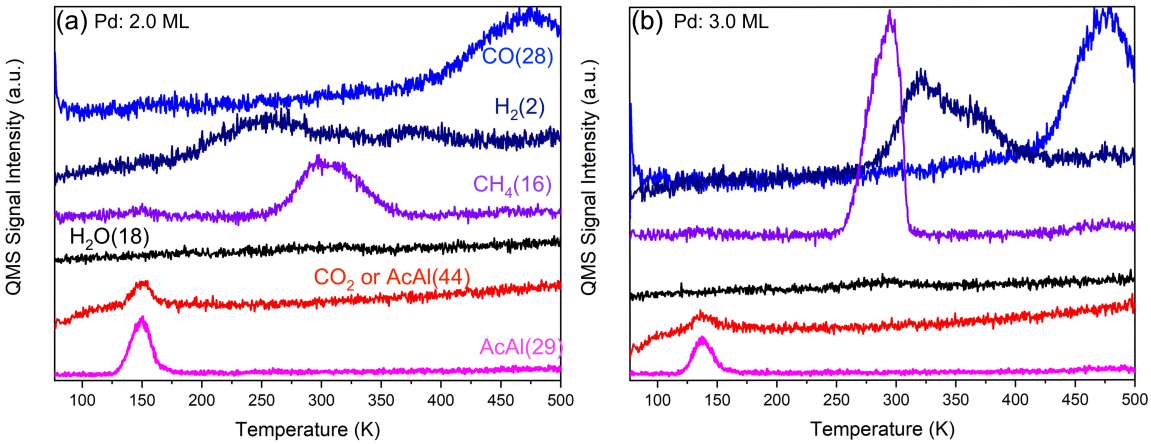


Figure C.6. Detailed TPD of 0.9 ML AcAl on (a) 2.0 ML Pd deposited surface and (b) 3.0 ML Pd deposited surface. (Both are bare surfaces.) The AcAl was impinged on the samples at 77 K *via* the molecular beam, and then the AcAl covered surfaces were heated to 500 K by 1 K/s with observing CO ($m/z^+ = 28$, blue), $H_2$ ($m/z^+ = 2$, dark blue), $CH_4$ ($m/z^+ = 16$, mauve), $CO_2$ or AcAl ($m/z^+ = 44$, red), and AcAl ($m/z^+ = 29$, magenta)

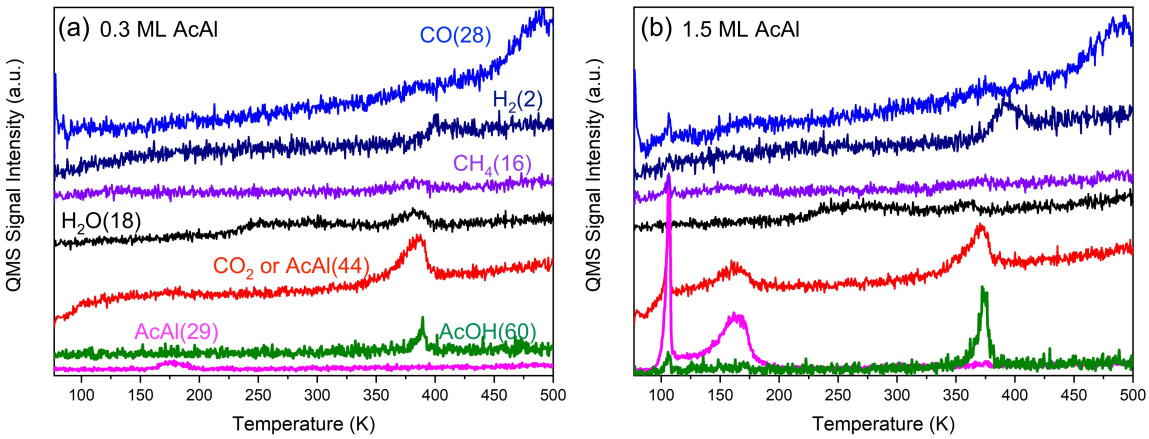


Figure C.7. Detailed product analysis during the desorption of (a) 0.3 ML AcAl and (b) 1.5 ML AcAl on the oxygen-precovered Pd–Au surface (Pd: 3.0 ML). Each coverage of the AcAl molecules was impinged on the samples at 77 K *via* the molecular beam, and then the AcAl covered surfaces were heated to 500 K by 1 K/s with observing CO ($m/z^+ = 28$, blue), $H_2$ ($m/z^+ = 2$, dark blue), $CH_4$ ($m/z^+ = 16$, mauve), $CO_2$ or AcAl ($m/z^+ = 44$, red), AcOH ($m/z^+ = 60$, green), and AcAl ($m/z^+ = 29$, magenta)

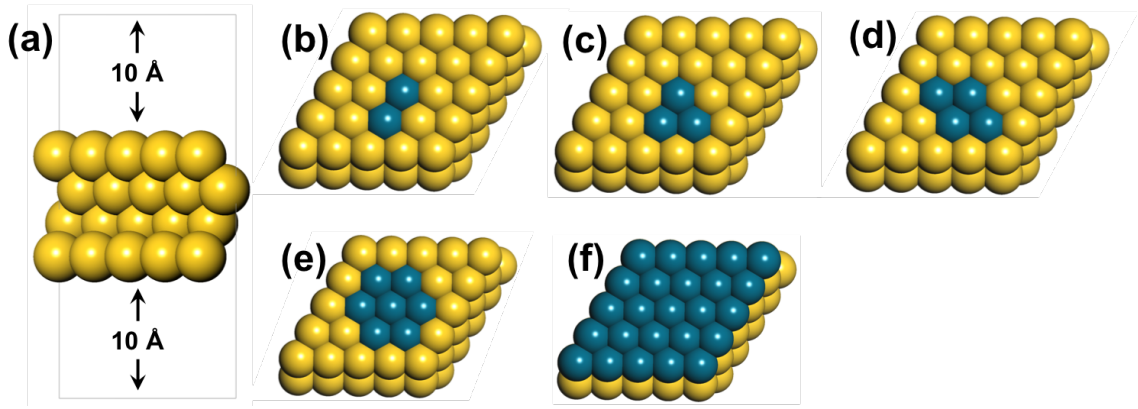


Figure C.8. Illustrations of Pd–Au (111) surfaces for density functional theory calculations. (a) shows the side view of our slab model, and (b) – (f) shows the top view of 2, 3, 4, 7, and 25 (1 ML) Pd atoms introduced Au(111) surface. The yellow and blue balls indicate Au and Pd respectively.

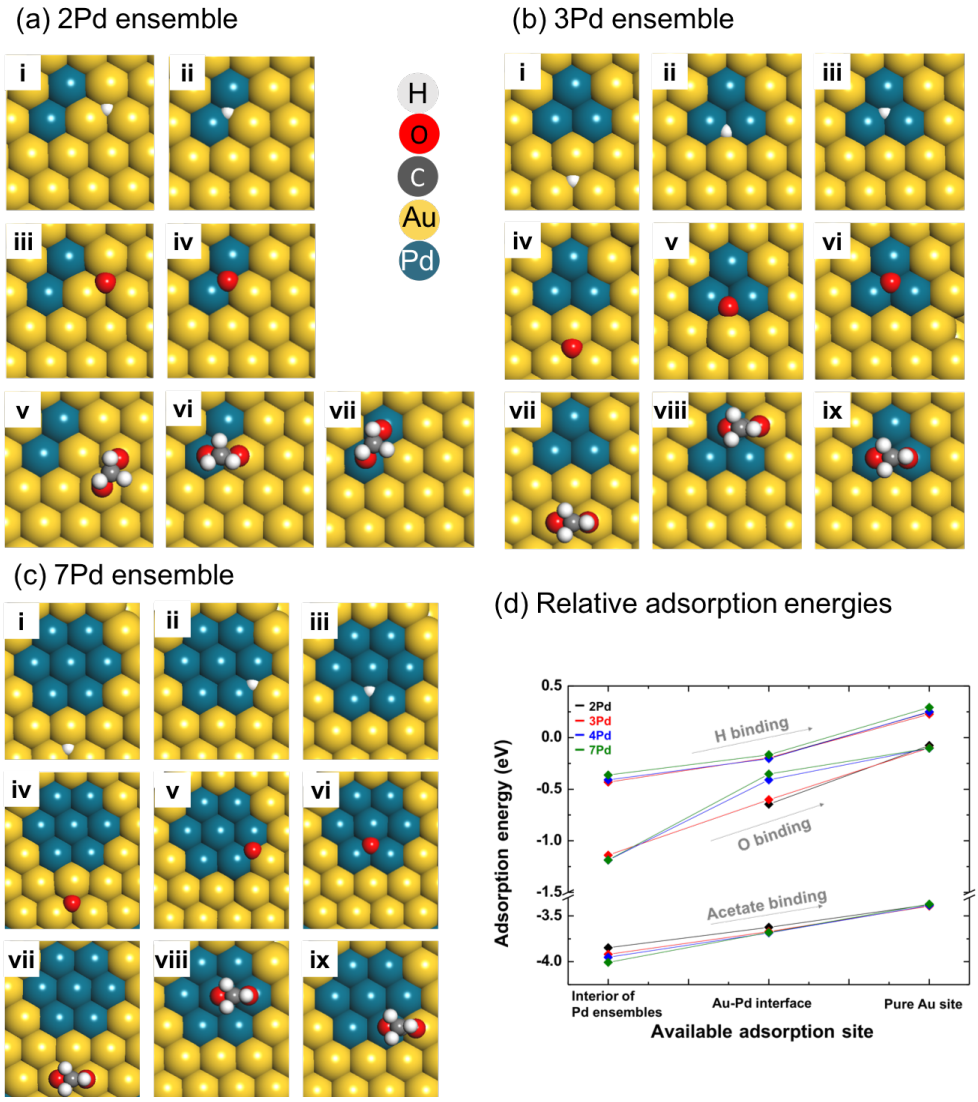


Figure C.9. Illustrations of calculated H, O and acetate ($CH_3COO$) adsorption sites on (a) 2Pd, (b) 3Pd, and (c) 7Pd ensembles on Au (111) surfaces. In (a) 2Pd ensemble case, **i** and **ii** show a H atom on a pure Au site and a Pd–Au interface site, **iii** and **iv** are for a O atom on a pure Au site and a Pd–Au interface site, and **v – vii** indicate an acetate on a pure Au site, a Pd–Au interface site, and the interior of Pd atoms respectively. In (b) 3Pd ensemble and (c) 7Pd ensemble, **i – iii** are for a H atom, **iv – vi** are for a O atom, and **vii – ix** are for an acetate formed on a pure Pd site, a Pd–Au interface site, and the interior of Pd atoms respectively. (d) shows the relative calculated energies of H, O, and acetate binding energies on 2, 3, 4, and 7Pd ensembles, where the more negative energy means the more stable configuration.

# Appendix D: Supporting Information for Solvent-free Vacuum Growth of Oriented HKUST-1 Thin Films

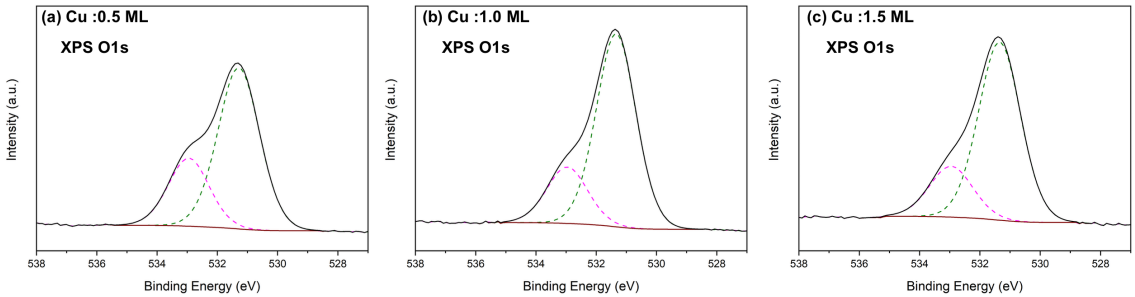


Figure D.1. The O1s XPS spectra for 5 cycled HKUST-1 thin films grown with (a) 0.5 ML Cu , (b) 1.0 ML Cu, and (c) 1.5 ML Cu depositions in each cycle. There is no component for copper oxides in all spectra, which is supposed to be shown at 530.5 – 529.5 eV.

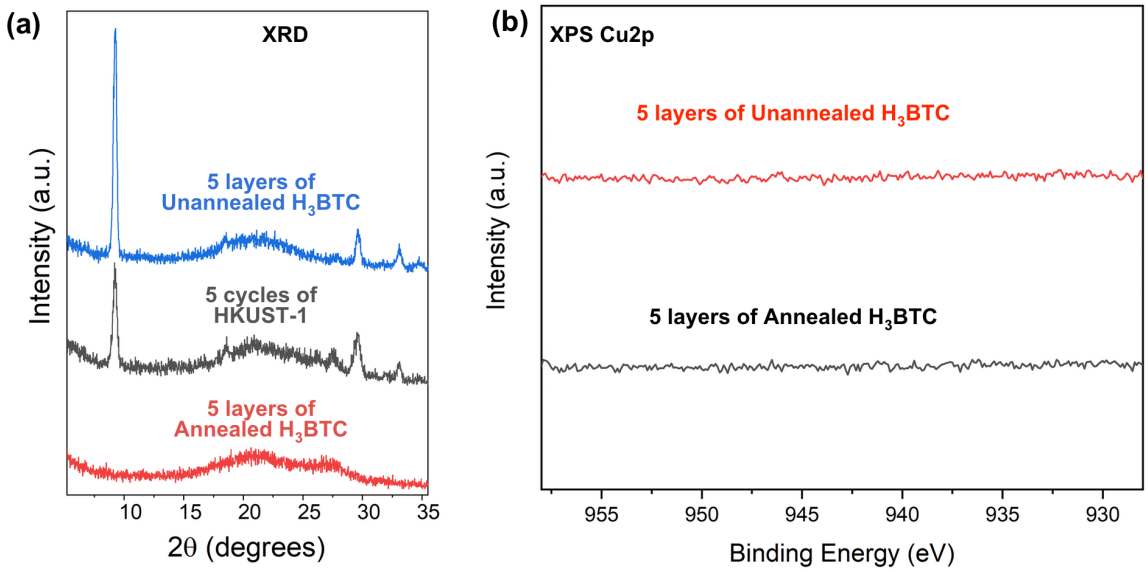


Figure D.2. (a) XRD patterns for the 5 layers of unannealed $H_3BTC$ (blue, 5 layers mean 5 times of $H_3BTC$ deposition for 3 minutes in each), the 5 cycles of HKUST-1 films (gray), and the 5 layers of annealed $H_3BTC$ at 343 K for 15 mins (red). (b) The Cu2p XPS spectra for 5 layers of unannealed (red) and annealed (black) $H_3BTC$

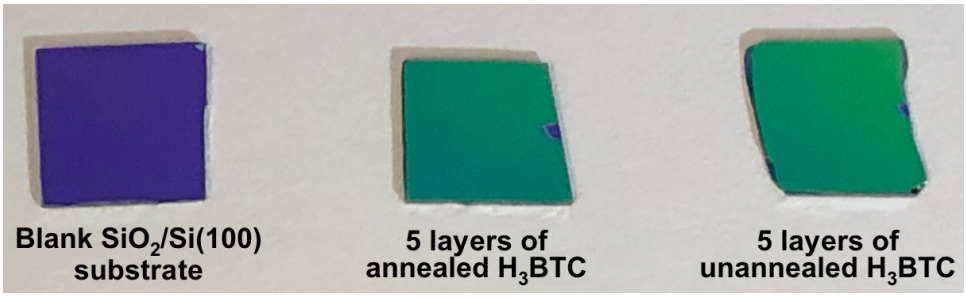


Figure D.3. Photographs of blank $SiO_2$/Si(100) substrate, 5 layers of annealed $H_3BTC$, and 5 layers of unannealed $H_3BTC$.

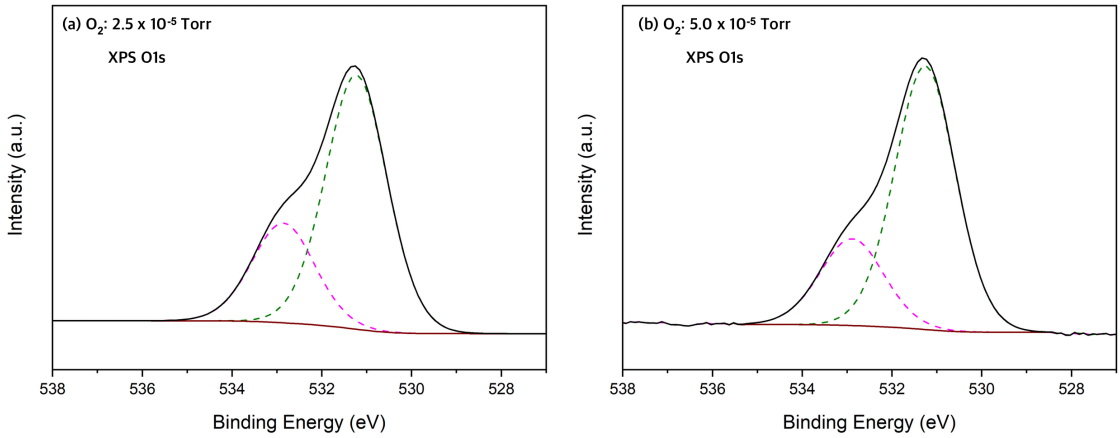


Figure D.4. The O1s XPS spectra for 5 cycled HKUST-1 thin films (1.0 ML Cu deposited in each cycle) grown with back-filled $O_2$ at (a) 2.5 x $10^{-5}$ Torr and (b) 5.0 x $10^{-5}$ Torr. There is no component for copper oxides in both spectra, which is typically located at 530.5 ~ 529.5 eV.

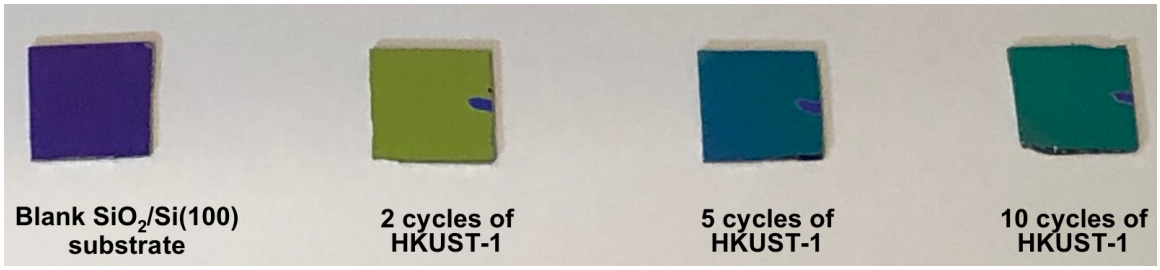


Figure D.5. Photographs of 2, 5, and 10 cycles of HKUST-1 films

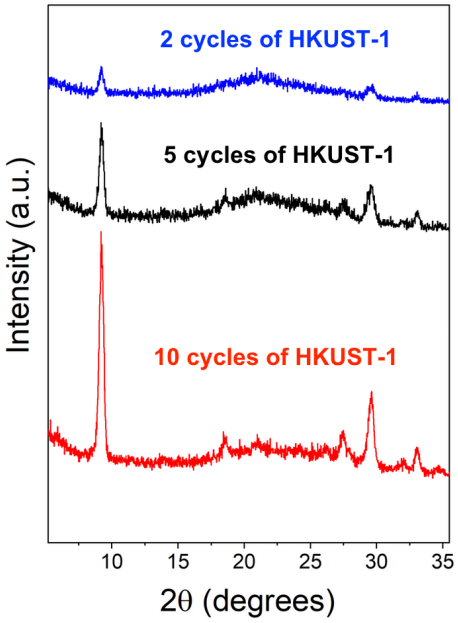


Figure D.6. XRD of 2, 5, and 10 cycles of HKUST-1 films.

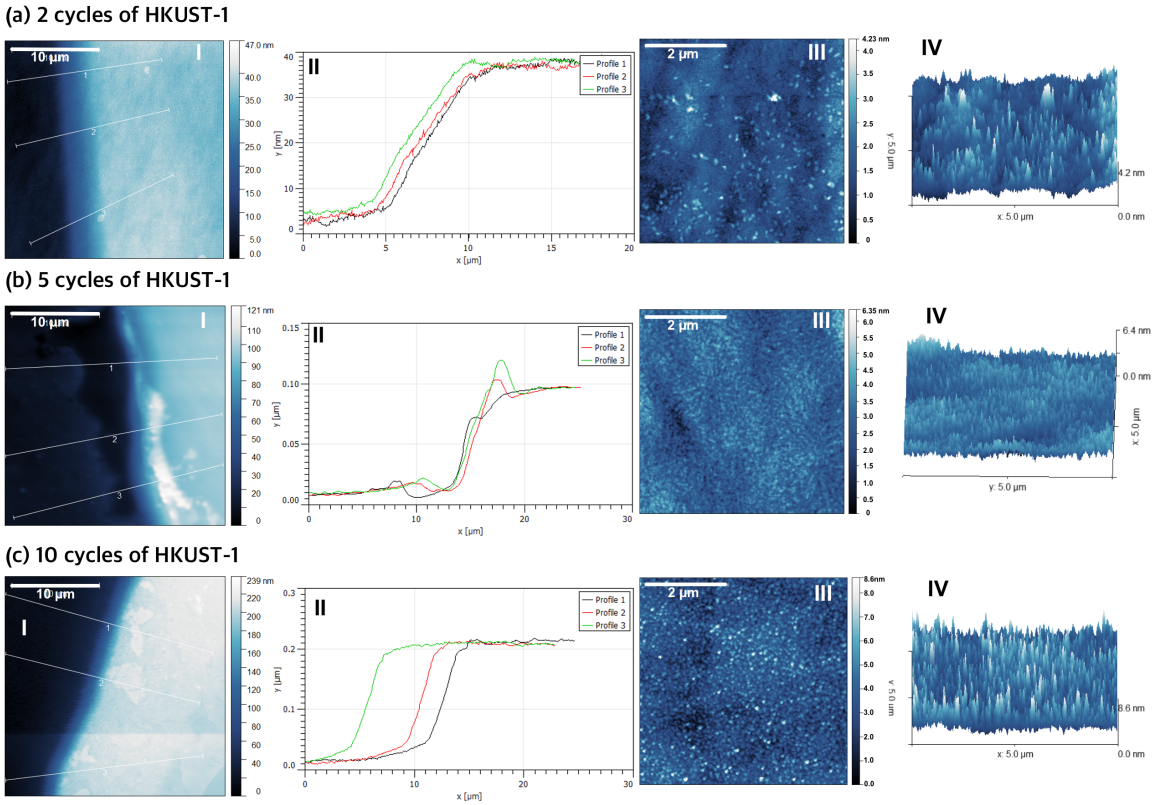


Figure D.7. AFM images of (a) 2 cycles, (b) 5 cycles, and (c) 10 cycles of HKUST-1 thin films. (I) and (II) show profiles for thickness, and III and IV describe top and lateral views of each sample respectively.

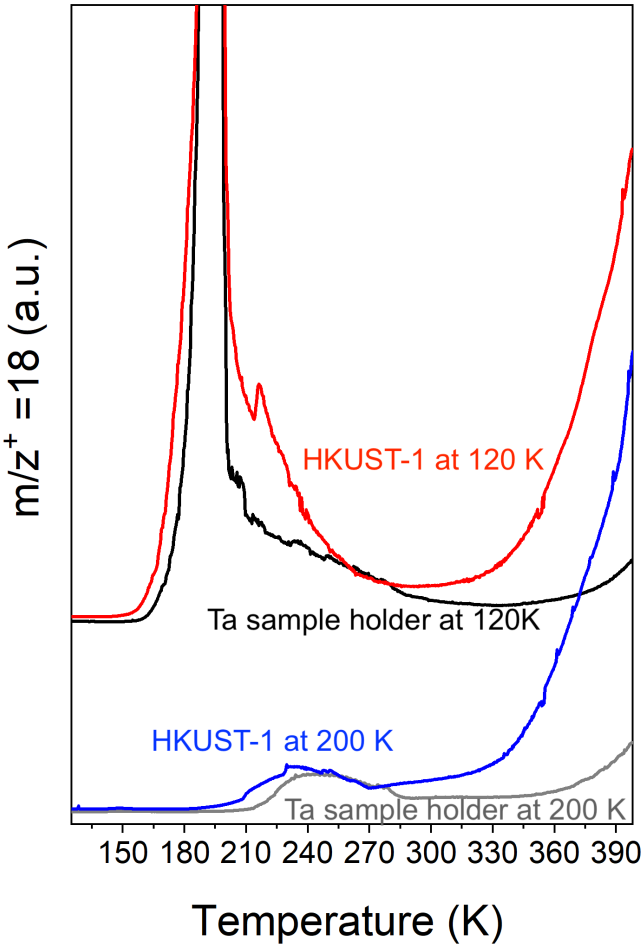


Figure D.8. Temperature programmed desorption (TPD) of $H_2O$ ($m/z^+$= 18) adsorbed on the 5 cycled HKUST-1 film at 120 K (red) and 200 K (blue) by 2.0 x $10^{-6}$ Torr of $H_2O$ for 30 mins. We also conducted the $H_2O$-TPD tests for the tantalum (Ta) sample holder with the same amount of $H_2O$ exposures at 120 K (black) and 200 K (gray).

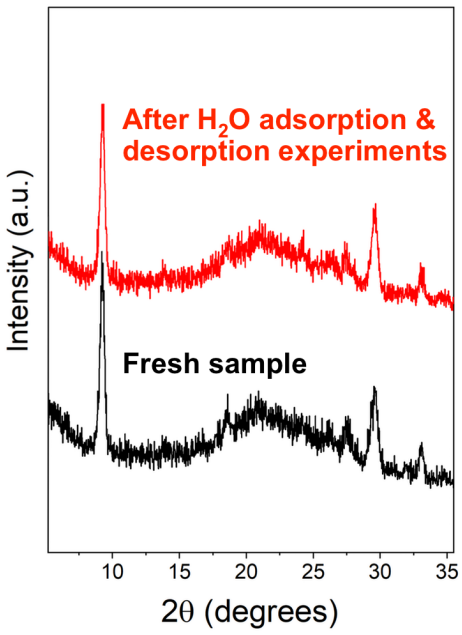


Figure D.9. XRD patterns of before (black) and after (red) $H_2O$ adsorption & desorption tests on the 5 cycled HKUST-1 thin film.

# Appendix E: Supporting Information for Methanol Oxidation Catalyzed by Copper Nanoclusters Incorporated in Vacuum-Deposited HKUST-1 Thin Films

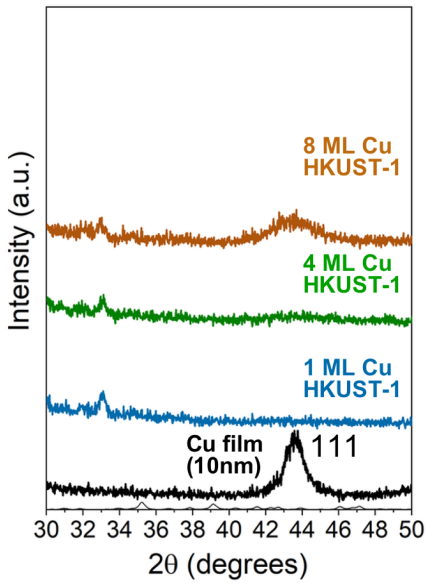


Figure E.1. XRD patterns of a polycrystalline Cu film (10 nm thick), 1 ML, 4 ML, and 8 ML Cu-HKUST-1 films in the range of 30° – 50° of 2θ.

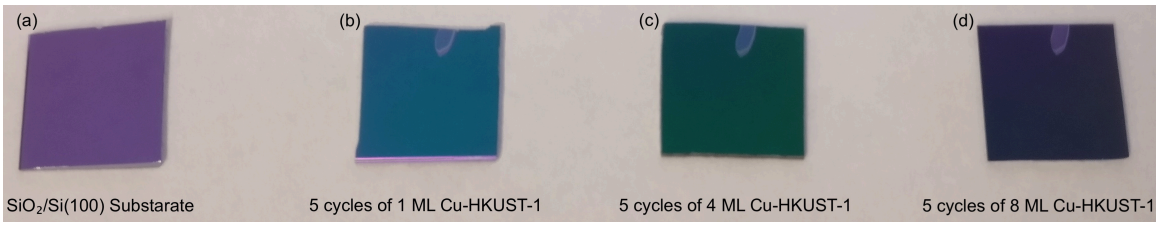


Figure E.2. Color variations of 5 cycled HKUST-1 thin films depending on the amount of deposited Cu. (a) SiO2/Si(100) substrate, (b) 5 cycles of 1 ML Cu-HKUST-1, (c) 5 cycles of 4 ML Cu-HKUST-1, and (d) 5 cycles of 8 ML Cu-HKUST-1.

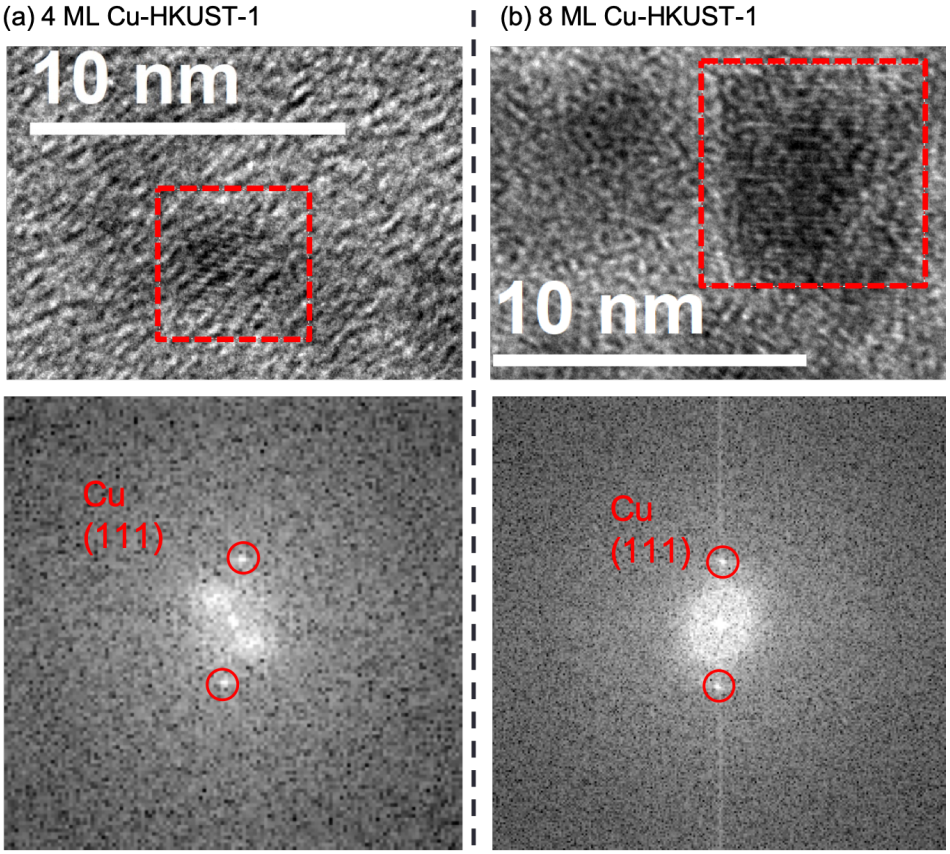


Figure E.3. Magnified TEM images of (a) 4 ML Cu-HKUST-1 (b) 8 ML Cu-HKUST-1 with FFT of their lattice fringes (red square box in each TEM images)

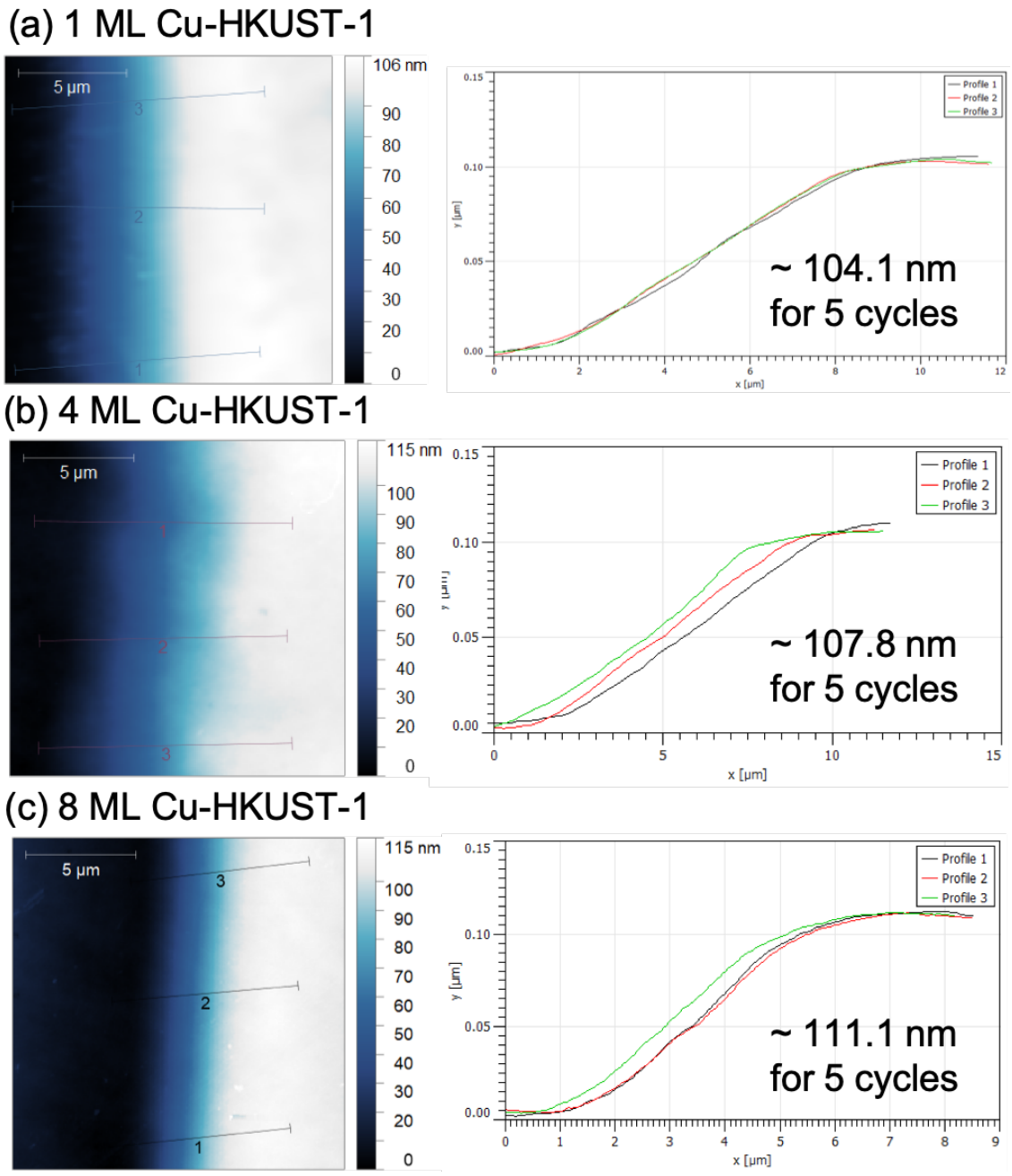


Figure E.4. The thickness of (a) 1 ML Cu-HKUST-1, (b) 4 ML Cu-HKUST-1, and (c) 8 ML Cu-HKUST-1 films (5 growth cycles in each film) measured by AFM.

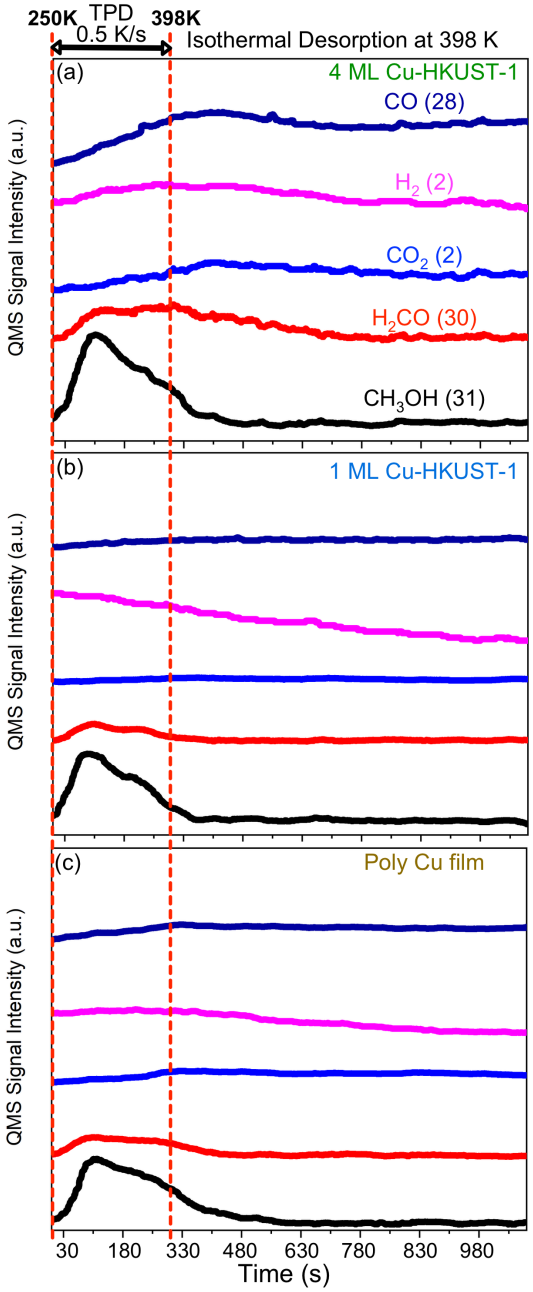


Figure E.5. The desorption spectra of $CH_3OH$ (black), $H_2CO$ (red), $CO_2$ ( blue), $H_2$ (magenta), CO (dark blue) from (a) 4 ML Cu-HKUST-1, (b) 1 ML Cu-HKUST-1 films (5 growth cycles in each), and (c) polycrystalline Cu film (10 nm thick). They were treated with 1.0 x $10^{-6}$ Torr of $O_2$ at 300 K for 3 minutes and then were exposed to 5.0 x $10^{-7}$ Torr of methanol at 250 K for 20 minutes. The sample were heated from 250 K to 398 K at a rate of 0.5 K/s, and they were isothermally held at 398 K for 15 minutes.

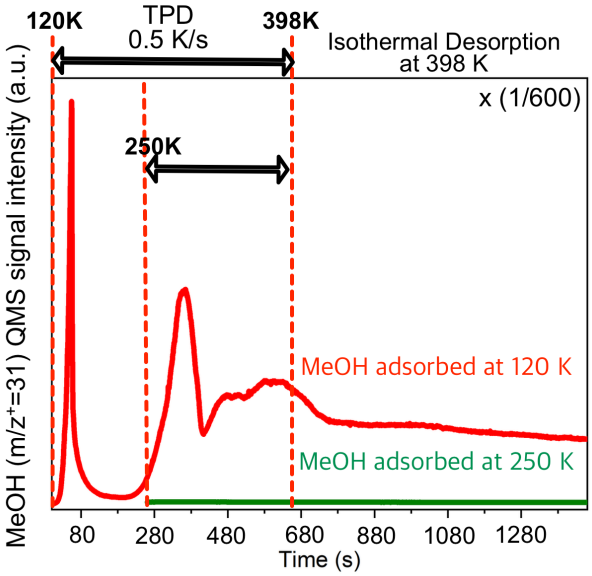


Figure E.6. The desorption spectra of $CH_3OH$ from the 5 cycled 4 ML Cu-HKUST-1 thin film. They were treated with 1.0 x $10^{-6}$ Torr of $O_2$ at 300 K for 3 minutes and then were exposed to 5.0 x $10^{-7}$ Torr of methanol at 120 K (red) and 250 K (green) for 20 minutes. The sample were heated from 120 K (red) and 250 K (green) to 398 K at a rate of 0.5 K/s, and they were isothermally held at 398 K for 15 minutes. The y-axis scale of this figure is 1/600 compared to other TPD spectra in this study.

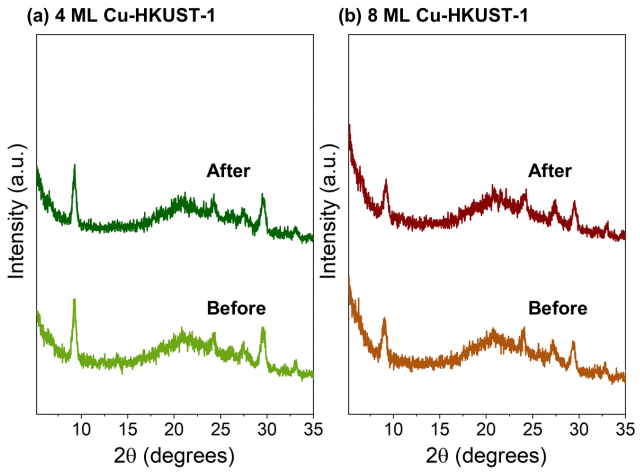


Figure E.7. XRD patterns regarding HKUST-1 structures on the 5 cycled 4 ML and 8 ML Cu-HKUST-1 thin films before and after the methanol oxidation experiment.

# References


(1) Bravo-Suárez, J. J.; Chaudhari, R. V.; Subramaniam, B. Design of Heterogeneous Catalysts for Fuels and Chemicals Processing: An Overview. In *ACS Symposium Series*; 2013; Vol. 1132, pp 3–68.

(2) Unnikrishnan, P.; Srinivas, D. Heterogeneous Catalysis. In *Industrial Catalytic Processes for Fine and Specialty Chemicals*; Elsevier, 2016; pp 41–111.

(3) Gao, F.; Goodman, D. W. Model Catalysts: Simulating the Complexities of Heterogeneous Catalysts. *Annu. Rev. Phys. Chem.* **2012**, *63*, 265–286.

(4) Gao, F.; Goodman, D. W. Pd–Au Bimetallic Catalysts: Understanding Alloy Effects from Planar Models and (Supported) Nanoparticles. *Chem. Soc. Rev.* **2012**, *41*, 8009.

(5) Chorkendorff, I.; Niemantsverdriet, J. W. *Concepts of Modern Catalysis and Kinetics*; Wiley, 2003.

(6) Ertl, G. Reactions at Surfaces: From Atoms to Complexity (Nobel Lecture). *Angew. Chemie - Int. Ed.* **2008**, *47*, 3524–3535.

(7) Ponec, V.; Bond, G. C. *Catalysis by Metals and Alloys*; Elsevier, 1995.

(8) Ponec, V. Alloy Catalysts: The Concepts. *Appl. Catal. A Gen.* **2001**, *222*, 31–45.

(9) Sinfelt, J. H. *Bimetallic Catalysts: Discoveries, Concepts, and Applications*; Exxon Monographs Series; Wiley, 1983.

(10) Edwards, J. K.; Hutchings, G. J. Palladium and Gold-Palladium Catalysts for the Direct Synthesis of Hydrogen Peroxide. *Angew. Chemie - Int. Ed.* **2008**, *47*, 9192–9198.

(11) Edwards, J. K.; Solsona, B.; N, E. N.; Carley, A. F.; Herzing, A. a; Kiely, C. J.; Hutchings, G. J. Switching Off Hydrogen Peroxide Hydrogenation in the Direct Synthesis Process. *Science* **2009**, *323*, 1037–1041.

(12) Wilson, N. M.; Priyadarshini, P.; Kunz, S.; Flaherty, D. W. Direct Synthesis of $H_2O_2$ on Pd and Au x Pd 1 Clusters: Understanding the Effects of Alloying Pd with Au. *J. Catal.* **2018**, *357*, 163–175.

(13) Kumar, D.; Chen, M. S.; Goodman, D. W. Synthesis of Vinyl Acetate on Pd-Based Catalysts. *Catal. Today* **2007**, *123*, 77–85.

(14) Han, Y.; Wanh, J.; Kumar, D.; Yan, Z.; Goodman, D. W. A Kinetic Study of Vinyl Acetate Synthesis over Pd-Based Catalysts: Kinetics of Vinyl Acetate Synthesis over Pd–Au/SiO and Pd/SiO Catalysts. *J. Catal.* **2005**, *232*, 467–475.

(15) Han, Y.-F.; Kumar, D.; Sivadinarayana, C.; Goodman, D. W. Kinetics of Ethylene Combustion in the Synthesis of Vinyl Acetate over a $Pd/SiO_2$ Catalyst. *J. Catal.* **2004**, *224*, 60–68.

(16) Kim, H. Y.; Henkelman, G. CO Adsorption-Driven Surface Segregation of Pd on Au/Pd Bimetallic Surfaces: Role of Defects and Effect on CO Oxidation. *ACS Catal.* **2013**, *3*, 2541–2546.

(17) Gao, F.; Wang, Y.; Goodman, D. W. CO Oxidation over AuPd(100) from Ultrahigh Vacuum to Near-Atmospheric Pressures: The Critical Role of Contiguous Pd Atoms. *J. Am. Chem. Soc.* **2009**, *131*, 5734–5735.

(18) Li, Z.; Gao, F.; Tysoe, W. T. Carbon Monoxide Oxidation over Au/Pd(100) Model Alloy Catalysts †. *J. Phys. Chem. C* **2010**, *114*, 16909–16916.

(19) Piednoir, A.; Languille, M. A.; Piccolo, L.; Valcarcel, A.; Cadete Santos. Aires, F. J.; Bertolini, J. C. Pd(111) versus Pd–Au(111) in Carbon Monoxide Oxidation under Elevated Pressures. *Catal. Letters* **2007**, *114*, 110–114.

(20) Venezia, A. M.; Liotta, L. F.; Pantaleo, G.; La Parola, V.; Deganello, G.; Beck, A.; Koppány, Z.; Frey, K.; Horváth, D.; Guczi, L. Activity of SiO2 Supported Gold-Palladium Catalysts in CO Oxidation. *Appl. Catal. A Gen.* **2003**, *251*, 359–368.

(21) Scott, R. W. J.; Sivadinarayana, C.; Wilson, O. M.; Yan, Z.; Goodman, D. W.; Crooks, R. M. Titania-Supported PdAu Bimetallic Catalysts Prepared from Dendrimer-Encapsulated Nanoparticle Precursors. *J. Am. Chem. Soc.* **2005**, *127*, 1380–1381.

(22) Xu, J.; White, T.; Li, P.; He, C.; Yu, J.; Yuan, W.; Han, Y.-F. Biphasic Pd−Au Alloy Catalyst for Low-Temperature CO Oxidation. *J. Am. Chem. Soc.* **2010**, *132*, 10398–10406.

(23) Hou, W.; Dehm, N. A.; Scott, R. W. J. Alcohol Oxidations in Aqueous Solutions Using Au, Pd, and Bimetallic AuPd Nanoparticle Catalysts. *J. Catal.* **2008**, *253*, 22–27.

(24) Enache, D. I.; Edwards, J. K.; Landon, P.; Solsona-Espriu, B.; Carley, A. F.; Herzing, A. A.; Watanabe, M.; Kiely, C. J.; Knight, D. W.; Hutchings, G. J. Solvent-Free Oxidation of Primary Alcohols to Aldehydes Using Au-Pd/TiO2 Catalysts. *Science* **2006**, *311*, 362–365.

(25) Tuteja, J.; Nishimura, S.; Choudhary, H.; Ebitani, K. Selective Oxidation of 1,6-Hexanediol to 6-Hydroxycaproic Acid over Reusable Hydrotalcite-Supported Au-Pd Bimetallic Catalysts. *ChemSusChem* **2015**, *8*, 1862–1866.

(26) Lee, A. F.; Gee, J. J.; Theyers, H. J. Aspects of Allylic Alcohol Oxidation—a Bimetallic Heterogeneous Selective Oxidation Catalyst. *Green Chem.* **2000**, *2*, 279–282.

(27) Chen, Y.; Lim, H.; Tang, Q.; Gao, Y.; Sun, T.; Yan, Q.; Yang, Y. Solvent-Free Aerobic Oxidation of Benzyl Alcohol over Pd Monometallic and Au-Pd

Bimetallic Catalysts Supported on SBA-16 Mesoporous Molecular Sieves. *Appl. Catal. A Gen.* **2010**, *380*, 55–65.

(28) Chen, M.; Kumar, D.; Yi, C.-W.; Goodman, D. W. The Promotional Effect of Gold in Catalysis by Palladium-Gold. *Science* **2005**, *310*, 291–293.

(29) Yu, W.-Y.; Mullen, G. M.; Flaherty, D. W.; Mullins, C. B. Selective Hydrogen Production from Formic Acid Decomposition on Pd–Au Bimetallic Surfaces. *J. Am. Chem. Soc.* **2014**, *136*, 11070–11078.

(30) Yu, W.-Y.; Mullen, G. M.; Mullins, C. B. Hydrogen Adsorption and Absorption with Pd–Au Bimetallic Surfaces. *J. Phys. Chem. C* **2013**, *117*, 19535–19543.

(31) Ogura, S.; Okada, M.; Fukutani, K. Near-Surface Accumulation of Hydrogen and CO Blocking Effects on a Pd–Au Alloy. *J. Phys. Chem. C* **2013**, *117*, 9366–9371.

(32) Lucci, F. R.; Darby, M. T.; Mattera, M. F. G.; Ivimey, C. J.; Therrien, A. J.; Michaelides, A.; Stamatakis, M.; Sykes, E. C. H. Controlling Hydrogen Activation, Spillover, and Desorption with Pd–Au Single-Atom Alloys. *J. Phys. Chem. Lett.* **2016**, *7*, 480–485.

(33) Furukawa, H.; Cordova, K. E.; O'Keeffe, M.; Yaghi, O. M. The Chemistry and Applications of Metal-Organic Frameworks. *Science* **2013**, *341*, 1230444–1230444.

(34) Chernikova, V.; Shekhah, O.; Eddaoudi, M. Advanced Fabrication Method for the Preparation of MOF Thin Films: Liquid-Phase Epitaxy Approach Meets Spin Coating Method. *ACS Appl. Mater. Interfaces* **2016**, *8*, 20459–20464.

(35) Chernikova, V.; Yassine, O.; Shekhah, O.; Eddaoudi, M.; Salama, K. N. Highly Sensitive and Selective SO 2 MOF Sensor: The Integration of MFM-300 MOF as a Sensitive Layer on a Capacitive Interdigitated Electrode. *J. Mater. Chem. A* **2018**, *6*, 5550–5554.

(36) Liu, J.; Wöll, C. Surface-Supported Metal–Organic Framework Thin Films: Fabrication Methods, Applications, and Challenges. *Chem. Soc. Rev.* **2017**, *46*, 5730–5770.

(37) Stassen, I.; Burtch, N.; Talin, A.; Falcaro, P.; Allendorf, M.; Ameloot, R. An Updated Roadmap for the Integration of Metal–Organic Frameworks with Electronic Devices and Chemical Sensors. *Chem. Soc. Rev.* **2017**, *46*, 3185–3241.

(38) Lu, G.; Hupp, J. T. Metal−Organic Frameworks as Sensors: A ZIF-8 Based Fabry−Pérot Device as a Selective Sensor for Chemical Vapors and Gases. *J. Am. Chem. Soc.* **2010**, *132*, 7832–7833.

(39) Galli, S.; Cimino, A.; Ivy, J. F.; Giacobbe, C.; Arvapally, R. K.; Vismara, R.; Checchia, S.; Rawshdeh, M. A.; Cardenas, C. T.; Yaseen, W. K.; Maspero, A.; Omary, M. A. Fluorous Metal–Organic Frameworks and Nonporous Coordination Polymers as Low-κ Dielectrics. *Adv. Funct. Mater.* **2019**, *29*, 1–11.

(40) Krishtab, M.; Stassen, I.; Stassin, T.; Cruz, A. J.; Okudur, O. O.; Armini, S.; Wilson, C.; De Gendt, S.; Ameloot, R. Vapor-Deposited Zeolitic Imidazolate Frameworks as Gap-Filling Ultra-Low-k Dielectrics. *Nat. Commun.* **2019**, *10*, 3729.

(41) Usman, M.; Mendiratta, S.; Lu, K. L. Semiconductor Metal–Organic Frameworks: Future Low-Bandgap Materials. *Adv. Mater.* **2017**, *29*, 1–5.

(42) Talin, A. A.; Centrone, A.; Ford, A. C.; Foster, M. E.; Stavila, V.; Haney, P.; Kinney, R. A.; Szalai, V.; El Gabaly, F.; Yoon, H. P.; Léonard, F.; Allendorf, M. D. Tunable Electrical Conductivity in Metal-Organic Framework Thin-Film Devices. *Science* **2014**, *343*, 66–69.

(43) Erickson, K. J.; Léonard, F.; Stavila, V.; Foster, M. E.; Spataru, C. D.; Jones, R. E.; Foley, B. M.; Hopkins, P. E.; Allendorf, M. D.; Talin, A. A. Thin Film Thermoelectric Metal-Organic Framework with High Seebeck Coefficient and Low Thermal Conductivity. *Adv. Mater.* **2015**, *27*, 3453–3459.

(44) Stavila, V.; Talin, A. A.; Allendorf, M. D. MOF-Based Electronic and Opto-Electronic Devices. *Chem. Soc. Rev.* **2014**, *43*, 5994–6010.

(45) Stassen, I.; Styles, M.; Grenci, G.; Gorp, H.; Vanderlinden, W.; Feyter, S.; Falcaro, P.; Vos, D. De; Vereecken, P.; Ameloot, R. Chemical Vapour Deposition of Zeolitic Imidazolate Framework Thin Films. *Nat. Mater.* **2016**, *15*, 304–310.

(46) Salmi, L. D.; Heikkilä, M. J.; Puukilainen, E.; Sajavaara, T.; Grosso, D.; Ritala, M. Studies on Atomic Layer Deposition of MOF-5 Thin Films. *Microporous Mesoporous Mater.* **2013**, *182*, 147–154.

(47) Lausund, K. B.; Petrovic, V.; Nilsen, O. All-Gas-Phase Synthesis of Amino-Functionalized UiO-66 Thin Films. *Dalt. Trans.* **2017**, *46*, 16983–16992.

(48) Lausund, K. B.; Nilsen, O. All-Gas-Phase Synthesis of UiO-66 through Modulated Atomic Layer Deposition. *Nat. Commun.* **2016**, *7*, 13578.

(49) Han, S.; Ciufo, R. A.; Meyerson, M. L.; Keitz, B. K.; Mullins, C. B. Solvent-Free Vacuum Growth of Oriented HKUST-1 Thin Films. *J. Mater. Chem. A* **2019**, *7*, 19396–19406.

(50) Kozachuk, O.; Yusenko, K.; Noei, H.; Wang, Y.; Walleck, S.; Glaser, T.; Fischer, R. a. Solvothermal Growth of a Ruthenium Metal–Organic Framework Featuring HKUST-1 Structure Type as Thin Films on Oxide Surfaces. *Chem. Commun.* **2011**, *47*, 8509.

(51) Prestipino, C.; Regli, L.; Vitillo, J. G.; Bonino, F.; Damin, A.; Lamberti, C.; Zecchina, A.; Solari, P. L.; Kongshaug, K. O.; Bordiga, S. Local Structure of Framework Cu(II) in HKUST-1 Metallorganic Framework: Spectroscopic Characterization upon Activation and Interaction with Adsorbates. *Chem. Mater.* **2006**, *18*, 1337–1346.

(52) Chui, S. S.-Y. A Chemically Functionalizable Nanoporous Material $[Cu_3(TMA)_2(H_2O)_3]N$. *Science* **1999**, *283*, 1148–1150.

(53) Hendon, C. H.; Walsh, A. Chemical Principles Underpinning the Performance of the Metal–Organic Framework HKUST-1. *Chem. Sci.* **2015**, *6*, 3674–3683.

(54) Liu, J.; Wang, Y.; Benin, A. I.; Jakubczak, P.; Willis, R. R.; LeVan, M. D. $CO_2/H_2$ Adsorption Equilibrium and Rates on Metal-Organic Frameworks: HKUST-1 and Ni/DOBDC. *Langmuir* **2010**, *26*, 14301–14307.

(55) Min Wang, Q.; Shen, D.; Bülow, M.; Ling Lau, M.; Deng, S.; Fitch, F. R.; Lemcoff, N. O.; Semanscin, J. Metallo-Organic Molecular Sieve for Gas Separation and Purification. *Microporous Mesoporous Mater.* **2002**, *55*, 217–230.

(56) Yang, Q.; Zhong, C. Electrostatic-Field-Induced Enhancement of Gas Mixture Separation in Metal-Organic Frameworks: A Computational Study. *ChemPhysChem* **2006**, *7*, 1417–1421.

(57) Wong-Foy, A. G.; Matzger, A. J.; Yaghi, O. M. Exceptional H2 Saturation Uptake in Microporous Metal-Organic Frameworks. *J. Am. Chem. Soc.* **2006**, *128*, 3494–3495.

(58) Wu, H.; Simmons, J. M.; Liu, Y.; Brown, C. M.; Wang, X.-S.; Ma, S.; Peterson, V. K.; Southon, P. D.; Kepert, C. J.; Zhou, H.-C.; Yildirim, T.; Zhou, W. Metal-Organic Frameworks with Exceptionally High Methane Uptake: Where and How Is Methane Stored? *Chem. - A Eur. J.* **2010**, *16*, 5205–5214.

(59) Alaerts, L.; Séguin, E.; Poelman, H.; Thibault-Starzyk, F.; Jacobs, P. A.; De Vos, D. E. Probing the Lewis Acidity and Catalytic Activity of the Metal–Organic Framework $[Cu_3(BTC)_2]$ (BTC=Benzene-1,3,5-Tricarboxylate). *Chem. - A Eur. J.* **2006**, *12*, 7353–7363.

(60) Jeong, N. C.; Samanta, B.; Lee, C. Y.; Farha, O. K.; Hupp, J. T. Coordination-Chemistry Control of Proton Conductivity in the Iconic Metal–Organic Framework Material HKUST-1. *J. Am. Chem. Soc.* **2012**, *134*, 51–54.

(61) Majano, G.; Martin, O.; Hammes, M.; Smeets, S.; Baerlocher, C.; Pérez-Ramírez, J. Solvent-Mediated Reconstruction of the Metal-Organic Framework HKUST-1 $(Cu_3(BTC)_2)$. *Adv. Funct. Mater.* **2014**, *24*, 3855–3865.

(62) Bradshaw, D.; Garai, A.; Huo, J. Metal–Organic Framework Growth at Functional Interfaces: Thin Films and Composites for Diverse Applications. *Chem. Soc. Rev.* **2012**, *41*, 2344–2381.

(63) Shekhah, O.; Liu, J.; Fischer, R. A.; Wöll, C. MOF Thin Films: Existing and Future Applications. *Chem. Soc. Rev.* **2011**, *40*, 1081.

(64) Biemmi, E.; Scherb, C.; Bein, T. Oriented Growth of the Metal Organic Framework $Cu_3(BTC)_2(H_2O)_3 \cdot x\ H_2O$ Tunable with Functionalized Self-Assembled Monolayers. *J. Am. Chem. Soc.* **2007**, *129*, 8054–8055.

(65) Shekhah, O.; Wang, H.; Kowarik, S.; Schreiber, F.; Paulus, M.; Tolan, M.; Sternemann, C.; Evers, F.; Zacher, D.; Fischer, R. A.; Wöll, C. Step-by-Step Route for the Synthesis of Metal−Organic Frameworks. *J. Am. Chem. Soc.* **2007**, *129*, 15118–15119.

(66) Zacher, D.; Baunemann, A.; Hermes, S.; Fischer, R. A. Deposition of Microcrystalline $[Cu_3(btc)_2]$ and $[Zn_2(bdc)_2(dabco)]$ at Alumina and Silica Surfaces Modified with Patterned Self Assembled Organic Monolayers: Evidence of Surface Selective and Oriented Growth. *J. Mater. Chem.* **2007**, *17*, 2785.

(67) Guo, Y.; Mao, Y.; Hu, P.; Ying, Y.; Peng, X. Self-Confined Synthesis of HKUST-1 Membranes from CuO Nanosheets at Room Temperature. *ChemistrySelect* **2016**, *1*, 108–113.

(68) Lemaire, P. C.; Zhao, J.; Williams, P. S.; Walls, H. J.; Shepherd, S. D.; Losego, M. D.; Peterson, G. W.; Parsons, G. N. Copper Benzenetricarboxylate Metal–Organic Framework Nucleation Mechanisms on Metal Oxide Powders and Thin Films Formed by Atomic Layer Deposition. *ACS Appl. Mater. Interfaces* **2016**, *8*, 9514–9522.

(69) Han, S.; Evans, E. J.; Mullen, G. M.; Mullins, C. B. $H_2O$-Improved $O_2$ Activation on the Pd–Au Bimetallic Surface. *Chem. Commun.* **2017**, *53*, 3990–3993.

(70) Han, S.; Mullins, C. B. Surface Alloy Composition Controlled $O_2$ Activation on Pd–Au Bimetallic Model Catalysts. *ACS Catal.* **2018**, *8*, 3641–3649.

(71) Han, S.; Shin, K.; Henkelman, G.; Mullins, C. B. Selective Oxidation of Acetaldehyde to Acetic Acid on Pd–Au Bimetallic Model Catalysts. *ACS Catal.* **2019**, *9*, 4360–4368.

(72) Zhang, G.; Wang, Y.; Wang, X.; Chen, Y.; Zhou, Y.; Tang, Y.; Lu, L.; Bao, J.; Lu, T. Preparation of Pd–Au/C Catalysts with Different Alloying Degree and Their Electrocatalytic Performance for Formic Acid Oxidation. *Appl. Catal. B Environ.* **2011**, *102*, 614–619.

(73) Dimitratos, N.; Villa A.; Wang, D.; Porta, F.; Su, D.; Prati, L. Pd and Pt Catalysts Modified by Alloying with Au in the Selective Oxidation of Alcohols. *J. Catal.* **2006**, *244*, 113–121.

(74) Edwards, J.; Solsona, B.; Landon, P.; Carley, A.; Herzing, A.; Kiely, C.; Hutchings, G. Direct Synthesis of Hydrogen Peroxide from $H_2$ and $O_2$ Using $TiO_2$-Supported Au–Pd Catalysts. *J. Catal.* **2005**, *236*, 69–79.

(75) Zhang, S.; Qing, M.; Zhang, H.; Tian, Y. Electrocatalytic Oxidation of Formic Acid on Functional MWCNTs Supported Nanostructured Pd–Au Catalyst. *Electrochem. commun.* **2009**, *11*, 2249–2252.

(76) Zhou, W.; Lee, J. Y. Highly Active Core-Shell Au@Pd Catalyst for Formic Acid Electrooxidation. *Electrochem. commun.* **2007**, *9*, 1725–1729.

(77) Yi, C.-W.; Luo, K.; Wei, T.; Goodman, D. W. The Composition and Structure of Pd−Au Surfaces. *J. Phys. Chem. B* **2005**, *109*, 18535–18540.

(78) Koel, B. E.; Sellidj, A.; Paffett, M. T. Ultrathin Films of Pd on Au(111): Evidence for Surface Alloy Formation. *Phys. Rev. B* **1992**, *46*, 7846–7856.

(79) Han, P.; Axnanda, S.; Lyubinetsky, I.; Goodman, D. W. Atomic-Scale Assembly of a Heterogeneous Catalytic Site. *J. Am. Chem. Soc.* **2007**, *129*, 14355–14361.

(80) Yu, W.-Y.; Zhang, L.; Mullen, G. M.; Henkelman, G.; Mullins, C. B. Oxygen Activation and Reaction on Pd–Au Bimetallic Surfaces. *J. Phys. Chem. C* **2015**, *119*, 11754–11762.

(81) Gao, F.; McClure, S. M.; Cai, Y.; Gath, K. K.; Wang, Y.; Chen, M. S.; Guo, Q. L.; Goodman, D. W. CO Oxidation Trends on Pt-Group Metals from Ultrahigh Vacuum to near Atmospheric Pressures: A Combined in Situ PM-IRAS and Reaction Kinetics Study. *Surf. Sci.* **2009**, *603*, 65–70.

(82) Gao, F.; Wang, Y.; Cai, Y.; Goodman, D. W. CO Oxidation on Pt-Group Metals from Ultrahigh Vacuum to Near Atmospheric Pressures. 2. Palladium and Platinum. *J. Phys. Chem. C* **2009**, *113*, 174–181.

(83) Flaherty, D. W.; Hahn, N. T.; Ferrer, D.; Engstrom, T. R.; Tanaka, P. L.; Mullins, C. B. Growth and Characterization of High Surface Area Titanium Carbide. *J. Phys. Chem. C* **2009**, *113*, 12742–12752.

(84) Matsushima, T. Dissociation of Oxygen Admolecules on Rh(111), Pt(111) and Pd(111) Surfaces at Low Temperatures. *Surf. Sci.* **1985**, *157*, 297–318.

(85) Kolasinski, K. W.; Cemic, F.; Hasselbrink, E. $O_2$/Pd(111). Clarification of the Correspondence between Thermal Desorption Features and Chemisorption States. *Chem. Phys. Lett.* **1994**, *219*, 113–117.

(86) Guo, X.; Hoffman, A.; Yates, J. T. Adsorption Kinetics and Isotopic Equilibration of Oxygen Adsorbed on the Pd(111) Surface. *J. Chem. Phys.* **1989**, *90*, 5787.

(87) Doering, D. L.; Madey, T. E. The Adsorption of Water on Clean and Oxygen-Dosed Ru(011). *Surf. Sci.* **1982**, *123*, 305–337.

(88) Ogasawara, H.; Yoshinobu, J.; Kawai, M. Water Adsorption on Pt(111): From Isolated Molecule to Three-Dimensional Cluster. *Chem. Phys. Lett.* **1994**, *231*, 188–192.

(89) Stuve, E. M.; Jorgensen, S. W.; Madix, R. J. The Adsorption of $H_2O$ on Clean and Oxygen-Covered Pd(100): Formation and Reaction of OH Groups. *Surf. Sci.* **1984**, *146*, 179–198.

(90) Clay, C.; Cummings, L.; Hodgson, A. Mixed Water/OH Structures on Pd(111). *Surf. Sci.* **2007**, *601*, 562–568.

(91) Tatarkhanov, M.; Ogletree, D. F.; Rose, F.; Mitsui, T.; Fomin, E.; Maier, S.; Rose, M.; Cerdá, J. I.; Salmeron, M. Metal- and Hydrogen-Bonding Competition during Water Adsorption on Pd(111) and Ru(0001). *J. Am. Chem. Soc.* **2009**, *131*, 18425–18434.

(92) Cerdá, J.; Michaelides, A.; Bocquet, M.-L.; Feibelman, P. J.; Mitsui, T.; Rose, M.; Fomin, E.; Salmeron, M. Novel Water Overlayer Growth on Pd(111) Characterized with Scanning Tunneling Microscopy and Density Functional Theory. *Phys. Rev. Lett.* **2004**, *93*, 116101.

(93) Ojifinni, R. A.; Froemming, N. S.; Gong, J.; Pan, M.; Kim, T. S.; White, J. M.; Henkelman, G.; Mullins, C. B. Water-Enhanced Low-Temperature CO Oxidation and Isotope Effects on Atomic Oxygen-Covered Au(111). *J. Am. Chem. Soc.* **2008**, *130*, 6801–6812.

(94) Guo, X.; Hoffman, A.; Yates, J. T. Adsorption Kinetics and Isotopic Equilibration of Oxygen Adsorbed on the Pd(111) Surface. *J. Chem. Phys.* **1989**, *90*, 5787–5792.

(95) Smith, R. S.; Huang, C.; Wong, E. K. L.; Kay, B. D. The Molecular Volcano: Abrupt $CCl_4$ Desorption Driven by the Crystallization of Amorphous Solid Water. *Phys. Rev. Lett.* **1997**, *79*, 909–912.

(96) McClure, S. M.; Safarik, D. J.; Truskett, T. M.; Mullins, C. B. Evidence That Amorphous Water below 160 K Is Not a Fragile Liquid. *J. Phys. Chem. B* **2006**, *110*, 11033–11036.

(97) Den Dunnen, A.; Van Der Niet, M. J. T. C.; Koper, M. T. M.; Juurlink, L. B. F. Interaction between $H_2O$ and Preadsorbed D on the Stepped Pt(553) Surface. *J. Phys. Chem. C* **2012**, *116*, 18706–18712.

(98) Pan, M.; Brush, A. J.; Pozun, Z. D.; Ham, H. C.; Yu, W.-Y.; Henkelman, G.; Hwang, G. S.; Mullins, C. B. Model Studies of Heterogeneous Catalytic Hydrogenation Reactions with Gold. *Chem. Soc. Rev.* **2013**, *42*, 5002–5013.

(99) Tao, F. Synthesis, Catalysis, Surface Chemistry and Structure of Bimetallic Nanocatalysts. *Chem. Soc. Rev.* **2012**, *41*, 7977.

(100) Chen, H.; Li, Y.; Zhang, F.; Zhang, G.; Fan, X. Graphene Supported Au-Pd Bimetallic Nanoparticles with Core-Shell Structures and Superior Peroxidase-like Activities. *J. Mater. Chem.* **2011**, *21*, 17658.

(101) Paalanen, P.; Weckhuysen, B. M.; Sankar, M. Progress in Controlling the Size, Composition and Nanostructure of Supported Gold–Palladium Nanoparticles for Catalytic Applications. *Catal. Sci. Technol.* **2013**, *3*, 2869.

(102) Kesavan, L.; Tiruvalam, R.; Rahim, M. H. A.; bin Saiman, M. I.; Enache, D. I.; Jenkins, R. L.; Dimitratos, N.; Lopez-Sanchez, J. A.; Taylor, S. H.; Knight, D. W.; Kiely, C. J.; Hutchings, G. J. Solvent-Free Oxidation of Primary Carbon-

Hydrogen Bonds in Toluene Using Au-Pd Alloy Nanoparticles. *Science* **2011**, *331*, 195–199.

(103) Pan, M.; Flaherty, D. W.; Mullins, C. B. Low-Temperature Hydrogenation of Acetaldehyde to Ethanol on H-Precovered Au(111). *J. Phys. Chem. Lett.* **2011**, *2*, 1363–1367.

(104) Gdowski, G. E.; Felter, T. E.; Stulen, R. H. Effect of Surface Temperature on the Sorption of Hydrogen by Pd(111). *Surf. Sci. Lett.* **1987**, *181*, L147–L155.

(105) Okuyama, H.; Siga, W.; Takagi, N.; Nishijima, M.; Aruga, T. Path and Mechanism of Hydrogen Absorption at Pd(100). *Surf. Sci.* **1998**, *401*, 344–354.

(106) Lucci, F. R.; Liu, J.; Marcinkowski, M. D.; Yang, M.; Allard, L. F.; Flytzani-Stephanopoulos, M.; Sykes, E. C. H. Selective Hydrogenation of 1,3-Butadiene on Platinum–Copper Alloys at the Single-Atom Limit. *Nat. Commun.* **2015**, *6*, 8550.

(107) Santana, J. A.; Rösch, N. Hydrogen Adsorption on and Spillover from Au- and Cu-Supported Pt3 and Pd3 Clusters: A Density Functional Study. *Phys. Chem. Chem. Phys.* **2012**, *14*, 16062.

(108) Evans, E. J.; Li, H.; Yu, W.-Y.; Mullen, G. M.; Henkelman, G.; Mullins, C. B. Mechanistic Insights on Ethanol Dehydrogenation on Pd–Au Model Catalysts: A Combined Experimental and DFT Study. *Phys. Chem. Chem. Phys.* **2017**, *19*, 30578–30589.

(109) Stuve, E. M.; Madix, R. J.; Brundle, C. R. CO Oxidation on Pd(100): A Study of the Coadsorption of Oxygen and Carbon Monoxide. *Surf. Sci.* **1984**, *146*, 155–178.

(110) Nyberg, C.; Uvdal, P. The Oxygen–Water Reaction on Pd(100): Observation of a Precursor Complex. *J. Chem. Phys.* **1986**, *84*, 4631–4635.

(111) Yu, W.-Y.; Zhang, L.; Mullen, G. M.; Evans, E. J.; Henkelman, G.; Mullins, C. B. Effect of Annealing in Oxygen on Alloy Structures of Pd–Au Bimetallic Model Catalysts. *Phys. Chem. Chem. Phys.* **2015**, *17*, 20588–20596.

(112) King, D. A.; Wells, M. G. Molecular Beam Investigation of Adsorption Kinetics on Bulk Metal Targets: Nitrogen on Tungsten. *Surf. Sci.* **1972**, *29*, 454–482.

(113) Davis, J. E.; Karseboom, S. G.; Nolan, P. D.; Mullins, C. B. Kinetics and Dynamics of the Initial Adsorption of Nitric Oxide on Ir(111). *J. Chem. Phys.* **1996**, *105*, 8362–8375.

(114) Kim, T. S.; Gong, J.; Ojifinni, R. a.; White, J. M.; Mullins, C. B. Water Activated by Atomic Oxygen on Au(111) to Oxidize CO at Low Temperatures. *J. Am. Chem. Soc.* **2006**, *128*, 6282–6283.

(115) Nolan, P. .; Lutz, B. .; Tanaka, P. .; Mullins, C. . Direct Verification of a High-Translational-Energy Molecular Precursor to Oxygen Dissociation on Pd(111). *Surf. Sci.* **1998**, *419*, L107–L113.

(116) Sjövall, P.; Uvdal, P. Oxygen Sticking on Pd(111): Double Precursors, Corrugation and Substrate Temperature Effects. *Chem. Phys. Lett.* **1998**, *282*, 355–360.

(117) Nolan, P. D.; Lutz, B. R.; Tanaka, P. L.; Davis, J. E.; Mullins, C. B. Translational Energy Selection of Molecular Precursors to Oxygen Adsorption on Pt(111). *Phys. Rev. Lett.* **1998**, *81*, 3179–3182.

(118) Nolan, P. D.; Lutz, B. R.; Tanaka, P. L.; Davis, J. E.; Mullins, C. B. Molecularly Chemisorbed Intermediates to Oxygen Adsorption on Pt(111): A Molecular Beam and Electron Energy-Loss Spectroscopy Study. *J. Chem. Phys.* **1999**, *111*, 3696.

(119) Nolan, P. .; Lutz, B. .; Tanaka, P. .; Meyer, R. .; Brown, S. .; Mullins, C. . Evidence of a Molecular Chemisorption-Mediated Mechanism for High Translational Energy Oxygen Adsorption on Pt(100)-Hex-R0.7°. *Chem. Phys. Lett.* **1999**, *309*, 111–116.

(120) Rettner, C. T.; Mullins, C. B. Dynamics of the Chemisorption of $O_2$ on Pt(111): Dissociation via Direct Population of a Molecularly Chemisorbed Precursor at High Incidence Kinetic Energy. *J. Chem. Phys.* **1991**, *94*, 1626–1635.

(121) Campbell, C. T.; Ertl, G.; Kuipers, H.; Segner, J. A Molecular Beam Study of the Adsorption and Desorption of Oxygen from a Pt(111) Surface. *Surf. Sci.* **1981**, *107*, 220–236.

(122) Davis, J. E.; Nolan, P. D.; Karseboom, S. G.; Mullins, C. B. Kinetics and Dynamics of the Dissociative Chemisorption of Oxygen on Ir(111). *J. Chem. Phys.* **1997**, *107*, 943–952.

(123) Wheeler, M. C.; Seets, D. C.; Mullins, C. B. Kinetics and Dynamics of the Initial Dissociative Chemisorption of Oxygen on Ru(001). *J. Chem. Phys.* **1996**, *105*, 1572–1583.

(124) Seets, D. C.; Wheeler, M. C.; Mullins, C. B. Trapping-Mediated and Direct Dissociative Chemisorption of Methane on Ir(110): A Comparison of Molecular Beam and Bulb Experiments. *J. Chem. Phys.* **1997**, *107*, 3986–3998.

(125) Mullins, C. B.; Weinberg, W. H. Dynamics of the Interaction of Ethane with Ir(110)-(1×2). *J. Vac. Sci. Technol. A Vacuum, Surfaces, Film.* **1990**, *8*, 2458–2462.

(126) Redhead, P. A. Thermal Desorption of Gases. *Vacuum* **1962**, *12*, 203–211.

(127) Kandoi, S.; Gokhale, A. A.; Grabow, L. C.; Dumesic, J. A.; Mavrikakis, M. Why Au and Cu Are More Selective Than Pt for Preferential Oxidation of CO at Low Temperature. *Catal. Letters* **2004**, *93*, 93–100.

(128) Su, H.; Yang, M.; Bao, X.; Li, W. The Effect of Water on the CO Oxidation on Ag(111) and Au(111) Surfaces: A First-Principle Study. *J. Phys. Chem. C* **2008**, *112*, 17303–17310.

(129) Li, Y.; Yu, Y.; Wang, J.-G.; Song, J.; Li, Q.; Dong, M.; Liu, C.-J. CO Oxidation over Graphene Supported Palladium Catalyst. *Appl. Catal. B Environ.* **2012**, *125*, 189–196.

(130) Pal, P.; Nayak, J. Acetic Acid Production and Purification: Critical Review Towards Process Intensification. *Sep. Purif. Rev.* **2017**, *46*, 44–61.

(131) Sano, K.; Uchida, H.; Wakabayashi, S. A New Process for Acetic Acid Production by Direct Oxidation of Ethylene. *Catal. Surv. from Asia* **1999**, *3*, 55–60.

(132) Chenier, P. J. *Survey of Industrial Chemistry*; Springer US: Boston, MA, 2002.

(133) Sunley, G. J.; Watson, D. J. High Productivity Methanol Carbonylation Catalysis Using Iridium. *Catal. Today* **2000**, *58*, 293–307.

(134) Yu, W.-Y.; Mullen, G. M.; Mullins, C. B. Interactions of Hydrogen and Carbon Monoxide on Pd–Au Bimetallic Surfaces. *J. Phys. Chem. C* **2014**, *118*, 2129–2137.

(135) Liu, X.; Xu, B.; Haubrich, J.; Madix, R. J.; Friend, C. M. Surface-Mediated Self-Coupling of Ethanol on Gold. *J. Am. Chem. Soc.* **2009**, *131*, 5757–5759.

(136) Davis, J. L.; Barteau, M. A. The Interactions of Oxygen with Aldehydes on the Pd(111) Surface. *Surf. Sci.* **1992**, *268*, 11–24.

(137) Davis, J. L.; Barteau, M. A. Hydrogen Bonding in Carboxylic Acid Adlayers on Pd(111): Evidence for Catemer Formation. *Langmuir* **1989**, *5*, 1299–1309.

(138) Li, Z.; Gao, F.; Tysoe, W. T. Surface Chemistry of Acetic Acid on Clean and Oxygen-Covered Pd(100). *Surf. Sci.* **2008**, *602*, 416–423.

(139) Kresse, G.; Furthmüller, J. Efficiency of Ab-Initio Total Energy Calculations for Metals and Semiconductors Using a Plane-Wave Basis Set. *Comput. Mater. Sci.* **1996**, *6*, 15–50.

(140) Blöchl, P. E. Projector Augmented-Wave Method. *Phys. Rev. B* **1994**, *50*, 17953–17979.

(141) Hammer, B.; Hansen, L.; Nørskov, J. Improved Adsorption Energetics within Density-Functional Theory Using Revised Perdew-Burke-Ernzerhof Functionals. *Phys. Rev. B* **1999**, *59*, 7413–7421.

(142) Monkhorst, H. J.; Pack, J. D. Special Points for Brillouin-Zone Integrations. *Phys. Rev. B* **1976**, *13*, 5188–5192.

(143) Shekhar, R.; Barteau, M. A.; Plank, R. V.; Vohs, J. M. Adsorption and Reaction of Aldehydes on Pd Surfaces. *J. Phys. Chem. B* **1997**, *101*, 7939–7951.

(144) Bowker, M.; Holroyd, R.; Perkins, N.; Bhantoo, J.; Counsell, J.; Carley, A.; Morgan, C. Acetaldehyde Adsorption and Catalytic Decomposition on Pd(110) and the Dissolution of Carbon. *Surf. Sci.* **2007**, *601*, 3651–3660.

(145) Kuhn, W. K.; Szanyi, J.; Goodman, D. W. CO Adsorption on Pd(111): The Effects of Temperature and Pressure. *Surf. Sci.* **1992**, *274*, L611–L618.

(146) Guo, X.; Yates, J. T. Dependence of Effective Desorption Kinetic Parameters on Surface Coverage and Adsorption Temperature: CO on Pd(111). *J. Chem. Phys.* **1989**, *90*, 6761–6766.

(147) Haley, R. D. R.; Tikhov, M. M. S.; Lambert, R. M. The Surface Chemistry of Acetic Acid on Pd{111}. *Catal. Letters* **2001**, *76*, 125–130.

(148) Li, Z.; Tysoe, W. T. The Adsorption of Acetic Acid on Clean and Oxygen-Covered Au/Pd(100) Alloy Surfaces. *Surf. Sci.* **2012**, *606*, 1934–1941.

(149) Li, Z.; Calaza, F.; Gao, F.; Tysoe, W. T. The Adsorption of Acetic Acid on Au/Pd(111) Alloy Surfaces. *Surf. Sci.* **2007**, *601*, 1351–1357.

(150) Davis, J. L.; Barteau, M. A. Polymerization and Decarbonylation Reactions of Aldehydes on the Pd( 11 1) Surface. *J. Am. Chem. Soc.* **1989**, *111*, 1782–1792.

(151) Zhao, D.; Timmons, D. J.; Yuan, D.; Zhou, H.-C. Tuning the Topology and Functionality of Metal-Organic Frameworks by Ligand Design. *Acc. Chem. Res.* **2011**, *44*, 123–133.

(152) Tranchemontagne, D. J.; Mendoza-Cortés, J. L.; O'Keeffe, M.; Yaghi, O. M. Secondary Building Units, Nets and Bonding in the Chemistry of Metal-Organic Frameworks. *Chem. Soc. Rev.* **2009**, *38*, 1257–1283.

(153) Suh, M. P.; Park, H. J.; Prasad, T. K.; Lim, D.-W. Hydrogen Storage in Metal-Organic Frameworks. *Chem. Rev.* **2012**, *112*, 782–835.

(154) Rosi, N. L.; Eckert, J.; Eddaoudi, M.; Vodak, D. T.; Kim, J.; O'Keeffe, M.; Yaghi, O. M. Hydrogen Storage in Microporous Metal-Organic Frameworks. *Science* **2003**, *300*, 1127–1129.

(155) Guo, Z.; Wu, H.; Srinivas, G.; Zhou, Y.; Xiang, S.; Chen, Z.; Yang, Y.; Zhou, W.; O'Keeffe, M.; Chen, B. A Metal-Organic Framework with Optimized Open Metal Sites and Pore Spaces for High Methane Storage at Room Temperature. *Angew. Chemie Int. Ed.* **2011**, *50*, 3178–3181.

(156) Ma, S.; Sun, D.; Simmons, J. M.; Collier, C. D.; Yuan, D.; Zhou, H.-C. Metal-Organic Framework from an Anthracene Derivative Containing Nanoscopic Cages Exhibiting High Methane Uptake. *J. Am. Chem. Soc.* **2008**, *130*, 1012–1016.

(157) Zhou, W.; Wu, H.; Yildirim, T. Enhanced $H_2$ Adsorption in Isostructural Metal-Organic Frameworks with Open Metal Sites: Strong Dependence of the Binding Strength on Metal Ions. *J. Am. Chem. Soc.* **2008**, *130*, 15268–15269.

(158) Montes-Andrés, H.; Orcajo, G.; Mellot-Draznieks, C.; Martos, C.; Botas, J. A.; Calleja, G. Novel Ni-IRMOF-74 Postsynthetically Functionalized for $H_2$ Storage Applications. *J. Phys. Chem. C* **2018**, *122*, 28123–28132.

(159) Kumar, K. V.; Preuss, K.; Titirici, M. M.; Rodríguez-Reinoso, F. Nanoporous Materials for the Onboard Storage of Natural Gas. *Chem. Rev.* **2017**, *117*, 1796–1825.

(160) Yazaydın, A. O.; Snurr, R. Q.; Park, T.-H.; Koh, K.; Liu, J.; LeVan, M. D.; Benin, A. I.; Jakubczak, P.; Lanuza, M.; Galloway, D. B.; Low, J. J.; Willis, R. R. Screening of Metal−Organic Frameworks for Carbon Dioxide Capture from Flue Gas Using a Combined Experimental and Modeling Approach. *J. Am. Chem. Soc.* **2009**, *131*, 18198–18199.

(161) Sumida, K.; Rogow, D. L.; Mason, J. a; McDonald, T. M.; Bloch, E. D.; Herm, Z. R.; Bae, T.-H.; Long, J. R. Carbon Dioxide Capture in Metal-Organic Frameworks. *Chem. Rev.* **2012**, *112*, 724–781.

(162) Lee, W. R.; Hwang, S. Y.; Ryu, D. W.; Lim, K. S.; Han, S. S.; Moon, D.; Choi, J.; Hong, C. S. Diamine-Functionalized Metal–Organic Framework: Exceptionally High $CO_2$ Capacities from Ambient Air and Flue Gas, Ultrafast $CO_2$ Uptake Rate, and Adsorption Mechanism. *Energy Environ. Sci.* **2014**, *7*, 744–751.

(163) Ding, M.; Flaig, R. W.; Jiang, H.-L.; Yaghi, O. M. Carbon Capture and Conversion Using Metal–Organic Frameworks and MOF-Based Materials. *Chem. Soc. Rev.* **2019**, *48*, 2783–2828.

(164) Bhatt, P. M.; Belmabkhout, Y.; Cadiau, A.; Adil, K.; Shekhah, O.; Shkurenko, A.; Barbour, L. J.; Eddaoudi, M. A Fine-Tuned Fluorinated MOF Addresses the Needs for Trace $CO_2$ Removal and Air Capture Using Physisorption. *J. Am. Chem. Soc.* **2016**, *138*, 9301–9307.

(165) Herm, Z. R.; Wiers, B. M.; Mason, J. a; van Baten, J. M.; Hudson, M. R.; Zajdel, P.; Brown, C. M.; Masciocchi, N.; Krishna, R.; Long, J. R. Separation of Hexane Isomers in a Metal-Organic Framework with Triangular Channels. *Science* **2013**, *340*, 960–964.

(166) Bloch, E. D.; Queen, W. L.; Krishna, R.; Zadrozny, J. M.; Brown, C. M.; Long, J. R. Hydrocarbon Separations in a Metal-Organic Framework with Open Iron(II) Coordination Sites. *Science* **2012**, *335*, 1606–1610.

(167) Bae, Y.-S.; Lee, C. Y.; Kim, K. C.; Farha, O. K.; Nickias, P.; Hupp, J. T.; Nguyen, S. T.; Snurr, R. Q. High Propene/Propane Selectivity in Isostructural Metal-Organic Frameworks with High Densities of Open Metal Sites. *Angew. Chemie Int. Ed.* **2012**, *51*, 1857–1860.

(168) Wang, H.; Dong, X.; Lin, J.; Teat, S. J.; Jensen, S.; Cure, J.; Alexandrov, E. V.; Xia, Q.; Tan, K.; Wang, Q.; Olson, D. H.; Proserpio, D. M.; Chabal, Y. J.; Thonhauser, T.; Sun, J.; Han, Y.; Li, J. Topologically Guided Tuning of Zr-MOF Pore Structures for Highly Selective Separation of C6 Alkane Isomers. *Nat. Commun.* **2018**, *9*, 1–11.

(169) Xue, D.-X.; Belmabkhout, Y.; Shekhah, O.; Jiang, H.; Adil, K.; Cairns, A. J.; Eddaoudi, M. Tunable Rare Earth Fcu -MOF Platform: Access to Adsorption Kinetics Driven Gas/Vapor Separations via Pore Size Contraction. *J. Am. Chem. Soc.* **2015**, *137*, 5034–5040.

(170) Guo, Q.; Ren, L.; Kumar, P.; Cybulskis, V. J.; Mkhoyan, K. A.; Davis, M. E.; Tsapatsis, M. A Chromium Hydroxide/MIL-101(Cr) MOF Composite Catalyst and Its Use for the Selective Isomerization of Glucose to Fructose. *Angew. Chemie Int. Ed.* **2018**, *57*, 4926–4930.

(171) Sun, M. H.; Huang, S. Z.; Chen, L. H.; Li, Y.; Yang, X. Y.; Yuan, Z. Y.; Su, B. L. Applications of Hierarchically Structured Porous Materials from Energy Storage and Conversion, Catalysis, Photocatalysis, Adsorption, Separation, and Sensing to Biomedicine. *Chem. Soc. Rev.* **2016**, *45*, 3479–3563.

(172) Otake, K.; Cui, Y.; Buru, C. T.; Li, Z.; Hupp, J. T.; Farha, O. K. Single-Atom-Based Vanadium Oxide Catalysts Supported on Metal–Organic Frameworks: Selective Alcohol Oxidation and Structure–Activity Relationship. *J. Am. Chem. Soc.* **2018**, *140*, 8652–8656.

(173) Shen, K.; Chen, X.; Chen, J.; Li, Y. Development of MOF-Derived Carbon-Based Nanomaterials for Efficient Catalysis. *ACS Catal.* **2016**, *6*, 5887–5903.

(174) Rogge, S. M. J.; Bavykina, A.; Hajek, J.; Garcia, H.; Olivos-Suarez, A. I.; Sepúlveda-Escribano, A.; Vimont, A.; Clet, G.; Bazin, P.; Kapteijn, F.; Daturi, M.; Ramos-Fernandez, E. V.; Llabrés i Xamena, F. X.; Van Speybroeck, V.; Gascon, J. Metal–Organic and Covalent Organic Frameworks as Single-Site Catalysts. *Chem. Soc. Rev.* **2017**, *46*, 3134–3184.

(175) Han, S.; Kim, H.; Kim, J.; Jung, Y. Modulating Magnetic Behavior of Fe-MOF-74 by High Electron Affinity of the Guest Molecule. *Phys. Chem. Chem. Phys.* **2015**, *17*, 16977–16982.

(176) Kurmoo, M. Magnetic Metal-Organic Frameworks. *Chem. Soc. Rev.* **2009**, *38*, 1353–1379.

(177) Dechambenoit, P.; Long, J. R. Microporous Magnets. *Chem. Soc. Rev.* **2011**, *40*, 3249–3265.

(178) Halder, G. J. Guest-Dependent Spin Crossover in a Nanoporous Molecular Framework Material. *Science* **2002**, *298*, 1762–1765.

(179) Stassen, I.; Bueken, B.; Reinsch, H.; Oudenhoven, J. F. M.; Wouters, D.; Hajek, J.; Van Speybroeck, V.; Stock, N.; Vereecken, P. M.; Van Schaijk, R.; De Vos, D.; Ameloot, R. Towards Metal–Organic Framework Based Field Effect Chemical Sensors: UiO-66-$NH_2$ for Nerve Agent Detection. *Chem. Sci.* **2016**, *7*, 5827–5832.

(180) Robinson, A. L.; Stavila, V.; Zeitler, T. R.; White, M. I.; Thornberg, S. M.; Greathouse, J. A.; Allendorf, M. D. Ultrasensitive Humidity Detection Using Metal–Organic Framework-Coated Microsensors. *Anal. Chem.* **2012**, *84*, 7043–7051.

(181) Ke, F.; Yuan, Y.-P.; Qiu, L.-G.; Shen, Y.-H.; Xie, A.-J.; Zhu, J.-F.; Tian, X.-Y.; Zhang, L.-D. Facile Fabrication of Magnetic Metal–Organic Framework Nanocomposites for Potential Targeted Drug Delivery. *J. Mater. Chem.* **2011**, *21*, 3843.

(182) Ariga, K.; Lvov, Y. M.; Kawakami, K.; Ji, Q.; Hill, J. P. Layer-by-Layer Self-Assembled Shells for Drug Delivery. *Adv. Drug Deliv. Rev.* **2011**, *63*, 762–771.

(183) Shete, M.; Kumar, P.; Bachman, J. E.; Ma, X.; Smith, Z. P.; Xu, W.; Mkhoyan, K. A.; Long, J. R.; Tsapatsis, M. On the Direct Synthesis of Cu(BDC) MOF Nanosheets and Their Performance in Mixed Matrix Membranes. *J. Memb. Sci.* **2018**, *549*, 312–320.

(184) Ranjan, R.; Tsapatsis, M. Microporous Metal Organic Framework Membrane on Porous Support Using the Seeded Growth Method. *Chem. Mater.* **2009**, *21*, 4920–4924.

(185) Ma, X.; Kumar, P.; Mittal, N.; Khlyustova, A.; Daoutidis, P.; Mkhoyan, K. A.; Tsapatsis, M. Zeolitic Imidazolate Framework Membranes Made by Ligand-Induced Permselectivation. *Science* **2018**, *361*, 1008–1011.

(186) Sapsanis, C.; Omran, H.; Chernikova, V.; Shekhah, O.; Belmabkhout, Y.; Buttner, U.; Eddaoudi, M.; Salama, K. Insights on Capacitive Interdigitated Electrodes Coated with MOF Thin Films: Humidity and VOCs Sensing as a Case Study. *Sensors* **2015**, *15*, 18153–18166.

(187) Bouchaala, A.; Jaber, N.; Yassine, O.; Shekhah, O.; Chernikova, V.; Eddaoudi, M.; Younis, M. Nonlinear-Based MEMS Sensors and Active Switches for Gas Detection. *Sensors* **2016**, *16*, 758.

(188) Stassen, I.; Styles, M.; Grenci, G.; Gorp, H. Van; Vanderlinden, W.; Feyter, S. De; Falcaro, P.; Vos, D. De; Vereecken, P.; Ameloot, R. Chemical Vapour Deposition of Zeolitic Imidazolate Framework Thin Films. *Nat. Mater.* **2016**, *15*, 304–310.

(189) Stassen, I.; De Vos, D.; Ameloot, R. Vapor-Phase Deposition and Modification of Metal-Organic Frameworks: State-of-the-Art and Future Directions. *Chem. - A Eur. J.* **2016**, *22*, 14452–14460.

(190) Keitz, B. K.; Yu, C. J.; Long, J. R.; Ameloot, R. Lithographic Deposition of Patterned Metal-Organic Framework Coatings Using a Photobase Generator. *Angew. Chemie Int. Ed.* **2014**, *53*, 5561–5565.

(191) Fabris, S.; Stepanow, S.; Lin, N.; Gambardella, P.; Dmitriev, A.; Honolka, J.; Baroni, S.; Kern, K. Oxygen Dissociation by Concerted Action of Di-Iron Centers in Metal–Organic Coordination Networks at Surfaces: Modeling Non-Heme Iron Enzymes. *Nano Lett.* **2011**, *11*, 5414–5420.

(192) Sheberla, D.; Sun, L.; Blood-Forsythe, M. A.; Er, S.; Wade, C. R.; Brozek, C. K.; Aspuru-Guzik, A.; Dincă, M. High Electrical Conductivity in $Ni_3$(2,3,6,7,10,11-hexaiminotriphenylene)$_2$ , a Semiconducting Metal–Organic Graphene Analogue. *J. Am. Chem. Soc.* **2014**, *136*, 8859–8862.

(193) Sakamoto, R.; Takada, K.; Pal, T.; Maeda, H.; Kambe, T.; Nishihara, H. Coordination Nanosheets (CONASHs): Strategies, Structures and Functions. *Chem. Commun.* **2017**, *53*, 5781–5801.

(194) Sheerin, G.; Cafolla, A. A. Self-Assembled Structures of Trimesic Acid on the Ag/Si(1 1 1)-(√3 × √3)R30° Surface. *Surf. Sci.* **2005**, *577*, 211–219.

(195) Kolotuchin, S. V; Fenlon, E. E.; Wilson, S. R.; Loweth, C. J.; Zimmerman, S. C. Self-Assembly of 1,3,5-Benzenetricarboxylic Acids(Trimesic Acids) and Several Analogues in the Solid State. *Angew. Chemie Int. Ed.* **1996**, *34*, 2654–2657.

(196) Classen, T.; Lingenfelder, M.; Wang, Y.; Chopra, R.; Virojanadara, C.; Starke, U.; Costantini, G.; Fratesi, G.; Fabris, S.; de Gironcoli, S.; Baroni, S.; Haq, S.; Raval, R.; Kern, K. Hydrogen and Coordination Bonding Supramolecular Structures of Trimesic Acid on Cu(110) †. *J. Phys. Chem. A* **2007**, *111*, 12589–12603.

(197) Kolotuchin, S. V.; Thiessen, P. A.; Fenlon, E. E.; Wilson, S. R.; Loweth, C. J.; Zimmerman, S. C. Self-Assembly of 1,3,5-Benzenetricarboxylic (Trimesic) Acid and Its Analogues. *Chem. - A Eur. J.* **1999**, *5*, 2537–2547.

(198) Nath, K. G.; Ivasenko, O.; Miwa, J. A.; Dang, H.; Wuest, J. D.; Nanci, A.; Perepichka, D. F.; Rosei, F. Rational Modulation of the Periodicity in Linear Hydrogen-Bonded Assemblies of Trimesic Acid on Surfaces. *J. Am. Chem. Soc.* **2006**, *128*, 4212–4213.

(199) Lackinger, M.; Griessl, S.; Kampschulte, L.; Jamitzky, F.; Heckl, W. M. Dynamics of Grain Boundaries in Two-Dimensional Hydrogen-Bonded Molecular Networks. *Small* **2005**, *1*, 532–539.

(200) Cebula, I.; Lu, H.; Zharnikov, M.; Buck, M. Monolayers of Trimesic and Isophthalic Acid on Cu and Ag: The Influence of Coordination Strength on Adsorption Geometry. *Chem. Sci.* **2013**, *4*, 4455.

(201) Griessl, S.; Lackinger, M.; Edelwirth, M.; Hietschold, M.; Heckl, W. M. Self-Assembled Two-Dimensional Molecular Host-Guest Architectures From Trimesic Acid. *Single Mol.* **2002**, *3*, 25–31.

(202) Messina, P.; Dmitriev, A.; Lin, N.; Spillmann, H.; Abel, M.; Barth, J. V.; Kern, K. Direct Observation of Chiral Metal-Organic Complexes Assembled on a Cu(100) Surface. *J. Am. Chem. Soc.* **2002**, *124*, 14000–14001.

(203) Jee, K. Y.; Kim, J. S.; Kim, J.; Lee, Y. T. Effect of Hydrophilic $Cu_3(BTC)_2$ Additives on the Performance of PVDF Membranes for Water Flux Improvement. *Desalin. Water Treat.* **2016**, *57*, 17637–17645.

(204) Peng, B.; Feng, C.; Liu, S.; Zhang, R. Synthesis of CuO Catalyst Derived from HKUST-1 Temple for the Low-Temperature $NH_3$-SCR Process. *Catal. Today* **2018**, *314*, 122–128.

(205) Chen, H.; Wang, L.; Yang, J.; Yang, R. T. Investigation on Hydrogenation of Metal–Organic Frameworks HKUST-1, MIL-53, and ZIF-8 by Hydrogen Spillover. *J. Phys. Chem. C* **2013**, *117*, 7565–7576.

(206) Wang, Y.; Lü, Y.; Zhan, W.; Xie, Z.; Kuang, Q.; Zheng, L. Synthesis of Porous $Cu_2O$/CuO Cages Using Cu-Based Metal-Organic Frameworks as Templates and Their Gas-Sensing Properties. *J. Mater. Chem. A* **2015**, *3*, 12796–12803.

(207) Niu, H.; Liu, S.; Cai, Y.; Wu, F.; Zhao, X. MOF Derived Porous Carbon Supported Cu/$Cu_2O$ Composite as High Performance Non-Noble Catalyst. *Microporous Mesoporous Mater.* **2016**, *219*, 48–53.

(208) Hall, A. S.; Kondo, A.; Maeda, K.; Mallouk, T. E. Microporous Brookite-Phase Titania Made by Replication of a Metal–Organic Framework. *J. Am. Chem. Soc.* **2013**, *135*, 16276–16279.

(209) Shekhah, O.; Liu, J.; Fischer, R. A.; Wöll, C. MOF Thin Films: Existing and Future Applications. *Chem. Soc. Rev.* **2011**, *40*, 1081–1106.

(210) Di Credico, B.; Redaelli, M.; Bellardita, M.; Calamante, M.; Cepek, C.; Cobani, E.; D'Arienzo, M.; Evangelisti, C.; Marelli, M.; Moret, M.; Palmisano, L.; Scotti, R. Step-by-Step Growth of HKUST-1 on Functionalized $TiO_2$ Surface: An Efficient Material for $CO_2$ Capture and Solar Photoreduction. *Catalysts* **2018**, *8*, 353.

(211) Jiang, P.; Prendergast, D.; Borondics, F.; Porsgaard, S.; Giovanetti, L.; Pach, E.; Newberg, J.; Bluhm, H.; Besenbacher, F.; Salmeron, M. Experimental and Theoretical Investigation of the Electronic Structure of $Cu_2O$ and CuO Thin Films on Cu(110) Using x-Ray Photoelectron and Absorption Spectroscopy. *J. Chem. Phys.* **2013**, *138*, 024704.

(212) Dan, Z.; Yang, Y.; Qin, F.; Wang, H.; Chang, H. Facile Fabrication of $Cu_2O$ Nanobelts in Ethanol on Nanoporous Cu and Their Photodegradation of Methyl Orange. *Materials.* **2018**, *11*, 446.

(213) Als-Nielsen, J.; Jacquemain, D.; Kjaer, K.; Leveiller, F.; Lahav, M.; Leiserowitz, L. Principles and Applications of Grazing Incidence X-Ray and Neutron Scattering from Ordered Molecular Monolayers at the Air-Water Interface. *Phys. Rep.* **1994**, *246*, 251–313.

(214) Inaba, K.; Kobayashi, S.; Uehara, K.; Okada, A.; Reddy, S. L.; Endo, T. High Resolution X-Ray Diffraction Analyses of (La,Sr)$MnO_3$/ZnO/Sapphire(0001) Double Heteroepitaxial Films. *Adv. Mater. Phys. Chem.* **2013**, *3*, 72–89.

(215) Bouroushian, M.; Kosanovic, T. Characterization of Thin Films by Low Incidence X-Ray Diffraction. *Cryst. Struct. Theory Appl.* **2012**, *01*, 35–39.

(216) Cebula, I.; Shen, C.; Buck, M. Isophthalic Acid: A Basis for Highly Ordered Monolayers. *Angew. Chemie Int. Ed.* **2010**, *49*, 6220–6223.

(217) Kanninen, L.; Jokinen, N.; Ali-Löytty, H.; Jussila, P.; Lahtonen, K.; Hirsimäki, M.; Valden, M.; Kuzmin, M.; Pärna, R.; Nõmmiste, E. Adsorption Structure and Bonding of Trimesic Acid on Cu(100). *Surf. Sci.* **2011**, *605*, 1968–1978.

(218) Dmitriev, A.; Lin, N.; Weckesser, J.; Barth, J. V.; Kern, K. Supramolecular Assemblies of Trimesic Acid on a Cu(100) Surface. *J. Phys. Chem. B* **2002**, *106*, 6907–6912.

(219) Xie, G.; Forslund, M.; Pan, J. Direct Electrochemical Synthesis of Reduced Graphene Oxide (RGO)/Copper Composite Films and Their Electrical/Electroactive Properties. *ACS Appl. Mater. Interfaces* **2014**, *6*, 7444–7455.

(220) López, G. P.; Castner, D. G.; Ratner, B. D. XPS O 1s Binding Energies for Polymers Containing Hydroxyl, Ether, Ketone and Ester Groups. *Surf. Interface Anal.* **1991**, *17*, 267–272.

(221) Cano, E.; Bastidas, J. M.; Polo, J. L.; Mora, N. Study of the Effect of Acetic Acid Vapor on Copper Corrosion at 40 and 80% Relative Humidity. *J. Electrochem. Soc.* **2001**, *148*, B431.

(222) Lu, S. Y.; Jin, M.; Zhang, Y.; Niu, Y. B.; Gao, J. C.; Li, C. M. Chemically Exfoliating Biomass into a Graphene-like Porous Active Carbon with Rational Pore Structure, Good Conductivity, and Large Surface Area for High-Performance Supercapacitors. *Adv. Energy Mater.* **2018**, *8*, 1–9.

(223) Kim, S.-Y.; Kim, A.-R.; Yoon, J. W.; Kim, H.-J.; Bae, Y.-S. Creation of Mesoporous Defects in a Microporous Metal-Organic Framework by an Acetic Acid-Fragmented Linker Co-Assembly and Its Remarkable Effects on Methane Uptake. *Chem. Eng. J.* **2018**, *335*, 94–100.

(224) Tien, H.-W.; Huang, Y.-L.; Yang, S.-Y.; Wang, J.-Y.; Ma, C.-C. M. The Production of Graphene Nanosheets Decorated with Silver Nanoparticles for Use in Transparent, Conductive Films. *Carbon N. Y.* **2011**, *49*, 1550–1560.

(225) Xu, Z. L.; Zhang, B.; Abouali, S.; Akbari Garakani, M.; Huang, J.; Huang, J. Q.; Kamali Heidari, E.; Kim, J. K. Nanocavity-Engineered Si/Multi-Functional Carbon Nanofiber Composite Anodes with Exceptional High-Rate Capacities. *J. Mater. Chem. A* **2014**, *2*, 17944–17951.

(226) Müller, K.; Malhi, J. S.; Wohlgemuth, J.; Fischer, R. A.; Wöll, C.; Gliemann, H.; Heinke, L. Water as a Modulator in the Synthesis of Surface-Mounted Metal–Organic Framework Films of Type HKUST-1. *Dalt. Trans.* **2018**, 16474–16479.

(227) Amirjalayer, S.; Tafipolsky, M.; Schmid, R. Surface Termination of the Metal-Organic Framework HKUST-1: A Theoretical Investigation. *J. Phys. Chem. Lett.* **2014**, *5*, 3206–3210.

(228) Li, H.; Eddaoudi, M.; O'Keeffe, M.; Yaghi, O. M. Design and Synthesis of an Exceptionally Stable and Highly Porous Metal-Organic Framework. *Nature* **1999**, *402*, 276–279.

(229) Umemura, A.; Diring, S.; Furukawa, S.; Uehara, H.; Tsuruoka, T.; Kitagawa, S. Morphology Design of Porous Coordination Polymer Crystals by Coordination Modulation. *J. Am. Chem. Soc.* **2011**, *133*, 15506–15513.

(230) Marghussian, V. Glass Crystallization. In *Nano-Glass Ceramics*; Marghussian, V. B. T.-N.-G. C., Ed.; Elsevier: Oxford, 2015; pp 1–62.

(231) Pallab Bhattacharya. *Semiconductor Optoelectronic Devices*, 2nd ed.; Prentice Hall, 1997.

(232) Kang, H. S.; Kang, J. S.; Kim, J. W.; Lee, S. Y. Annealing Effect on the Property of Ultraviolet and Green Emissions of ZnO Thin Films. *J. Appl. Phys.* **2004**, *95*, 1246–1250.

(233) Yao, M.-S.; Lv, X.-J.; Fu, Z.-H.; Li, W.-H.; Deng, W.-H.; Wu, G.-D.; Xu, G. Layer-by-Layer Assembled Conductive Metal-Organic Framework Nanofilms for Room-Temperature Chemiresistive Sensing. *Angew. Chemie Int. Ed.* **2017**, *56*, 16510–16514.

(234) Gutiérrez-Sevillano, J. J.; Vicent-Luna, J. M.; Dubbeldam, D.; Calero, S. Molecular Mechanisms for Adsorption in Cu-BTC Metal Organic Framework. *J. Phys. Chem. C* **2013**, *117*, 11357–11366.

(235) Gutiérrez-Sevillano, J. J.; Calero, S.; Krishna, R. Selective Adsorption of Water from Mixtures with 1-Alcohols by Exploitation of Molecular Packing Effects in CuBTC. *J. Phys. Chem. C* **2015**, *119*, 3658–3666.

(236) Castillo, J. M.; Vlugt, T. J. H.; Calero, S. Understanding Water Adsorption in Cu−BTC Metal−Organic Frameworks. *J. Phys. Chem. C* **2008**, *112*, 15934–15939.

(237) Henninger, S. K.; Schmidt, F. P.; Henning, H.-M. Water Adsorption Characteristics of Novel Materials for Heat Transformation Applications. *Appl. Therm. Eng.* **2010**, *30*, 1692–1702.

(238) Grajciar, L.; Bludský, O.; Nachtigall, P. Water Adsorption on Coordinatively Unsaturated Sites in CuBTC MOF. *J. Phys. Chem. Lett.* **2010**, *1*, 3354–3359.

(239) Al-Janabi, N.; Hill, P.; Torrente-Murciano, L.; Garforth, A.; Gorgojo, P.; Siperstein, F.; Fan, X. Mapping the Cu-BTC Metal–Organic Framework (HKUST-1) Stability Envelope in the Presence of Water Vapour for $CO_2$ Adsorption from Flue Gases. *Chem. Eng. J.* **2015**, *281*, 669–677.

(240) Álvarez, J. R.; Sánchez-González, E.; Pérez, E.; Schneider-Revueltas, E.; Martínez, A.; Tejeda-Cruz, A.; Islas-Jácome, A.; González-Zamora, E.; Ibarra, I. A. Structure Stability of HKUST-1 towards Water and Ethanol and Their Effect on Its $CO_2$ Capture Properties. *Dalt. Trans.* **2017**, *46*, 9192–9200.

(241) Van Assche, T. R. C.; Duerinck, T.; Gutiérrez Sevillano, J. J.; Calero, S.; Baron, G. V.; Denayer, J. F. M. High Adsorption Capacities and Two-Step Adsorption of Polar Adsorbates on Copper–Benzene-1,3,5-Tricarboxylate Metal–Organic Framework. *J. Phys. Chem. C* **2013**, *117*, 18100–18111.

(242) Küsgens, P.; Rose, M.; Senkovska, I.; Fröde, H.; Henschel, A.; Siegle, S.; Kaskel, S. Characterization of Metal-Organic Frameworks by Water Adsorption. *Microporous Mesoporous Mater.* **2009**, *120*, 325–330.

(243) Biemmi, E.; Darga, A.; Stock, N.; Bein, T. Direct Growth of $Cu_3(BTC)_2(H_2O)_3 \cdot xH_2O$ Thin Films on Modified QCM-Gold Electrodes – Water Sorption Isotherms. *Microporous Mesoporous Mater.* **2008**, *114*, 380–386.

(244) Hodgson, A.; Haq, S. Water Adsorption and the Wetting of Metal Surfaces. *Surf. Sci. Rep.* **2009**, *64*, 381–451.

(245) Sharp, C. H.; Abelard, J.; Plonka, A. M.; Guo, W.; Hill, C. L.; Morris, J. R. Alkane-OH Hydrogen Bond Formation and Diffusion Energetics of n-Butane within UiO-66. *J. Phys. Chem. C* **2017**, *121*, 8902–8906.

(246) Adil, K.; Belmabkhout, Y.; Pillai, R. S.; Cadiau, A.; Bhatt, P. M.; Assen, A. H.; Maurin, G.; Eddaoudi, M. Gas/Vapour Separation Using Ultra-Microporous Metal–Organic Frameworks: Insights into the Structure/Separation Relationship. *Chem. Soc. Rev.* **2017**, *46*, 3402–3430.

(247) Reed, D. A.; Keitz, B. K.; Oktawiec, J.; Mason, J. A.; Runčevski, T.; Xiao, D. J.; Darago, L. E.; Crocellà, V.; Bordiga, S.; Long, J. R. A Spin Transition

Mechanism for Cooperative Adsorption in Metal–Organic Frameworks. *Nature* **2017**, *550*, 96–100.

(248) Yang, Q.; Xu, Q.; Jiang, H.-L. Metal–Organic Frameworks Meet Metal Nanoparticles: Synergistic Effect for Enhanced Catalysis. *Chem. Soc. Rev.* **2017**, *46*, 4774–4808.

(249) Jiang, J.; Yaghi, O. M. Brønsted Acidity in Metal–Organic Frameworks. *Chem. Rev.* **2015**, *115*, 6966–6997.

(250) Dai, H.; Xia, B.; Wen, L.; Du, C.; Su, J.; Luo, W.; Cheng, G. Synergistic Catalysis of AgPd@ZIF-8 on Dehydrogenation of Formic Acid. *Appl. Catal. B Environ.* **2015**, *165*, 57–62.

(251) Fu, F.; Wang, C.; Wang, Q.; Martinez-Villacorta, A. M.; Escobar, A.; Chong, H.; Wang, X.; Moya, S.; Salmon, L.; Fouquet, E.; Ruiz, J.; Astruc, D. Highly Selective and Sharp Volcano-Type Synergistic $Ni_2Pt$@ZIF-8-Catalyzed Hydrogen Evolution from Ammonia Borane Hydrolysis. *J. Am. Chem. Soc.* **2018**, *140*, 10034–10042.

(252) Jiang, H.; Liu, B.; Akita, T.; Haruta, M.; Sakurai, H.; Xu, Q. Au@ZIF-8: CO Oxidation over Gold Nanoparticles Deposited to Metal−Organic Framework. *J. Am. Chem. Soc.* **2009**, *131*, 11302–11303.

(253) Li, P. Z.; Aranishi, K.; Xu, Q. ZIF-8 Immobilized Nickel Nanoparticles: Highly Effective Catalysts for Hydrogen Generation from Hydrolysis of Ammonia Borane. *Chem. Commun.* **2012**, *48*, 3173–3175.

(254) Zahmakiran, M. Iridium Nanoparticles Stabilized by Metal Organic Frameworks (IrNPs@ZIF-8): Synthesis, Structural Properties and Catalytic Performance. *Dalt. Trans.* **2012**, *41*, 12690.

(255) Dang, T. T.; Zhu, Y.; Ngiam, J. S. Y.; Ghosh, S. C.; Chen, A.; Seayad, A. M. Palladium Nanoparticles Supported on ZIF-8 As an Efficient Heterogeneous Catalyst for Aminocarbonylation. *ACS Catal.* **2013**, *3*, 1406–1410.

(256) Müller, M.; Hermes, S.; Kähler, K.; van den Berg, M. W. E.; Muhler, M.; Fischer, R. A. Loading of MOF-5 with Cu and ZnO Nanoparticles by Gas-Phase Infiltration with Organometallic Precursors: Properties of Cu/ZnO@MOF-5 as Catalyst for Methanol Synthesis. *Chem. Mater.* **2008**, *20*, 4576–4587.

(257) Hermes, S.; Schröter, M.-K.; Schmid, R.; Khodeir, L.; Muhler, M.; Tissler, A.; Fischer, R. W.; Fischer, R. A. Metal@MOF: Loading of Highly Porous Coordination Polymers Host Lattices by Metal Organic Chemical Vapor Deposition. *Angew. Chemie Int. Ed.* **2005**, *44*, 6237–6241.

(258) Stubbs, A. W.; Braglia, L.; Borfecchia, E.; Meyer, R. J.; Román- Leshkov, Y.; Lamberti, C.; Dincă, M. Selective Catalytic Olefin Epoxidation with $Mn^{II}$-Exchanged MOF-5. *ACS Catal.* **2018**, *8*, 596–601.

(259) Zhen, W.; Li, B.; Lu, G.; Ma, J. Enhancing Catalytic Activity and Stability for CO 2 Methanation on Ni@MOF-5 via Control of Active Species Dispersion. *Chem. Commun.* **2015**, *51*, 1728–1731.

(260) Liu, J.; Ye, J.; Li, Z.; Otake, K.; Liao, Y.; Peters, A. W.; Noh, H.; Truhlar, D. G.; Gagliardi, L.; Cramer, C. J.; Farha, O. K.; Hupp, J. T. Beyond the Active Site: Tuning the Activity and Selectivity of a Metal–Organic Framework-Supported Ni Catalyst for Ethylene Dimerization. *J. Am. Chem. Soc.* **2018**, *140*, 11174–11178.

(261) Ikuno, T.; Zheng, J.; Vjunov, A.; Sanchez-Sanchez, M.; Ortuño, M. A.; Pahls, D. R.; Fulton, J. L.; Camaioni, D. M.; Li, Z.; Ray, D.; Mehdi, B. L.; Browning, N. D.; Farha, O. K.; Hupp, J. T.; Cramer, C. J.; Gagliardi, L.; Lercher, J. A. Methane Oxidation to Methanol Catalyzed by Cu-Oxo Clusters Stabilized in NU-1000 Metal–Organic Framework. *J. Am. Chem. Soc.* **2017**, *139*, 10294–10301.

(262) Redfern, L. R.; Li, Z.; Zhang, X.; Farha, O. K. Highly Selective Acetylene Semihydrogenation Catalyzed by Cu Nanoparticles Supported in a Metal–Organic Framework. *ACS Appl. Nano Mater.* **2018**, *1*, 4413–4417.

(263) Zheng, J.; Ye, J.; Ortuño, M. A.; Fulton, J. L.; Gutiérrez, O. Y.; Camaioni, D. M.; Motkuri, R. K.; Li, Z.; Webber, T. E.; Mehdi, B. L.; Browning, N. D.; Penn, R. L.; Farha, O. K.; Hupp, J. T.; Truhlar, D. G.; Cramer, C. J.; Lercher, J. A. Selective Methane Oxidation to Methanol on Cu-Oxo Dimers Stabilized by Zirconia Nodes of an NU-1000 Metal–Organic Framework. *J. Am. Chem. Soc.* **2019**, *141*, 9292–9304.

(264) Abdel-Mageed, A. M.; Rungtaweevoranit, B.; Parlinska-Wojtan, M.; Pei, X.; Yaghi, O. M.; Jürgen Behm, R. Highly Active and Stable Single-Atom Cu Catalysts Supported by a Metal-Organic Framework. *J. Am. Chem. Soc.* **2019**, *141*, 5201–5210.

(265) An, B.; Zhang, J.; Cheng, K.; Ji, P.; Wang, C.; Lin, W. Confinement of Ultrasmall Cu/$ZnO_x$Nanoparticles in Metal-Organic Frameworks for Selective Methanol Synthesis from Catalytic Hydrogenation of $CO_2$. *J. Am. Chem. Soc.* **2017**, *139*, 3834–3840.

(266) Wu, R.; Qian, X.; Zhou, K.; Liu, H.; Yadian, B.; Wei, J.; Zhu, H.; Huang, Y. Highly Dispersed Au Nanoparticles Immobilized on Zr-Based Metal–Organic Frameworks as Heterostructured Catalyst for CO Oxidation. *J. Mater. Chem. A* **2013**, *1*, 14294.

(267) Yazdi, A.; Abo Markeb, A.; Garzón-Tovar, L.; Patarroyo, J.; Moral-Vico, J.; Alonso, A.; Sánchez, A.; Bastus, N.; Imaz, I.; Font, X.; Puntes, V.; Maspoch, D. Core–Shell Au/$CeO_2$ Nanoparticles Supported in UiO-66 Beads Exhibiting Full CO Conversion at 100 °C. *J. Mater. Chem. A* **2017**, *5*, 13966–13970.

(268) Rungtaweevoranit, B.; Baek, J.; Araujo, J. R.; Archanjo, B. S.; Choi, K. M.; Yaghi, O. M.; Somorjai, G. A. Copper Nanocrystals Encapsulated in Zr-Based

Metal–Organic Frameworks for Highly Selective $CO_2$ Hydrogenation to Methanol. *Nano Lett.* **2016**, *16*, 7645–7649.

(269) Bakuru, V. R.; Velaga, B.; Peela, N. R.; Kalidindi, S. B. Hybridization of Pd Nanoparticles with UiO-66(Hf) Metal-Organic Framework and the Effect of Nanostructure on the Catalytic Properties. *Chem. - A Eur. J.* **2018**, *24*, 15978–15982.

(270) Liu, H.; Chang, L.; Bai, C.; Chen, L.; Luque, R.; Li, Y. Controllable Encapsulation of "Clean" Metal Clusters within MOFs through Kinetic Modulation: Towards Advanced Heterogeneous Nanocatalysts. *Angew. Chemie - Int. Ed.* **2016**, *55*, 5019–5023.

(271) Zhang, W.; Lu, G.; Cui, C.; Liu, Y.; Li, S.; Yan, W.; Xing, C.; Chi, Y. R.; Yang, Y.; Huo, F. A Family of Metal-Organic Frameworks Exhibiting Size-Selective Catalysis with Encapsulated Noble-Metal Nanoparticles. *Adv. Mater.* **2014**, *26*, 4056–4060.

(272) Guo, Z.; Xiao, C.; Maligal-Ganesh, R. V.; Zhou, L.; Goh, T. W.; Li, X.; Tesfagaber, D.; Thiel, A.; Huang, W. Pt Nanoclusters Confined within Metal–Organic Framework Cavities for Chemoselective Cinnamaldehyde Hydrogenation. *ACS Catal.* **2014**, *4*, 1340–1348.

(273) Zhao, X.; Xu, H.; Wang, X.; Zheng, Z.; Xu, Z.; Ge, J. Monodisperse Metal–Organic Framework Nanospheres with Encapsulated Core–Shell Nanoparticles Pt/Au@Pd@{$Co_2(oba)_4(3\text{-}bpdh)_2$}$4H_2O$ for the Highly Selective Conversion of $CO_2$ to CO. *ACS Appl. Mater. Interfaces* **2018**, *10*, 15096–15103.

(274) Bakuru, V. R.; Kalidindi, S. B. Synergistic Hydrogenation over Palladium through the Assembly of MIL-101(Fe) MOF over Palladium Nanocubes. *Chem. - A Eur. J.* **2017**, *23*, 16456–16459.

(275) DeCoste, J. B.; Weston, M. H.; Fuller, P. E.; Tovar, T. M.; Peterson, G. W.; LeVan, M. D.; Farha, O. K. Metal-Organic Frameworks for Oxygen Storage. *Angew. Chemie Int. Ed.* **2014**, *53*, 14092–14095.

(276) Jeremias, F.; Fröhlich, D.; Janiak, C.; Henninger, S. K. Water and Methanol Adsorption on MOFs for Cycling Heat Transformation Processes. *New J. Chem.* **2014**, *38*, 1846–1852.

(277) Wachs, I. E.; Madix, R. J. The Selective Oxidation of $CH_3OH$ to $H_2CO$ on a Copper(110) Catalyst. *J. Catal.* **1978**, *53*, 208–227.

(278) Leibsle, F. M.; Francis, S. M.; Haq, S.; Bowker, M. Aspects of Formaldehyde Synthesis on Cu(110) as Studied by STM. *Surf. Sci.* **1994**, *318*, 46–60.

(279) Davies, P. R.; Mariotti, G. G. Oxidation of Methanol at Cu(110) Surfaces: New TPD Studies. *J. Phys. Chem.* **1996**, *100*, 19975–19980.

(280) Carley, A. F.; Davies, P. R.; Mariotti, G. G.; Read, S. Reaction Pathways in Methanol Oxidation at Cu(110) Surfaces. *Surf. Sci.* **1996**, *364*, L525–L529.

(281) Carley, A. F.; Owens, A. W.; Rajumon, M. K.; Roberts, M. W.; Jackson, S. D. Oxidation of Methanol at Copper Surfaces. *Catal. Letters* **1996**, *37*, 79–87.

(282) Sexton, B. A.; Hughes, A. E.; Avery, N. R. Surface Intermediates in the Reaction of Methanol, Formaldehyde and Methyl Formate on Copper (110). *Appl. Surf. Sci.* **1985**, *22–23*, 404–414.

(283) Bowker, M.; Madix, R. J. XPS, UPS and Thermal Desorption Studies of Alcohol Adsorption on Cu(110). *Surf. Sci.* **1980**, *95*, 190–206.

(284) Sexton, B. A.; Hughes, A. E.; Avery, N. R. A Spectroscopic Study of the Adsorption and Reactions of Methanol, Formaldehyde and Methyl Formate on Clean and Oxygenated Cu(110) Surfaces. *Surf. Sci.* **1985**, *155*, 366–386.

(285) Francis, S. M.; Leibsle, F. M.; Haq, S.; Xiang, N.; Bowker, M. Methanol Oxidation on Cu(110). *Surf. Sci.* **1994**, *315*, 284–292.

(286) Varazo, K.; Parsons, F. W.; Ma, S.; Chen, D. A. Methanol Chemistry on Cu and Oxygen-Covered Cu Nanoclusters Supported on $TiO_2$(110). *J. Phys. Chem. B* **2004**, *108*, 18274–18283.

(287) Stavila, V.; Volponi, J.; Katzenmeyer, A. M.; Dixon, M. C.; Allendorf, M. D. Kinetics and Mechanism of Metal–Organic Framework Thin Film Growth: Systematic Investigation of HKUST-1 Deposition on QCM Electrodes. *Chem. Sci.* **2012**, *3*, 1531.

(288) Meckler, S. M.; Li, C.; Queen, W. L.; Williams, T. E.; Long, J. R.; Buonsanti, R.; Milliron, D. J.; Helms, B. A. Sub-Micron Polymer–Zeolitic Imidazolate Framework Layered Hybrids via Controlled Chemical Transformation of Naked ZnO Nanocrystal Films. *Chem. Mater.* **2015**, *27*, 7673–7679.

(289) Nečas, D.; Klapetek, P. Gwyddion: An Open-Source Software for SPM Data Analysis. *Open Phys.* **2012**, *10*, 181–188.

(290) Fan, S.; Dong, W.; Huang, X.; Gao, H.; Wang, J.; Jin, Z.; Tang, J.; Wang, G. In Situ-Induced Synthesis of Magnetic Cu-$CuFe_2O_4$ @HKUST-1 Heterostructures with Enhanced Catalytic Performance for Selective Aerobic Benzylic C–H Oxidation. *ACS Catal.* **2017**, *7*, 243–249.

(291) Niveditha, C. V.; Fatima, M. J. J.; Sindhu, S. Comprehensive Interfacial Study of Potentio-Dynamically Synthesized Copper Oxide Thin Films for Photoelectrochemical Applications. *J. Electrochem. Soc.* **2016**, *163*, H426–H433.

(292) Brown, K. E. R.; Choi, K.-S. Electrochemical Synthesis and Characterization of Transparent Nanocrystalline Cu2O Films and Their Conversion to CuO Films. *Chem. Commun.* **2006**, *1*, 3311.

(293) Zhou, L.; Niu, Z.; Jin, X.; Tang, L.; Zhu, L. Effect of Lithium Doping on the Structures and $CO_2$ Adsorption Properties of Metal-Organic Frameworks HKUST-1. *ChemistrySelect* **2018**, *3*, 12865–12870.

(294) Baddorf, A. P.; Wendelken, J. F. High Coverages of Oxygen on Cu(110) Investigated with XPS, LEED, and HREELS. *Surf. Sci.* **1991**, *256*, 264–271.

(295) Bange, K.; Grider, D. E.; Madey, T. E.; Sass, J. K. The Surface Chemistry of H2O on Clean and Oxygen-Covered Cu(110). *Surf. Sci.* **1984**, *137*, 38–64.

(296) Polak, M. On the Structure and Bonding of $H_2O$ Adsorbed on Cu(110). *Surf. Sci.* **1994**, *321*, 249–260.

(297) Therrien, A. J.; Zhang, R.; Lucci, F. R.; Marcinkowski, M. D.; Hensley, A.; McEwen, J.-S.; Sykes, E. C. H. Structurally Accurate Model for the "29"-Structure of $Cu_xO$/Cu(111): A DFT and STM Study. *J. Phys. Chem. C* **2016**, *120*, 10879–10886.

(298) Jensen, F.; Besenbacher, F.; Lægsgaard, E.; Stensgaard, I. Oxidation of Cu(111): Two New Oxygen Induced Reconstructions. *Surf. Sci.* **1991**, *259*, 0–6.

(299) Matsumoto, T.; Bennett, R. a.; Stone, P.; Yamada, T.; Domen, K.; Bowker, M. Scanning Tunneling Microscopy Studies of Oxygen Adsorption on Cu(111). *Surf. Sci.* **2001**, *471*, 225–245.

(300) Malas, A.; Bharati, A.; Verkinderen, O.; Goderis, B.; Moldenaers, P.; Cardinaels, R. Effect of the GO Reduction Method on the Dielectric Properties, Electrical Conductivity and Crystalline Behavior of PEO/RGO Nanocomposites. *Polymers.* **2017**, *9*, 613.

(301) Eland, J. H. D.; Treves-Brown, B. J. The Fragmentation of Doubly Charged Methanol. *Int. J. Mass Spectrom. Ion Process.* **1992**, *113*, 167–176.

(302) Fisher, I. A.; Bell, A. T. A Mechanistic Study of Methanol Decomposition over Cu/$SiO_2$, $ZrO_2$/$SiO_2$, and Cu/$ZrO_2$/$SiO_2$. *J. Catal.* **1999**, *184*, 357–376.

(303) Clarke, D. B.; Lee, D. K.; Sandoval, M. J.; Bell, A. T. Infrared Studies of the Mechanism of Methanol Decomposition on Cu/$SiO_2$. *J. Catal.* **1994**, *150*, 81–93.

(304) Greeley, J.; Mavrikakis, M. Methanol Decomposition on Cu(111): A DFT Study. *J. Catal.* **2002**, *208*, 291–300.

(305) Mei, D.; Xu, L.; Henkelman, G. Potential Energy Surface of Methanol Decomposition on Cu(110). *J. Phys. Chem. C* **2009**, *113*, 4522–4537.

(306) Jiang, Z.; Guo, S.; Fang, T. Theoretical Investigation on the Dehydrogenation Mechanism of $CH_3OH$ on Cu (100) Surface. *J. Alloys Compd.* **2017**, *698*, 617–625.

(307) Henderson, M. A.; Mitchell, G. E.; White, J. M. The Decomposition of Formaldehyde on Pt(111): A TPD and Hreels Study. *Surf. Sci.* **1987**, *188*, 206–218.

(308) Houtman, C.; Barteau, M. A. Reactions of Formic Acid and Formaldehyde on Rh(111) and Rh(111)-(2 × 2)O Surfaces. *Surf. Sci.* **1991**, *248*, 57–76.

(309) Davis, J. L.; Barteau, M. A. Polymerization and Decarbonylation Reactions of Aldehydes on the Pd(111) Surface. *J. Am. Chem. Soc.* **1989**, *111*, 1782–1792.

# Vita

Sungmin Han was born in Anyang, Korea Republic. He received a B.S. in Materials Science and Engineering at Hanyang University in 2013. During his undergrad, he conducted research about the self-assembly of $TiO_2$ and β-cyclodextrin under the supervision of Prof. William Nichols. After that, he moved to Korea Advanced Institute of Science and Technology (KAIST) for his master degree. While staying in KAIST, he conducted DFT calculations for the magnetism of Fe-MOF-74 under the supervision of Prof. Yousung Jung. In 2015, He finished his master degree in KAIST and joined the University of Texas at Austin to pursue his Ph. D. in Chemistry under the supervision of Prof. C. Buddie Mullins. For his Ph. D., He investigated oxidative reactions on the Pd–Au(111) bimetallic surface under ultrahigh vacuum and developed the growth method for HKUST-1 MOF thin films under vacuum

Email address: sungmin.han@utexas.edu

This dissertation was typed by the author.